20 July 2012 | $10

Science

AAAS

EDITORIAL

NEWS OF THE WEEK

NEWS & ANALYSIS

NEWS FOCUS

LETTERS

BOOKS *ET AL.*

POLICY FORUM

PERSPECTIVES

CONTENTS continued >>

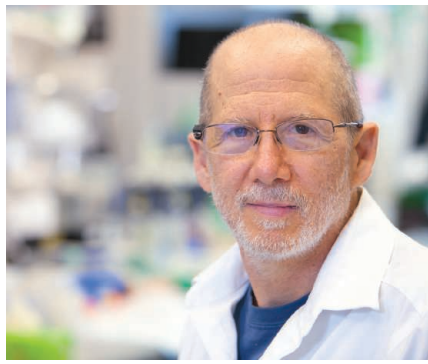

page 282

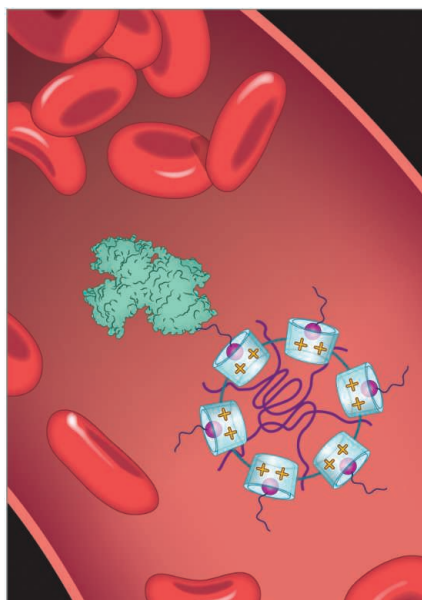

page 303

COVER

Lake El'gygytgyn, measuring 12 kilometers in diameter and 170 meters in depth, is located in a meteorite impact crater 100 kilometers to the north of the Arctic Circle in northeastern Russia. An international drilling campaign recovered a sediment record from the bottom of the lake, which sheds new light on the climate history of the Arctic over the past 2.8 million years. See page 315.

Photo: Petr Tikhomirov

DEPARTMENTS

REVIEW

RESEARCH ARTICLE

REPORTS

CONTENTS continued >>

pages 306 & 349

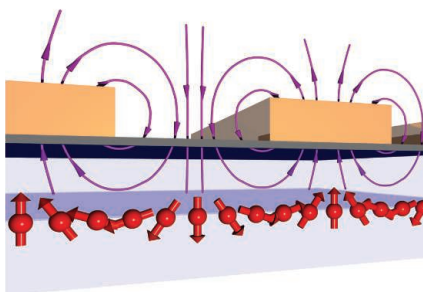

pages 307 & 324

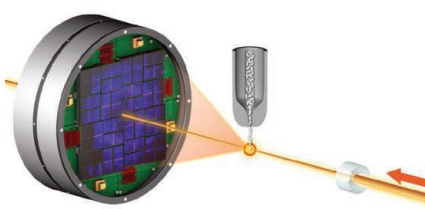

page 362

CREDIT: (MIDDLE) TOBIAS DOLLINGER/UNIVERSITÄT REGENSBURG

SCIENCEONLINE

SCIENCEXPRESS
www.sciencexpress.org

A Reversible and Higher-Rate Li-O_2 Battery
Z. Peng et al.
A viable lithium-oxygen battery is demonstrated using dimethylsulfoxide electrolyte and a porous gold cathode.
10.1126/science.1223985

Earthquake in a Maze: Compressional Rupture Branching During the 2012 M_w 8.6 Sumatra Earthquake
L. Meng et al.
The mechanics of the largest strike-slip earthquake ever recorded give clues about how intraplate earthquakes rupture.
10.1126/science.1224030

TLR13 Recognizes Bacterial 23*S* rRNA Devoid of Erythromycin Resistance–Forming Modification
M. Oldenburg et al.
A region of ribosomal RNA that confers antibiotic resistance is also recognized by mouse innate immune receptors.
10.1126/science.1220363

A Single Progenitor Population Switches Behavior to Maintain and Repair Esophageal Epithelium
D. P. Doupé et al.
Dividing cells in the mouse esophagus contribute to wound healing without the need for quiescent stem cells.
10.1126/science.1218835

Drosophila Dosage Compensation Involves Enhanced Pol II Recruitment to Male X-Linked Promoters
T. Conrad et al.
Boosting gene expression from the entire X chromosome in males happens mainly at the level of transcription initiation.
10.1126/science.1221428

Strategy-Dependent Encoding of Planned Arm Movements in the Dorsal Premotor Cortex
T. M. Pearce and D. W. Moran
The amount of preparatory neural activity in the brain depends on movement complexity and conscious planning.
10.1126/science.1220642

TECHNICALCOMMENTS

Comment on "Illusions Promote Mating Success in Great Bowerbirds"
G. Borgia et al.
Full text at www.sciencemag.org/cgi/content/full/337/6092/292-b

Response to Comment on "Illusions Promote Mating Success in Great Bowerbirds"
J. A. Endler et al.
Full text at www.sciencemag.org/cgi/content/full/337/6092/292-c

SCIENCENOW
www.sciencenow.org
Highlights From Our Daily News Coverage

Imagining Tomorrow's Computers Today
Intel futurist Brian David Johnson tries to forecast how we will interact with technology in 2020.
http://scim.ag/Future_Computers

Europe Opens Door to Young NSF Grantees
A new agreement lets early-career scientists join ERC-funded groups for up to one year.
http://scim.ag/Young-Grantees

Sailing Expedition Reveals Oceans' Tiniest Secrets
A worldwide plankton sampling effort yields 1.5 million taxa.
http://scim.ag/Tiniest-Secrets

SCIENCESIGNALING
www.sciencesignaling.org
The Signal Transduction Knowledge Environment
17 July issue: http://scim.ag/ss071712

RESEARCH ARTICLE: Epidermal Growth Factor Receptor Is Essential for Toll-Like Receptor 3 Signaling
M. Yamashita et al.
Growth factor receptor activity contributes to the antiviral response.

RESEARCH ARTICLE: Abl Family Kinases Modulate T Cell–Mediated Inflammation and Chemokine-Induced Migration Through the Adaptor HEF1 and the GTPase Rap1
J. J. Gu et al.
Inhibitors of Abl family kinases block T cell migration and could be used to treat inflammatory diseases.

PERSPECTIVE: GSK3-Like Kinases Integrate Brassinosteroid Signaling and Stomatal Development
S. A. Casson and A. M. Hetherington
Brassinosteroid signaling is crucial for stomatal development.

SCIENCETRANSLATIONAL MEDICINE
www.sciencetranslationalmedicine.org
Integrating Medicine and Science
18 July issue: http://scim.ag/stm071812

STATE OF THE ART REVIEW: HIV-1 Reservoirs in Breast Milk and Challenges to Elimination of Breast-Feeding Transmission of HIV-1
P. Van de Perre et al.
The breast milk of HIV-infected mothers contains reservoirs of HIV, even when they are successfully treated with antiretroviral therapy; new approaches to prophylactic therapy are needed to prevent HIV transmission to their infants through breast-feeding.

RESEARCH ARTICLE: Rapid Evolution of HIV-1 to Functional $CD8^+$ T Cell Responses in Humanized BLT Mice
T. E. Dudek et al.
Humanized BLT mice accurately develop human HIV-specific $CD8^+$ T cell responses capable of rapidly selecting for CTL escape mutations.

RESEARCH ARTICLE: Cardiac Glycosides Exert Anticancer Effects by Inducing Immunogenic Cell Death
L. Menger et al.
Cardiac glycosides kill cancer cells in a way that stimulates the immune response.

RESEARCH ARTICLE: Continuous Intravesical Lidocaine Treatment for Interstitial Cystitis/Bladder Pain Syndrome—Safety and Efficacy of a New Drug Delivery Device
J. C. Nickel et al.
Interstitial cystitis/bladder pain syndrome patients tolerate and experience symptomatic relief from a bladder-borne device that provides continuous lidocaine delivery.

COMMENTARY: Reporting Actionable Research Results—Shared Secrets Can Save Lives
L. E. Hunter et al.
Controlled use of a cryptographic method for returning research results to human subjects can improve medical care with a modest cost to privacy.

SCIENCECAREERS
www.sciencecareers.org/career_magazine
Free Career Resources for Scientists

Tooling Up: Advice from the C-Suite
D. Jensen
Advice from top executives reflects long experience climbing the corporate ranks, hiring people, and watching others succeed and fail.
http://scim.ag/CSuiteAdvice
>> Science *Podcast*

How to Collaborate
S. A. Holgate
Scientist seeks honest, reliable partner for meaningful research discussions and possibly more, ideally for a long-term relationship.
http://scim.ag/CollaborateEffectively

SCIENCEPODCAST
www.sciencemag.org/multimedia/podcast
Free Weekly Show

On the 20 July *Science* Podcast: generating new sex chromosomes, observing climate change in action, advice from the C-suite, and more.

SCIENCE (ISSN 0036-8075) is published weekly on Friday, except the last week in December, by the American Association for the Advancement of Science, 1200 New York Avenue, NW, Washington, DC 20005. Periodicals Mail postage (publication No. 484460) paid at Washington, DC, and additional mailing offices.

AAAS
ADVANCING SCIENCE, SERVING SOCIETY

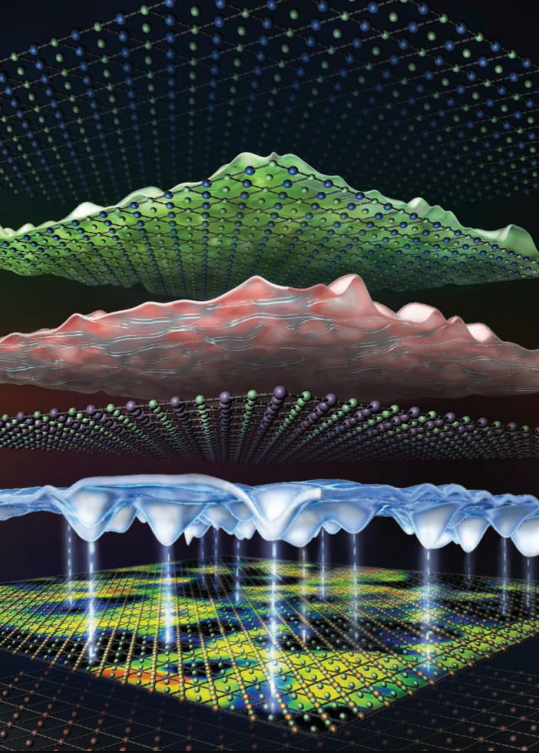

It's the Oxygens

Scanning tunneling microscopy of cuprate high-temperature superconductors has revealed surprising inhomogeneity of the energy scales known as the superconducting gap, pseudogap, and the critical temperature. Some of these effects have been correlated with chemical disorder of the materials caused by doping, but, because of technical limitations, only the dopants in a limited energy range have been imaged. **Zeljkovic *et al.*** (p. 320) extend this range to reveal the positions of the remaining oxygen defects in $Bi_{2+y}Sr_{2-y}CaCu_2O_{8+x}$.

The Primordial Soup

Protons and neutrons were originally thought to be indivisible, but we now know that they have constituent parts—quarks. Quarks are bound together tightly through gluons and can only come apart under extreme conditions—conditions believed microseconds after the Big Bang to have formed a hot, dense "soup" of quarks and gluons, called the quark-gluon plasma (QGP). QGP can be made experimentally in heavy ion colliders, where extremely high temperatures are reached. **Jacak and Müller** (p. 310) review the progress in this field and its unexpected ties to cold atomic gases and string theory.

Crater Core

The high-northern latitudes of the Arctic have an important influence on climate and constitute a region with a unique array of complex feedbacks that make it difficult to understand the workings of its climate. **Melles *et al.*** (p. 315, published online 21 June) developed a 2.8-million-year record of Arctic climate, using a sediment core from a lake in northeastern Russia that was formed more than 3.5 million years ago by a meteorite impact. Pronounced glacial episodes began 2.6 million years ago but did not achieve orbital pacing for another 700,000 years.

A Different Spin Transistor

A typical transistor consists of a source and a drain; the current that makes it to the drain is controlled by applying voltage to the third terminal, called the gate. In spin-based electronics, where spin current is used instead of charge, the source and the drain are ferromagnetic materials connected by a narrow semiconducting channel. This design, however, suffers from low efficiency. **Betthausen *et al.*** (p. 324; see the Perspective by **Žuti and Lee**) combined homogeneous and helical magnetic fields to change the orientation of the spin on its way to the drain, preserving spin information over distances many times the spin mean free path. The transistor is "on" when the transport is adiabatic—i.e., slow enough for the spin to be able to adapt to the local magnetic field—and "off" otherwise.

Magnetically Bound

At the macroscopic scale associated with daily life on Earth, magnetic attraction can seem fairly strong—think of the great loads moved by magnetized cranes. Microscopically, however, the field strengths attainable by human construction act as just a small perturbation on the Coulombic forces that bind atoms into molecules. **Lange *et al.*** (p. 327; see the Perspective by **Schmelcher**) used theoretical calculations to examine atomic behavior in environments very close to certain stars, where magnetic fields exceed those attainable on Earth by factors of 10,000 or more. The results predict a distinct type of chemical bonding in which spin-parallel hydrogen atoms or ground-state helium atoms are drawn together into pairs.

Who Influences Who?

A goal in social science is how to assess people's influence over one. **Aral and Walker** (p. 337, published online 21 June) describe a generalized method for identifying influential and susceptible members of social networks based on large-scale in vivo randomized experimentation. The method was used to estimate peer effects in consumer demand for a commercial Facebook application in a representative sample of 12 million Facebook users. Older users were more influential than younger users, women were more influential over men than men over women, and married individuals were the least susceptible to influence in the decision to adopt the product studied.

Sex Chromosome Evolution

The fly genus *Drosophilia* has repeatedly generated evolutionarily new sex chromosomes. To understand the changes shaping the X and Y chromosomes, **Zhou and Bachtrog** (p. 341), sequenced the genome of *D. miranda*, which formed neo-X and neo-Y chromosomes approximately 1 million years ago. The data illuminate the ongoing conflict between selection for male and female function on the sex chromosomes and show that Y chromosome evolution is characterized both by a loss of gene function and selection for male-specific adaptations in genes beneficial to male functions.

More than a Dash of Sea Salt

The cycling of major elements, such as sulfur, in the oceans depends on a number of processes, from bacterial respiration of organic matter to venting of gases from hydrothermal vents on the seafloor. Over geologic time, sediment deposited on the seafloor preserves chemical records of major changes in sulfur cycling and seawater chemistry (see the Perspective by **Hurtgen**).

Halevy *et al.* (p. 331) observed swings in sulfur isotopes in a stratigraphic database covering North America and the Caribbean that, when modeled, corresponded to variable evaporite preservation and high turnover of sedimentary pyrite. **Wortmann and Paytan** (p. 334) modeled the two most recent major swings in sedimentary sulfur isotopes over the last 130 million years and suggest that short periods of rapid fluxes in sulfur cycling were at least in part caused by the growth and dissolution of evaporite deposits.

Continued on page 268

CREDITS (TOP TO BOTTOM): KRISTA SHAPTON/BLOT MEDIA INC.; SHANAN PETERS

Continued from page 267

Redox Status Incites Gametogenesis

Germ cells differ from somatic cells in their chromosomal complement, being haploid rather than diploid. In animals, the germ cells are generally produced by a separate lineage set aside early in development. Plants, however, lack a reserved germ cell lineage. **Kelliher and Walbot** (p. 345; see the Perspective by **Whipple**) now show that, in maize, the key signal for germ cell production is hypoxia, which triggers differentiation of anther germ cells from a generalized field of progenitors. The specializing germ cells then induce differentiation of supportive somatic cells.

Diversity of Interactions

The diversity in interactions that occur between different species—such as predation, competition, and mutualism—is a fundamental feature of natural ecological systems. Using a theoretical model, **Mougi and Kondoh** (p. 349; see the Perspective by **Boyd**) show that the diversity of ecological relationship helps a biological community to be stable and thus may be key to the maintenance of biodiversity itself.

Lysosomal Amino Acid Transporter

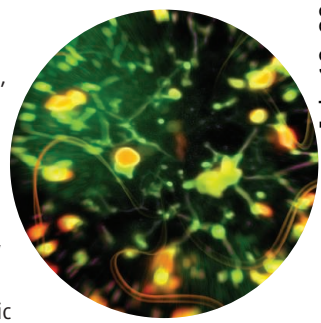

Cystinosis is characterized by intralysosomal accumulation of free cystine, which results in age-dependent problems in the kidney, muscle, retina, and central nervous system. The disease-causing gene encodes a lysosomal cystine transporter. The most effective therapeutic agent for cystinosis, cysteamine, depletes lysosomal free cystine by converting it to cysteine and the mixed disulfide cysteine-cysteamine, which can then be exported from lysosomes as a lysine analog through a putative lysine/cationic amino acid transporter. Using an unbiased genetic screen for *Caenorhabditis elegans* mutants with increased accumulation of apoptotic cells or autophagosomes, **Liu *et al.*** (p. 351) now reveal the molecular identity of a lysosomal lysine/arginine transporter that plays a role in maintaining lysosome function and amino acid homeostasis and that can explain how cysteamine alleviates a lysosomal storage disease.

Never Let Me Go

Kinetochores are the structures within chromosomes that interact with the microtubules of the mitotic spindle during mitosis. By measuring the deformation of individual kinetochores in live mammalian cells, **Dumont *et al.*** (p. 355, published online 21 June) asked, how do kinetochores harness the free energy of microtubule depolymerization without losing grip of microtubules? Kinetochores contacted microtubules using two distinct mechanical interfaces: an active, force-generating interface near the microtubule tip, and a passive, frictional interface at least 20 nanometers away along the microtubule lattice. The separate active and passive interfaces allowed for intermittent force generation and persistent microtubule attachment—both required for accurate chromosome segregation.

Born to Stay Together

For as many neurons as there are in the brain, there are many more astrocytes. These backstage workers perform a variety of functions, such as sustaining the blood-brain barrier and providing a stabilized environment for neurons. Diversity of astrocyte function is reflected in different molecular expression profiles. **Tsai *et al.*** (p. 358, published online 28 June) selectively labeled astrocytes that originated from different domains of the mouse spinal cord and found that not all astrocytes are created equal: Neighborhoods of astrocytes were defined by shared birthplaces.

Size Matters Less

X-ray crystallography is a central research tool for uncovering the structures of proteins and other macromolecules. However, its applicability typically requires growth of large crystals, in part because a sufficient number of molecules must be present in the lattice for the sample to withstand x-ray–induced damage. **Boutet *et al.*** (p. 362, published online 31 May) now demonstrate that the intense x-ray pulses emitted by a free-electron laser source can yield data in few enough exposures to uncover the high-resolution structure of microcrystals.

CREDIT: IMAGE PREPARED BY BIN LIU AND NING YANG/NATIONAL INSTITUTE OF BIOLOGICAL SCIENCES, BEIJING

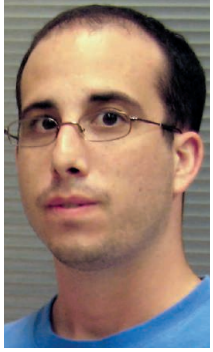

Aaron D. Gitler is an associate professor of Genetics at the Stanford University School of Medicine in Stanford, CA. E-mail: agitler@stanford.edu.

Ruth Lehmann is the Laura and Isaac Perlmutter Professor of Cell Biology and an Investigator of the Howard Hughes Medical Institute at the Skirball Institute of Biomolecular Medicine and the New York University School of Medicine in New York. E-mail: Ruth.Lehmann@med.nyu.edu.

Modeling Human Disease

THE ASTONISHING RECENT ADVANCES IN THE TECHNOLOGY FOR DETERMINING DNA SEQUENCES HAVE made personalized genomics a foreseeable reality for the doctor's office. This technology has started a whole new gold rush for human disease gene discovery and produced an onslaught of information that represents a new challenge in personalized medicine: connecting genotype to phenotype. Experimental organisms such as yeast, worms, fruit flies, zebrafish, and mice have long been critical for discovering the molecular mechanisms fundamental to life, thereby providing a shortcut to understanding human biology. The new developments allow these model organisms to also provide key insights into the association of specific genes with human disease.

Much of what we know about cancer can be traced back to basic studies in yeast cells aimed at decoding cell division. Likewise, studies in the worm revealed the mechanisms of programmed cell death and identified molecular targets that hold great promise for anticancer therapies. The fruit fly, an experimental workhorse in genetics for over a century, has elucidated cellular signaling pathways critical for human development, which often cause disease when dysregulated. And vertebrate model systems such as zebrafish, frogs, rats, and mice have provided insights into basic principles of cell and developmental biology with direct relevance to human disease. Yet despite their indisputable role in fundamental discoveries, some critics are questioning the continued need for model organism research, arguing that new tools such as whole-genome sequencing and patient-derived cells have now made humans and their cells accessible for studies of genes and gene products.

Such arguments ignore the massive amount that scientists have yet to learn in order to understand the function of even a single gene within the context of a living organism. Today, it is not possible to assign a function to at least half of the tens of thousands of proteins in vertebrate cells; moreover, it is the networks of interactions between them that make life possible, and the staggering complexity of these networks will require the innovative use of model organisms to decipher how these networks are used during embryonic development, adapted during aging and when environmental changes occur, and dysregulated in disease. Examples include using inexpensive, readily accessible model systems to tackle very complicated problems, such as how errors in protein folding cause neurodegeneration or discovering and understanding the astonishing and ever-expanding role of noncoding RNAs in regulating almost every aspect of cellular function.

How is work in model organisms valuable to research on specific human diseases? The best recent examples come from genome-sequencing technologies that are being applied to discover possible causes of rare and common genetic diseases. This has led to the surprising finding that there are more variants in the coding regions of genes than previously anticipated. Moreover, there is compelling evidence for a major role of noncoding genetic variation in human disease, associated with changes in gene regulation. How does each of the many variants in genes and gene regulatory regions contribute to the risk for specific diseases or disease outcomes? Insights may come from modeling these variants in genetically more amenable organisms.

We suggest a future in which model organisms will be deployed to work out the basic biology of newly discovered disease genes, assign functions to disease-associated variants, and even to uncover previously unknown disease genes. Remarkably, a goal to define all genetic contributors to a human disease is now fathomable. Some genes will be straightforward to find, but others (perhaps most) will require creative strategies. For example, unbiased genetic interaction screens in model organisms can be combined with human genetics to discover and validate disease genes. It is not time to abandon tried-and-true model organisms but rather to embrace the traditional model systems, develop new models, and forge collaborations between human geneticists and model organism researchers. Let's combine the powerful advances in human genetics with the versatility of model organisms to fulfill the promise of personalized medicine.

– Aaron D. Gitler and Ruth Lehmann

10.1126/science.1227179

Published by AAAS

SOCIOLOGY

Intimidated by Equations?

Although there is general agreement on the value of a strong tie between theory and data, forging links between theoretical and empirical approaches (and practitioners) is not as straightforward as it should be. New evidence of this disconnect comes from the work of Fawcett and Higginson, who examined the use of mathematical equations in 649 papers dealing with ecology and evolution that were published in 1998. They gathered citation data, excluding instances of self-citation. An increase in the number of equations per page of main text corresponded to a lower rate of citations. Overall, each additional equation in the main text of a paper was associated with a 28% decrease in the citation rate. Burying the equations in an appendix had a salutary effect on citation rate. When the citing papers were divided into theoretical and nontheoretical on the basis of their use of the word "model" in the abstract or title, the authors observed that the negative effect was due to the nontheoretical papers not citing papers with equations. There are caveats to the conclusions—examinations over longer periods of time, analysis of the relative content of the papers, and examination of the effect for online rather than print publication are all warranted. Although the authors conclude that better math education for biologists is the best long-term solution, they suggest that more immediate strategies could include the addition of explanatory text between equations. — BJ

Proc. Natl. Acad. Sci. U.S.A. **109**, 10.1073/pnas.1205259109 (2012).

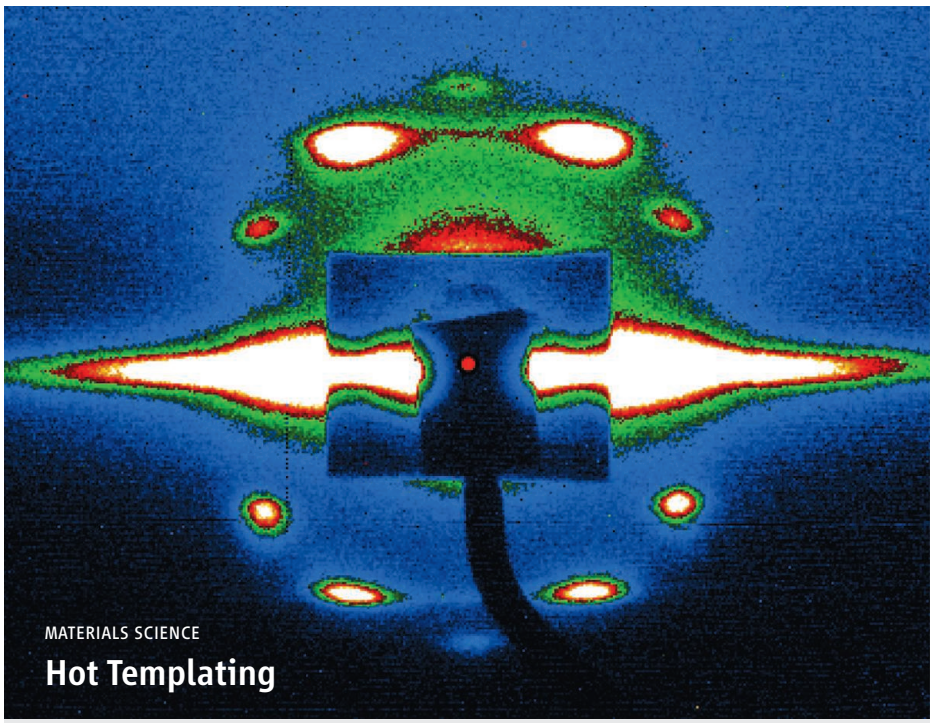

MATERIALS SCIENCE

Hot Templating

One method for creating ordered mesoporous materials is to use the phase separation of block copolymers to create a mold for patterning a second material. Typically, the structure of the template is fixed after solvent evaporation. Schuster *et al*. applied small-angle x-ray scattering (SAXS) to follow the pyrolytic formation of mesoporous carbon films using commercial triblock polymers as templates and oligomeric resol as a carbon precursor. They spin-coated these solutions onto silicon substrates or spread them onto the surface of porous anodic alumina membranes, then monitored the thermal evolution of their structures with grazing incidence or in situ SAXS, respectively. Analysis showed that the self-assembly of the mesoporous phase (cylindrical holes in a face-centered orthorhombic or circular hexagonal structure, respectively) does not occur after solvent evaporation but during pyrolysis, and that changes in the heating rate can lead to changes in the unit-cell parameters. — PDS

J. Am. Chem. Soc. **134**, 10.1021/ja208941s (2012).

ECOLOGY

Half Truths

Deception is complicated because it requires the cognitive skills to both assess the potential for its efficacy and to carry it off. Cephalopods are known masters of deceptive behavior, often using camouflage as a way to rapidly mimic their environment, or even other organisms, in their attempts to avoid predation. Brown *et al*. now show that mourning cuttlefish (*Sepia plangon*) have taken this exceptional deceptive ability a step farther than mere run-of-the-mill camouflage. In most cuttlefish species, courting males assume a particular coloration when attempting to mate with females. This coloration attracts females but can also attract rival males, who may displace the courting male. In order to avoid attracting these potential competitors but still maintain the female's attention, males will often perform split coloration displays. They mimic female coloration on the side of their bodies facing a rival, while displaying male courtship coloration on the side facing the female. Males perform this split display only when they are approached by a single male, presumably because it is only under these circumstances that they are able to maintain an appropriately deceptive angle. These results confirm the idea that mimicry can be highly advantageous in many contexts and suggest that these types of social and deceptive interactions may have helped to shape the high cognitive functioning of cephalopods. — SNV

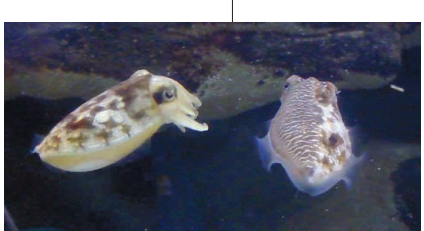

Biol. Lett. **8**, 10.1098/rsbl.2012.0435 (2012).

CHEMISTRY

A Glimpse of Gold

Gold nanoparticles supported on titania have high catalytic activity; for example, in the oxidation of carbon monoxide at room temperature. What are the structural properties of the Au/TiO_2 catalyst that enable this catalytic activity? Transmission electron microscopy has provided structural information, but the strong electron beam can damage the system, and it remains unclear whether the associated images represent the active structure of the catalyst. Kuwauchi

CREDITS (TOP TO BOTTOM): SCHUSTER *ET AL*., *J. AM. CHEM. SOC.* **134**, 10.1021/JA208941S (2012); BROWN *ET AL*., *BIOL. LETT.* **8**, 10.1098/RSBL.2012.0435 (2012)

Published by AAAS

et al. now report the use of environmental transmission electron microscopy, which allows the catalyst to be studied under reaction conditions. They find that the nanoparticle morphology varies systematically in differing environments, changing from faceted to round, depending on the gases present. In contrast, the support maintains its crystallinity throughout the experiments, and the interface between the particles and the support also remains stable. By systematically studying the effects of electron irradiation on the structure, the authors derive conditions under which no detectable structural damage occurs, thus making it possible to deduce the intrinsic structure of the catalyst under reaction conditions. — JFU

Angew. Chem. Int. Ed. **51**, 10.1002/anie.201201283 (2012).

PHYSICS

Intrinsic Origins

Interfacing two unlike materials may give rise to unexpected properties resulting from the asymmetry of the structure. Such is the case in two-dimensional interfaces of perovskite oxide films; in the best-known example of the $LaAlO_3$/$SrTiO_3$ (LAO/STO) interface, ferromagnetism has been observed even though neither of the two materials is magnetic in the bulk. This and other interface effects are thought to originate from STO, but whether they are an intrinsic property of the electron liquid in STO is not known. Moetakef *et al.* study the magnetism in STO using two systems: $GdTiO_3$/STO heterostructures and La-doped STO films; in both cases, STO is doped with carriers, from the interface or the La dopants, respectively. The authors observe ferromagnetism in both systems, and superconductivity coexisting with magnetism in the doped films. The ferromagnetic Curie temperature increases strongly with the carrier density measured through the Hall effect, and the data from the two systems fall onto the same curve, indicating universal dependence and an intrinsic mechanism. — JS

Phys. Rev. X **2**, 021014 (2012).

CHEMISTRY

Figure Nine

Nitrogen occurs naturally as a rather tightly bound neutral dimer, and anionic azide (N_3^-) salts have long been accessible as well. A cation composed purely of nitrogen arrived only much more recently on the scene, with the preparation of an N_5^+ salt about a decade ago. The heavier congener phosphorus has followed a similar path: a variety of well-established neutral and negatively charged morphologies, but until now no tractable cation salts. Köchner *et al.* have filled the gap with the preparation of a P_9^+ salt. Key to its isolation was the use of an especially inert, aluminum-centered counterion adorned with trifluoromethyl groups. The synthesis entailed oxidation of neutral P_4 by the nitrosonium salt of this counterion in dichloromethane solvent. Ultraviolet irradiation facilitated reaction of an apparent $[P_4NO]^+$ intermediate (and precipitation of excess neutral phosphorus) without damaging the ultimate product, which was isolable as a yellow-orange powder. Nuclear magnetic resonance spectroscopy in conjunction with theoretical calculations revealed a figure 8-type structure, of D_{2d} symmetry, in which a central tetracoordinate P atom bridges two clusters of four P atoms each. The salt was also characterized by mass spectrometry and infrared and Raman spectroscopy, and persisted for weeks in room-temperature solution. The authors envision prospective applications of the salt in currentless deposition protocols. — JSY

Angew. Chem. Int. Ed. **51**, 6529 (2012).

ECOLOGY

Diversity Persists

Marine ecosystems are characterized by high tropical and low polar biodiversity, and are correlated with water temperature. Fossil evidence hints at the persistence of such gradients for over 270 million years, but little is known about the details. Yasuhara *et al.* have chosen to examine the fossil record for North Atlantic

zooplankton, because the fossils are abundant and the record is the most complete of any marine taxon. Times slices spanning the past 3 million years showed that tropical-high and polar-low diversity persisted throughout this period, with highest diversities during the mid-Pliocene. It seems that the species that have gone extinct since the Pliocene had narrower thermal tolerances than modern species and were selected out by the glaciation. — CA

Ecol. Lett. **15**, 10.1111/j.1461-0248.2012.01828.x (2012).

CREDIT: © BUCKWINKEL/ALAMY

Published by AAAS

AROUND THE WORLD

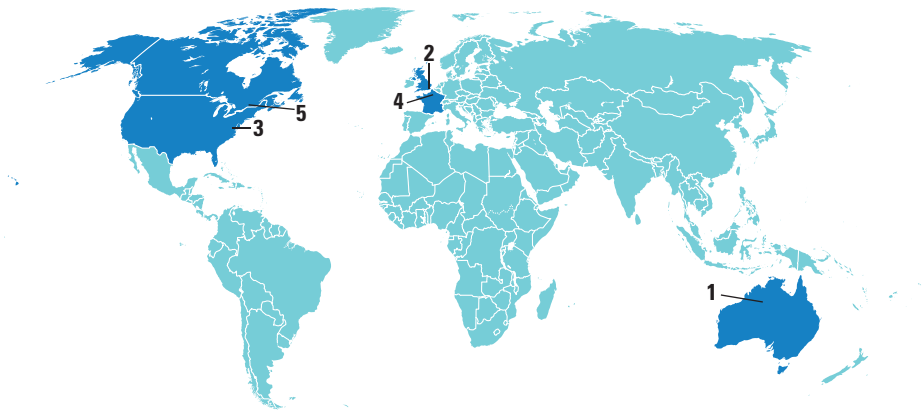

Tanami Desert, Australia **1**

Conservation in the Desert

The Australian government has designated 10 million hectares of land in the Tanami Desert of the Northern Territory as a conservation zone—the largest in the country. The Tanami Desert is home to many endangered species, including the bilby, a long-eared marsupial (shown), and the great desert skink, a burrowing lizard that builds elaborate tunnel systems. The animals have been threatened by feral cats and foxes, as well as brush fires and cattle grazing.

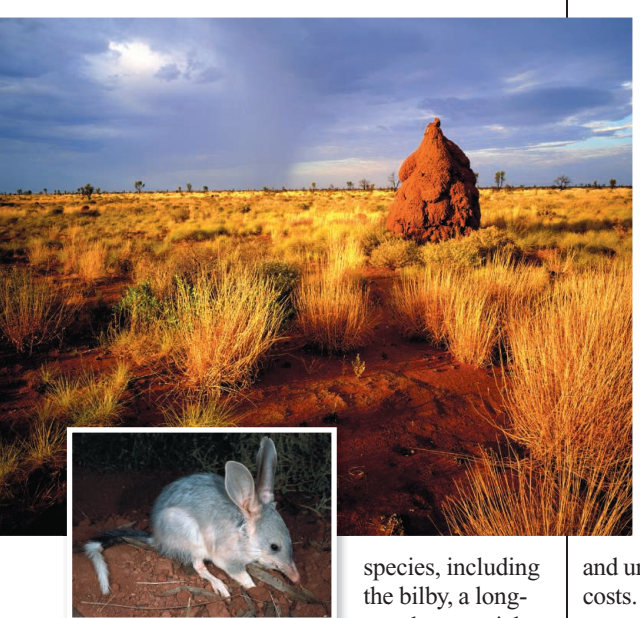

The region will be administered as an Indigenous Protected Area, under the supervision of indigenous communities. The government plans to spend $1.6 million over the next 2 years to fund the rangers; the Nature Conservancy will also contribute $500,000 to help manage the area.

London **2**

U.K. Moves Toward Open Access

The U.K. government has accepted the recommendations of a report released last month that encouraged greater open access publishing of publicly funded research. Officials announced on 16 July that over the next year, they will work to require studies wholly or partly funded by taxpayers to be published in journals that are free to readers. The government's decision means that by 1 April 2013, all papers from government-funded research must be published in an open access journal; if not, the journal must make the paper open access after 6 months.

The original report, chaired by sociologist Janet Finch, recommended the open access publication requirement because it would maximize the economic benefit of government-funded research.

But the move is getting a critical response from some researchers and universities who fear it could increase costs. The government's decision could also mean extra costs for U.K. universities, critics say, because in addition to paying article processing charges, research and university libraries will also have to continue paying for subscriptions until other countries adopt similar policies. **http://scim.ag/Finchrep**

Washington, D.C. **3**

Panel Pushes to Scale Down Agro-Defense Lab

Earlier this year, the Obama Administration suspended plans for a $1 billion, highly secure laboratory for studying dangerous animal diseases, called the National Bio and Agro-Defense Facility (NBAF). Now, a new study from the U.S. National Academies suggests rescuing the facility by scaling it down.

NBAF was intended as a replacement for the aging Plum Island Animal Disease Center in New York. But amid controversies—including environmental groups' concerns for the site's planned location in Manhattan, Kansas, over the potential release of pathogens—the Department of Homeland Security (DHS) has struggled to secure funding from Congress, and the estimated cost of the facility grew from $450 million to more than $1 billion.

DHS had asked the National Academies to study whether NBAF's mission could be achieved by continuing with the Plum Island center or relying on biocontainment labs in other countries. The study concludes that neither option can enable the United States to protect animal and public health in the long term; instead, it recommends reducing the price tag for NBAF by scaling down activities such as training, research on small animals, and vaccination research, and outsourcing them to existing animal pathogen labs. **http://scim.ag/AgroLab**

Paris **4**

Researchers Receive Controversial UNESCO Awards

A tumultuous and divisive episode at the United Nations Educational, Scientific and Cultural Organization (UNESCO) ended Tuesday when three researchers received a life sciences award sponsored by Teodoro Obiang Nguema Mbasogo, the dictator of Equatorial Guinea. A broad coalition of human rights advocates, scientists, and health experts had fought almost until the last minute to prevent the ceremony from happening. They say the award is an attempt by Obiang to buy credibility for his regime, which stands accused of human rights violations.

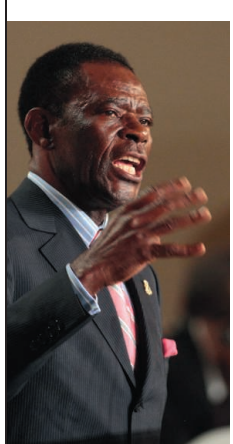

The winners of the prize are Maged Al-Sherbiny from Egypt, for his research on vaccines and diagnostics against hepatitis

CREDITS (TOP TO BOTTOM): © THEO ALLOFS/CORBIS; (INSET) © GREG HAROLD/AUSCAPE/MINDEN PICTURES/CORBIS; REBECCA BLACKWELL/AP PHOTO

Published by AAAS

Ottawa, Canada **5**

Scientists Protest Canada's Budget Cuts as Antiscience

Led by the Grim Reaper, a mock funeral procession of more than 2000 scientists marched on Canada's Parliament last week to protest what organizers called a "systemic attack on science" by the country's Conservative government. The "Death of Evidence" rally was organized by students at the University of Ottawa to protest budget cuts that will close the Experimental Lakes Area in northwestern Ontario and the Polar Environment Atmospheric Research Laboratory, two key environmental research programs; eliminate funding for a national science adviser; and convert the mandatory long form of the Canadian national census into a voluntary one, among other changes (*Science,* 29 June, p. 1627).

The rally was timed to coincide with a large, international meeting of evolutionary biologists, many of whom joined the march. "Recent actions by the federal government suggest that our state is frightened by evidence and is retreating into a fantasy world," says Arne Mooers, a biologist at Simon Fraser University, Burnaby. The Canadian government says the cuts are necessary to balance the budget and fund other, more-applied areas of science.

CREDITS (TOP TO BOTTOM): MICHAEL & RICHARD WEBSTER; CHAETOEROS - MARINA MONTRESOR, SZN/ALFRED WEGENER INSTITUTE

C and schistosomiasis; plant scientist Felix Dapare Dakora from Tshwane University of Technology, Pretoria, in South Africa for his work on legumes and soil bacteria; and Rossana Arroyo of the Centre for Research and Advanced Studies of Mexico's National Polytechnic Institute, who studies trichomoniasis, a parasitic disease. All three were at the ceremony, which was boycotted by many Western countries. UNESCO Director-General Irina Bokova, who opposed the prize but was overruled in March by UNESCO's 58-member Executive Board, didn't attend either. **http://scim.ag/Obiangaward**

THEY SAID IT

"I can't find anyone in my peer group who believes in BioWatch. … The only times it goes off, it's wrong. I just think it's a colossal waste of money. It's a stupid program."

—Ned Calonge, former chief medical officer for the Colorado Department of Public Health and Environment, to *The Los Angeles Times* on 7 July about the Department of Homeland Security's efforts to equip cities with devices to detect a biological terrorist attack.

FINDINGS

Fertilized Blooms Deposit Carbon To Deep Sea

For the first time, scientists have direct evidence that carbon formed from algal blooms fertilized with iron does sink to the deep ocean—a finding that might renew interest in using iron fertilization as a way to sequester carbon dioxide and possibly mitigate climate change.

Iron is a limiting nutrient in many parts of the ocean. Previous studies have shown that adding iron to the upper ocean stimulates blooms of phytoplankton, which in turn take up increased amounts of carbon dioxide from the atmosphere. But it was unclear whether that carbon would then be prevented from interacting with the atmosphere by sequestering it away in the deep ocean.

As part of the 2004 European Iron Fertilization Experiment, oceanographer Victor Smetacek of the Alfred Wegener Institute for Polar and Marine Research in Bremerhaven, Germany, and colleagues

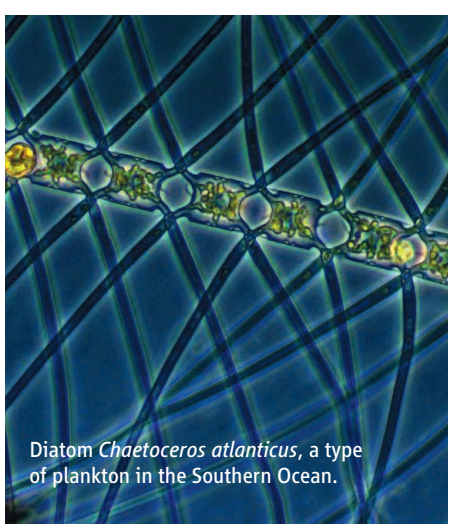

Diatom *Chaetoceros atlanticus*, a type of plankton in the Southern Ocean.

tracked particles of phytoplankton biomass in the Southern Ocean as they sank from the surface to the ocean floor. More than half of the carbon captured by the algal bloom during the iron fertilization experiment sank more than 1000 meters, they reported this week in *Nature*. **http://scim.ag/ironfert**

Published by AAAS

Random Sample

Swan Song for the Cernettes

A woman in a puffy pink prom dress croons plaintively; three backup singers with beehive hairstyles sway and sing. Behind them all, a familiar giant particle accelerator curves away into the distance.

"You never spend your nights with me. … You only love your collider."

"*Ooooh … wop wop*."

For 22 years, Les Horribles Cernettes—CERN's favorite 1960s-style girl group—have been serenading Geneva-based physicists with songs such as "Strong Interaction," "Antiworld," "Mr. Higgs," and the aforementioned "Collider," all written by the band's creator, manager, composer, and keyboardist/bassist, Silvano de Gennaro. But on 21 July, the Cernettes' era will come to an end, with one last performance at the CERN Hadronic Festival. (The show will be available on YouTube, http://www.youtube.com/user/cernettes).

It all started in 1990, when a CERN secretary—tired of feeling neglected by her always-on-shift physicist boyfriend—asked de Gennaro (then a CERN computer scientist and former musician) to turn her tale of woe into a song. De Gennaro says he opted for doo-wop "because the average age at CERN was mid-50s." He assembled singers and a band to perform the song, and the Cernettes were born.

Over the years, about a dozen different singers have been in the group—CERN secretaries and interns, and outside talent from Geneva's operatic society. "We never played for money," de Gennaro says. "We played to get the physicists to smile and dance."

But now de Gennaro is retiring, so the act must disband. Ironically, the Cernettes went briefly viral last week, when news outlets reported that a 1992 still of the group was the first photo ever uploaded to the World Wide Web. De Gennaro demurs: When the photo was posted to CERN's Web site, "they told me that this was the first photo *of a band* that appeared on the Web," he says. "Somehow, this got twisted."

BY THE NUMBERS

1.5 million Number of different plankton taxa in the oceans according to a preliminary analysis of 27,000 samples collected by Tara Oceans, a scientific sailing expedition, from the Mediterranean Sea and the Red Sea to the Pacific Ocean and the Antarctic region.

91 Percentage of the world's 103 lemur species that are listed as critically endangered, endangered, or vulnerable by the International Union for Conservation of Nature.

>>FINDINGS

Global Warming Punched Up Some 2011 Extremes

Human-induced global warming is increasing the chances that Texas will be hit with record heat and dryness or that the United Kingdom will have an unusually mild winter—but linking extreme weather to global warming isn't always that simple, note a group of analyses in the July issue of the *Bulletin of the American Meteorological Society*. For example, the strengthening greenhouse had nothing to do with last year's flooding in Thailand, the new analyses find.

Researchers under the aegis of the U.S. National Oceanic and Atmospheric Administration and the U.K. Met Office used a variety of techniques to search for any link between the atmosphere's mounting greenhouse gases and extreme weather and climate around the world. Some methods involved climate modeling, while others drew on long climate records for the regions involved.

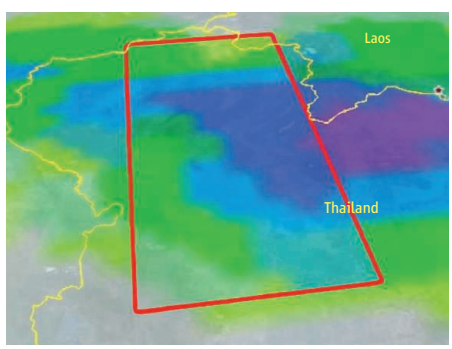

Rainfall in the catchment basin (red box) of Thailand's Chao Phraya river was not unusual in 2011; flood losses were likely due to floodplain building.

The backers of this first prompt analysis of extreme climate and weather events plan to make it an annual "attribution service" to sort out global warming's effects on high-profile events while they are still fresh in the minds of the public and decision makers. **http://scim.ag/2011extremes**

Science LIVE

Join us on Thursday, 26 July, at 3 p.m. EDT for a live chat with leading experts on a hot topic in science. **http://scim.ag/science-live**

Published by AAAS

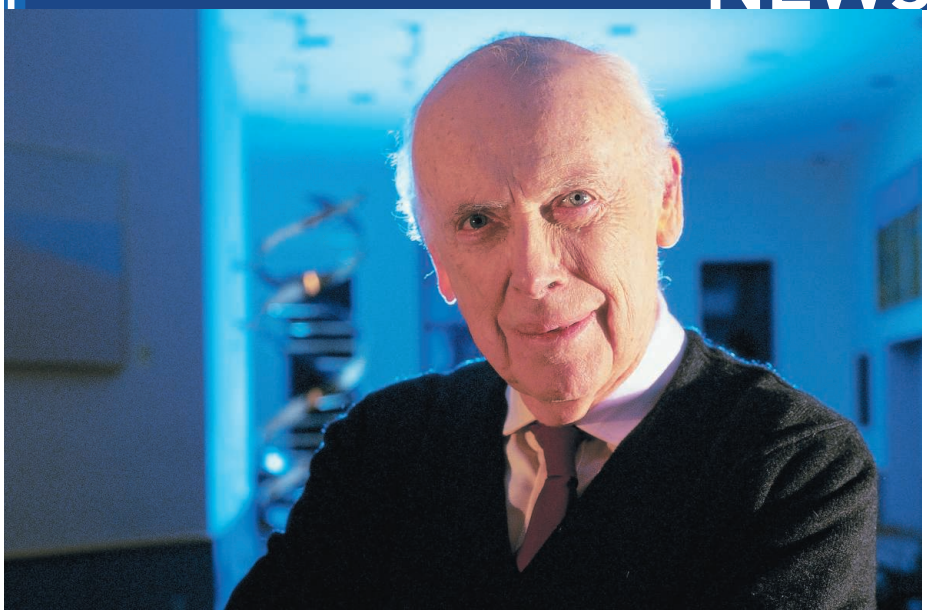

CREDIT: COLD SPRING HARBOR LABORATORY

PATENTS

U.S. Appeals Court Hears Gene Patent Arguments

James Watson, co-discoverer of DNA's double helix, has signed up as the most celebrated champion of a lawsuit that aims to block patents on human genes. With a strongly worded amicus brief filed last month, Watson joined a long list of scientists and doctors who have intervened in the test case, scheduled for oral argument on 20 July. A three-judge panel in the U.S. Court of Appeals for the Federal Circuit (CAFC) in Washington, D.C., will consider whether to invalidate patents on breast cancer genes owned by the Utah diagnostic company Myriad Genetics. Biotech leaders claim that if the patent critics win, their industry could suffer; they're campaigning to preserve the status quo.

At the center of this fight is a challenge to patents on the *BRCA1* and *BRCA2* genes, owned by Myriad since the late 1990s. Myriad's opponents—led by nonprofit attorney Daniel Ravicher and colleagues at two New York City advocacy organizations, the Public Patent Foundation and the American Civil Liberties Union—hope to end Myriad's monopoly on *BRCA* genes and undercut many other DNA patents. They argue that genes are "products of nature," not inventions, and for that reason are not patentable. Although U.S. courts have allowed such patents for more than 3 decades, opponents say it's not too late to reject them. Some judges have agreed.

A U.S. district court in New York sided with Ravicher and his allies in 2010, invalidating many of Myriad's claims (*Science*, 9 April 2010, p. 153). That decision was partly overturned, however, when it reached the CAFC on appeal in 2011. The case then went to the Supreme Court, which didn't issue an opinion; instead, it cited its own 9–0 rejection of a different nongene diagnostic patent this spring and ordered the CAFC in March to take a fresh look at the matter in the light of that rejection (*Science*, 30 March , p. 1550).

> ***"Life's instructions ought not be controlled by legal monopolies created at the whim of Congress or the courts."***
>
> **—JAMES WATSON, 1962 NOBEL LAUREATE**

The prolonged fight could well bounce back to the Supreme Court before it's over, says a longtime follower of the case, attorney Harold Wegner of Foley & Lardner in Washington, D.C. What he finds "amazing" is the skill with which Ravicher and colleagues have kept the case moving, rallying public opinion to a cause that they portray as good social policy. Other combatants have focused more narrowly on the "nuts and bolts" of patent law, Wegner says, and the legal tacticians now appear to be on the defensive.

The loudest shot fired at Myriad's position so far, Wegner says, was from Watson. The brief filed by the 1962 Nobelist argues that courts should recognize that human genes are not ordinary molecules but are "fundamentally unique" because they "transmit the instructions for creating humans." Watson writes: "Life's instructions ought not be controlled by legal monopolies created at the whim of Congress or the courts."

Watson gives a first-person account of the discovery of the double helix, explains how DNA encodes proteins, and notes that even great legal minds can falter when they offer an opinion on genetics—citing a comment by Supreme Court Justice Oliver Wendell Holmes Jr. in 1927 on the beneficial use of genetics to eliminate "imbeciles" from the population. Watson writes that he has long opposed human gene patents, saying that he was "forced to resign" as the head of the Human Genome Project at the National Institutes of Health in 1992 because his views conflicted with those of the agency. He cites another Nobel winner, University of Manchester geneticist John Sulston, who wrote that gene patents will "get in the way of [genetics-based] treatment unless you have a lot of money." Watson argues that biotech companies don't need human gene patents to make a profit and warns that multigene testing methods could be "unnecessarily delayed" or halted by a thicket of patent claims.

Myriad disagrees. In its brief, it argues that the Supreme Court's 9–0 decision in March rejecting a diagnostic patent held by Prometheus Laboratories is not relevant to this case. And the company reiterates an argument made before, that patents on *BRCA1* and *BRCA2* do not run afoul of the ban on patenting natural products because they are based on sequences taken from "isolated BRCA molecules" created in a lab.

More than a dozen groups have filed amicus briefs, some for and some against gene patents. Some support gene patents in principle without specifically backing Myriad's claims. The Biotechnology Industry Association (BIO), in a brief with the Association of University Technology Managers (AUTM) and others, argues that gene patents should not be restricted and warns of "far reaching negative consequences" if this advice is ignored. The BIO–AUTM brief says that "innumerable other patents claiming medically and industrially useful compounds that are isolated or derived from natural sources" would be endangered, such as the antianemia agent erythropoietin, the antibacterial prod-

Published by AAAS

uct rapamycin, and a monoclonal antibody (muromonab-CD3) derived from the mouse and used in transplant therapy.

The threat to biotech patents may not be as great as BIO suggests, says Robert Cook-Deegan, an expert on genetics and patents at Duke University's Institute for Genome Sciences and Policy in Durham, North Carolina. But he thinks that a sweeping ban on patenting natural DNA sequences would affect key industrial and agricultural products. He likes an amicus brief filed by the U.S. Justice Department, a view significantly not endorsed by the Patent and Trademark Office. It proposes a distinction between naturally occurring DNA and DNA that has been "markedly" or "significantly" altered to create a new invention during discovery. In this reading, the latter type of DNA is patentable but the former is not. Cook-Deegan thinks this fine-grained logic may be persuasive to judges at CAFC and the Supreme Court. If this rule were applied, Myriad might keep certain patent claims and lose others. **–ELIOT MARSHALL**

SCIENCE FUNDING

Stability at Last for Australian Synchrotron?

MELBOURNE, AUSTRALIA—"Last week I was on Europa," says Helen Maynard-Casely. The planetary scientist, based here at the Australian Synchrotron, wasn't just imagining a trip to the jovian moon. She has been using the third-generation machine's intense x-rays to probe the structure of water and sulfate minerals at high pressure and low temperature, simulating the composition and conditions of Europa's ice sheet.

A few months ago, Maynard-Casely's virtual voyages to Europa were in jeopardy. Roiled by management disputes, the Australian Synchrotron, brought online in 2007, was set to run out of funding last month before the federal and state governments rode in with a 4-year rescue package. Now, the facility may find long-term stability. The federal government is expected to announce next month that the Australian Nuclear Science and Technology Organisation (ANSTO) in Sydney will take the troubled facility under its wing. "I have great expectations," says William Thomlinson, former director of the Canadian Light Source and a former adviser to the Australian Synchrotron. "ANSTO will bring the synchrotron up to speed. I've seen them in action."

Thomlinson and others hope ANSTO's stewardship will close a woeful chapter in the young synchrotron's history. The saga began in October 2009, when the facility's governors sacked Director Robert Lamb (*Science*, 1 January 2010, p. 20). Staff protested Lamb's removal by staging a 3-month work slowdown: They ran the facility on a 9-to-5 schedule instead of the usual round-the-clock. In the meantime, seven of nine members of the synchrotron's International Scientific Advisory Committee resigned.

Another blow came when the $248.5 million facility was deprived of its champion, Victoria State Premier John Brumby. In November 2010, Brumby's party lost elections and the government changed hands. Victoria's new leadership did not offer ongoing operating funds nor did the federal government pick up the bill, leaving the synchrotron's fate after June 2012 uncertain.

The management turmoil happened despite the machine's admirable performance. In 2006, it set a world record for the fastest time for a synchrotron to start producing x-rays and set another record for reliability. Research highlights include solving the elusive structures of perforin and the pre-T-cell antigen receptor. "We're getting a lot of firsts," says Tom Caradoc-Davies, leader of the macromolecular crystallography team.

What faltered instead was the synchrotron's complex governance. It was managed by a board reporting to five state governments, the federal government, the New Zealand government, 30 universities, and 41 other organizations. ANSTO's Richard Garrett, architect of the organization's proposal to operate the synchrotron, recalls intricate white-board diagrams of the Australian Synchrotron's management structure. "I remember wondering, 'Where's the synchrotron?' "

Fissures in the ungainly alliance began to appear when it was time for the machine to grow. When it opened, the Australian Synchrotron had eight beamlines and a ninth in development for diverting x-rays and infrared light to experimental setups. But the machine was designed for 38 beamlines, each of which costs up to $10 million and requires major design input. "There was no one clearly charged with strategizing future growth, spending time with the government and so on," says ANSTO Chief Executive Adi Paterson. As a result, the synchrotron has added no new beamlines since number nine.

Under pressure. Helen Maynard-Casely uses the synchrotron to simulate conditions on Europa.

CREDIT: AUSTRALIAN SYNCHROTRON

The synchrotron user community in Australia, meanwhile, has been growing at a rate of 600 per year. That has forced some scientists to go overseas for beam time. Keith Nugent, the director of the Australian Synchrotron, says it "has a 20-year lifetime as a state-of-the-art machine. We're already 5 years in and well behind." By comparison, he says, the Canadian Light Source is barely 3 years older than Australia's but already has 17 beamlines.

The first ray of hope came last March, when Federal Science Minister Chris Evans announced a $103 million rescue package, of which the lion's share will come from the Australian Research Council and universities. Welcome as it was, the package required a 10% spending cut, forcing the facility to let several staff go, Nugent says.

Now a lasting solution is at hand. Under an agreement that is still being finalized, an ANSTO-operated company will operate the synchrotron. If the deal goes through, Maynard-Casely plans to make the most of her time at the facility, where she has 1 year left on her contract. Earlier this week, another beam run would bring her deep under the surface of Europa's ice sheet, where, she says, "the pressure is equivalent to five elephants standing on a stiletto." It's up to ANSTO to remove the real-world pressure Maynard-Casely and her colleagues have been enduring. **–ELIZABETH FINKEL**

Elizabeth Finkel is the author of *The Genome Generation*.

Published by AAAS

ECOLOGY

The Metatron: Experimental Ecology Gets Connected

Nestled in the foothills of the Pyrenees in France, an unusual new ecological laboratory called the Metatron is set to provide insights into how animals disperse across landscapes—a sometimes mysterious process that can be crucial to conservation. Composed of dozens of large, interconnected white tents laid out across a 4-hectare field, the sensor-rich facility will enable researchers to explore how factors such as light, temperature, and rainfall influence animal movements. "There's really nothing else like it," says ecologist Joshua Tewksbury of the University of Washington, Seattle. But he and others caution that the Metatron won't be appropriate for studying all kinds of animals and that it isn't an exact replica of the natural world. Still, initial studies published this week suggest that the facility, which celebrated its official ribbon-cutting earlier this month, can mimic natural conditions for some small creatures—such as lizards and butterflies—that can be hard to track in the wild.

The Metatron is the brainchild of Jean Clobert, director of research for the Experimental Ecology Station of the French national research agency (CNRS) in Moulis, France. Clobert has studied the dispersal ecology of lizards for years, and he conducted some small-scale experiments that allowed the reptiles to move through cages and corridors. But he was frustrated by the inability to control the environmental conditions that can influence movement, or to better replicate natural communities by introducing other types of animals to his system. Adding this kind of complexity would have required "a big jump," he says.

In 2007, Clobert took that leap, raising €1.6 million for the Metatron from the European Union, the French government, and other sources. Clobert's team chose the name to reflect the Metatron's focus on metapopulations and metacommunities: groups of organisms living in different places that interact in various ways. The name is also a nod to the 20-year-old Ecotron, a pioneering indoor laboratory facility at Imperial College London, Silwood Park.

The Metatron offers researchers a lot of flexibility and control. Its 48 insect- and rodent-proof tents enable them to create many replicates, increasing the statistical power of experiments. Each tent covers 100 square meters of grass—a sizable amount of habitat for smaller animals. Motorized roofs allow scientists to vary the amount of light, while sprinklers control precipitation and influence humidity. What's most novel are the corridors. Tents have up to four doors leading into passageways to adjacent tents, each of which can have different environmental conditions. The doors can be closed at the top or bottom to give flying or walking animals choices for where they would like to go next.

Clobert and his colleagues started two pilot experiments in August 2010, when the facility was half-finished. They released 339 common Eurasian lizards (*Zootoca vivipara*) and tracked them for 10 months. Many of the lizards spread among the chambers and reproduced at natural rates, the team reports online this week in *Nature Methods*. Another project showed that large white butterflies (*Pieris brassicae*) appeared to behave normally in the Metatron. "What they've done is show that it works" with two very different types of organisms, says Marc Cadotte of the University of Toronto, Scarborough.

A-maze-ing. Metatron tents can be darkened and cooled by shutters to study animal dispersal.

The big question is exactly how realistic the Metatron can be. For example, the butterflies used in the pilot experiment may be too mobile to gain robust ecological insights, says Nick Haddad of North Carolina State University in Raleigh; they can fly greater distances than the entire Metatron, he points out. And although the setup is "very impressive," says Ran Nathan of the Hebrew University of Jerusalem, its corridors are not as interconnected as in nature. Life in captivity may also skew results. To sort out which behaviors and patterns might be a byproduct of the Metatron, researchers will need to conduct control studies of the same species in natural settings, predicts Martin Wikelski of the University of Konstanz in Germany.

Clobert agrees, and he has a head start from studying natural populations of Eurasian lizards for 24 years in the Massif Central. Now, he's using the Metatron to examine the impact of higher temperatures on lizard dispersal, as well as how they prey on insects in fragmented landscapes. Other researchers have started a menagerie of experiments with bumblebees, damselflies, and amphibians, hoping to discover, for example, whether butterflies move to new habitats to avoid inbreeding and how climate warming affects simple food webs. The facility will consider other proposals, which a small committee evaluates for merit and ability to contribute to operating expenses.

Ultimately, the Metatron could yield basic insights in ecology. "Its primary payoff to the scientific community will be by testing fundamental principles and theoretical predictions," Cadotte says. And although such basic work may not immediately contribute to conservation, Haddad imagines diverse applications: The Metatron could be used to test whether conservation corridors can unintentionally spread invasive species, for instance, or whether genetically modified organisms, such as mosquitoes or crops, alter ecosystems.

In the meantime, Clobert and his team plan to enhance the Metatron by adding an animal tracking system and connections among corridors to make them more realistic. They've also submitted a proposal to build equivalent systems for streams and ponds.

–ERIK STOKSTAD

CREDIT: QUENTIN BÉNARD

TRAINING AND WORKFORCE

What If the Science Pipeline Isn't Really Leaking?

The metaphor of a leaky pipeline is a fixture in discussions of whether enough U.S. students are pursuing careers in science and engineering. And scholars have explored in great detail why so many who profess a passion for science lose that inclination as they move through the education system.

However, a new book on the overall health of the U.S. scientific enterprise argues not only that the pipeline isn't leaky, but that it's the wrong metaphor. "There is little evidence that science suffers a 'leaky pipeline' during the college years that disproportionately steers students away from scientific fields and toward non-scientific studies," write Yu Xie of the University of Michigan, Ann Arbor, a sociologist and longtime analyst of the scientific workforce, and Alexandra Killewald, his former doctoral student, who this month joined the faculty at Harvard University.

Xie and Killewald argue that the pipeline paradigm ignores two important variables: students who obtain an undergraduate science degree after switching from a nonscience field, and those who drop out of school before earning any degree. Those omissions, the authors assert, make the pipeline a fatally flawed description of a system that they believe is actually doing a pretty good job of meeting the country's need for scientific talent.

While that conclusion goes against the accepted wisdom, experts find the new book persuasive. "I think they have made a pretty good case [on both issues]," says sociologist Robert Hauser, head of the Division of Behavioral and Social Sciences and Education at the National Research Council of the U.S. National Academies. In particular, he adds, "the pipeline is clearly a much more complicated story [than most people realize]. It doesn't look like there is a wholesale slaughter of kids hoping to become scientists."

Xie and Killewald draw their conclusion from national longitudinal studies of high school seniors and their career aspirations. In particular, the pair found that the percentage of college graduates who earned a degree in natural sciences or engineering was higher than the percentage of high school students who said they hoped to earn such a degree. In the most recent cohort—students who graduated from high school in 1992 with plans to attend college—the comparable figures for men are 28.3% and 27.5%; for women, it's 13.2% and 10.5%. The numbers are comparable for the 1972 and 1982 cohorts. (A study following students who graduated from high school in 2004 is still under way.)

Those figures don't mean there is no attrition. Individual students do drop out of science, Killewald says, and moving into science at the graduate level is much more difficult, Xie adds. But at the undergraduate level, those turning away from science are outnumbered by "switchers," or those who enter from nonscience fields. The phenomenon is especially noticeable among women who decide to go into the life sciences. In fact, Killewald says, the pipeline paradigm "captures less than 40% of the women who end up with science degrees."

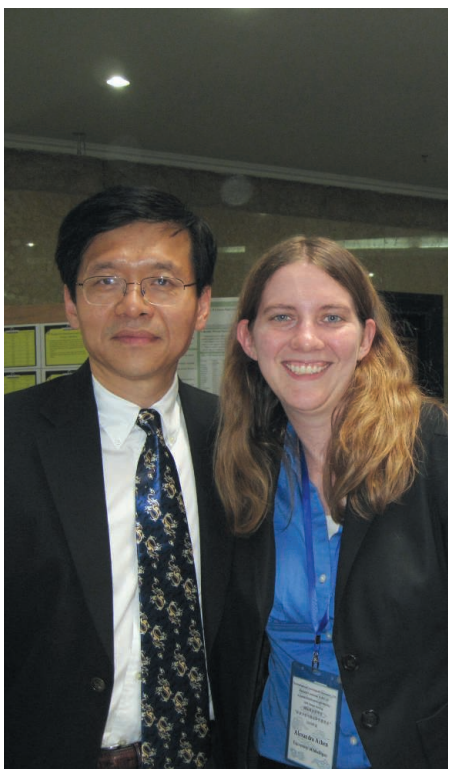

New message. Yu Xie and Alexandra Killewald reexamine accepted wisdom on scientific workforce trends.

The other big flaw in the pipeline paradigm, Xie and Killewald argue, is its failure to distinguish between students who abandon science for other fields and those who simply drop out of university. Among men in the 1992 cohort who fall short of their goal of earning a science degree, Killewald says, "70% receive no college degree at all, while only 30% receive a nonscience degree."

Aspiring science and engineering majors actually have a lower dropout rate than those planning to earn nonscience degrees—45% versus 51% for men, and 34% versus 40% for women. Those numbers, Killewald says, suggest that "the leaks in the science pipeline are really leaks in the education pipeline." What she calls an "unequal access to higher education," a combination of economic, educational, and cultural factors that make it harder for students to attend and complete college, also undermines attempts to attract more Latino and African-American students into science.

The authors give a flat no to the book's title question, *Is American Science in Decline?* Stagnant salaries, gloomy job prospects for academics, and growing international competition are indeed cause for concern, they write. But U.S. science is holding up surprisingly well, they say, and the country is more likely to benefit than be hurt by scientific advances elsewhere.

The book also takes issue with the widely cited figure that only one in three persons with science and engineering degrees is working in a science-related job. It's a statistic used by those who argue that the country already has too many scientists. "The real figure is between one-half and two-thirds," Xie says. The discrepancy comes chiefly from including those with social science degrees, a group that comprises half of all science degrees but for whom Xie says there exists "a weak linkage" between their degrees and their careers. The authors say it makes more sense to track only those with degrees in the natural sciences and engineering.

Hauser, who says "they are dead right on the definition of the workforce," also believes the authors' analysis has important implications for the broader, ongoing debate about training scientists (*Science*, 22 June, p. 1489). "It really comes down to how many folks you want to see in these fields," Hauser says. "If you think that the nation requires a lot more scientists, then you'll be troubled that the numbers aren't growing more rapidly."

Although Xie and Killewald believe there is compelling evidence for the need to rethink U.S. policies on training scientists, the authors do not plan to lead that debate. "We will not be making any clear-cut policy recommendations," they write. "On a subject as complicated and difficult as the scientific workforce, we feel that any attempt to do so would be presumptuous and foolhardy."

–JEFFREY MERVIS

CREDIT: PHOTO COURTESY OF YU XIE

Published by AAAS

COMMERCIALIZING RESEARCH

NSF Program Offers Start-Up 101 To Its Grantees

New technologies are a dime a dozen. But a new technology with the right business plan behind it is much rarer. This week, the U.S. National Science Foundation announced it is expanding a program to teach budding scientific entrepreneurs how best to tailor ideas from their NSF-funded research to attract investors and, eventually, customers.

The program is called Innovation Corps, or I-Corps. It was launched last fall at Stanford University, which developed an 8-week pilot course to train scientists in how to take that first step from the laboratory to the marketplace. This month, Stanford-trained instructors welcomed the next round of 54 I-Corps grantees to classes being held at the Georgia Institute of Technology and the University of Michigan, each of which have received grants of $1.5 million to extend the program. On 18 July, NSF issued a solicitation to award similar grants to five more institutions. NSF hopes to spend a total of $19 million on I-Corps in 2013, up from $7.5 million this year.

"We're wildly supportive of I-Corps," says Lesa Mitchell, vice president of innovation and networks for the Ewing Marion Kauffman Foundation, which specializes in promoting entrepreneurship. "It's implementing everything that we have been trying to do. And we're eager to see how they scale up the program."

I-Corps has also caught the eye of some members of Congress, although a partisan divide has emerged about whether it's something NSF should do. Representative Dan Lipinski (D–IL), a member of the House science committee, is so gung ho about the program's potential to teach academics how to start a small business that he attended the final presentation of the second I-Corps cohort in May. He also cajoled Representative Mo Brooks (R–AL), who chairs the science committee's research panel, into holding a hearing on the topic this week in his Chicago district.

"NSF spends all of this money on basic research," says Lipinski, a systems engineer turned politician. "So let's try to teach some of these grantees how to be successful entrepreneurs and see if it winds up producing new products."

Brooks didn't address the program's educational component when he opened the hearing. Instead, he raised the familiar Republican criticism about federal programs that try, in his words, "to determine which companies succeed and which fail." He wondered if NSF has the expertise to make such decisions and if, as a $7 billion basic research agency, it should even be funding such activities.

Although NSF officials would be delighted if the program helps to revive a sluggish U.S. economy, program manager Errol Arkilic says the agency's goal is more modest: "to take an idea in an academic's head and somehow get it out of the academic institution." The process of testing the market is similar to what researchers do every day in their labs, explains serial entrepreneur Steve Blank, who agreed to adapt his Lean LaunchPad course at Stanford for I-Corps: "Come up with an idea, fail, learn from your failure, and repeat as necessary in the shortest possible amount of time." Toward that end, I-Corps grantees are expected to get feedback from at least 100 industry contacts while taking the course.

Each $50,000 I-Corps grant is shared among a three-member team: a principal investigator on a current or recent NSF grant that generated the underlying technology, a graduate student or postdoc with the itch to become an entrepreneur, and a mentor with a history of successful start-ups willing to share his or her experience. "Most professors aren't interested in leaving academia, and they have a lot of other things going on," Arkilic says. "But there may be someone in their lab who's motivated by all the potential upside of the technology and who's willing to jump over all the hurdles that stand in the way of commercializing it."

Jason Gu is such a person. In December 2010, Gu, then 26, received his Ph.D. from Carnegie Mellon University (CMU) in Pittsburgh, Pennsylvania, under Lisa Porter. By August 2011, he was co-founder and CEO of SenSevere, which, based on results from an NSF grant that Porter received, has developed a novel chemical sensor technology capable of withstanding high-pressure, high-temperature environments. Next month, the company will begin a field test of its sensors at an industrial plant in the Midwest. (A nondisclosure agreement prevents Gu from providing details.)

Gu, Porter, and Robert Davis, another CMU professor and successful entrepreneur, were in the first cohort of I-Corps grantees. Right now, Gu is the only paid employee of SenSevere, which maintains a lab at CMU under a licensing agreement with the university. "There's no such thing as a part-time entrepreneur," Gu says about his long days and weeks. But his new job, he adds, "is a lot more fun than being a postdoc because you have more ownership in what you're doing. I can even see a little bit of myself in the company."

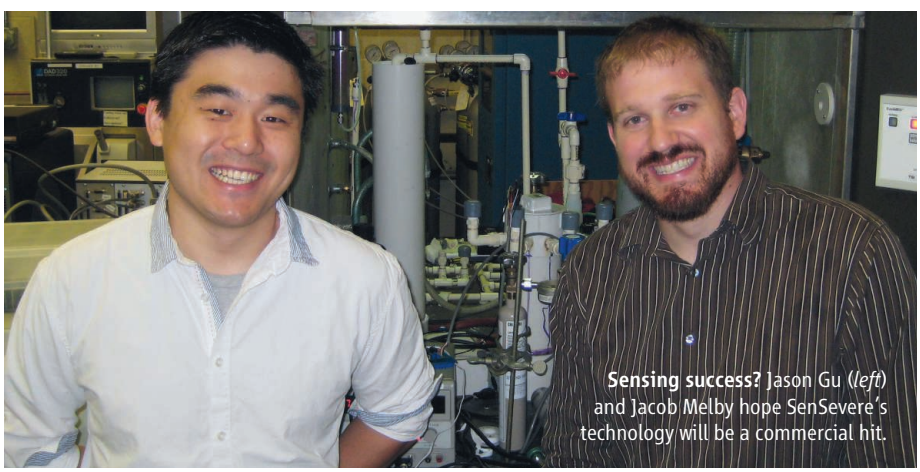

Sensing success? Jason Gu (*left*) and Jacob Melby hope SenSevere's technology will be a commercial hit.

CREDIT: JASON GU

Porter has no plans to leave academia and become an entrepreneur. But she's pleased to assist those with such a bent. Another of her graduate students, Jacob Melby, expects to become SenSevere's second employee after he completes his Ph.D. this summer, and a third student is weighing the commercial applications of a potentially patentable invention from an unrelated project in her lab.

"A business plan for a start-up is completely different than a business plan for a large company," Porter says. "You have to be very flexible and nimble in adapting to what you're hearing. And I'm in a much better position now to recognize and help those around me who want to become entrepreneurs."

–JEFFREY MERVIS

Published by AAAS

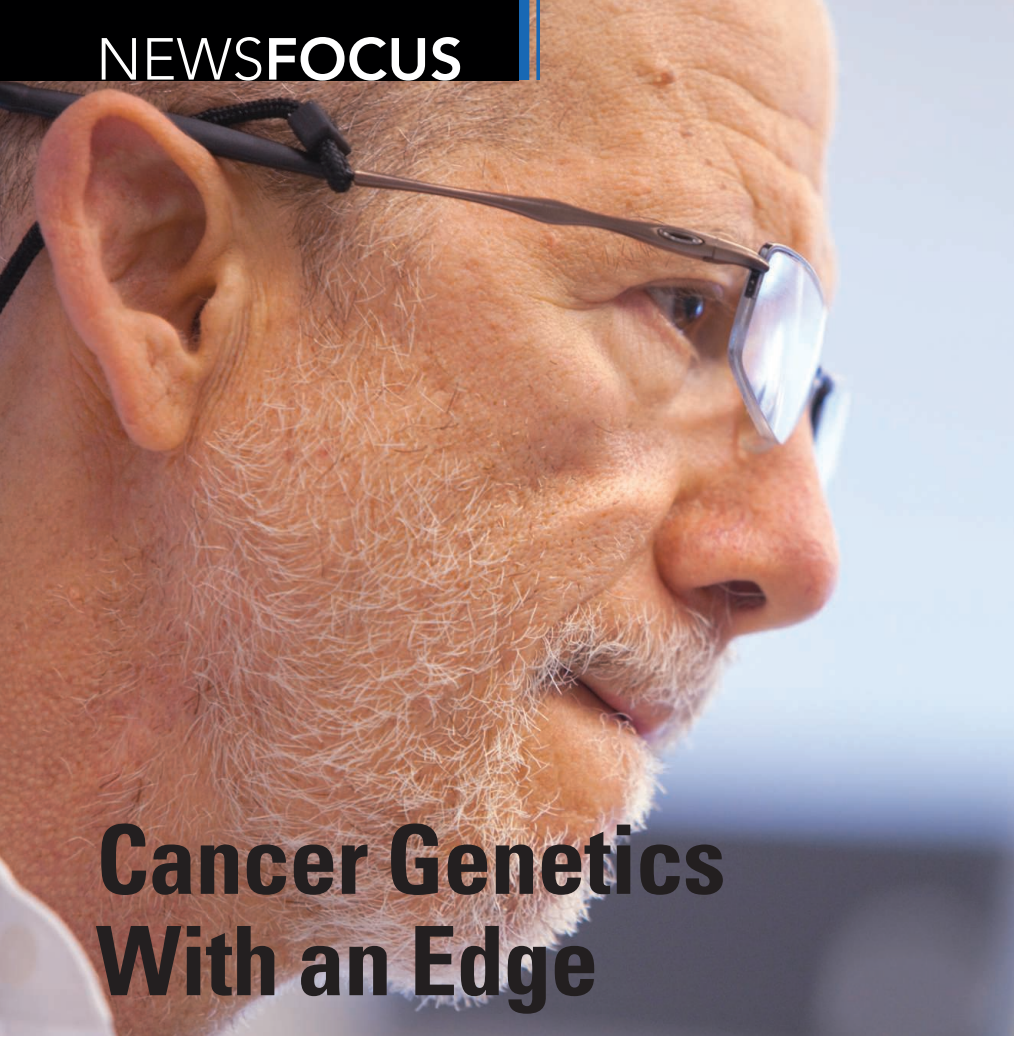

Cancer Genetics With an Edge

Their lab helped reveal how faulty genes cause cancer, but Bert Vogelstein and Kenneth Kinzler sometimes irk colleagues with their "reality check" comments on genomic medicine

IN APRIL, AS SCIENTISTS AT A CANCER meeting in Chicago were wowing audiences with their new DNA studies, geneticist Bert Vogelstein stood by with a bucket of cold water. At a briefing, he told a roomful of reporters that his own work shows how little value a key genetic approach—whole-genome sequencing—will have for preventing cancer. Using data from identical twins, his team estimated how well whole-genome tests could spot individuals at risk. Most people, the model showed, would get a negative result because inherited mutations very rarely predispose us to cancer. Yet about one-third of those who test negative will still develop cancer, triggered by environmental factors and bad luck. "It would be great if we could determine who will and will not get cancer from sequencing their DNA, but the reality is, we won't," Vogelstein said later.

Vogelstein's sobering message, picked up by *The New York Times* and other publications, irritated some scientists: They claimed the study had flaws and wasn't saying anything new. True, papers with similar findings had been published before, unnoticed by the press. But Vogelstein says that although the bottom line may have been familiar to some scientists, his study used a novel model to quantify the limits of personal genomes for public health. He says he also wanted to drive home the message that the only sure way to reduce cancer is through screening and a healthy lifestyle.

Some colleagues say the paper was a typical dart thrown by Vogelstein, who is known as a contrarian. Vogelstein (a longtime member of *Science*'s board of reviewing editors) and collaborator Kenneth Kinzler, who co-directs their lab at the Johns Hopkins University medical campus, helped lay the foundation of cancer genetics by revealing how mutations in key genes lead to a tumor. Their work helped inspire others to use genetics to predict cancer risks and develop personalized cancer treatments. Yet today, Vogelstein often offers what he calls a "reality check" on such efforts. Last month, for example, his team warned about a flaw in so-called targeted drugs that dramatically shrink tumors: They inevitably fail when resistant tumor cells take over.

Gene wizard. Bert Vogelstein helped launch modern cancer genetics after discovering key mutations.

"He sees things in very interesting and provocative ways," says cancer geneticist Stephen Chanock of the U.S. National Cancer Institute (NCI) in Bethesda, Maryland. Vogelstein "wants to make a quick difference and a quick hit. I would guess he thinks his job is to push the field along," says cancer geneticist Joe Gray of Oregon Health & Science University in Portland. Gray adds: "But whenever Bert talks, I listen."

In the past few years, Vogelstein and Kinzler have shifted away from discovering new cancer genes to a less glamorous pursuit: using genetic tests to detect common tumors as early as possible, when they are easiest to cure. This is not mainstream work, they say: "Society is fixated on curing advanced cancer. It's considered a success even if you're just reducing patients' cancer burden for a few months, not prolonging their lives for a long time," Vogelstein says. But it's a natural progression of earlier research, the two said in a recent interview at their upper-floor lab in downtown Baltimore, Maryland, two blocks from where Vogelstein was born.

Vogelstein, 63, small and trim with a grizzled beard, irreverent and humorous, wore his usual jeans and a white dress shirt. Kinzler, a tall, boyish-looking 50, was in khakis. Their research was never driven by curiosity about biology, Vogelstein says, but by "an overwhelming desire to empty the cancer clinics across the street."

Cancer genes

After studying mathematics at the University of Pennsylvania, Vogelstein went to medical school at Johns Hopkins, becoming a pediatric oncologist. His frustration at being unable to explain cancer—to tell parents why their 4-year-old daughter had leukemia, for example—inspired him to pursue research. In 1989, while working with colon tumor tissue, which they could obtain for different cancer stages, his group showed that the mutated *TP53* gene was not a cancer driver as had been thought but a tumor suppressor. Mutations that cause the gene to lose its function occur often in many different cancer types. Vogelstein says his decision to work with "messy" human tumors, not cell lines or animals, might be the reason why it took him three tries to get a grant from NCI.

In the late 1980s, Vogelstein also unveiled what's now a textbook model of how colorec-

CREDIT: JOE RUBINO

Published by AAAS

tal cancer develops. He and Kinzler, who joined the lab as a graduate student, later showed how the slow accumulation of mutations in specific genes leads to tumor growth. They went on to discover a string of major colon cancer genes. These studies all started by analyzing human tumors for mutations. Their guiding principle was that if a gene drives cancer, it will often be mutated. Trying to figure out a gene's importance by studying its function, they say, can be misleading. Just because the mutation alters a disease process doesn't mean it's the cause. It was "a completely different view" from what many other scientists believed, Vogelstein says.

The two built a highly competitive lab whose members played as hard as they worked. They installed a Ping-Pong table near the postdocs' desks; the lab held basketball and tennis tournaments. They had a rock band, Wild Type, composed of cancer biologists, with Vogelstein on keyboard and Kinzler on drums. Lab members got free use of a beach house. A quirky tradition arose in interviews of prospective postdocs: Candidates were asked to wear a Burger King crown when they spoke about their graduate work. "If you were not willing to wear the crown, you were probably a little too high-strung for the lab," says Devin Dressman, a former Vogelstein postdoc who is now at Life Technologies in Beverly, Massachusetts.

Vogelstein and Kinzler rarely travel to speak at meetings. They prefer to stay involved in their lab's experiments and avoid being swayed by what's popular, or the "herd effect," Vogelstein says. Instead, Vogelstein keeps up on the latest science by devouring the literature: "He reads more than any other human I know," Dressman says.

Cancer's own genome project

After human DNA was fully sequenced in 2003, cancer geneticists around the world began to envision their own genome project. Instead of homing in only on suspected cancer genes, they would do a more sweeping search and systematically sequence the entire genome of patients' tumors and compare the results to DNA in normal cells to find all possible cancer genes. Vogelstein and Kinzler declined to join the pilot phase of a proposed $1 billion project funded by NCI called The Cancer Genome Atlas (TCGA). Instead, using private funding, they set out to sequence the first "cancer genome" in a handful of breast and colorectal tumor samples—enough, according to their theory, to find the most important genes. They narrowed the search to focus on protein-coding DNA, the so-called exome.

It was an ambitious goal, especially because high-throughput sequencing machines weren't available. They accomplished it by brute force, performing about 200,000 polymerase chain reaction experiments on each of 22 patient tumor samples to amplify 13,000 or so genes. They sent the DNA to a commercial lab for traditional Sanger sequencing. Then they waited for results.

The gamble paid off: In 2006, Vogelstein's group published the first rough exomes for breast and colorectal cancers in *Science* (13 October 2006, p. 268). Data revealed both known and new cancer genes in varying frequencies—the authors called them mountains and hills—as well as daunting variations in patterns from one tumor to the next. Some researchers were critical: In Technical Comments in *Science*, TCGA leader and genome researcher Eric Lander of the Broad Institute in Cambridge, Massachusetts, among others, argued that the Johns Hopkins team had used faulty statistical methods and tested too few tumors to yield meaningful results.

Vogelstein and Kinzler moved on to glioblastoma exomes in 2008 and found an important new oncogene, *IDH1*. This was a slight embarrassment for the NCI collaboration, whose glioma project sequenced only a set of candidate cancer genes in a large number of tumors and missed *IDH1*.

Reviewing work by his group and others in his talks, Vogelstein seems ambivalent about the value of tumor DNA scans. More than 1000 of these surveys have added only a few dozen new cancer-driver genes to the 80 or so that were previously known, Vogelstein says. This includes some intriguing new genes, however. He and Kinzler agree that the more comprehensive NCI-backed genome atlas work is "invaluable" because it will find rare mutations and fill in gaps in our knowledge about the pathways that lead to uncontrolled tissue growth. But their own lab is moving on to other things after sequencing exomes for 20 cancer types. "We're focusing on different questions now—applications as opposed to discovery," Kinzler says.

Twins and cancer

One question that drew the Johns Hopkins group was: What fraction of the population would benefit from whole-genome sequencing? They had already used exome sequencing in 2009 to look for genes linked to pancreatic cancer common in one family. (Researchers compared the genomes of affected and nonaffected family members to pinpoint a responsible gene, *PALB2*.) Like screening for the *BRCA* breast cancer genes, identifying individuals with rare but high-risk pancreatic cancer genes might help some avoid death from the disease. This work led the group to wonder what might be gained if everyone's entire genome were sequenced, Vogelstein says. If a major fraction of the population carried high-risk genes, then sequencing everyone might make sense.

Because homozygous twins have identical genomes, the researchers could learn about their inherited disease risks without DNA sequencing, by comparing health records. Data on nearly 54,000 twin pairs, most in Europe, allowed the Johns Hop-

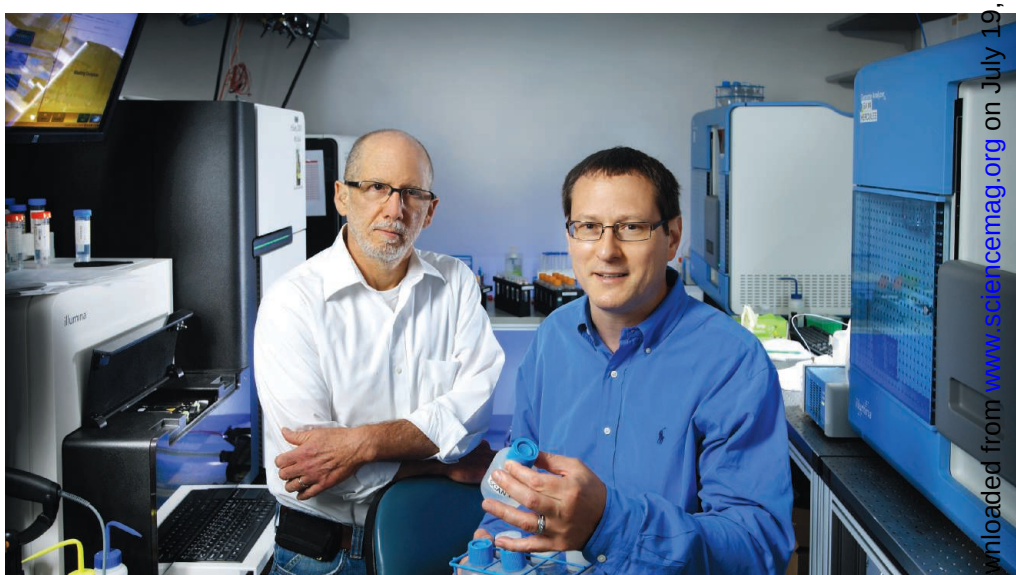

Reality check. Vogelstein and Kenneth Kinzler have identified flaws in some plans to use cancer genomics for treatment and risk prediction. They aim to develop a blood screening test to find early cancers.

CREDIT: KEITH WELLER

Published by AAAS

kins group to model how risks were distributed across the population. They found that genome testing had potential value. With a positive result defined as an overall disease risk of 10%, the average person would likely test positive for at least one disease, such as heart disease or diabetes. But genome scans would not help much with identifying risks for common cancers, they reported in *Science Translational Medicine* and at the meeting of the American Association for Cancer Research (AACR) in Chicago in April. For most people, the risks associated with inherited DNA are small or nonexistent, they found—and trivial compared to risks from random mutations and factors such as smoking and obesity.

NCI's Chanock suggests that the twins data included too few cases of specific cancers to yield definitive results: "I would not take this as the final word on the value of the genome," he says. But Lander, despite his criticism of the group's work on tumor exomes, says the twins study "makes an important point" even if it just "confirms what we have known all along: Genes are not everything." Lander says his own view has always been that genetic risk studies are most useful for pointing to the biology underlying diseases, not for predicting personal risks.

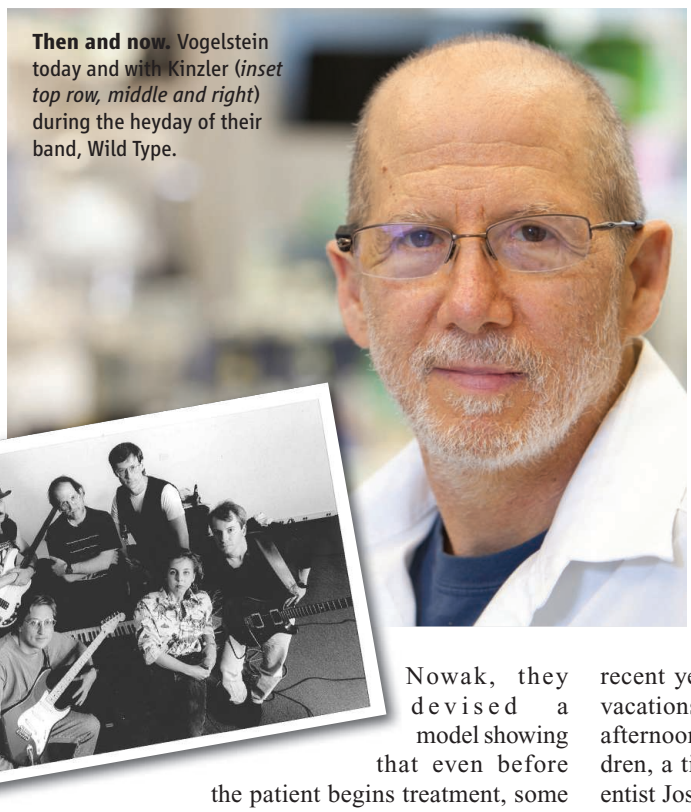

Then and now. Vogelstein today and with Kinzler (*inset top row, middle and right*) during the heyday of their band, Wild Type.

Antihype

Vogelstein seems to enjoy pricking balloons. Recently, he has focused on a new target: exuberance over targeted cancer drugs. He says he got interested after seeing a paper last year on melanoma therapy. It included photos of the torso of a man with melanoma who had received a new drug aimed at a mutated gene called *BRAF*. Before treatment, the patient's skin was riddled with metastatic tumors; soon after treatment, the tumors vanished, and the man looked perfectly healthy. Five months later, the tumors reappeared in exactly the same locations. The photos "blew my mind," Vogelstein says. "Why do the tumors all return at roughly the same time? It's almost as miraculous as when they disappear."

Targeted drugs for other cancers usually stop working after about the same number of months, presumably because rare resistant cells in the tumors continue to grow and ultimately proliferate. To investigate, Luis Diaz and others in the Vogelstein-Kinzler lab drew on a sensitive technique they had developed for detecting mutations in the very small amount of tumor DNA present in a cancer patient's blood. They collected a series of these "liquid biopsy" measurements from patients with advanced colorectal cancer whose tumors had become resistant to a targeted cancer drug. With Harvard University computational biologist Martin Nowak, they devised a model showing that even before the patient begins treatment, some tumor cells always carry genes with random mutations that can support resistance to targeted drugs. This form of resistance, they wrote last month in *Nature*, is therefore "a fait accompli."

But the modeling study also suggested that this resistance can be delayed by combining two drugs that target different pathways. Indeed, Vogelstein and colleagues suggest that once a targeted drug has passed initial safety trials, it's so clear that single-drug therapy will fail that they consider it unethical to give patients just one such drug. "Why shouldn't you design a large, very expensive trial to incorporate more than one agent?" Vogelstein asks.

Memorial Sloan-Kettering Cancer Center cancer researcher Charles Sawyers, who helped develop Gleevec, the leukemia drug that paved way the way for other targeted therapies, says he agrees with Vogelstein's message: "We have to move to combinations as quickly as possible."

The Vogelstein-Kinzler lab is attacking cancer from several new angles, including an unusual clinical trial that involves destroying tumors by injecting them with bacteria. But the project closest to Vogelstein's heart right now is an effort to develop the liquid biopsy method as a general cancer-screening test. The aim is to look for a set of mutations commonly found in tumors that can be isolated from circulating blood.

Vogelstein and Kinzler argue that DNA mutations offer "clarity" compared to other blood-sampling approaches that focus on more complex protein or gene-expression markers. At the AACR meeting, Vogelstein described his group's latest blood test results for 304 patients with several types of cancer. Nearly all with metastatic tumors had detectable mutations in their circulation; more than 50% of those whose cancer had not yet metastasized had them; and none of 82 controls. "I think we're getting very close with the technology," says Vogelstein, who owns stock in a German company, Inostics, that is commercializing the test.

Although Vogelstein seems as passionate about research as ever, he has stepped back in recent years, others say. He now goes on vacations. Lately, he's been spending two afternoons a week with his two grandchildren, a time that Johns Hopkins neuroscientist Joshua Vogelstein (their uncle) thinks is probably "the best part of his week." The lab has gotten "leaner and meaner," Kinzler says: It's down from a peak of about 40 lab workers (including six faculty members) to perhaps 30—one reason is that sequencing now involves less lab work. Wild Type hasn't picked up their instruments since Kinzler's wife fell ill with leukemia 10 years ago and died 6 months later. "We had to stop and we never started up again," Vogelstein says.

Vogelstein has no plans to retire: "I was born here and when I die they'll wheel me out on a cart," he says. Before that, he says, he has one overriding goal: that a cancer-screening test based on mutations in tumors will become a routine part of everyone's annual physical exam. "I just want one of those tests to be the standard of care. That's the one thing." **–JOCELYN KAISER**

CREDITS (TOP TO BOTTOM): JOE RUBINO; (INSET) ZUHAIR KAREEM, THE JOHNS HOPKINS HOSPITAL

Published by AAAS

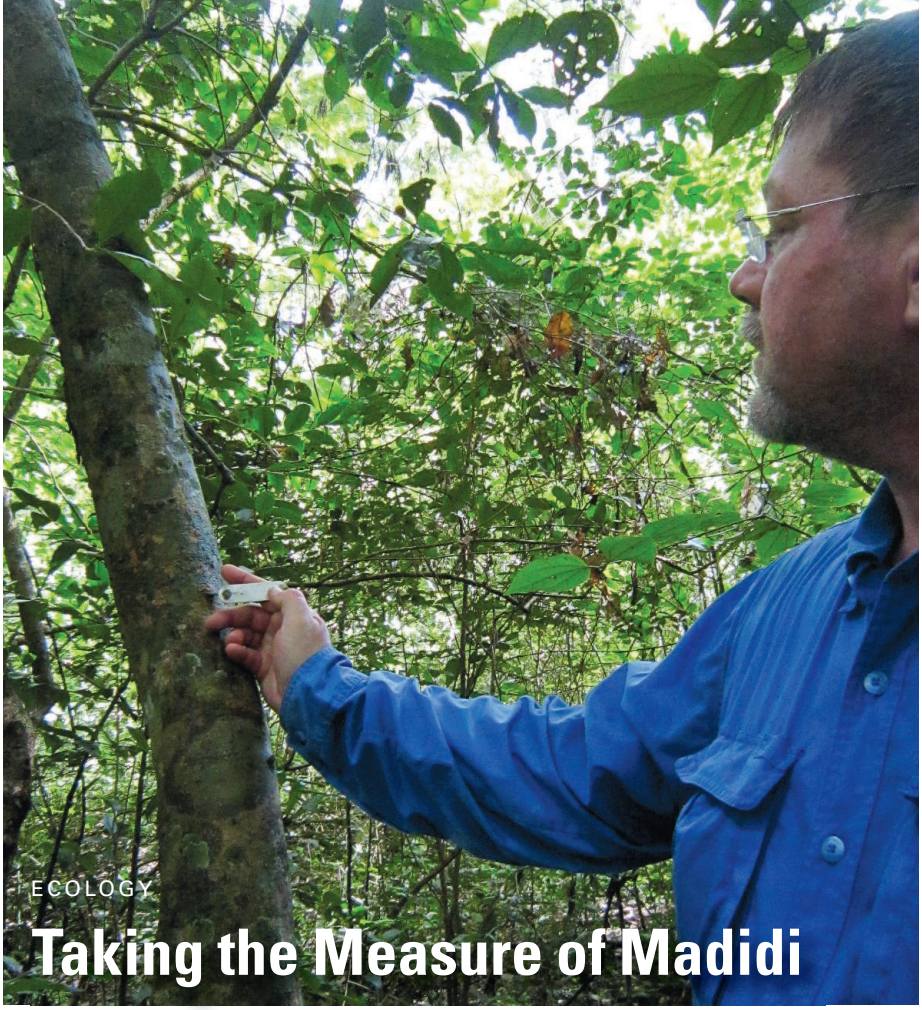

Tracking trees. Peter Jørgensen started tagging trees in 2004 to understand forest diversity.

ECOLOGY

Taking the Measure of Madidi

Researchers journey into one of the world's most diverse areas to help predict the future of our planet's trees

MADIDI NATIONAL PARK, BOLIVIA—It felt like an old-fashioned treasure hunt. For 5 days, two biologists, a botanist, and their students braved collapsing cliff-side roads, clambered across rushing rivers, and hacked their way through forest to reach this spot on their map. The researchers fanned out through the jungle, navigating thorny underbrush and armies of stinging ants, in search of small metal tags. A shout broke through over the rush of the nearby creek: "Number 191!" Moments later, calls from all directions: "Sixteen is over here!" "Seventy-two!" "I've got 12!" The excitement mounted as they located and read off dozens of numbered tags that had been nailed into trees 7 years ago.

Despite the giddiness, the endeavor was serious. This was day one of fieldwork in a 3-week expedition, part of the ongoing Madidi Project, to measure tree growth here in one of the planet's most unusual protected areas. For the students, locating silver strips obscured by moss or leaves in the middle of a forest the size of Vermont was like discovering buried treasure. For the Madidi Project's director, Peter Jørgensen of the Missouri Botanical Garden in St. Louis, who started tagging Madidi's trees almost a decade ago, it was "like finding old friends."

Those friends, it turns out, have an increasingly important tale to tell. Botanists and biologists have long grounded their understanding of the natural world on long-term projects such as Madidi. Recurrent surveys of the same communities generate data that help researchers figure out how species interact in the face of environmental change or nearby human activity. As climate change descends upon us, it's becoming critical to identify factors influencing tree survival. "Local populations of trees have three options," says Nathan Kraft, a biologist at the University of Maryland, College Park. "They can move, adapt, or die off." By "move," he means that trees have the ability to shift their range when threatened in their current habitat, say by long-term drought or a more competitive species. Through seed dispersal and other regeneration mechanisms, trees can move to a better area. Otherwise, to survive, they must adapt, evolving traits better suited to the new conditions. The choices will determine the biodiversity of future forests. "Only once we know how species will behave can we figure out how to save them," not just in Madidi but elsewhere as well, Jørgensen says.

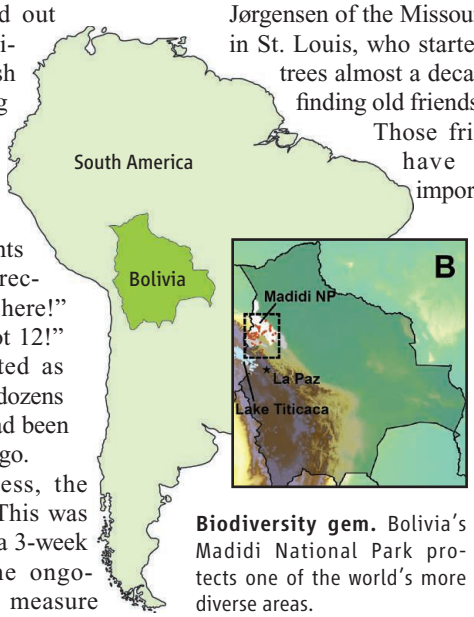

Biodiversity gem. Bolivia's Madidi National Park protects one of the world's more diverse areas.

It's not easy being a botanist

Madidi National Park is home to 11% of the world's bird species and an estimated 12,000 plant species. Located in northwestern Bolivia, it is one of the largest, most diverse protected areas on the planet, on par with Madagascar's national parks and Colombia's Chocó jungle. It is also remarkably untouched. Aside from the handful of communities living inside the park and limited ecotourism on its eastern edge, human activity is scarce in the area. "Madidi is exceptional for scientific study," says Peter Raven, president emeritus of the Missouri Botanical Garden, the main sponsor of ongoing studies here, "because of this lack of disturbance."

For biodiversity researchers, it has another attribute: the longest continuous elevation gradient on the planet. The park ranges from Andean peaks of just over 6000 meters above sea level to the Amazon basin, approximately 180 meters above sea level. "Madidi is like a laboratory for climate change," says the Madidi Project's Bolivia coordinator, Alfredo Fuentes, a La Paz–based botanist at the Higher University of San Andrés in La Paz, Bolivia, Bolivia's largest university. Because temperatures drop as the elevation increases, species in Madidi can theoretically shift uphill instead of adapting to global warming in place. "Madidi offers an excellent opportunity to watch reactions to climatic change," Fuentes says.

Online
sciencemag.org
Podcast interview with Jean Friedman-Rudovsky (http://scim.ag/pod_6092).

CREDITS (TOP TO BOTTOM): JEAN FRIEDMAN-RUDOVSKY; ISTOCKPHOTO.COM/MISSOURI BOTANICAL/MADIDI FOREST GARDEN

Published by AAAS

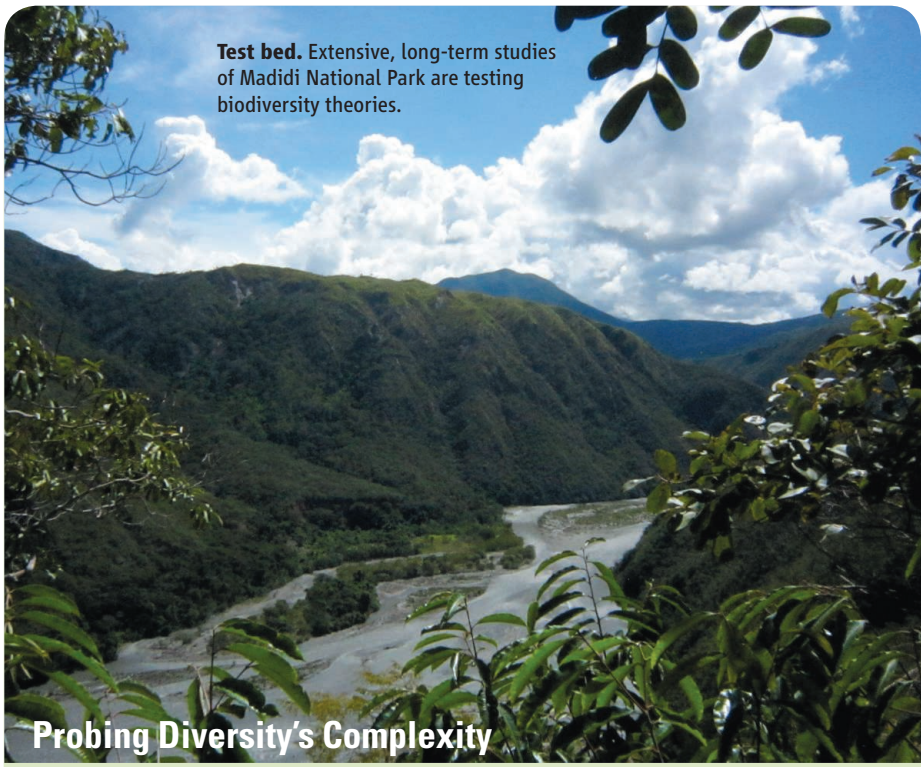

Test bed. Extensive, long-term studies of Madidi National Park are testing biodiversity theories.

Probing Diversity's Complexity

Rainforests may be the conservationist's poster child, but they fall short as models of the true complexity of our planet's biodiversity. So says Peter Jørgensen, a botanist at the Missouri Botanical Garden in St. Louis, whose long-term project in Bolivia promises to shake up our understanding of the distribution of tree species in tropical South America. The Madidi Project (see main text) charts the changes in tree communities growing along an elevation gradient that plunges from above 6000 meters in the mountains to 180 meters above sea level. By identifying all trees at least 10 centimeters in diameter within hundreds of research plots along this gradient, Jørgensen and his colleagues have built a database that allows them to examine spatial patterns of diversity in ways not possible from studies limited to rainforests, which tend to be comparatively homogeneous because they are confined to the lowlands.

The Madidi Project focuses on comparing the rate of turnover of species in a sample of plots—a concept known as beta diversity. "It's about trying to understand why a certain species lives in one area and not in another nearby," says Brad Boyle, a biologist at the University of Arizona in Tucson. To gauge beta diversity, researchers count the number of species in various plots. Then they ask: How many species are common to the plots? How many are different? The higher the number of species found in only one plot, the greater an area's beta diversity.

Researchers want to know why beta diversity is higher in some areas than others. Why do some species thrive in two different areas while some drop out? "There are many different factors," says Nathan Kraft, a biologist at the University of Maryland, College Park, including climatic tolerance, soil quality, rainfall, and the differences in the dispersal abilities of species. "The really important next step is determining the relative importance of these factors and how they interact."

His work shows that the high beta diversity along elevation gradients arises because so many species are capable of living in these areas that by chance each plot has numerous species not found in another nearby (*Science*, 23 September 2011, p. 1755). But Jørgensen and his colleagues suspect that chance is not the most important factor. They think that high beta diversity in tropical mountain forests like those of Madidi is driven by a special mix of environmental factors. They hope an analysis under way will prove them right. "The value of [the Madidi Project] is in testing diversity theories of a landscape with real actual data, which is very rare," says Thomas Lovejoy, biodiversity chair at the Heinz Center in Washington, D.C. "It speaks to the importance of matching theories and what happens in nature."

Kraft is eager to see the results: "The strength of the Madidi data set is that it's intensively sampled and spans a broad elevation gradient. It will be a great step forward." **–J.F.-R.**

The Madidi Project, launched by the Missouri Botanical Garden in 2001, has begun to capitalize on an opportunity not only to look at the effects of climate change but also to test existing theories about what controls biodiversity. Researchers are looking in particular at factors that influence the composition of plant communities, a concept known as beta diversity (see sidebar). The project's entire data set includes more than 206,000 trunks and about 2400 tree species. "Nothing along these lines has been done before," says Thomas Lovejoy, biodiversity chair at the Heinz Center in Washington, D.C.

From 2001 to 2010, the project established 442 small plots (0.1 hectare) and 50 large ones (1 hectare) throughout the park, each of which are now demarcated by small plastic tubes topped by a strand of orange fabric. Within each plot, researchers mapped, identified, tagged, and noted the characteristics of all trees with at least a 10-centimeter diameter, establishing a baseline.

Now, several expeditions a year here measure these trees, ideally returning to each plot every 5 years to take stock of the changes. During this visit in April, the group will remeasure more than 1600 trees from three plots in a semideciduous tract of Madidi ranging between 900 and 1100 meters above sea level. (One plot is on the banks of a river, one on a slope, and another on a crest.) Every tagged tree's location is double-checked against a map from the plot's establishment, and if a tagged tree has died, the team tries to establish the cause of death by examining the stump or remaining limbs for evidence of infection or other impacts such as a lightning strike.

Before their first trip, "everyone thinks it's like being on vacation," says Denmark-born Jørgensen as he swats away swarming mariwees, gnatlike insects that sting. It's the first day working the plots, and his neck is already swollen from bee stings and ant bites in the campground the night before.

Around him, the number calls continue, but they are no longer random. Rather, at each tagged tree, the researchers methodically sound off with codes that correspond to every possible characteristic: width, height, smell, bark texture, closeness to canopy, leaf patterns, and more. "I've got to be very careful to enter everything right," says Esther Mosqueria of the Higher University of San Andrés. Her undergraduate biology thesis will be on Madidi's tree population. She scribbles furiously to keep up with her colleagues' shouts.

One of the local guides accompanying the group is 3 meters off the ground, balancing on a thick branch leaned against a tree. He wraps a tape measure around the midsec-

CREDIT: JEAN FRIEDMAN-RUDOVSKY

Published by AAAS

tion of a large trunk. Many trees in this area have aboveground root structures, so team members must climb to measure the trunk diameter accurately. Tree height is estimated (with roughly 90% accuracy) because taking an exact measurement through triangulation would triple the fieldwork time.

Species identification is a key component of the project; the team double-checks trees identified in the past, taking samples back for confirmation if there's any doubt. "You can have a ton of data, but it doesn't mean anything if you can't consistently identify and standardize the species," says Brian Enquist, an ecologist and evolutionary biologist at the University of Arizona in Tucson. While identifying tree species might seem the task of a third-grader, "in tropical areas, the extreme number of species means identification is exceptionally difficult," says Iván Jiménez, a botanist at the Missouri Botanical Garden who analyzes the Madidi Project's data.

More than 6 hours later, everyone has worked up a sweat—better to be covered from head to toe than ravaged by insects and spiky trunks and bushes. Just before sundown, they head back to the small campsite, which is roughly one-quarter the size of a football field and took a day of machete-slashing to clear. Shared tents ring a common area with a large table and benches built out of branches and 8-meter-tall river grass stalks, held together with string. The wife of one of the guides prepares meals and boils stream water for drinking. But not even the burning fire can mask an omnipresent odor of nearby "wild-garlic" trees.

At night, wearing headlamps, team members press leaf samples into old newspapers to store them intact for the trip back. They listen to Bolivian rock on a battery-operated MP3 player and tell bad jokes until they collapse onto their foam sleeping pads, anticipating a dawn wake-up call to repeat the day's activity.

How big? Researchers go to great lengths to measure trunk diameters of surveyed trees.

"It's not easy being a botanist," says biology student Eber Renjito of the Higher University of San Andrés.

How forests work

The scale of the Madidi Project makes the hardships worthwhile. Already a decade old, the project is slated to go on for at least one more year or longer if continued funding can be found. Other similar biodiversity studies are smaller and have a shorter life span. Relatively few are based in the tropics, even though tropical plant species are among the most susceptible to climate change. And very little is known about tree patterns in tropical mountainous zones such as the Andes.

What is known points to a move-rather-than-adapt strategy for coping with climate change. Miles Silman, a biologist at Wake Forest University in Winston-Salem, North Carolina, has studied an area of Peru with a similar elevation gradient to Madidi. His work has shown that many trees are in fact shifting their ranges to higher, cooler ground rather than trying to adapt in place to increasing temperatures.

That's what Sebastian Tello, a biologist with the Madidi Project based at the Missouri Botanical Garden, thinks is going on in Madidi. Adaptation requires genetic change that occurs over the course of generations. Woody plants have long lives, so the shifts in genetic composition are extremely slow. "In general, we hypothesize that it's easier for tree species to move than adapt," Tello says.

Yet other environmental factors may impede geographical shifts by certain species, causing them to be left behind even as community compositions change. For example, the project's research has found a species-rich belt within Madidi, between 1000 and 1500 meters above sea level, that mixes trees from the lowlands and the mountains. "What will happen to this belt is uncertain," Jørgensen says, "since species adapted to lowlands and flat areas are not particularly well adapted to growing on sloping terrain." Trees with large buttresses, for instance, might be in danger because they may not be able to survive on a hill. "The high-diversity belt may shrink or disappear completely," he says.

Having even a vague idea of whether a community or species is at exceptional risk of disappearing is a main goal. "This kind of research is fundamental if you want to have representative ecosystems going into the future," Lovejoy says. Ideally, research like the Madidi Project gives policymakers an idea of which areas are most in jeopardy and in need of protection. "Since there is limited money for conservation," Jørgensen says, "we want to make sure the areas with greatest range of species, as well as the species that may have less chance for survival, are protected."

He warns, though, against drawing firm conclusions about climate change's effect on forests even after accumulating a mass of data over 10 years. A decade is not long enough. Sustaining the work over many decades may be the most important element to advancing this research. But Jørgensen admits that his own days of fieldwork might be nearing their end. "I'm getting a little too old for this," says the 54-year-old, red in the face and tired already. He hopes his Bolivian colleagues will take over the expeditions while he focuses on taxonomy and data analysis back at his desk in St. Louis. "It may be decades before we can really understand how our forests will change," he says. "But Madidi is a start."

–JEAN FRIEDMAN-RUDOVSKY

Jean Friedman-Rudovsky is a journalist based in La Paz, Bolivia.

For the record. The location of each tagged tree is mapped and recorded for future visits.

CREDITS: JEAN FRIEDMAN-RUDOVSKY

Published by AAAS

The Ingredients for a 4000-Year-Old Proto-Curry

When cooks in the ancient Indus River civilization prepared their meals 4000 years ago, the results may not have been much different from what you might order today in an Indian restaurant. Recent studies presented at the meeting found a surprisingly diverse Indus diet that incorporated spices such as ginger and turmeric, beans such as lentils and mung, grains such as rice and millet, and even bananas. An explosion in food-related studies, thanks to both new tools and new interest in rural villages, provides exciting clues to day-to-day life in the Indus, says Indus expert Jonathan Mark Kenoyer of the University of Wisconsin, Madison, who was not directly involved in the studies.

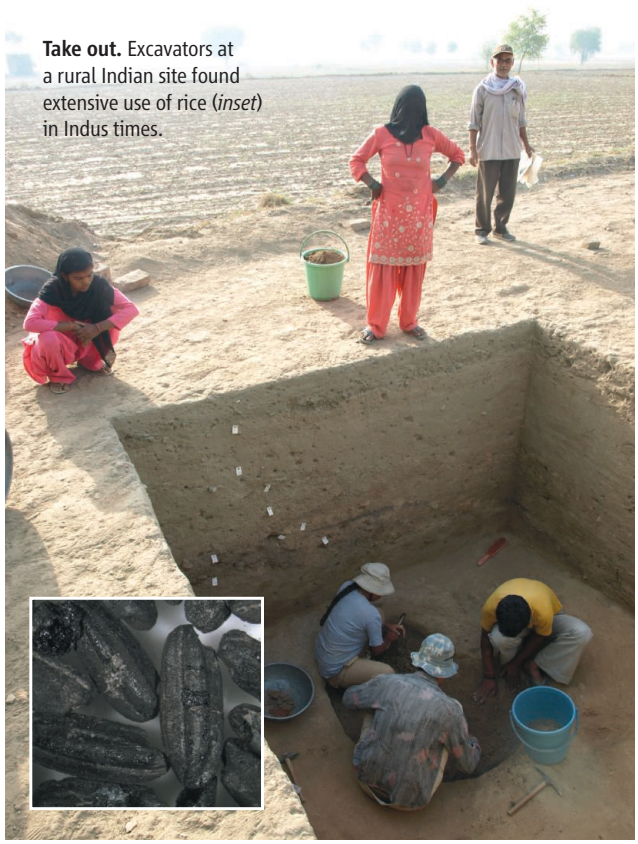

Take out. Excavators at a rural Indian site found extensive use of rice (*inset*) in Indus times.

CREDIT (MAIN AND INSET): C.A. PETRIE, LAND, WATER AND SETTLEMENT PROJECT

With Egypt and Mesopotamia, the Indus was among the first urban civilizations, centered on today's Pakistan and India. The Indus people built a half-dozen massive cities around 2500 B.C.E. that mostly fell into ruin after 1800 B.C.E. No Indus texts have been deciphered, however, and few images found, leaving scholars with fundamental questions about how the people lived, worked, and worshipped. But some of their traditions, including food preparation, may live on.

Archaeologists have long spotted burnt grains such as wheat, barley, and millet at Indus sites, but identifying vegetables, fruits, nuts, roots, and tubers has been more challenging. Researchers are increasingly using phytoliths—the mineral secretions left by plants—to identify specific plant remains, as well as starch grain analysis (*Science*, 2 July 2010, p. 28). Plants store starch granules as food, and the microscopic leftovers can be identified by researchers. For example, anthropologists Arunima Kashyap and Steve Weber of Washington State University, Vancouver, in Canada analyzed starch grains from human teeth from the ancient town of Farmana, west of Delhi, and found remains of cooked ginger and turmeric. They also found those ingredients inside a cooking pot. Dated to between 2500 and 2200 B.C.E., the finds are the first time either spice has been identified in the Indus. Cow teeth from Pakistan's Harappa—a major Indus city—yielded the same material. "It's like India today," Weber says. "Cattle wander around eating trash," including the remains of cooked meals. In some Indian regions such as the western province of Gujarat, some families still leave food remains outside the house as a ritual offering to cattle.

Whether or not these spices represent the earliest curry is not clear: Kashyap and Weber note that what makes curry curry is disputed even today. Black pepper and chili peppers, for example, are common in the dish today but were later imports to India.

Even bananas, not known to have been cultivated here until late medieval times, have turned up at three scattered Indus sites. A team led by Marco Madella, a Barcelona archaeologist with the Spanish National Research Council, found phytoliths of banana on grinding stones at Farmana. Phytoliths at the site of Loteshwar in Gujarat and at Kot Diji in the Indus heartland in Pakistan were also found. "I'm not confident in saying it was cultivated," Madella says. "But clearly the Indus people were in direct contact with people to the east," where the plant grew wild.

Indus farmers also grew a surprisingly wide array of grains and beans. Many archaeologists once thought that the society depended primarily on crops such as wheat and barley, which were planted in winter. But new data from rural villages challenge that idea. Examining two sites near today's Masudpur, west of Delhi, University of Cambridge archaeologist Jennifer Bates compared carbonized seed and phytolith density per liter of soil near hearths to determine the relative abundance of crops by period and site. Bates found that both villages practiced summer and winter cropping, and both ate wheat, barley, millet, and rice from early Indus times, as shown by nearby pottery; she also identified lentils and mung beans. Rice has long been assumed to be only a late addition in the Indus, yet one village apparently ate more rice than wheat or barley, although millet dominated.

Many of these crops have uses in addition to pleasing Indus palates, Kenoyer notes. Burned bananas produce salt, ginger can treat illness, and turmeric is used for both poultices and dyeing cloth. The data may also shed light on how specialized and exotic foods reflected class differences, he says. **–A.L.**

Diving Into the Indian Ocean's Past

Nearly 15 years ago, two fishers in the waters off the southern coast of Sri Lanka hauled up a stone slab etched with ancient Hindu symbols. During a brief 2008 dive, archaeologists retrieved pottery and glass ingots. Then, in December 2011, with funding from the U.S. National Endowment for the Humanities and other sources, researchers began the first systematic dives to examine what appears to be the oldest known shipwreck in the Indian Ocean, radiocarbon dated to between the 2nd and 1st centuries B.C.E. Because almost nothing was known about seafaring in this time and place, the wreck promises to remake our understanding of the region and era, says team

Clear sailing. Divers explore an ancient Sri Lankan wreck that could offer clues to early Indian Ocean trade.

member Osmund Bopearachchi, a historian at the University of Paris, Sorbonne.

Archaeologists suspected that traders crisscrossed the Indian Ocean at this time, but the evidence was slim. Just a century or so later, merchants from India and the Roman Empire plied the Indian Ocean, trading cotton, glass, and spices. But textual references and archaeological evidence of earlier maritime trade are extremely rare; the only known South Asian shipwrecks date from medieval times. Indians and Arabs dominated the medieval trade, which connected Europe and China, but its origins are murky.

The Sri Lankan wreck offers the first good look at such trade. The island, which lies off the southeastern coast of India, was an important Buddhist kingdom that eventually became a wealthy port of call. The ship remains lie near the estuary of Walawe Ganga, one of the nation's few navigable rivers. Just upstream lies Godavaya, a recently excavated monastery dating to the 2nd century B.C.E.; monastic settlements often played an important economic role at this time. Other nearby settlements go back to the 4th century B.C.E., says Bopearachchi, who works with underwater archaeologist Deborah Carlson of Texas A&M University, College Station, as well as the maritime unit of the Sri Lanka Department of Archaeology.

Only surface surveys have been done to date, examining artifacts spread across 40 meters of ocean floor that mark it as the site of a sunken ship. Massive glass ingots, used to make expensive vessels, were part of the ship's cargo and provide what Bopearachchi calls "the best physical evidence for the early exchange of raw glass in South Asia." Samples from both the glass and nearby pieces of metal point to an Indian origin, and the ship may have been bound for the port, he says.

Its remains lie in 34 meters of water amid strong currents, but the water is crystal clear, and conditions are good for diving during the winter monsoon. Archaeologists hope that the ship itself may lie below the bottom, providing evidence of shipbuilding technology. The team plans to begin excavating at the end of this year. The results "might lead to a rewriting of the economic, social, religious, and cultural history of the area," Bopearachchi says. Others agree that the find will shed needed light on a critical trade route. "This is the Silk Road of the sea," says Hans-Joachim Weisshaar of the German Archaeological Institute in Bonn.

–A.L.

CREDIT (TOP TO BOTTOM): SHEILA MATTHEWS/DEPARTMENT OF ARCHAEOLOGY OF SRI LANKA AND THE INSTITUTE OF NAUTICAL ARCHAEOLOGY; ROLAND BESENVAL

Persians Made the Afghan Desert Bloom

North-central Afghanistan is a harsh desert of dunes long thought to have been uninhabited save for the occasional hardy nomad; even today the region is sparsely settled. But a French team surveying the region north and west of Mazar-i-Sharif has recently discovered large settlements organized around an impressive water system dating back 2500 years. No other culture before or since has managed to support large settlements in this desolate region. The find could provide exciting new information on irrigation techniques that made the early central Asian desert bloom, say the small cadre of archaeologists who work here.

Roland Besenval, an archaeologist with the French national research agency in Paris; Eric Fouache, a geoarchaeologist at the University of Paris, Sorbonne; and others identified more than 30 large settlements, all dating to the period of the Achaemenid Persian Empire, which flourished from the shores of Greece to western India in the 5th and 4th centuries B.C.E. The empire was overwhelmed by Alexander the Great late in the 4th century B.C.E. The archipelago of northern Afghan settlements appears to have died out at that time or a little earlier, and has been largely uninhabited ever since.

Many of these towns or garrisons had massive walls that have been hidden in the sands. One site, Altin Dilyar Tepe, first noted by Russian researchers in the 1970s, sits on a hill that the French team determined was an artificial mound, showing that enormous manpower was used to build it, Besenval says.

Using a tiny, instrument-filled drone called a hexacopter, the team spotted a 2-meter-wide linear feature that led to a 60-by-80-meter basin near Altin Dilyar Tepe. The mud-brick canal stretches for nearly 10 kilometers, pierced periodically with at least two other large basins that coincide with settlements. Besenval says this apparent aqueduct likely carried water for farming from the Balkh River, which flows out of the mountains, across the harsh desert. Achaemenid pottery found nearby dates the structure as early as the 5th century B.C.E. By the 4th century B.C.E., a drying climate may have made this always-marginal land too difficult to farm even with irrigation, Besenval adds.

In Central Asia, where water remains a key and scarce resource, the discovery of a sophisticated water system this ancient excited archaeologists at the meeting. Besenval's interpretation of the feature "is very convincing," says archaeologist Pierfrancesco Callieri of the University of Bologna in Italy, who has dug in Central Asia. Besenval also recently found signs of irrigation at a site in Tajikistan that dates back long before the Achaemenids, as early as the 4th millennium B.C.E., suggesting that irrigation has old roots in the area.

Water lifeline. The sands of northern Afghanistan (*background*) have covered this ancient canal (*foreground*).

Because of security issues, the researchers couldn't stay overnight near the Afghan sites, so they have yet to establish details such as the aqueduct's gradient or whether it stretches another dozen kilometers to reach the Amu Darya river to the north. Besenval is eager to return to gather more data, but security concerns kept him out of the field entirely last season. "Our visits have been too short," he says in frustration. "And we have so many questions to ask."

–ANDREW LAWLER

See abstracts at http://www.easaa.cnrs.fr/

Published by AAAS

Better policies for HIV care

298

Ecosystem dynamics

306

LETTERS

edited by Jennifer Sills

Retraction

On the basis of new experiments (NMR studies with ^{17}O-labeled compounds and varying pH, additional x-ray crystallography, and others), the authors of the Report "A late-transition metal oxo complex: $K_7Na_9[O{=}Pt^{IV}(H_2O)L_2]$, $L = [PW_9O_{34}]^{9-}$" (*1*) have concluded that the full body of data does not support structural assignment of the title compound as a terminal platinum oxo. As a result, we retract the publication. The assignment is clarified in (*2*).

TRAVIS M. ANDERSON,[1] WADE A. NEIWERT,[2] MARTIN L. KIRK,[3] PAULA M. B. PICCOLI,[4] ARTHUR J. SCHULTZ,[5] THOMAS F. KOETZLE,[6] DJAMALADDIN G. MUSAEV,[7] KEIJI MOROKUMA,[7] RUI CAO,[8] CRAIG L. HILL[7]*

[1]Sandia National Laboratories, Albuquerque, NM 87185–0754, USA. [2]Department of Chemistry, Bethel University, St. Paul, MN 55112–6999, USA. [3]Department of Chemistry and Chemical Biology, University of New Mexico, Albuquerque, NM 87131–0001, USA. [4]Madison, WI 59719, USA. [5]La Grange, IL 60525, USA. [6]Dix Hills, NY 11746–4920, USA. [7]Department of Chemistry, Emory University, Atlanta, GA 30322, USA. [8]Department of Chemistry, Renmin University of China, Beijing 100872, China.

*To whom correspondence should be addressed. E-mail: chill@emory.edu

References

1. T. M. Anderson *et al.*, *Science* **306**, 2074 (2004).
2. K. P. O'Halloran *et al.*, *Inorg. Chem.* **51**, 7025 (2012).

Human Conflict: Beware Politicized Science

I AM WRITING IN REACTION TO THE COVER photo and accompanying caption selected for the 18 May special issue on Human Conflict. It seems disingenuous to claim that of all the world's conflicts, a building identified as destroyed by the Israel Defense Forces (IDF) was "not [chosen] for any political message or endorsement." Nobody eschews war more than Israelis, who, unfortunately, also know the consequences.

If the editors wanted striking visual impact and gruesome evidence of inhumanity, there were better choices: the killing fields of Cambodia, the destruction of the World Trade Center, Rwanda, Dresden, Hiroshima, Bataan, Darfur, Armenia, Normandy, Auschwitz... unfortunately, the list of greater carnage is nearly endless.

By identifying the IDF as perpetrators, the caption undermined the photo's role as a generic illustration of the consequences of conflict. Indeed, there was no need to identify the details. They were a distraction. The photo no longer represented abstract human violence, but rather one more illustration of Israel, taken out of context. Portraying Israel as the aggressor obscures the fact that the country is trying to defend itself against decades of assaults provoked by ethnic hostility—attacks still taking place. That is politicized science, which serves to encourage—not discourage—conflict.

JOHN R. COHN

Department of Medicine and Pediatrics, Thomas Jefferson University and Hospitals, Philadelphia, PA 19107, USA. E-mail: john.cohn@jefferson.edu

Human Conflict: Pacifists at Heart

THE BREADTH AND DEPTH OF THE HUMAN Conflict issue (18 May, p. 818) brings to mind Otto Rank's observation in *Psychology and the Soul* (*1*) that we still have primitive beliefs about death—for example, that heroic, spectacular, or sacrificial death conveys immortality, and that killing an enemy is killing death itself. After centuries of analyzing war, with its heroics and pathos, we have recently learned that most humans are like other social animals, which fight but instinctively stop short of intraspecies killing (*2*). Cited in 3 of the 11 special section Reviews and Perspectives, D. Grossman (*2*) found that most people, including soldiers, would sooner die than kill a person at close range. About 2% lack such inhibition (*2*); that characteristic is often expressed in military heroics. In civilian circumstances, the same characteristic is associated with tendencies toward antisocial behavior, including violent crime. This atypical group receives disproportionate attention in history and fiction, news and entertainment.

Those in the pacifist majority can be disinhibited if ordered by an authority and supervised, confirming Stanley Milgram's findings that most of us will comply with orders that violate some of our principles (*3*). Modern psychological conditioning of U.S. troops has contributed to an increased shoot-to-kill percentage, from only 20% in World War II to 90% in Vietnam (*2*), but evidently at high cost. As S. Maguen reports (p. 843), soldiers who have killed suffer post-traumatic stress disorder (PTSD) at higher rates. Veterans Administration psychologists recently coined the term "moral injury" (*4*), which relates to Maguen's point. The optimistic essay on PTSD by R. J. McNally (p. 872) omits mention of suicide, which has reached alarming levels among U.S. troops and veterans (*5*).

E. JAMES LIEBERMAN

Department of Psychiatry, George Washington University School of Medicine, Washington, DC 20052, USA. E-mail: ejl@gwu.edu

References
1. O. Rank, *Psychology and the Soul* (Franz Deuticke, Lepzig, Germany, 1930); translated by G. C. Richter (Johns Hopkins Univ. Press, Baltimore, MD, 1998).
2. D. Grossman, *On Killing* (Hachette Book Group, New York, 1995; revised and updated, 2009).
3. S. Milgram, *The Perils of Obedience* (Harpers, New York, 1973).
4. K. D. Drescher, *Traumatology* **17**, 8 (2011).
5. T. Williams, "Suicides outpacing war deaths for troops," *The New York Times* (9 June 2012), p. A10; www.nytimes.com/2012/06/09/us/suicides-eclipse-war-deaths-for-us-troops.html.

Human Conflict: Targeting Natural Resources

THE SPECIAL ISSUE ON HUMAN CONFLICT (18 May, p. 818) largely ignores a central dimension of violent conflict: the complex role of natural resources in the onset (*1*) and conduct of conflict, peacemaking, and recovery from conflict.

Grievances over access to land have been central to wars in countries such as Guatemala, El Salvador, and Nepal (*2*, *3*). Inequitable distribution of oil and gas revenues drove secessionist conflicts in places such as Indonesia's Aceh and southern Sudan (*4*).

Since the end of the Cold War, conflicts based on resources have grown rapidly in number: Armed groups in at least 18 conflicts have relied on revenues from diamonds, timber, coltan, and a range of agricultural crops from cacao to coca (*5*). For centuries, armies have targeted natural resources and the environment to deprive enemies of cover, food, and support (*6*), and the increased use of resources to finance conflicts has enhanced their value as a military objective (*7*).

Between 1946 and 2008, 40 to 60% of all intrastate conflicts were linked to natural resources (*8*). Resource-related conflicts are more likely to relapse, and do so twice as quickly compared with situations following conflicts without a link to natural resources (*8*).

There is growing recognition of the role of natural resources in building peace. A 4-year research project coordinated by the Environmental Law Institute, the United Nations Environment Programme, the University of Tokyo, and McGill University found that between 1989 and 2004, 51 of 94 peace agreements had provisions relating to natural resources, and all major peace agreements since then have included natural resources (*9*).

This study's analysis of experiences across more than 60 conflict-affected countries shows that successful peacebuilding can rely on aspects of natural resource management in terms of livelihoods and macroeconomic recovery; the provision of basic services, including water, sanitation, and electricity; governance and rule of law; and cooperation. For example, approximately 60 to 80% of livelihoods in conflict-affected countries depend directly on land, forests, and other natural resources; over 50% of a post-conflict country's gross domestic product usually comes from agriculture and extractive industries; and 50 to 80% of exports (and sometimes more than 95%) come from natural resources (*10*–*12*).

CARL BRUCH,[1]* DAVID JENSEN,[2] MIKIYASU NAKAYAMA,[3] JON UNRUH[4]

[1]Environmental Law Institute, Washington, DC 20036, USA. [2]Post-Conflict and Disaster Management Branch, United Nations Environment Programme, CH-1219 Geneva, Switzerland. [3]Graduate School of Frontier Sciences, University of Tokyo, Chiba, 277-8563, Japan. [4]Department of Geography, McGill University, Montreal, QC, H3A 2K6, Canada.

*To whom correspondence should be addressed. E-mail: bruch@eli.org

References
1. M. Ross, *J. Peace Res.* **41**, 227 (2004).
2. K. Macours, *Oxford Econ. Pap.* **63**, 1 (2011).
3. C. Kay, *Third World Quart.* **22**, 741 (2001).
4. P. Collier, A. Hoeffler, in *High-Value Natural Resources and Post-Conflict Peacebuilding,* P. Lujala, S. A. Rustad, Eds. (Earthscan, London, 2012), pp. 297–312.

5. United Nations Environment Programme, *From Conflict to Peacebuilding: The Role of Natural Resources and the Environment* (Nairobi, 2009).
6. J. E. Austin, C. E. Bruch, Eds., *The Environmental Consequences of War: Legal, Economic, and Scientific Perspectives* (Cambridge Univ. Press, Cambridge, 2000).
7. S. Autesserre, *The Trouble with the Congo: Local Violence and the Failure of International Peacebuilding* (Cambridge Univ. Press, New York, 2010).
8. S. A. Rustad, H. M. Binningsbø, "Rapid recurrence: Natural resources, armed conflict, and peace," (Centre for the Study of Civil War, working paper, Oslo, Norway, 2010).
9. United Nations Environment Programme, *Greening the Blue Helmets: Environment, Natural Resources, and Peacekeeping* (Nairobi, 2012).
10. C. Bruch, M. Boulicault, S. Talati, D. Jensen, *Rev. Eur. Commun. Int. Environ. Law* **21**, 44 (2012).
11. P. Lujala, S. A. Rustad, Eds., *High-Value Natural Resources and Post-Conflict Peacebuilding* (Earthscan, London, 2012).
12. International Labour Organization, *LABORSTA* (http://laborsta.ilo.org).

CORRECTIONS AND CLARIFICATIONS

News & Analysis: "Europe mulls plans to boost research in poorer regions" by L. Laursen (8 June, p. 1222). Robert-Jan Smits, director-general for research and innovation at the European Commission, is quoted saying, "Many countries say, 'Just give us the money, trust us, and leave us alone.'" He was referring to European Union structural funds, not funding for the E.U. Horizon 2020 program, as the article implied.

Reports: "The aftermath of megafaunal extinction: Ecosystem transformation in Pleistocene Australia" by S. Rule *et al.* (23 March, p. 1483). In the charts of pollen, dung, and charcoal variation in figs. S1 and S2, the numerical values on the truncated peaks were illegible because of low resolution. These values have now been clarified in a new version of the supporting online material on *Science* Online (http://www.sciencemag.org/content/335/6075/1483/suppl/DC1). In addition, the Fig. 1 legend in the main paper should have referred the reader to figs. S1 and S2 for the details of the scales of the charts and the values on the truncated peaks.

TECHNICAL COMMENT ABSTRACTS

Comment on "Illusions Promote Mating Success in Great Bowerbirds"

Gerald Borgia, Brian J. Coyle, Jason Keagy

Kelley and Endler (Reports, 20 January 2012, p. 335) claim that male great bowerbirds construct a visual illusion, using display object gradients, that affects mating success. We argue that they provide inadequate statistical support for their hypothesis, inappropriately exclude important data, and do not consider other display traits that explain mating success. We propose a more plausible alternative hypothesis to explain display object patterns.

Full text at www.sciencemag.org/cgi/content/full/337/6092/292-b

Response to Comment on "Illusions Promote Mating Success in Great Bowerbirds"

John A. Endler, Paul W. Mielke Jr., Laura A. Kelley

Borgia *et al.* raise some questions about our recent study showing that great bowerbirds create visual illusions that are used in mate choice. We address them by providing further details about our methods and results. We also provide detailed descriptions of our geometric calculations to address their measurement and analysis questions.

Full text at www.sciencemag.org/cgi/content/full/337/6092/292-c

Letters to the Editor

Letters (~300 words) discuss material published in *Science* in the past 3 months or matters of general interest. Letters are not acknowledged upon receipt. Whether published in full or in part, Letters are subject to editing for clarity and space. Letters submitted, published, or posted elsewhere, in print or online, will be disqualified. To submit a Letter, go to www.submit2science.org.

Comment on "Illusions Promote Mating Success in Great Bowerbirds"

Gerald Borgia,[1]* Brian J. Coyle,[1] Jason Keagy[2]

Kelley and Endler (Reports, 20 January 2012, p. 335) claim that male great bowerbirds construct a visual illusion, using display object gradients, that affects mating success. We argue that they provide inadequate statistical support for their hypothesis, inappropriately exclude important data, and do not consider other display traits that explain mating success. We propose a more plausible alternative hypothesis to explain display object patterns.

Kelley and Endler's (*1*) forced perspective model makes two major predictions: that male mating success is (i) positively related to the slope of the display object size gradient (width, Wslope; depth, Dslope) on the bower display court and (ii) negatively related to the standard deviation of the visual angles among display objects (width, $SD\Phi_W$; depth, $SD\Phi_D$). (We do not use their term "gesso" because this implies a functional differentiation of display objects that has not been demonstrated.) Their multiple regression models show an overall significant result for the slope and SDΦ variables. To meet predictions of their forced perspective argument, however, it is necessary that the regression slopes of variables in the model show the predicted association with mating success. In their regression, the Wslope variable is nonsignificant, and both Wslope and $SD\Phi_W$ have slopes opposite to the predicted direction. Separate regressions of each variable with male mating rate provide a more straightforward test of their predictions and show that for decoration gradients only, Dslope ($r^2 = 0.58$, df = 1,6, $P = 0.017$) is significant, and Wslope ($r^2 = 0.017$, df = 1,6, $P = 0.33$) is not. Neither visual angle variable is significant ($SD\Phi_w$: $r^2 = 0.06$, df = 1,6, $P = 0.46$; $SD\Phi_D$: $r^2 = 0.16$, df = 1,6, $P = 0.18$). So, their predictions are confirmed in only one of four cases (Fig. 1).

We disagree with Kelley and Endler's (*1*) suggestion that depth rather than width variables should more closely match their predictions. They claim to be assessing object size the way females see them, but their measurements are based on photos taken from above the display objects. This is different from the female's more horizontal perspective from inside the bower that can affect her perception of object depth. For example, this near-horizontal view can prevent females from seeing the depth of rounded snail shells and stones because the rear edge is hidden by their raised middle portion.

Kelley and Endler (*1*) describe glitches in their video recording system that may have affected estimates of their mating rate variable. They suggest that the lack of a correlation of recording time with matings and courtships indicates no bias; however, this is not a reasonable test because mating success rates in bowerbirds are highly skewed (*2*, *3*) and represent a fraction of all behaviors that may trigger cameras. Also, their near-significant result for courtships ($P = 0.06$) does not strongly support the suggested lack of association. Alternatively, male courtship success—the proportion of displays that lead to copulations—is a more reliable measure of male attractiveness in bowerbirds when cameras are fully operational and females are either individually marked (*4*) or unmarked (*5*). It more directly measures male display performance (*4*) (relevant for testing the effect of an illusion) and thus should more effectively correct for camera malfunctions. We found no correlation between the mating rate measured by Kelley and Endler (*1*) and courtship success ($r^2 = 0.07$, df = 1,6, $P = 0.49$), which suggests that their use of mating rate may be flawed. There was no significant relationship between male courtship success with Wslope ($r^2 = 0.09$, df = 1,6, $P = 0.55$), Dslope ($r^2 = 0.15$, df = 1,6, $P = 0.82$), Φ_W ($r^2 = 0.16$, df = 1,6, $P = 0.18$), or Φ_D ($r^2 = 0.16$, df = 1, $P = 0.91$), which does not support their prediction that display object gradients measured directly or as standard deviation of visual angles affects male attractiveness (Fig. 2).

Kelley and Endler excluded 9 of 17 bowers from their analysis in cases where they determined that females had insufficient time for "gazing at the scene on the court" [supporting online material for (*1*)]. Females who observed males for less than 55% of the time did not mate, and they indicate that they used this measure of female behavior to exclude males from their sample. However, three females who did not mate spent more than 55% of the time gazing at the scene in the bowers of excluded males [figure S3 and table S2 of (*1*)]. By their criteria, these males should have been included in the analysis. Also, several of the reasons the authors give for a display object gradient to correlate with male mating rate do not require females to look at males for any particular percentage of time, so excluding such a large number of males for whom they have information on display object gradients is inappropriate.

Kelley and Endler (*1*) do not consider any other hypothesis that might explain decoration gradients on great bowerbird bowers. An obvious alternative is that males avoid placing large objects on display courts near the bower so as not to hamper their own movements during courtship displays to females; this is consistent with the step-like pattern of size change seen in decorations of other species (*5*).

Finally, bowerbird display is complex and consists of multiple interrelated traits. Anderson

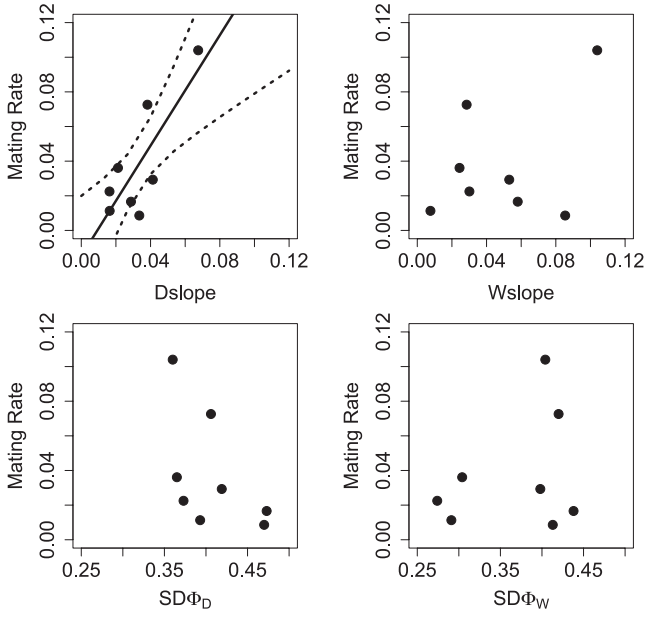

Fig. 1. Relationship between mating rate and display object gradients (Dslope and Wslope) or the standard deviation of the visual angles (Φ_W and Φ_D). Significant regression for Dslope is indicated with a solid regression line, with dotted lines denoting 95% confidence intervals.

[1]Department of Biology, University of Maryland, College Park, MD 20742, USA. [2]Department of Zoology, Michigan State University, East Lansing, MI 48824, USA.

*To whom correspondence should be addressed. E-mail: Borgia@umd.edu

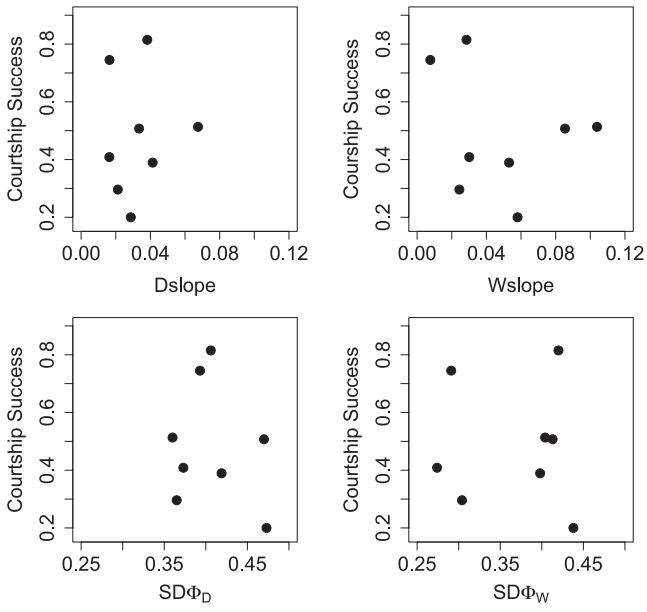

Fig. 2. Relationship between courtship success and display object gradients (Dslope and Wslope) or the standard deviation of the visual angles (Φ_W and Φ_D). None of the relationships are significant.

(*6*) noted that Kelley and Endler (*1*) failed to consider bower symmetry, which is known to explain male mating success in other bowerbirds, as possibly accounting for variation in mating success in their study. He is correct, but he understates the problem. Mating success is affected by multiple male display traits in bowerbird species, including number of decorations (*2*, *4*, *5*, *7*), bower quality (*2*, *3*), bower stick diameter (*2*), bower size (*8*), vocal display quality (*9*, *10*), and intensity of male courtship display (*4*, *9*). These display elements are commonly significantly correlated (*2*, *3*, *11*) and shared across species, which suggests that any effect of gradients on great bowerbird mating success should have been considered in relation to these other variables.

These considerations cause us to question whether male great bowerbirds construct illusions that affect male mating success.

References

1. L. A. Kelley, J. A. Endler, *Science* **335**, 335 (2012).
2. G. Borgia, *Anim. Behav.* **33**, 266 (1985).
3. G. Borgia, U. Mueller, *Emu* **92**, 11 (1992).
4. G. L. Patricelli, J. A. C. Uy, G. Borgia, *Behav. Ecol.* **15**, 297 (2004).
5. G. Borgia, *Anim. Behav.* **49**, 1291 (1995).
6. B. L. Anderson, *Science* **335**, 292 (2012).
7. J. R. Madden, *Behav. Ecol. Sociobiol.* **53**, 269 (2003).
8. J. A. C. Uy, G. Borgia, *Evolution* **54**, 273 (2000).
9. G. Borgia, D. C. Presgraves, *Anim. Behav.* **56**, 1121 (1998).
10. S. W. Coleman, G. L. Patricelli, B. J. Coyle, J. Siani, G. Borgia, *Biol. Lett.* **3**, 463 (2007).
11. G. Borgia, *Am. Sci.* **83**, 542 (1995).

20 February 2012; accepted 7 June 2012
10.1126/science.1220775

Response to Comment on "Illusions Promote Mating Success in Great Bowerbirds"

John A. Endler,[1]* Paul W. Mielke Jr.,[2] Laura A. Kelley[1]

Borgia *et al.* raise some questions about our recent study showing that great bowerbirds create visual illusions that are used in mate choice. We address them by providing further details about our methods and results. We also provide detailed descriptions of our geometric calculations to address their measurement and analysis questions.

Borgia *et al.* (*1*) questioned the validity of our recent study (*2*) showing that great bowerbirds' geometric illusions promote mating success. Here, we answer all their criticisms and further substantiate our results.

Our predictions were about the entire pattern (*2*), not width or depth independently. Borgia *et al.*'s (*1*) suggestion of separate analysis of visible width and depth (*w* and *d*) and the associated visual angles ($ø_w$ and $ø_d$) is statistically invalid, and there is no contradiction in the fact that the partial regression coefficients have opposite signs. This arises because *w* and *d* are different aspects of the same object. For any object other than a sphere, as the object orientation changes, if *w* increases, *d* must decrease and vice versa (see Fig. 1 and supplementary materials). Because bower objects are nonspherical, and often elongated, it is very difficult for a bowerbird to make good gradients in both *w* and *d* at the same time, making it very difficult to minimize both $s_{øw}$ and $s_{ød}$. Univariate measures simply ignore this tight relationship and also ignore the fact that there are a large number of equally good layouts with different combinations of $s_{øw}$ and $s_{ød}$ [figure 3 in (*2*)]. The prediction planes are tilted, yielding partial regression coefficients of opposite signs because on average the birds attend more to the effects of *d* than *w* and the two effects are strongly negatively related.

Distinguishing the noncolored (gesso) and colored objects is fully justified. Color and luminance are processed separately by the retina and brain (*3*). In several thousand hours of video recordings in several localities, about 3.5% of the objects picked up by males and waved at female were gesso. Including all objects in the analysis had no effect on any results.

Vertical photographs are excellent for reconstructing visual angles (ø). Females view the court from a height of ~30 cm and a distance of 30 to 80 cm, and this was included in our analysis. At this natural viewing height and distance, the hiding effects are very small. The size gradients reduce the effect even more because larger objects are behind smaller objects. Hiding does not affect the rank differences among bowers, and there is no significant effect of recalculating for all objects, even unrealistically assuming that all are spherical. (See the supplementary materials for details.)

Our mating assessment is accurate because direct measurement of mating success (number of matings) is always more accurate than related measures such as the proportion of successful courtships. The recording time used in our analysis was the time that cameras were primed to record, not the time that the cameras were triggered and actually recording. Our cameras were constantly primed to record during daylight hours, and we adjusted camera triggering by setting the region of interest, the minimum pixel change per frame, and frame changes for that region. Only movement within the avenue triggered recording, and false triggers were very rare. Our cameras did not "malfunction" as Borgia *et al.* suggested (*1*). Each bower had periods where cameras were not recording due to battery discharge, but these interruptions were randomly distributed over the whole 2.5-month mating period (*2*). We calculated mating rate as the number of matings observed during the time a camera was ready to record, and found no relationship between this measure and the number of matings ($r^2 = 0.10$, df = 18, $P = 0.68$). We disagree that male courtship success is a more reliable measure of male attractiveness compared with direct mating measures, and it does not take into account the duration of courtships. We found that courtship duration and mating success were correlated, whether courtship duration included the entire time a female was near the avenue ($r^2 = 0.61$, df = 18, $P = 0.004$) or whether it only included the time that a female was within the avenue ($r^2 = 0.59$, df = 18, $P = 0.006$). We found no relationship between the number of matings per minute of courtship and recording time ($r^2 = 0.06$, df = 18, $P = 0.27$).

Exclusion of bowers had nothing to do with the time females gazed at the court. We restricted our analysis to males that obtained one or more matings. This excluded earlier choice criteria and ensured that females were recorded (sexual dimorphism is negligible in this species, and young males frequently spend time in bower avenues). Mating refusals can result from many courtship and bower traits that are assessed before forced perspective comes into play. It is invalid to assume that criteria used early in a courtship sequence are necessarily correlated with criteria used later (*4*, *5*). We explored the conditional probability of mating given that a proven female was in the bower. There are many failures before that, but they are irrelevant to this question (*6*).

We tested the hypothesis that gradients might result if males put larger objects away from where they stand during the displays to avoid uneven footing. If true, then the objects would show steps, jumping to larger sizes where the male does not stand. For each court, we fitted a linear, quadratic, cubic, and sigmoid regression (generalized linear) model to the data and asked which model fit the data with the least error. The quadratic indicates whether object size increases in a faster-than-linear relationship as distance increases; some bowers have very large bones near the outer court edge. The cubic is sensitive to steps,

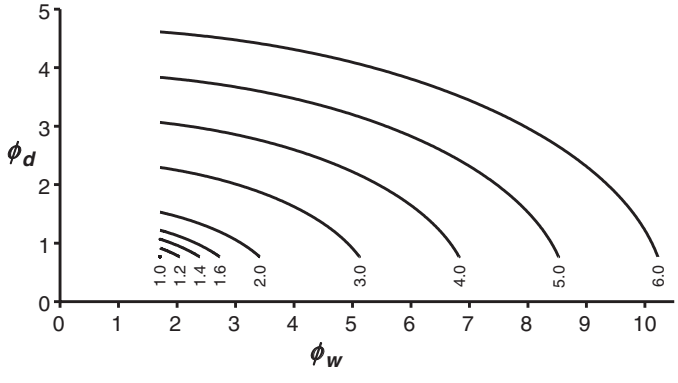

Fig. 1. Relationship between visual angles $ø_w$ and $ø_d$ (degrees) of circular (dot) or elliptical (lines) court objects with various aspect ratios (length/width, numbers along bottom), rotated from parallel to perpendicular to the avenue-object axis, and seen from typical natural height and distance. For reference, the Sun subtends about 0.5 degrees. See the supplementary materials for details and effects of other sizes and distances.

[1]Centre for Integrative Ecology, School of Life and Environmental Sciences, Deakin University, 75 Pigdons Road, Geelong VIC 3216, Australia. [2]Department of Statistics, Colorado State University, Fort Collins, CO 80523–1877, USA.

*To whom correspondence should be addressed. E-mail: john.endler@deakin.edu.au

but past the steps it turns toward the mean, so would be sensitive to very large objects in the outer court with smaller ones beyond and vice versa. The sigmoid fits simulated data with steps much better than the cubic. We tested both courts of 44 bowers in 2 years [typical data in figure S4 of (*7*)]. In 2009, all fit the linear model. In 2010, 96% fit the linear and 4% the cubic. The 4% fit to the cubic is either type I error or arises from a few large bones toward the end of the court, with smaller objects behind them. Therefore, stable footing is unlikely to explain the presence of object gradients in this population.

We considered courtship traits that are important to great bowerbirds (*2*, *7*, *8*), not traits that are important in all other species. Different bowerbird species are known to produce different sexual displays; for example, Borgia *et al*. (*1*) cite vocal mimicry, which is not part of the sexual display in great bowerbirds. Furthermore, different bowerbird species use different mate choice criteria. For example, object count predicts male mating success in some species (*9*–*11*) but not in others, including ours (*12*, *13*), and we also found no effect of decoration count on mating success ($P >> 0.05$). Moreover, female preferences even differ among populations of spotted bowerbirds (*14*), so factors that are important in mate choice are highly variable within and among bowerbird species. It is invalid to assume that all populations or species assess mates in the same way.

References

1. G. A. Borgia, B. J. Coyle, J. Keagy, *Science* **337**, 292 (2012); www.sciencemag.org/cgi/content/full/337/6092/292-b
2. L. A. Kelley, J. A. Endler, *Science* **335**, 335 (2012).
3. J. A. Endler, P. W. Mielke Jr., *Biol. J. Linn. Soc. Lond.* **86**, 405 (2005).
4. J. A. Endler, *Environ. Biol. Fishes* **9**, 173 (1983).
5. K. A. Young, M. J. Genner, M. P. Haesler, D. A. Joyce, *Evolution* **64**, 2246 (2010).
6. C. R. Fox, J. Levav, *J. Exp. Psychol. Gen.* **133**, 626 (2004).
7. J. A. Endler, L. C. Endler, N. R. Doerr, *Curr. Biol.* **20**, 1679 (2010).
8. C. B. Frith, D. W. Frith, *The Bowerbirds* (Oxford Univ. Press, Oxford, 2004).
9. G. Borgia, *Anim. Behav.* **49**, 1291 (1995).
10. J. A. C. Uy, G. Borgia, *Evolution* **54**, 273 (2000).
11. J. R. Madden, *Behav. Ecol. Sociobiol.* **53**, 269 (2003).
12. N. Lenz, *Emu* **94**, 263 (1994).
13. Y. Katsuno, T. Okida, N. Yamaguchi, *J. Yamashina Inst. Ornithol.* **42**, 19 (2010).
14. J. R. Madden, *Ibis* **148**, 425 (2006).

Supplementary Materials

www.sciencemag.org/cgi/content/full/337/6092/292-c/DC1
Supplementary Text
Figs. S1 to S5
References (*15*–*17*)

15 March 2012; accepted 7 June 2012
10.1126/science.1221690

Summer Reading

Looking for stimulation? Here are some suggestions and reviews from graduate students and postdocs.

Counterintuitive Solutions

Paradox: The Nine Greatest Enigmas in Science. Jim Al-Khalili. Bantam, London, 2012. 251 pp. £16.99. ISBN 9780593069295.

Paradoxes in physics have long been used to highlight knots in our understanding of how the world works. Jim Al-Khalili's *Paradox* examines nine celebrated examples and carefully disentangles them—demonstrating they are not logical paradoxes when cast in the right light. These run from the well known (Zeno's paradox, Maxwell's demon, and Schrödinger's half-immortal cat) to the less so (the pole in the barn paradox, Laplace's demon, and Olbers' paradox).

The paradox commonly attributed to Olbers provides the book's high point. The underlying question—why is the night sky dark?—is easy to state and equally easy to overlook. In explaining its resolution (a finite, expanding universe), Al-Khalili (a physicist at the University of Surrey) offers an enchanting portrait of our evolving understanding of the universe from Ptolemy through to Einstein. That the first correct solution was proposed by writer Edgar Allan Poe in his *Eureka: A Prose Poem*, an altogether fantastic and arguably unhinged intertwining of poetic and scientific passion (*1*), left me wondering whether this paradox held the seed of a more compelling book. The author's recollection of his first glimpse of the Andromeda galaxy through a telescope provides hints of his own passion and thrill of discovery. The thrill, unfortunately, is quickly dispelled by the aside that follows, "Physicists often tend to think in this strange way."

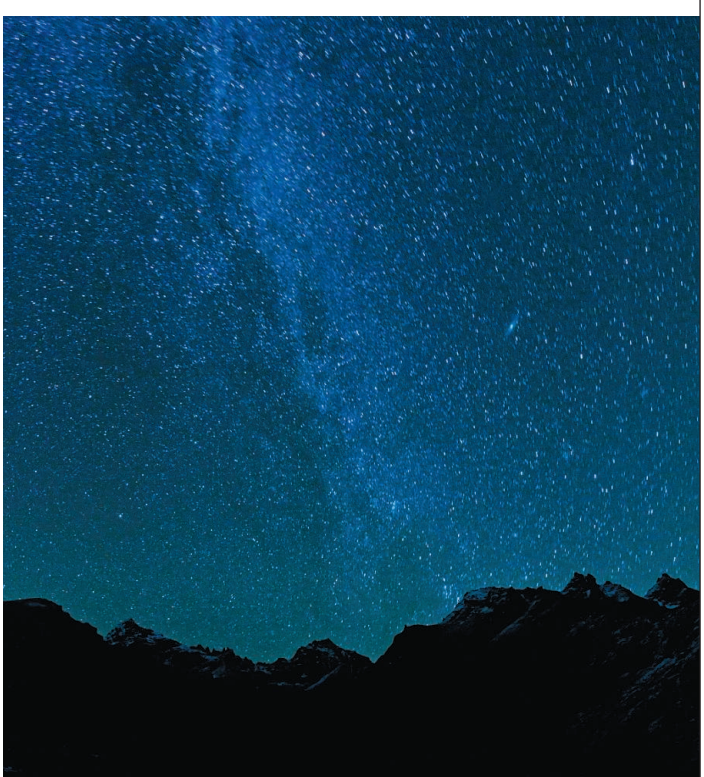

Dark despite all of the stars.

CREDITS: (LEFT) FOTOVOYAGER/WWW.ISTOCK.COM; (RIGHT) COURTESY NATIONAL LIBRARY OF MEDICINE

[1]Clarendon Laboratory, University of Oxford, Parks Road, Oxford OX1 3PU, UK. E-mail: michael.sprague@physics.ox.ac.uk

The book's tone resembles the pleasant patter of a magician who carefully offers his hat up for inspection before pulling out the rabbit. In many instances, the revelation delights—such as Al-Khalili's untangling of the Monty Hall paradox and, as an example in miniature, his discussion of the claim that "every Scotsman who travels south to England raises the average IQ of both countries." In other cases, we are left wanting. The discussion of Maxwell's demon, a creature that can seemingly create order from randomness, ends with the exasperated decree: "We can never defeat the Second Law of Thermodynamics. Always remember that." Nonetheless, Al-Khalili clearly summarizes all of the paradoxes, and he attempts solutions from several different angles for completeness.

Paradox provides a serviceable and, at times, compelling field guide to some of the most important and fascinating conundrums in physics. Al-Khalili engagingly describes the tools necessary to disarm them and bits of lore that enrich them. If he doesn't convincingly convey the most luminous tint of a particular paradox, that is all the more reason to venture forth in search of your own answers in your own strange way.

–Michael R. Sprague[1]

References

1. http://xroads.virginia.edu/~hyper/poe/eureka.html.

The Mind Inside Our Skull

Neuromania: On the Limits of Brain Science. Paolo Legrenzi and Carlo Umiltà; translated by Frances Anderson. Oxford University Press, Oxford, 2011. 132 pp. $29.95, £14.99. ISBN 9780199591343.

It was noon, and church bells were ringing as a doctor carefully examined a patient who had traumatic lesions in the frontal cranial bone. He noticed that pulsations in the cerebral arteries had become stronger, but, curiously, that change was not linked to changes in pulse rate and blood pressure measured on the patient's arm. The patient then confirmed his doctor's somewhat weird suspicion: the ringing bells reminded him it was time to say a prayer. This experience led the Italian physiologist Angelo Mosso (1846–1910) to the first attempt to relate variations of blood flow in the brain to mental activity, a link that is at the core of modern neuroimaging techniques such as functional magnetic resonance imaging (fMRI). Such techniques have allowed scientists to shed some light on the neural substrates underlying ongoing mental processes.

Angelo Mosso.

Mosso's research is one of several important contributions that 19th-century neurologists made toward establishing the relationship between the mind and the brain and that are reviewed in *Neuromania*. In this brief book, neuropsychologists Paolo Legrenzi (Ca'Foscari University, Venice) and Carlo Umiltà (University of Padua) bring a welcome appraisal of brain research to a broad audience. They provide an insightful and comprehensible overview of methods and techniques from the origins of brain science to today's MRI scanners. However, rather than emphasizing state-of-the-art procedures and technologies, they focus on the limitations of the field, covering methodological aspects and controversial assumptions that are commonly unknown to the general public.

Published by AAAS

Legrenzi and Umiltà put brain science in a broader perspective and discuss its sociopolitical implications, something scientists often neglect when presenting their own fields. The advent of neuroimaging opened many new lines of research. Because the question "what happens in the brain when … ?" fits practically any aspect of human activity, fMRI has been applied to a wide range of issues—from people's artistic or religious experiences to their preferences for specific products or political parties. As a consequence, many established concepts in the social sciences gained the prefix "neuro-" and a profusion of new disciplines emerged (neuroaesthetics, neurotheology, and neuropolitics, to mention a few). Putting these disciplines under scrutiny, Legrenzi and Umiltà highlight that old knowledge may have been presented as novel just by changing "mind" to "brain," without bringing actual scientific progress.

In the authors' reading, the brain has become the system of reference in explanations of human mind and behavior, relegating to the background an alternative approach that emphasized the social and cultural aspects of the human mind. A word of caution: The important issue is not a matter of which perspective should prevail but that many decisions regarding human life depend on how society defines the mind-body relationship. If only one aspect appears in the foreground, there may be drastic differences when dealing with thorny topics such as abortion and euthanasia. Answers to the complex questions raised by technological and scientific progress toward controlling life and death depend on ethical and ideological choices. To think about such issues from a strictly biological point of view may be misleading—after all, inside our skull there is more than just a brain. **– Ricardo Basso Garcia**[1]

Headed home. Rock pigeon (*Columba livia*).

Finding Their Place In the World

Nature's Compass: The Mystery of Animal Navigation. James L. Gould and Carol Grant Gould. Princeton University Press, Princeton, NJ, 2012. 310 pp. $29.95, £19.95. ISBN 9780691140452.

For most of human history, the clear understanding of the position of the Sun, the Moon, and stars and their movements across the sky was invaluable to human navigation. Sailing, especially on the open ocean without any visible landmarks, posed serious challenges to early civilizations. Nowadays, with the help of technologies such as Global Positioning Systems (GPS), navigation has become seemingly trivial. However, many nonhuman animals (including birds, turtles, and butterflies) can migrate thousands of kilometers and locate places with a precision we have only recently achieved. In *Nature's Compass*, evolutionary biologist James Gould (Princeton University) and science writer Carol Grant Gould discuss how animals carry out such extraordinary feats using only their senses.

While focusing mostly on honey bees and homing pigeons (which they have studied extensively in their own lab), the authors provide nonspecialists with a clear introduction to animal navigation. They warn that in analyzing animals' abilities to know locations and directions, we are prone to "imagining that animals see challenges" and "use the same strategies to solve the problems" as we do. In fact, the mechanisms used—the position of the sun and stars, polarized light and color gradients, endogenous timers, landmark memory and cognitive maps, magnetic fields, and more—vary both among taxa and within individuals (depending on context and age).

The Goulds guide readers through the multiple ways in which honey bees illuminate animals' navigation systems. In one intriguing example, forager bees were trained to a food location on a boat in a lake. Even though their dances back at the hive were vigorous, no recruits came to the boat. However, once the boat was moved close to the far shore, new bees began to appear. Bees do not usually fly over water, and the authors suggest that the bees at the hive decoded the direction and distance cues. But when positioning the food source in their mental maps located it in the middle of the lake, they decided not to act on the information.

Having been bred to return to their loft quickly and directly, homing pigeons provide a means for addressing essential questions that would be difficult to answer when working with "wide-ranging, twice-a-year migrants." The authors describe how the disruptive effects of solar storms on homing ability led Gould and others to propose that the pigeons have magnetic maps. Further testing revealed that the birds' location sense is greatly perturbed by magnetic-field anomalies. Using a magnetic map to return requires that the birds be able to sense small differences in field strength and direction. The Goulds mention the putative detector (a magnetite-rich organ in the beak), but they also note recent alternative findings. In addition to birds, sea turtles, spiny lobsters, and newts have been shown to use magnetic information to orient themselves.

The authors conclude with a short consideration of how understanding migration and its evolution may prove crucial for conservation in the face of habitat loss and changing climate.

Nature's Compass provides a wonderful account of efforts to unravel the mysteries of animal migration. Effectively drawing on their own experiences and the extensive scientific literature in the field, the Goulds explain what we currently know about how animals locate their positions. Their survey also offers an accessible starting point for those who might wish to improve our understanding of the topic. **–Homare Yamahachi**[2]

Evolution and Robots

Darwin's Devices: What Evolving Robots Can Teach Us About the History of Life and the Future of Technology. John Long. Basic Books, New York, 2012. 281 pp. $26.99, C$30, £17.99. ISBN 9780465021413.

I am envious of those who when asked what they work on can respond, "I study the evolution of robots." John Long (a vertebrate physiologist at Vassar College) is one such researcher, and reading *Darwin's Devices* is like listening, over drinks, to a voluble, engaging, and funny scientist tell you about his work. On occasion, his jargon gets a little heavy, he will toss in an unexplained concept, or he will digress about his youthful dreams to join the Navy. But for the most part, Long draws you into a compelling and wide-ranging conversation. This includes discussions of the mechanics of fish backbones, how we practice science, the nature of evolution, what it means to be intelligent, our dystopian

[1]Departamento de Psicologia (PG-Psicobiologia), Faculdade de Filosofia, Ciências e Letras de Ribeirão Preto, Universidade de São Paulo, Avenida Bandeirantes 3900. CEP 14040-901, Ribeirão Preto, SP, Brasil. E-mail: rbgarcia@pg.ffclrp.usp.br

[2]Kavli Institute for Systems Neuroscience and Centre for the Biology of Memory, Medical Technical Research Centre, Norwegian University of Science and Technology, 7030 Trondheim, Norway. E-mail: homare.yamahachi@ntnu.no

Published by AAAS

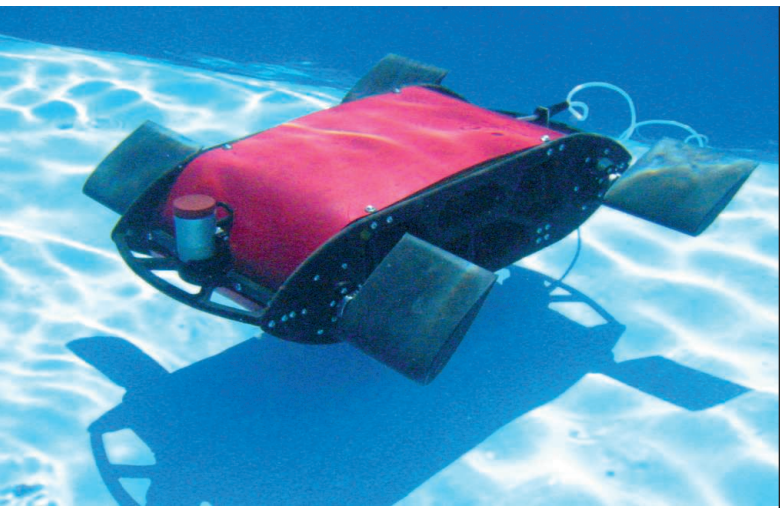

Robot Madeleine, an aquatic tetrapod.

robot future, and, most important, the crucial role of good models in science.

Darwin's Devices recounts the efforts of Long and his colleagues to study the biomechanics and evolution of vertebrae in fish using autonomous, aquatic robots as models. Long is interested in whether natural selection for more efficient food-seeking behavior could have led to the appearance of stiff backbones in the earliest vertebrates. By allowing robots with different backbone properties to compete with each other and by having the winners pass their traits down to the next generation of robots, Long and his collaborators follow backbone evolution in their population of robotic fish.

As Long explains his work, he presents an insider's tour of the practice of science. He offers hints on how to justify your research proposal to reviewers, carefully plan your experiments, deal with results that refute your hypothesis ("[i]n science this kind of failure is called progress"), and respond to criticism of your conclusions. He also includes accessible and careful discussions of the basic principles of evolutionary biology, which are nicely illustrated in the robot experiments. These features of the book will reward lay readers, because the scientific process and evolutionary biology are widely misunderstood.

Another topic commonly misunderstood, even within the scientific community, is the use of models. Not surprisingly, Long was challenged to justify to colleagues and reviewers his use of robotic fish as models of vertebrate evolution, because the simple robots clearly lack many important features of actual fish. *Darwin's Devices* presents an extended argument for why his robots are good models; in the process, it demonstrates why simple models of complex systems are powerful tools in biology.

Models capture our ideas about a system in concrete form, and they enable us to explore the implications of those ideas. Good models do not merely recreate the behavior of the represented system. They also provide a means to test hypotheses about key causal relationships that underlie the system's behavior. Their focused simplicity enables scientists to address specific questions without the obscuring influence of the full complexity of the original system. Embodied representations, robot models enjoy an advantage over in silico simulations in that they never inadvertently violate physical laws.

Long designs his robotic experiments to evaluate specific hypotheses that would be impossible to test in live fish, much less extinct ones. His informative, and often surprising, results serve as an interesting case study that illustrates the value of models in biology.

Accessible and thought-provoking, *Darwin's Devices* provides an exemplary account of scientific practice for the general reader. Of course, it benefits from the inclusion of stories about robots. **–Michael A. White**[1]

[1]Department of Genetics, Washington University, 4444 Forest Park Avenue, St. Louis, MO 63108–2212, USA. E-mail: mwhite@genetics.wustl.edu

Life from a Rooted Perspective

What a Plant Knows: A Field Guide to the Senses. Daniel Chamovitz. Scientific American/Farrar, Straus and Giroux, New York, 2012. 187 pp. $23. ISBN 9780374288730.

Think of your fondest memories. How many of those contain some kind of plant? Perhaps you recall a vacation visit to awe-inspiring giant sequoias; the vibrant yellows, oranges, and reds of a New England fall; or receiving roses on a special occasion. Although we often draw emotional ties to plants, it's easy to pass them daily with little regard. However, have you ever stopped and thought about the plants' ability to sense us?

In *What a Plant Knows*, Daniel Chamovitz guides readers through the landscape of plant biology and describes how it is not all that different from our own biological complexity. Chamovitz (a plant biologist at Tel Aviv University) draws on centuries of landmark research on plants' sensory capabilities, including Darwin's observations that canary grass grows toward light sources and growth experiments in the near-weightless conditions of the International Space Station.

Although a plant is rooted in one spot, it is not insensitive to the world. It must be able to detect and respond to environmental changes. Chamovitz discusses several examples, drawing parallels between human senses and those of plants. Plants "see" using cryptochrome, a blue-light receptor, to determine the time of the day that imparts circadian rhythm. Cryptochromes are now known from every kingdom of life. When a caterpillar nibbles on the leaves of a white poplar, the victim alerts neighboring brethren of the attack by emitting a hormone that surrounding trees can "smell." They respond by producing toxic compounds in their leaves to ward off the pest. The classic example of the Venus flytrap highlights that plant's ability to feel the pressure of an unsuspecting lunch and quickly close its jaws, operating via action potentials much like our own nerves.

Whereas plants cannot hear per se, a number of genes involved in hearing impairments in humans have been found in plants. These affect myosin, which is crucial for the function of the hair cells in our inner ear and the root hairs of plants (which allow them to absorb water and nutrients from the soil). Needing to know where the earth is, plants sense gravity. Employing a mechanism similar to that we use for balance, plants contain heavy starchy sacks that sink, thus indicating the down direction. And in order to time their next flowering, many plants remember whether they have experienced a cold season.

Tune deaf. Music does not affect the growth of marigold (*Tagetes erecta*).

Published by AAAS

The author never claims that plants are sentient beings with feelings and instead emphasizes their lack of nerves and brains. In fact, he often spotlights the faults of pseudoscience that has advanced alternative claims about plant sentience. (Such reports often lack proper scientific controls and set back the overall progress of plant biology.) Rather, Chamovitz tries to convey the interesting aspects of plants that we may take for granted.

Early on, Chamovitz reminds us that several of the most important discoveries in biology—including Robert Hooke's identification of cells (in cork) and Barbara McClintock's recognition of jumping genes (in corn)—arose through the study of plants. He gently hints that we should have a greater appreciation of plants' complexity and perceptiveness. Although he doesn't make any controversial arguments, he does suggest that we reconsider what it means to be aware. If plants can see, smell, feel, know where they are, and remember, then perhaps they do possess some kind of intelligence. Maybe that is worth reflecting on the next time you casually stroll past a plant. **–Chelsie Eller**[1]

Hot Seat in Our Warming World

The Hockey Stick and the Climate Wars: Dispatches from the Front Lines.
Michael E. Mann. Columbia University Press, New York, 2012.
413 pp. $28.95, £19.95. ISBN 9780231152549.

Just as the tobacco industry long denied that cigarettes are bad for human health, stakeholders in the fossil-fuel industry have disputed that humans cause climate change—and often that climate is changing—in order to protect their extremely profitable business. They have poured immense amounts of money into campaigns that have influenced politicians, media, the public, and even scientists, fueling the perception that the science remains in dispute. However, the strong consensus within the scientific community is that we are witnessing substantial shifts in climate and that those changes are largely due to human activities.

Climate change deniers have sought to discredit the scientific consensus by isolating researchers and attacking their credibility. Perhaps their hardest-hit target in the United States is Michael Mann, codeveloper of the hockey stick, a graph of Northern Hemisphere temperatures over the past millennium. Few have dealt with the contrarians more than Mann, the recipient of false accusations (such as fabricating data and conspiring with colleagues) for over a decade and a victim of Climategate. In *The Hockey Stick and the Climate Wars*, Mann seeks to share his experiences and science with the public and to expose the climate change deniers' fraudulent disinformation campaigns.

Anecdotes from Mann's childhood reveal a bright, passionate, and somewhat nerdy character. Whereas fellow high schoolers partied on the weekends, for instance, Mann was determined to develop a tic-tac-toe game on the computer. In addition to bringing out the author's personality, these stories introduce concepts that crucially help readers understand subsequent events. For example, while programming the tic-tac-toe game, Mann eventually discovered a clever shortcut, something often referred to as a trick in math and science. Years later, the discovery of the word "trick" in the hacked e-mails of prominent climate scientists would lead climate change skeptics to incorrectly accuse scientists of hiding data.

Mann's comprehensive rendition of every event—including names of all individuals involved—builds credibility for his account, as do the 100-plus pages of supporting notes with references. The author covers both sides of the debate, drawing details from scientific publications, blog posts, media coverage, letters from congressmembers, political decisions, courtroom trials, and investigations. Mann presents most of the events through the lens of his personal experiences, but the book also recounts various incidents experienced by other climatologists. Additionally, he complements the stories with accessible explanations of scientific tools and processes.

Dissecting numerous well-orchestrated attacks on climate science, Mann refutes each denialist argument with a wealth of broadly accepted evidence. He clearly demonstrates how science is a self-correcting process and that thousands of independent studies from various institutions and countries build on one another to form our current state of knowledge. Through an approach more humorous than accusatory, Mann lets the mistakes of the skeptics speak for themselves. For example, the Wegman report (*1*) highly regarded by contrarians is mostly plagiarized from works of credible climate scientists, with words twisted intermittently to support the views of the skeptics. Furthermore, Mann painstakingly explains how every phrase highlighted in the Climategate scandal—"one of the best-coordinated 'swiftboat' campaigns in modern history"—was taken out of context.

The book's thoroughness seems essential to accomplishing its goals. Still, *The Hockey Stick and the Climate Wars* may be difficult for some to read because of dense, unfamiliar terminology; the extensive name-dropping; and various distracting technical tangents. One can forget who is who, what is what, and who did what. Nevertheless, Mann's honest and thorough testimony on the attacks against climate science is a critical step toward resolving the climate change debate. **–Ilissa B. Ocko**[2]

References

1. http://republicans.energycommerce.house.gov/108/home/07142006_Wegman_report.pdf.

From the Belly of a Whale

Floating Gold: A Natural (and Unnatural) History of Ambergris.
Christopher Kemp. University of Chicago Press, Chicago, 2012.
209 pp. $22.50, £14.50. ISBN 9780226430362.

Carefully and thoughtfully written, Christopher Kemp's *Floating Gold* can take a place on the bookshelf among my favorite natural histories. Those peer at their subject from many angles, combining facts with observations of the places and people that have become part of its history. Kemp (a molecular biologist) tells stories about ambergris: fragrant stuff, produced in the gut of the sperm whale, that for centuries has been both a prized commodity and a compellingly mysterious substance.

Ambergris begins to form when the sharp, undigested beaks of ingested squid cause irritation in a sperm whale's intestines. In response, the whale produces a secretion that surrounds the beaks, forming proto-ambergris. A lucky whale might pass the growing mass like feces, or the concretion might eventually cause an intestinal blockage so complete as to be fatal.

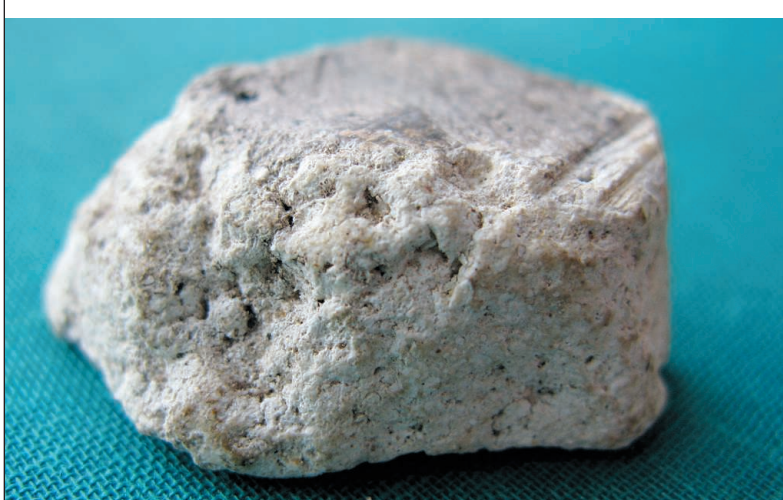

CREDIT: CHRISTOPHER KEMP

Fine white ambergris.

[1]Department of Biochemistry, University of Wisconsin, Madison, WI 53706–1544, USA. E-mail: eller@wisc.edu

[2]Atmospheric and Oceanic Sciences Program, Princeton University, 300 Forrestal Road, Sayre Hall, Princeton, NJ 08544, USA. E-mail: iocko@princeton.edu

Either way, the black, sticky, fecal-smelling mess of fresh ambergris may end up floating in the ocean. There it matures by degrees over a period of months to years, lightening in color to gray and then white and changing in odor until it achieves a scent that is, by all accounts, distinctive and hard to describe yet not unpleasant. Eventually, the ambergris might be washed up on a beach almost anywhere, found, and collected. Prized, at various times, as a perfume ingredient, a medicine, or a spice in gourmet recipes, its value can rival that of gold.

Given that convoluted process, it may not be surprising that the exact origin of ambergris was contentious well into the 20th century. The recent, somewhat tentative resolution of an old mystery sets the tone of the book, which manages to be both historical and immediate. Kemp intersperses historical notes related to ambergris, scientific findings on its production and its properties, accounts of correspondence and meetings with ambergris experts, and finally journal-like accounts of his compulsion to search local beaches for his own piece of treasure.

The author presents tantalizing descriptions of his research to discover everything there is to know about ambergris and enticing reports of his conversations with the often guarded, sometimes eccentric people who make a living as ambergris hunters or dealers. He manages to convey the ambiguities and peculiarities that arise when building a livelihood on a rare, practically impossible-to-synthesize natural substance whose existence depends on the misfortunes of a sick whale and the vagaries of a long aging process.

One recurring theme is wonder at the mystery and improbability of ambergris production and consumption—from the belly of a deep-diving whale, via ocean winds and currents, to the hands of an elite and secretive buyer. I understand that it's in such a spirit that Kemp often emphasizes how little is known about what sperm whales do during their deep dives. Even so, I felt some disappointment at the relatively little attention he gives to recent findings on the natural history of sperm whales.

That aside, I admit that I now find it hard to walk a beach without keeping an eye out for objects with strong, strange-but-not-unpleasant scents. I'm definitely waiting for a chance to smell the singular scent of ambergris (assuming that the stuff a Moroccan tour guide wanted to sell me was phony), although reading Kemp's fantastic description of his own attempts to eat ambergris was much more satisfying that trying the experiment myself. In other words, *Floating Gold* offers an enticing initiation into the shadowy and intriguing history of ambergris.

–Stacy DeRuiter[1]

MANIACal Roots

Turing's Cathedral: The Origins of the Digital Universe. George Dyson. Pantheon, New York, 2012. 443 pp. $29.95, C$34. ISBN 9780375422775. Allen Lane, London. £25. ISBN 9780713997507.

There's a certain vertiginous rush that new programmers experience when they make that transition from being barely able to get a computer to do their bidding to genuine mastery of the machine. It's the rush of vast possibilities opening up. *Turing's Cathedral* captures that feeling of possibility while recounting the path of computer science from groundwork mathematics to the realization of the first computing engines. George Dyson follows the stories of John von Neumann and other members of the Institute for Advanced Study (IAS) at Princeton from the theoretical foundations of computing to the invention of the first general-purpose computer.

Technology writer Dyson does an excellent job showing how most modern sciences, from nuclear physics to the beginnings of meteorology and genetics,

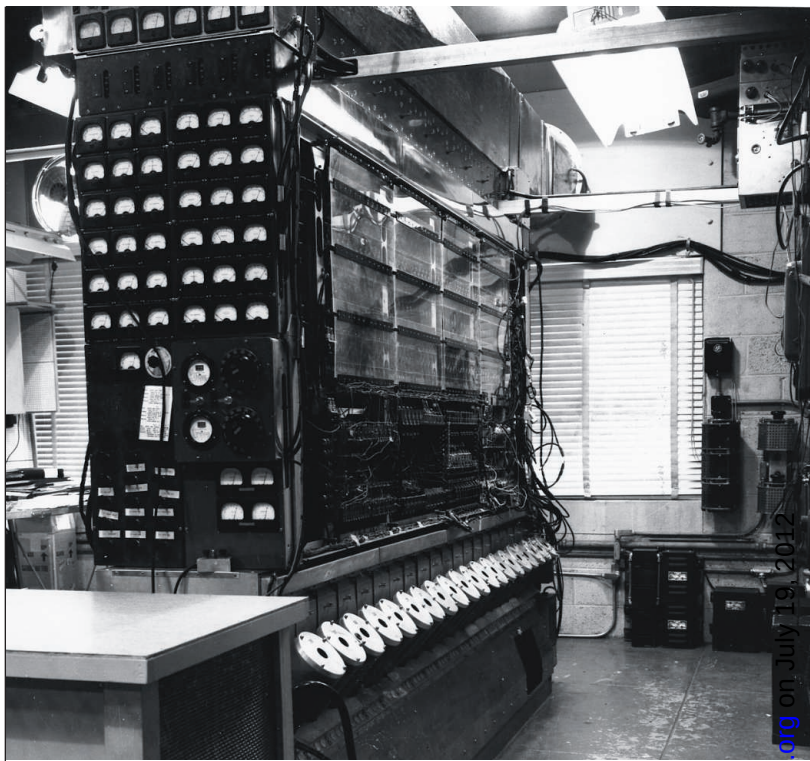

CREDIT: ALAN RICHARDS/SHELBY WHITE AND LEON LEVY ARCHIVES CENTER, INSTITUTE FOR ADVANCED STUDY, PRINCETON, NJ

MANIAC, the IAS computer.

have been driven and influenced by computational models. Nuclear weapons and the computer essentially enabled each other's invention. A roll call of notable scientists from Robert Oppenheimer and Martin Schwarzschild to Albert Einstein make their impact on—and are impacted by—the computer project. Dyson also records the creation of computer science as a separate discipline from mathematics.

The foundations of computer science came from something of a crisis in traditional mathematics. Kurt Gödel, who later joined the IAS, proved that no logical system (including mathematics) can prove its own consistency. Dyson traces how this problem directly led from the incompleteness theorem to the halting problem to the first working general-purpose computers. The halting problem (which asks whether it is possible to predict if a Turing machine running a particular program will finish in less than infinite time), it turns out, offers a key distinction between conventional mathematics and computer science. It essentially means that many things in computer science cannot be proven but must be determined through experimentation.

That they were witnessing the birth of a new science went unappreciated by most mathematicians at the IAS. The tension between them and the engineers and scientists who were designing and building the computer is clearly illustrated in the story of Julian Bigelow, von Neumann's chief engineer and computer architect. Dyson also records how Klári von Neumann, John's wife, became one of the world's first computer programmers when she was recruited from population research to perform the first Monte Carlo simulations on the critical mass reactions in atomic weapons.

Dyson is at his weakest when relating some older ideas to potential modern counterparts. For instance, he draws a line from the pioneering ideas of artificial life that drove some early experiments on computers to modern apps, which are simply well-packaged computer applications. A better comparison might have been to computer worms and viruses, which serve as software agents that infiltrate computers to particular ends. But these are quibbles. Dyson offers a wonderful description of the worlds of possibility that opened up as computer science first established itself in a corner of Olden Farm in New Jersey.

–James P. McCusker[2]

[1]Centre for Research into Ecological and Environmental Modeling, University of St. Andrews, St. Andrews, Fife KY16 9LZ, Scotland, UK. E-mail: sldr@st-andrews.ac.uk

[2]Tetherless World Constellation, Rensselaer Polytechnic Institute, and Department of Pathology, Yale University School of Medicine, New Haven, CT 06510, USA. E-mail: james.mccusker@yale.edu

Published by AAAS

PUBLIC HEALTH

Getting HIV Treatment to the Most People

Delivering HIV care effectively and ensuring long-term retention of patients requires innovative strategies and tools—and policies that enable their widespread use.

Sharonann Lynch,[1] Nathan Ford,[2] Gilles van Cutsem,[3] Helen Bygrave,[4] Bart Janssens,[5] Tom Decroo,[6] Isabelle Andrieux-Meyer,[7] Teri Roberts,[7] Suna Balkan,[8] Esther Casas,[9] Cecilia Ferreyra,[10] Marielle Bemelmans,[5] Jen Cohn,[11] Patricia Kahn,[12]* Eric Goemaere[4]

The new understanding that antiretroviral therapy (ART) can significantly reduce HIV transmission (*1*) has stimulated scientific and political leaders to claim that ending the AIDS epidemic is now a realistic goal. At the same time and despite last year's major international political commitments to put 15 million people on treatment by 2015 (*2*), large funding gaps threaten the gains already made and limit the potential to capitalize on the latest scientific progress. Underresourced clinics are managing ever-increasing numbers of people on treatment, even though there is attrition all along the care continuum, from testing to treatment initiation and long-term retention in care (*3*).

Doctors Without Borders or Médecins Sans Frontières (MSF) began offering ART in developing countries in 2000 and now supports some of the longest-running treatment cohorts; today, we support more than 220,000 people on ART in 23 countries, mainly in Africa. This article draws from our operational experience, which in turn draws partly on evidence from other providers, to present a perspective on the innovations required to deliver affordable, quality care for more people. We also compare this perspective with current realities on the ground, as assessed through a survey on HIV policies and practices, carried out in May to June 2012 by MSF teams in 16 countries where we work (see the table). Survey methodology and findings are presented online as Supplementary Materials (see table S1).

Models of care

Distance from clinics, patient fees, transportation costs, long clinic wait times, and competing demands (such as work schedules and child care) are all associated with attrition and poor adherence to treatment (*4*). Programs have responded by decentralizing free ART services to local health centers, with demonstrable improvements in retention (*5*). For example, in rural Lesotho, 2-year outcomes of patients receiving free ART at the primary-care level showed higher retention rates than outcomes from other programs (*6*). Decentralization also implies placing management of ART principally in the hands of nurses and other nonphysician providers, a strategy found in randomized trials to be safe and effective (*7*).

A community ARV group meeting (Tete, Mozambique).

Our survey shows some encouraging signs of progress on decentralization: ART is now available at more than 40% of public sector facilities in 4 countries (and >20% of facilities in 8), and 10 countries allow nurses to initiate ART. Thirteen out of 16 countries surveyed allow lay counselors to provide ART adherence counseling. However, four countries with an HIV prevalence above 1% are still below 25% facility coverage, and six countries do not allow nurses to initiate ART—restrictions that impede decentralization and integration with primary, tuberculosis (TB), and prenatal care. Mozambique is the only country with an HIV prevalence >5% that does not allow nurses to initiate ART or follow up ART patients. Shortages of nurses and lack of support for lay health workers at the primary-care level have also limited some countries' efforts to decentralize ART. Moreover, policy and practice sometimes diverge. For example, nurses and midwives can prescribe in Guinea, but only under a doctor's supervision—which reduces the impact of the task-shifting policy. In Malawi, shifts to first-line regimens with fewer side effects and to viral load monitoring for all patients on ART are included in the guidelines, but full rollout has been deferred due to funding shortfalls. Uganda and Zimbabwe regularly provide up to 2 months of refills, although this is not written policy.

Looking ahead, care providers and policymakers increasingly recognize the need to move HIV/AIDS care out of the clinic entirely, i.e., to manage patients in their communities. Over the past few years, MSF and others working in a range of high HIV-burden settings have piloted community-based programs with varying degrees of peer- and self-management. One successful example is the community ART groups established in rural Mozambique, where six patients per group take turns traveling to the clinic each month to receive their 6-monthly medical check-up and to pick up antiretroviral (ARV) medicines for themselves and group members. Implemented at 20 health facilities in Tete province, 1384 people formed 291 groups between February 2008 and May 2010; to date, only 0.2% of these patients have been lost to follow-up (compared with a regional average of 15% at 2 years) (*8*). On the basis of this success, in July 2011, Mozambique's Ministry of Health announced plans to roll out community ART groups across the country. Over the last 6 months, delegations from the ministries of health of Malawi, South Africa, Swaziland, and Zimbabwe have visited this program to assess its feasibility and

[1]Médecins Sans Frontières (MSF) Access Campaign, New York, NY 10001, USA. [2]MSF, London EC1N 8QX, UK. [3]MSF, South Africa and Lesotho, Capetown, 7700 South Africa. [4]MSF, South Africa Medical Unit, Johannesburg, 2017 South Africa. [5]MSF, 1090 Brussels, Belgium. [6]MSF, Tete, Mozambique. [7]MSF Access Campaign, 1211 Geneva 21, Switzerland. [8]MSF, 75011 Paris, France. [9]MSF, 1018 DD Amsterdam, Netherlands [10]MSF, 08001 Barcelona, Spain. [11]MSF Access Campaign, Nairobi, 00200 Kenya. [12]MSF, New York, NY 10001, USA.

*Author for corrrespondence. E-mail: patricia.kahn@newyork.msf.org

Published by AAAS

appropriateness for their own countries, and Malawi has now launched a pilot program.

Other decentralized approaches aim to relieve the burden on patients and health-care systems by providing multiple-month routine ARV refills and simplified clinic appointments. For example, patients in Zimbabwe who were given 3-month refills per visit had outcomes comparable to those receiving their pills monthly (*9*). However, policies in several countries limit implementation of these strategies: Only 7 of 16 countries surveyed allow multiple-month ARV refills for stable patients. A further impediment to implementation is inadequate drug supplies—when stocks (and/or funds) are low, clinics sometimes dispense as little as weekly refills (*10*).

Highly mobile populations require further adaptations in treatment delivery (*11*). In one example, MSF found that cross-border seasonal migrant farm workers in South Africa's Musina district (on the border with Zimbabwe) treated at a mobile HIV/TB clinic were more likely to start and continue ART than they were before the mobile service began. An initial screening had found lower ART coverage among farm workers than among their Zimbabwean or South African national counterparts, reflecting the former group's fear of discovery (of their undocumented status), and sometimes because clinics denied them treatment out of concern over adherence and continuity of care. To address this, in 2011, MSF and the Limpopo Department of Health launched a mobile HIV/TB service providing weekly visits to six farms (population 7500). Patients planning on returning temporarily to Zimbabwe receive a 3-month ART supply plus "tail protection" (1 week supply of two ARVs, to prevent development of resistance to nevirapine or efavirenz—longer half-life drugs in first-line ARV regimens—in case of a forced treatment disruption) and a transfer letter to another ART clinic. All patients carry a health "passport" containing records of their treatments, medications, and laboratory results (*12*). Given the prevalence of migration in Southern Africa, this model (or adaptations of it) could potentially benefit many regional ART programs.

Better tools

Viral load monitoring is an essential tool used routinely in Western countries but rarely available in low-resource settings. Regular monitoring enables care providers to distinguish patients who are poorly adherent to treatment from those who have developed drug resistance and need to switch regimens (*13*). Without it, patients failing treatment are

HIV POLICY AND PROGRESS INDICATORS ACROSS 16 COUNTRIES

Parameter	Cameroon	CAR	DRC	Ethiopia	Guinea	India	Kenya	Lesotho	Malawi
Population (millions)	20.10	5.10	73.6	93.8	10.9	1210.2	43	1.9	16.3
HIV adult prevalence rate§	4.30	4.9†	2.6	1.5	1.5	0.3*	6.2	23*	10.6†
Service coverage and availability									
Percentage of people in need receiving ART	49.6	26.1	12.3	86*	56.9	33.8‡	72.1‡	61	57.70
Number (and %) of public sector facilities offering ART	108 (4.4)	76	222	743	41 (9)	1297 (3)	1242 (34.8)	197 (94)†	487 (80.4)
Viral load testing¶									
For confirmation of treatment failure	OPT	OPT	OPT	No	OPT	REQ	OPT	OPT	REQ
For routine monitoring of people on ART	OPT	No	No	No	No	No	No	No	No
Available	LTD	LTD	LTD	LTD	LTD	LTD	Yes	LTD	LTD
Task shifting and treatment simplification									
Nurses can initiate ART	NF	Yes	No	Yes	Yes	No	Yes	Yes	Yes
Lay workers–testing and ART adherence counseling	ART	ART	Yes	No	HIV	Yes	Yes	Yes	Yes
Routine refills at 2–3 months	No	No	No	2	No	2	2–3	No	2–3

	Mozambique	Myanmar	South Africa	Swaziland	Uganda	Zambia	Zimbabwe
Population (millions)	23.5	54.6	48.8	1.4	35.9	14.3	12.6
HIV adult prevalence rate§	11.5*	0.5	16.6	26‡	6.7	14.6*	13.1
Service coverage and availability							
Percentage of people in need receiving ART	45.5	33.4	52	80	54.3	77.6	79.7
Number (and %) of public sector facilities offering ART	261 (22)	100 (3.4)	2552 (68)	110 (42)	1424	1784 (25.4)†	590 (36)
Viral load testing¶							
For confirmation of treatment failure	OPT	OPT	REQ	OPT	OPT	OPT	OPT
For routine monitoring of people on ART	REQ	No	REQ	No	OPT	OPT	No
Available	No	LTD	Yes	LTD	LTD	LTD	LTD
Task shifting and treatment simplification							
Nurses can initiate ART	No	No	Yes	Yes	NF	Yes	Yes
Lay workers–testing and ART adherence counseling	HIV	No	Yes	Yes	Yes	Yes	Yes
Routine refills at 2–3 months	No	No	3	3	No	3	No

HIV policy and progress indicators across 16 countries. Further information and references for all data are in Supplementary Materials. HIV program and policy data are from 2011 except where indicated (*2009; †2010, ‡2012). Population figures are as of 1 January 2012, except for India, which is from the end of 2011. There are some caveats to the data on percentage of people in need and receiving ART: In Ethiopia, need is based on CD4 <200; in India, the coverage figure is based on the number of people registered to be in need of ART; ART facilities in Malawi include some Christian Health Association (part MOH-supported) sites, and Uganda figures include both MOH and non-MOH sites. §Age 15–49 years. ¶Included in national plan and available. OPT: Viral load testing for this purpose is recommended, but optional in the national protocol. REQ: Viral load testing for this purpose is required in the national protocol. LTD: Limited. NF: Nurses provide follow-up to patients but are not allowed to initiate ART. HIV: HIV testing administration and counseling only. ART: ART adherence counseling only.

Published by AAAS

often underdetected and undertreated (*14*). Besides compromising individual care, treatment failure diminishes the community benefit of ART through both increased morbidity and the transmission of drug-sensitive and drug-resistant strains (*15*).

A study comparing outcomes of ART patients in South Africa, where routine viral load monitoring is available, to those in Malawi and Zambia, where it is not, found significant differences: In South Africa more people were appropriately switched to second-line therapies (9.8 versus 2.1%), and fewer people died (4.3 versus 6.3%) or were lost to care (9.2 versus 15.3%) (*16*). Another study in South Africa found that over two-thirds of patients with detectable viral load reverted to undetectable levels after enhanced adherence support (*17*). However, not all studies have shown benefit (*18*), and although most care providers would agree that viral load monitoring is desirable, considerable debate remains about its feasibility given the limitations of current tools.

Recent studies found viral load monitoring to be a cost-effective strategy compared with current (clinical and CD4 cell count) monitoring. Further cost reductions can be expected as the volume of viral load testing increases (*19*).

Despite being recommended for a decade (*20*), few programs in Africa have access to routine viral load testing. Of the 16 countries surveyed, only South Africa routinely monitors viral load, and although 15 of the 16 surveyed countries recommend viral load testing for confirmation of treatment failure, in practice it is not widely available.

Until recently, access has been limited by the lack of simple, affordable viral load monitoring technologies. However, the landscape is changing: New tests appropriate to district-level laboratories, plus several point-of-care tests, will become available in 2013 (*21*). Sufficient funds for implementation will be essential to ensure that the best products reach the market and that multiple manufacturers are encouraged to enter the market, to create much-needed price competition. At the same time, cost-reducing strategies such as pooled viral load testing and less frequent testing of stable patients should be further explored (*22*). Expanded access to viral load monitoring—which provides an early warning tool and a safety net for patients—could, at the community level, facilitate greater program simplification and decentralization and help shift routine follow-up to nonmedical staff outside health facilities.

Evidence from these and other settings suggests that increased task shifting, treatment simplification, and viral load testing will support further scale-up, improved adherence to treatment, and improved detection of treatment failure.

Better policies

Even with the most innovative strategies and tools, confronting and reversing the HIV epidemic will fail without sufficient increases in funding and decreases in drug prices. Given all the promising science and progress, this year is an opportune time for countries (particularly donors to the Global Fund) to announce increases to next year's HIV/AIDS funding. Otherwise, opportunities to implement improved policies and strategies and to reach more people will be further delayed, as will the chance to help countries struggling most, such as those in our survey where ART reaches one-third or less of those who need it (Central African Republic, Democratic Republic of Congo, India, and Myanmar).

Although efficiencies can be made in the system, more funding in the short term is needed to achieve longer-term cost savings (*23*). Efforts to reduce cost by adapting services should take into consideration the longer-term benefits of providing an optimized package of care, including viral load testing and accelerated access to treatment. For example, introducing viral load monitoring increases the cost of ART per person per year but is likely to save money down the road by preserving first-line (less expensive) treatment longer and by detecting and treating drug-resistant HIV strains earlier. As costing models demonstrate, scaling up faster now makes financial sense over the long term (*24*).

Options for making high-priced patented medicines affordable include negotiating voluntary licenses (*25*) or issuing a "compulsory license" to override a patent. Compulsory licenses for HIV drugs issued by Brazil and Thailand set an important precedent for access to medicines that have been priced out of reach. Countries should be encouraged to exercise this right more regularly.

At a time when donors are calling for greater efficiencies in the global AIDS response, bilateral trade agreements are being pursued that, paradoxically, seek to increase intellectual property protection and further threaten access to affordable medicines. Examples include the EU-India Free Trade Agreement and the Trans-Pacific Partnership Agreement, with the United States seeking unprecedented levels of intellectual property protection with 10 Pacific Rim nations.

Such obstacles, combined with an increasingly difficult funding environment, present hurdles that must be overcome to reach the 7.6 million more people who still need treatment, to retain people in long-term care, and to move toward policies of treating earlier. Although some countries are making progress by moving HIV care closer to where people live and delivering it in ways that better fit into patients' lives, most national programs require a quantum leap forward to build community-based platforms for HIV testing and ARV delivery.

References and Notes

1. M. S. Cohen *et al.*, *N. Engl. J. Med.* **365**, 493 (2011).
2. United to end AIDS: Achieving the targets of the 2011 Political Declaration: Report of the Secretary-General, United Nations General Assembly 66th Session, 2 April 2012.
3. S. Rosen, M. P. Fox, *PLoS Med.* **8**, e1001056 (2011).
4. E. J. Mills *et al.*, *PLoS Med.* **3**, e438 (2006).
5. G. Fatti, A. Grimwood, P. Bock, *PLoS ONE* **5**, e12888 (2010).
6. R. Cohen *et al.*, *J. Int. AIDS Soc.* **12**, 23 (2009).
7. I. Sanne *et al.*, *Lancet* **376**, 33 (2010).
8. T. Decroo *et al.*, *J. Acquir. Immune Defic. Syndr.* **56**, e39 (2011).
9. K. Kuwenyi *et al.*, Sixth IAS Conference on HIV Pathogenesis and Treatment, abstr. no. MOPE429.
10. MSF, No time to quit: HIV/AIDS treatment gap widening in Africa (May 2010; www.doctorswithoutborders.org/publications/reports/2010/MSF-No-Time-to-Quit-HIV-AIDS.pdf).
11. H. Bygrave *et al.*, *PLoS ONE* **5**, e13198 (2010).
12. T. Matambo *et al.*, presented at MSF-UK Scientific Day, 25 May 2012; http://presenter.qbrick.com/?pguid=c37366ab-d37e-4b07-a39a-b0568f16c075.
13. K. C. Sigaloff *et al.*, *J. Acquir. Immune Defic. Syndr.* **58**, 23 (2011).
14. World Health Organization and Joint UN Programme on HIV/AIDS (UNAIDS), Joint WHO/UNAIDS Annual Consultation with Pharmaceutical Companies: Global Forecasts of Antiretroviral Demand 2012–2013. (WHO, Geneva, 2011), pp. 1–23.
15. R. L. Hamers *et al.*, *Lancet Infect. Dis.* **11**, 750 (2011).
16. O. Keiser *et al.*, *AIDS* **25**, 1761 (2011).
17. A. Calmy *et al.*, *Clin. Infect. Dis.* **44**, 128 (2007).
18. P. Mugyenyi *et al.*, *Lancet* **375**, 123 (2010).
19. R. L. Hamers *et al.*, *AIDS* 1 (2012).
20. WHO, Scaling up antiretroviral therapy in resource-limited settings: Guidelines for a public health approach (WHIO, Geneva, 2003).
21. M. M. Murtagh, HIV/AIDS diagnostic landscape. *UNITAID Tech. Rep.* May 2012.
22. G. U. van Zyl *et al.*, *Clin. Infect. Dis.* **52**, 264 (2011).
23. B. Schwartländer *et al.*, *Lancet* **377**, 2031 (2011).
24. B. Ventelou *et al.*, *PLoS ONE* **7**, e34101 (2012).
25. J. Bermudez, E. 't Hoen, *Open AIDS J.* **4**, 37 (2010).

Acknowledgments: Our deep thanks go to the MSF staff, field teams, and Access Campaign staff for their work in gathering the national policy data presented here; the Joint United Nations Programme on AIDS (UNAIDS) for input into the survey design and support for the survey; D. Holtzman, K. Kalaris, and M. French for help with compiling and fact-checking these data; K. P. Q. Phelan and S. Shettle for their help with manuscript preparation; W. Owen for graphics work; and J. MacAllister for work on the survey table. We especially thank the mission staffs and our community counterparts who have contributed to MSF's fight against HIV over the years.

Supplementary Materials

www.sciencemag.org/cgi/content/full/1225702/DC1

Published online 12 July 2012
10.1126/science.1225702

PLANT SCIENCE

Defining the Plant Germ Line—Nature or Nurture?

Cellular redox state affects cell fate determination during germline development in plants.

Clinton Whipple

Teasing apart environmental from inherent or genetic causes in human development is notoriously difficult. Although both likely play important roles, we tend to favor one or the other to explain why we turn out the way we do. A similar nature-nurture tension is at play in the acquisition of cell fates during development. A fertilized zygote must not only divide, but its daughter cells must acquire distinct identities. Are cell fates determined by lineage, such that a mother cell can only give rise to daughter cells of a certain type, or can daughter cells adopt multiple identities depending on their environment? On page 345 in this issue, Kelliher and Walbot (*1*) show that germline cell identity in maize (corn) is specified by cellular redox potential (the oxidation-reduction state of a cell) under the influence of the environment, and not by cell lineage, as previously thought.

Whereas the animal germ line is established early in development and maintained as a segregated lineage until maturity (*2*), plants can specify multiple germ lines late in development. Challenging the view that the plant male germ line is also lineage controlled (*3*), Kelliher and Walbot carefully followed cell division and fate in male reproductive organs, or anthers. By manipulating the redox state of normal and mutant anthers, the authors show that a series of environmental and cellular signals establish the male germ line (see the figure). In the first step, *male sterile converted anther 1* (*msca1*) gene activity and the low redox potential of early anther induces a germline fate. Subsequently, these germline cells secrete a signaling molecule, MULTIPLE ARCHESPORIAL CELLS 1 (MAC1), which both stops further germline proliferation and causes neighboring cells to become supportive tissue. Modulating O_2 levels revealed that a hypoxic environment can induce any cell of the early anther to differentiate as germ line. Because maize anther development is initiated within tightly enclosing leaves that block gas exchange, the authors propose a model in which a hypoxic environment inside the leaves creates a natural redox gradient, diminishing toward the center of the anther. Internal cells respond to a low redox potential by differentiating as germ line.

The study by Kelliher and Walbot adds to a growing body of evidence connecting modulation of cellular redox state and developmental decisions in plants. The maize *msca1* gene encodes a glutaredoxin protein involved in redox homeostasis. In the model plant *Arabidopsis thaliana*, the *ROXY* genes also encode glutaredoxins that regulate floral organ number and germline development (*4*). Both *ROXY* and *msca1* belong to a plant-specific class of glutaredoxins that modify regulatory proteins in the cell, including developmental regulators (*5*). Another recent study emphasizes the role of redox homeostasis in root meristem development (*6*). All these examples from plants are intimately associated with developmental decisions in the germ line or in meristem tissue (undifferentiated tissue as at the tip of a shoot or root), all of which comprise stem cell niches. Thus,

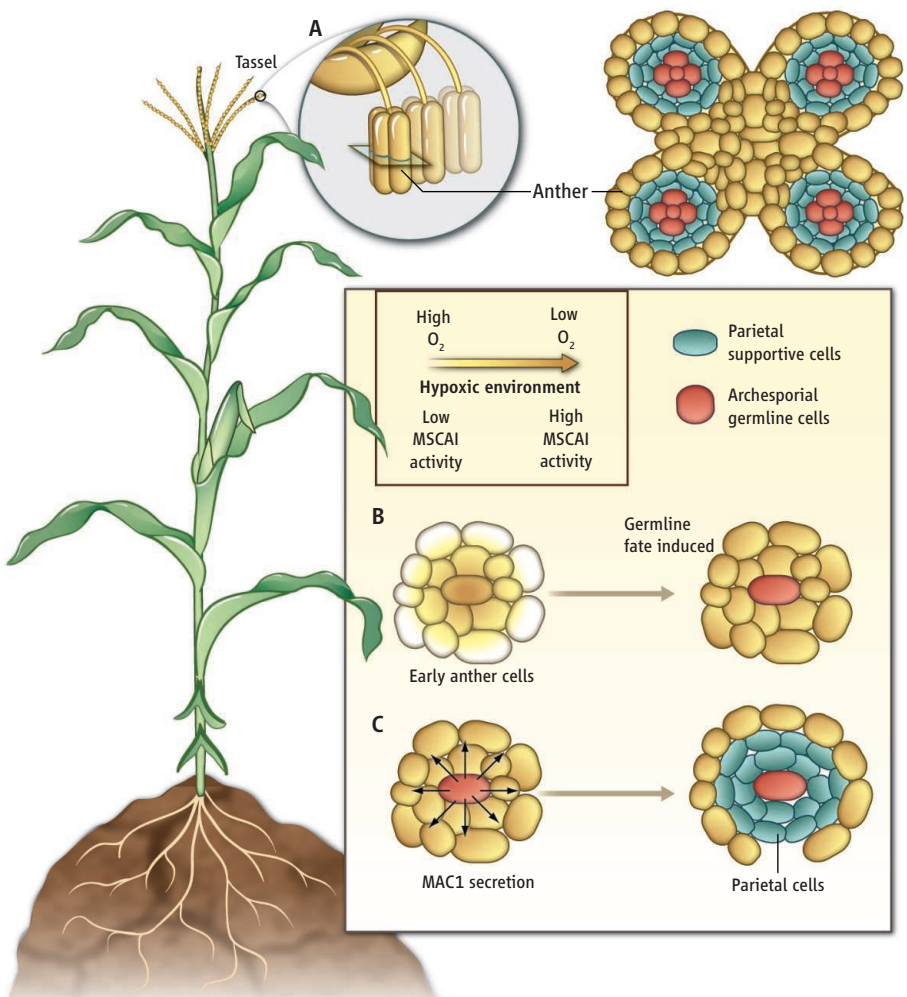

Establishing the germ line. (**A**) A cross section of an anther (male reproductive organ) shows lobes where somatic cells establish germline niches. Centrally located germline archesporial cells undergo meiosis. Two layers of parietal cells surround the germ line and become supportive tissue. (**B**) A cellular gradient is created by naturally decreasing O_2 concentration and the activity of the glutaredoxin MSCA1. Central cells have sufficiently low redox potential to become archesporial. (**C**) The newly specified archesporial cell releases the small protein MAC1, which signals adjacent cells to divide and form supportive tissue.

CREDIT: B. STRAUCH/*SCIENCE*

Department of Biology, Brigham Young University, Provo, UT 84602, USA. E-mail: whipple@byu.edu

Published by AAAS

cell redox state is emerging as a factor regulating the plant stem cell niche, similar to what has been described in animals (*7*).

Although the determinants of the germ line in maize, including *mac1* and *msca1*, are still being characterized, more is known in *Arabidopsis* where a similar signaling module allows adjacent cell layers to communicate and maintain the stem cell niche (*8*–*11*). The findings of Kelliher and Walbot show that maize employs a conserved mechanism, which is not surprising. More unexpected is the striking resemblance to the signaling module that maintains the plant shoot meristem in which a secreted peptide binds to receptors in adjacent cell layers (*12*). The protective leaves that usually cover vegetative meristems may promote a hypoxic environment near the meristem. If this is true, then manipulation of redox state could have a similar effect on the vegetative meristem. Further studies on the role of redox homeostasis in vegetative meristem development may provide answers.

Perhaps the most intriguing implication of the study by Kelliher and Walbot is that a naturally arising redox gradient can serve as a developmental signal. It remains to be seen if a similar mechanism is at work in plants such as *Arabidopsis* that develop their flowers outside of enclosing leaves. Indeed, maize and other grasses are not typical of most land plants whose developing reproductive structures are much more exposed, potentially making it difficult to maintain the proposed redox gradient. Maybe future germline cells modulate their own redox state, as has been described in root meristem differentiation (*6*). If redox state is directly regulated by the cell, a patterning mechanism is still required to distinguish the cells that will initiate this regulation. Does *msca1* respond to a naturally arising redox gradient, or does it directly participate in lowering the redox state? Distinguishing nature from nurture may not be so easy after all.

References

1. T. Kelliher, V. Walbot, *Science* **337**, 345 (2012).
2. C. Juliano, G. Wessel, *Science* **329**, 640 (2010).
3. C. L. H. Hord, H. Ma, *Plant Cell Monogr.* **9**, 361 (2007).
4. S. Xing, S. Zachgo, *Plant J.* **53**, 790 (2008).
5. S. Li *et al.*, *Plant Cell* **21**, 429 (2009).
6. H. Tsukagoshi *et al.*, *Cell* **143**, 606 (2010).
7. B. Keith, M. C. Simon, *Cell* **129**, 465 (2007).
8. S. L. Yang *et al.*, *Plant Cell* **15**, 2792 (2003).
9. C. L. Hord *et al.*, *Plant Cell* **18**, 1667 (2006).
10. U. Schiefthaler *et al.*, *Proc. Natl. Acad. Sci. U.S.A.* **96**, 11664 (1999).
11. W. C. Yang *et al.*, *Genes Dev.* **13**, 2108 (1999).
12. H. Schoof *et al.*, *Cell* **100**, 635 (2000).

10.1126/science.1224362

CHEMISTRY

Molecule Formation in Ultrahigh Magnetic Fields

An extreme magnetic field applied perpendicular to a diatomic or linear molecule increases its bond strength through a paramagnetic interaction.

Peter Schmelcher

Strong electric and magnetic fields tend to have opposite effects on the formation and structure of molecules. Strong electric fields always tend to separate the oppositely charged particles (electrons and nuclei), which causes molecules to ionize and dissociate. However, for strong homogeneous and static magnetic fields, binding can be strengthened. For hydrogen, the simplest atom, a certain class of its quantum states, including the ground state, becomes increasingly bound with increasing magnetic field strength (*1*–*3*). The electronic cloud shrinks transverse to the magnetic field, and because of the immediate proximity of the attractive nucleus, the overall energy decreases. This feature transfers to diatomic and linear-chain molecules, where the chemical binding energy increases and the corresponding bond distances decrease. The field strengths needed are far beyond the strongest available in the laboratory (30 to 40 T) but can be encountered in the atmospheres of magnetic white dwarfs (10^2 to 10^5 T) and neutron stars (>10^7 T). On page 327 of this issue, Lange *et al*. (*4*) show that, in addition to this diamagnetic enhanced binding, there exists an elementary paramagnetic bonding mechanism that occurs for the perpendicular orientation of a diatomic molecule with respect to the external magnetic field.

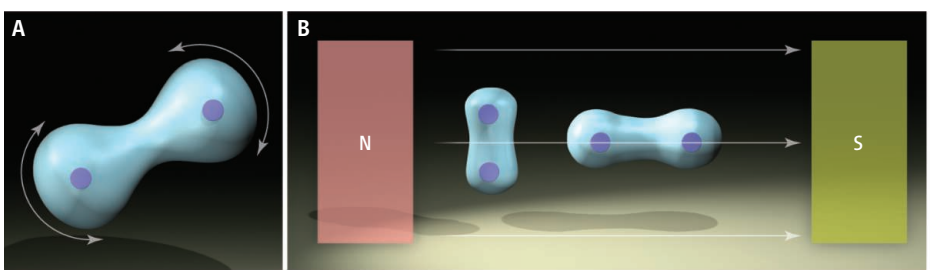

Stronger against the field. A schematic illustration of (**A**) a rotating diatomic molecule in field-free space and (**B**) the parallel and orthogonal configuration of the molecule in the presence of a high magnetic field. Lange *et al*. show that the bond strength increases for the perpendicular case through paramagnetic interactions.

Strong magnetic fields cause novel effects in molecular structures and dynamics mainly because of the pronounced anisotropic character of the magnetic forces. Accounting for these effects requires the development of innovative computational approaches for their theoretical description (*5*, *6*). In the absence of electric and magnetic fields (a field-free space), the binding of the nuclei via the electrons depends only on the internuclear distance. In a magnetic field, however, the orientation of the internuclear axis of a diatomic molecule with respect to the external field plays a crucial role, and the electronic binding energy becomes a two-dimensional potential energy surface (see the figure).

For a diatomic or linear molecule, the lowest-energy configuration is typically that of the molecular axis parallel to the magnetic field. The corresponding angular motion of the molecular axis changes from free rotation in zero field to a hindered rotation and finally pure vibrational motion in strong fields. This response is found by Lange *et al*. for the ground state of $^1\Sigma_g$ symmetry of H_2. With increasing field strength, the spin-triplet states (unpaired spins) decrease their energy gap to the spin-singlet states through the corresponding Zeeman shift. Finally, above a

Zentrum für Optische Quantentechnologien, Universität Hamburg, 22761 Hamburg, Germany. E-mail: pschmelc@physnet.uni-hamburg.de

Published by AAAS

certain critical field strength, the $^3\Sigma_u$ state represents the ground state of H_2, which is then, for even stronger fields, replaced by the $^3\Pi_u$ state (*7*, *8*).

The $^3\Sigma_u$ state in field-free space cannot accommodate any vibrational states, nor can it even for strong fields for molecular and magnetic field axes aligned parallel. However, for a perpendicular magnetic field, dramatic changes were found by Lange *et al*. through extensive quantum chemical computations. The antibonding orbitals responsible for the unbound character of the $^3\Sigma_u$ state undergo a metamorphosis for a perpendicular field that stabilizes the molecule. The field-induced bonding in this case is neither of covalent nor of ionic nature, but represents a different bonding mechanism with paramagnetic character. The latter is based on the lowering of the kinetic energy and the antiparallel orientation of the acquired spatial angular momentum in the presence of a strong magnetic field. A simple model for the field-dependent molecular orbitals confirms this basic mechanism.

The paramagnetic bonding mechanism is not based on the correlations of the electronic motion, although they slightly change it quantitatively. It already appears within Hartree-Fock theory, in which the electrons move in their respective averaged field. To confirm the appearance of this mechanism beyond the hydrogen molecule, Lange *et al*. have explored the He_2 spin-singlet ground state that is weakly bound by dispersion forces if there is no external field. In a strong field on the order of a few 10^5 T, He_2 exhibits a perpendicular orientation while its bond distance decreases by a factor of 3 and its dissociation energy increases several hundred times. Here, the same mechanism is at work as in the case of the $^3\Sigma_u$ state of H_2, triggered by the change of character of the antibonding orbitals.

Atoms, molecules, and condensed matter systems exposed to strong magnetic fields represent a fascinating topic, and the work by Lange *et al*. has added a key bonding mechanism. The competition between the anisotropy-introducing magnetic field and the attractive and repulsive Coulomb forces is responsible for an enormous complexity and diversity of the microscopic behavior. Indeed, the existing investigations show that different excited states of a molecule, or ground states of similar molecules, can behave in a vastly different manner, and provide a first look at a largely unexplored area: the world of magnetized matter.

It might seem that this world is hidden from us by the requirement of enormous laboratory field strengths. However, available field strengths are progressively increasing, in particular for pulsed magnetic fields in the milli- or microsecond regime that are already achieving fields of hundreds of teslas. Besides this, standard laboratory magnetic fields of a few teslas are sufficient to introduce novel magnetic properties into highly excited Rydberg states (*3*, *9*), for which the weakened Coulomb force is comparable to the paramagnetic or diamagnetic forces, or both. In this respect, the very weakly bound Rydberg molecules with a huge bond length and a large electric dipole moment, originally predicted by Greene *et al*. (*10*) and recently found for a specific class experimentally by Pfau and co-workers (*11*), are of particular interest and might be an ideal system to probe strong magnetic field effects in the laboratory.

References

1. H. Ruder, G. Wunner, H. Herold, F. Geyer, *Atoms in Strong Magnetic Fields* (Springer-Verlag, Berlin, 1994).
2. P. Schmelcher, W. Schweizer, Eds., *Atoms and Molecules in Strong External Fields* (Plenum, New York, 1998).
3. H. Friedrich, H. Wintgen, *Phys. Rep.* **183**, 37 (1989).
4. K. K. Lange *et al*., *Science* **337**, 327 (2012).
5. P. Schmelcher, L. S. Cederbaum, *Phys. Rev. A* **37**, 672 (1988).
6. E. I. Tellgren *et al*., *J. Chem. Phys.* **129**, 154114 (2008).
7. Yu. P. Kravchenko, M. A. Liberman, *Phys. Rev. A* **56**, R2510 (1997).
8. T. Detmer *et al*., *Phys. Rev. A* **57**, 1767 (1998).
9. T. F. Gallagher, *Rydberg Atoms* (Cambridge Univ. Press, Cambridge, 1994).
10. C. H. Greene *et al*., *Phys. Rev. Lett.* **85**, 2458 (2000).
11. V. Bendkowsky *et al*., *Nature* **458**, 1005 (2009).

10.1126/science.1224869

CHEMISTRY

Nanomaterials for Drug Delivery

Nanometer-scale polymeric materials are increasingly used to surmount the barriers faced by drugs and vaccines on their way to their site of action.

Jeffrey A. Hubbell[1] and Ashutosh Chilkoti[2]

All drugs face several transport barriers on their tortuous journey from their site of introduction to their molecular site of action. Critical barriers include rapid filtration in the kidney and clearance via the reticulo-endothelial system (RES)—particularly for drugs that spend a lot of time in the bloodstream—as well as transport from the bloodstream to target cells within tissues. At the tissue or cellular target, the drug must cross the plasma membrane, and within the cell, it must escape the harsh acidic environment of endolysosomes, within which biomolecular drugs such as proteins and oligonucleotides may be inactivated or degraded. Other barriers are the nuclear membrane and the multiple drug resistance mechanisms that pathological cells can develop. Recent studies illustrate some particularly promising ways in which nanomaterials as drug or vaccine carriers can assist in navigating these barriers, with a particular focus on administration by injection.

For drugs administered through injection, the vasculature provides both a road to the destination—the site of disease—and many detours for the drug to be lost in transit. Transport in the vasculature and in the tissues that those vessels perfuse depends on convection in the circulation as well as diffusion and convection in the tissue interstitium (i.e., between the blood capillaries and the lymphatic capillaries) (*1*). One challenge has been to attenuate the filtration rate of molecules from the bloodstream, especially into the kidney, and to avoid premature clearance by the RES.

To address this, the hydrodynamic radius of protein drugs has been increased to ~10 nm by grafting the hydrophilic polymer poly(ethylene glycol). This technology, referred to as PEGylation, is based on the twin observations that larger hydrophilic molecules are filtered by the kidney more slowly than smaller ones and that PEGylated proteins more successfully evade premature clearance through the RES. Gao *et al*. recently created site-specific, PEG-like conjugates by polymerizing very long polymer chains from one of the protein termini. This approach increased the hydrodynamic radius from 3 nm for the native protein to >20 nm for the conjugate (*2*). In a similar, genetically encoded approach,

[1]Institute of Bioengineering, School of Life Sciences and School of Engineering, and Institute of Chemical Sciences and Engineering, School of Basic Sciences, Ecole Polytechnique Fédérale de Lausanne, CH-1015 Lausanne, Switzerland. [2]Department of Biomedical Engineering and Center for Biologically Inspired Materials and Materials Systems, Duke University, Durham, NC 27708, USA. E-mail: jeffrey.hubbell@epfl.ch

Schellenberger *et al*. expressed therapeutic proteins as fusions with a long, unstructured, hydrophilic polypeptide that seems to share many of the valuable attributes of PEG. Such fusions led to projected extension of circulation half-lives of exenatide, an important peptide drug for type 2 diabetes, from 2 hours to >100 hours (*3*).

The tumor vasculature is much leakier to colloidal objects than the healthy vasculature, allowing micelles and associated drugs to accumulate there. For tumor-targeting protein drugs, the approaches described above can lead to enhancement in circulation lifetime by a factor of 10 and improved accumulation in tumors relative to the native protein (*2*).

Even larger self-assembled polymer micelles are being developed to target specific tissues and even subcellular compartments in tumors. In one such approach, MacKay *et al*. (*4*) conjugated a hydrophobic cancer drug via an acid labile linker to an elastin-like polypeptide. Driven by the hydrophobicity of the conjugated drug, these polymers self-assemble into micelles <50 nm in diameter. These micelles then localize to tumors. In the acidic environment of the endolysosomes of the tumor cells, the drug is cleaved to reach its nuclear target, leading to a potent therapeutic response in an animal model.

In a remarkable feat of multifunctional polymer design, Murakami *et al*. have developed micelles that form a complex with a platinum-based DNA-targeting anticancer drug in a pH- and Cl^--dependent manner, with drug release and activation favored at acidic pH and high Cl^- (*5*). The latter conditions are unique to late endosomes (just prior to endosomal fusion with lysosomes) and lysosomes. Late endosomes are localized near the cell nucleus, allowing directed delivery of the drug close to its DNA target, thus escaping the cytoplasmic resistance mechanisms that often inactivate the free drug.

Other micelle approaches abound (*6*, *7*). Notable among these is an optimization of micelle shape for highly prolonged circulation (*8*). Polymer micelles for use in drug delivery are typically formed by self-assembly of block copolymers with a hydrophobic domain (which drives polymer association in the presence of water) and a hydrophilic domain (which restricts this association to the nanometer dimension). The relative volume of the two polymer segments controls the shape of the resulting micelle. Christian *et al*. have shown that polymer architectures that lead to cylindrical micelles enable highly prolonged circulation in the blood stream, thereby reducing off-target toxicity and increasing efficacy in tumor killing with drugs such as paclitaxel (*8*).

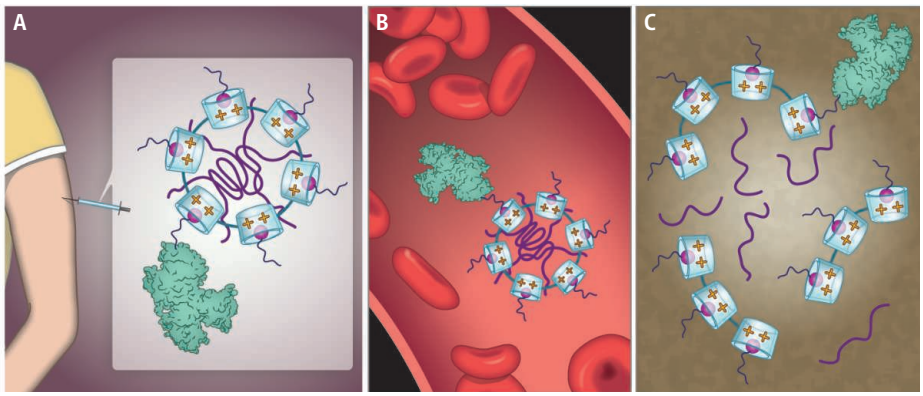

An example of nanomaterials design. A complex structure helps siRNA to be carried to the tumor cell surface, internalized by endocytosis, and then released from the endolysosome into the cytoplasm. (**A**) Chains of positively charged cyclodextrins (light blue) form electrostatic nanoparticles with the negatively charged siRNA (purple). These complexes are administered by injection. (**B**) In the bloodstream, nanoparticle clearance is blocked by PEG chains terminated with hydrophobic moieties that bind as guests in the hydrophobic host center of the cyclodextrin. The nanoparticles are further functionalized with transferrin (green) as a tumor-targeting moiety (many tumor cells overexpress the transferrin receptor), using the PEG as a linker. (**C**) In the tumor cell, the particle dissociates to release the siRNA into the cytoplasm.

Other features of tumors have been used for targeting to amplify a signal at the tumor site. For example, von Maltzahn *et al*. have targeted nanomaterials to molecular features unique to the tumor endothelium to induce coagulation there; the resulting coagulum was then targeted with drugs that bind biochemically to the nascent clot (*9*). Because coagulation is autocatalytic, substantial signal amplification occurs between the initial tumor targeting step and the final binding of the drug to the coagulum. Here, biomolecular recognition was used in the first step to localize the procoagulant nanoparticles to the tumor endothelium through binding of a nanoparticle-conjugated domain of tissue factor receptor, targeting the tissue factor that is naturally up-regulated on the pathological tumor endothelium (*9*).

Annexin 1 is also highly expressed on the tumor endothelium. A short peptide sequence has recently been discovered that serves as a ligand for this marker, providing efficient drug localization to the tumor endothelium (*10*). This ligand can presumably be used to target micelles to tumor vasculature, as has been done with other peptides to target sites of atherosclerotic plaque after intravascular injection (*11*).

Biomacromolecular drugs typically cannot permeate through membranes to access targets in the cytoplasm. An exciting example of nanomaterials to penetrate these barriers is the delivery of small interfering RNA (siRNA) using cationic nanocarriers. As the cell attempts to neutralize the basic charge of the nanomaterials, the resulting osmotic imbalance destabilizes the endolysosomal membranes and releases the drug into the cytoplasm (*12*). Additional features to promote stability and targeting have been designed into this Lego-like nanomaterial (see the figure). Initial evidence for gene knockdown in tumors in patients supports the function of this nanomaterial design (*12*).

Vaccines are another area in which size matters. In the interstitium of most tissues, fluid flows between the blood capillaries and the draining lymphatics. After injection (e.g., intradermally), nanomaterials that are sufficiently small (sub-100 nm) to avoid entrapment in the tissue interstitium are efficiently transported by this interstitial flow into the draining lymphatics and lymph nodes. Here they can be collected by lymph node–resident dendritic cells—the first key cellular player in generating an immune response (*13*).

Particulate antigen from outside the cell is most frequently processed and presented on class II major histocompatibility complex (MHC) molecules, which results in humoral immunity. The resulting antibodies can be useful for preventing disease, for example by binding and neutralizing a virus, but are less useful for killing aberrant cells, such as cells already infected by the virus. To achieve this, the antigen must be presented on MHC class I molecules, leading to the induction of lymphocytes that can kill virally infected cells and even tumor cells.

Antigen presented on MHC class I usually derives from protein within the cell, such as viral proteins. However, under some circumstances, antigen from extracellular sources can be shuttled to MHC class I. This "antigen cross-presentation" is particularly effective when antigen is conjugated to nanopar-

CREDIT: P. HUEY/*SCIENCE*

Published by AAAS

ticles by a reducible disulfide bond (*14*), which is cleaved in the reductive environment within the endosome, resulting in strong cellular immunity that can kill aberrant cells. Such small nanoparticles can also very effectively target antigen-presenting cells after pulmonary administration to induce a potent immune response in the lung and at other mucosal surfaces, to protect from viral infections such as influenza (*15*). Other nanomaterial designs have also been shown to lead to strong cross-presentation, including multilamellar vesicles, stabilized by interlamellar cross-linking, carrying antigen as well as adjuvant molecules (*16*).

The level of sophistication of designing nanocarriers to be functionally responsive has recently been taken to new levels with compelling demonstrations in vitro. Douglas *et al*. have used DNA origami—intricately folded nanoscale DNA structures—to develop hollow nanocontainers with DNA aptamer–based locks (*17*). These aptamers also bind to particular biomolecular signals; when the aptamer detects the binding antigen key, the nanocontainer is opened and the payload is released.

These examples show how highly functional multicomponent polymeric nanostructures can guide drugs to tissues, coax them through the biological barriers at the surfaces of and within cells, and escape drug clearance and drug resistance. However, in translation to human clinical trials, the devil is often in the details: Materials must be developed that maintain their stability, size distribution, and targeting specificity in the complex and concentrated protein environment of the body, that can be eliminated from the body at the same rate as planned administration to avoid accumulation, and that can be processed by the body without formation of untoward metabolites.

References

1. J. W. Baish *et al*., *Proc. Natl. Acad. Sci. U.S.A.* **108**, 1799 (2011).
2. W. Gao, W. Liu, T. Christensen, M. R. Zalutsky, A. Chilkoti, *Proc. Natl. Acad. Sci. U.S.A.* **107**, 16432 (2010).
3. V. Schellenberger *et al*., *Nat. Biotechnol.* **27**, 1186 (2009).
4. J. A. MacKay *et al*., *Nat. Mater.* **8**, 993 (2009).
5. M. Murakami *et al*., *Sci. Transl. Med.* **3**, 64ra2 (2011).
6. R. A. Petros, J. M. DeSimone, *Nat. Rev. Drug Discov.* **9**, 615 (2010).
7. J. W. Yoo *et al*., *Nat. Rev. Drug Discov.* **10**, 521 (2011).
8. D. A. Christian *et al*., *Mol. Pharm.* **6**, 1343 (2009).
9. G. von Maltzahn *et al*., *Nat. Mater.* **10**, 545 (2011).
10. S. Hatakeyama *et al*., *Proc. Natl. Acad. Sci. U.S.A.* **108**, 19587 (2011).
11. D. Peters *et al*., *Proc. Natl. Acad. Sci. U.S.A.* **106**, 9815 (2009).
12. M. E. Davis *et al*., *Nature* **464**, 1067 (2010).
13. S. T. Reddy *et al*., *Nat. Biotechnol.* **25**, 1159 (2007).
14. S. Hirosue *et al*., *Vaccine* **28**, 7897 (2010).
15. C. Nembrini *et al*., *Proc. Natl. Acad. Sci. U.S.A.* **108**, E989 (2011).
16. J. J. Moon *et al*., *Nat. Mater.* **10**, 243 (2011).
17. S. M. Douglas *et al*., *Science* **335**, 831 (2012).

10.1126/science.1219657

GEOCHEMISTRY

The Marine Sulfur Cycle, Revisited

Model studies point to a larger role of the sulfur cycle in maintaining atmospheric oxygen levels than previously recognized.

Matthew T. Hurtgen

Sulfur takes part in many biogeochemical reactions that affect the global carbon and oxygen cycles. On short time scales and in the absence of oxygen, many microbes use organic carbon to reduce sulfate to sulfide, which may then react with iron to form pyrite. On much longer time scales, the net addition of oxygen to the atmosphere through organic carbon burial promotes sulfide oxidation on land and increases the amount of sulfate carried by rivers to the oceans. Two reports in this issue, by Wortmann and Paytan (*1*) on page 334 and Halevy *et al*. (*2*) on page 331, show that on time scales of millions of years, changes in the formation and dissolution of evaporite minerals can strongly impact marine chemistry and the carbon cycle (see the figure). On longer time scales, the sulfur cycle played a much greater role in regulating atmospheric oxygen levels than previously recognized.

Earth scientists have long appreciated that marine sulfate concentrations have changed substantially through time as a result of varying sulfur fluxes to and from the ocean. The story has generally been framed in terms of changing inputs. The sulfate content of the ocean should track the oxidation history of the Earth's surface. As oxygen levels increase, so, too, should sulfide oxidation on land and the resulting flux of sulfate via rivers to the ocean. Because oxygen levels at the Earth's surface are thought to have been relatively stable since ~580 million years ago, marine sulfate concentrations would be expected to have been largely unchanged through the Phanerozoic (since ~542 million years ago).

However, over the past decade, scientists have found that Phanerozoic sulfate concentrations varied considerably (*3*). Sulfate concentrations in the modern ocean are 28 mM, but the composition of fluid inclusions in halite suggests that Phanerozoic levels may have fluctuated between ~5 and 25 mM. The time resolution of these data is quite low, but this work suggests that the flux of sulfur into

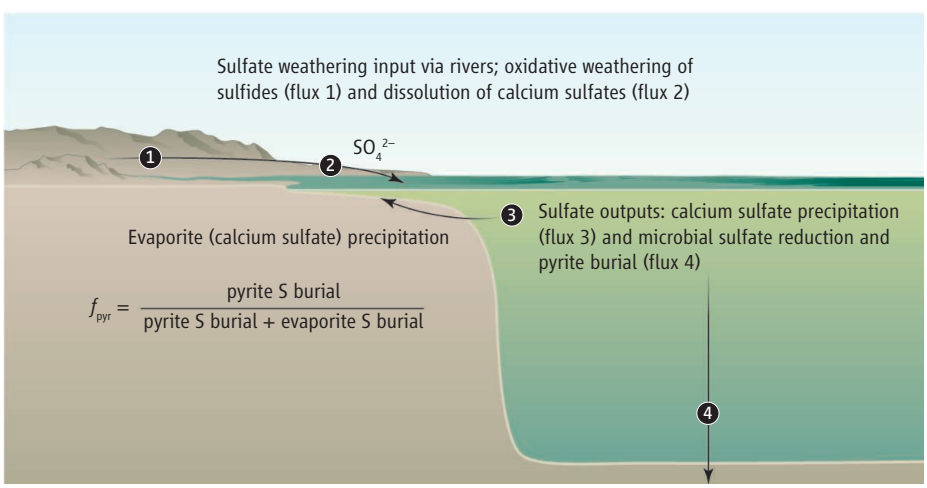

Reassessing marine sulfur fluxes. The main sulfur inputs to the ocean are the dissolution of evaporite minerals and oxidative weathering of pyrite; the main sulfur outputs are the formation and burial of evaporites and pyrite. During the Phanerozoic, pyrite deposition and weathering have dominated these fluxes (*2*). However, episodic, massive changes in evaporite formation (*1*, *2*) and dissolution (*1*) strongly impact the marine sulfur cycle on million-year time scales.

CREDIT: P. HUEY/SCIENCE

Earth and Planetary Sciences, Northwestern University, Evanston, IL 60208, USA. E-mail: matt@earth.northwestern.edu

Published by AAAS

and out of the ocean has fluctuated much more than previously recognized.

To better constrain sulfur fluxes to and from the ocean, Wortmann and Paytan use a model that tracks the mass and sulfur isotope composition of fluxes into and out of the ocean. Most sulfur in the ocean is brought there by rivers as a result of oxidative weathering of sulfides and dissolution of calcium sulfates. Sulfur is removed from the ocean through microbial sulfate reduction followed by pyrite burial, and by calcium sulfate (evaporite) deposition. Evaporite deposition does not have a large effect on the sulfur isotopic composition, but microbial sulfate reduction does, because microbes prefer to use ^{32}S over ^{34}S during the production of sulfide (*4*). As a result, the sulfur isotope composition ($\delta^{34}S_{sulfate}$) of river inputs today is ~6 per mil (‰) (*5*), but that of seawater sulfate is ~20‰.

Variations in $\delta^{34}S_{sulfate}$ are traditionally interpreted to reflect changes in the total amount of sulfur buried in ocean sediments as pyrite—a parameter referred to as f_{pyr}.

Wortmann and Paytan conclude that a 5‰ negative $\delta^{34}S_{sulfate}$ shift in ~120-million-year-old rocks was caused by massive seawater sulfate removal that accompanied large-scale evaporite deposition during the opening of the South Atlantic Ocean. Evaporite formation does not cause sulfur isotope fractionation; in the model, the negative $\delta^{34}S_{sulfate}$ shift is driven by lower pyrite burial rates resulting from substantially reduced marine sulfate levels. The authors attribute a 5‰ positive $\delta^{34}S_{sulfate}$ shift about 50 million years ago to an abrupt increase in marine sulfate concentrations as a result of large-scale dissolution of freshly exposed evaporites; they argue that the higher sulfate concentrations led to more pyrite burial.

Halevy *et al*. likewise study past sulfur fluxes to and from the ocean, but over longer time scales (the past 500 million years). They quantify sulfate evaporite burial rates through time with the help of a database that contains surface and subsurface information on sedimentary strata from locations across North America and the Caribbean. They then scale these rates to obtain a global estimate.

The results indicate that sulfate burial rates were higher than previously estimated, but also greatly variable. When Halevy *et al*. integrated these improved evaporite burial fluxes with seawater sulfate concentration estimates (*3*) and sulfur isotope constraints (*6, 7*), their calculations implied that Phanerozoic f_{pyr} values were ~100% higher on average than previously recognized. These surprisingly high and constant pyrite burial outputs must have been balanced by equally high and constant inputs of sulfate to the ocean via sulfide oxidation (weathering).

The relatively high and constant rates of pyrite weathering and burial over long geologic time scales, identified by Halevy *et al*., suggest that the consumption and production of oxygen via these processes played a larger role in regulating Phanerozoic atmospheric oxygen levels than previously recognized—perhaps by as much as 50%. However, both studies recognize the importance of episodic evaporite burial on the sulfur cycle, and Wortmann and Paytan show that large-scale deposition and dissolution of these evaporites over relatively short geologic time scales can have an enormous impact on marine sulfate concentrations, pyrite burial rates, and the carbon cycle.

The studies by Wortmann and Paytan and Halevy *et al*. highlight the dynamic nature of the Phanerozoic sulfur cycle and its importance in regulating the chemistry of the ocean-atmosphere system. Future work should focus on better constraining marine sulfate levels and global sulfate burial rates through time, the relationship between marine sulfate concentrations and pyrite burial rates, and the role of sulfur in regulating ocean nutrient cycling, the carbon cycle, and ultimately climate.

References

1. U. G. Wortmann, A. Paytan, *Science* **337**, 334 (2012).
2. I. Halevy *et al*., *Science* **337**, 331 (2012).
3. T. K. Lowenstein *et al*., *Geology* **31**, 857 (2003).
4. D. E. Canfield, *Geochim. Cosmochim. Acta* **65**, 1117 (2001).
5. M. A. Arthur, *Encyclopedia of Volcanoes* (Academic Press, San Diego, CA, 2000).
6. A. Paytan *et al*., *Science* **304**, 1663 (2004).
7. A. Kampschulte, H. Strauss, *Chem. Geol.* **204**, 255 (2004).

10.1126/science.1225461

ECOLOGY

The Art of Ecological Modeling

Ecological models have limited predictive power, but can provide insights into what makes an ecosystem vulnerable to disturbance.

Ian L. Boyd

Scientists appear to have a very limited capacity to predict the behavior of nonlinear dynamic systems, including ecological systems (*1*). As understanding of these systems improves, uncertainty around system behavior tends to increase rather than decline (*2*). The reason for this paradoxical observation is that the uncertainty in the models used for prediction has been underestimated. Many of today's ecological models have excessively optimistic ambitions to predict ecosystem and population dynamics. Some recent studies (*3*–*5*)—including that by Mougi and Kondoh (*6*) on page 349 of this issue—help to specify where the limits of prediction may lie.

Mougi and Kondoh used network models to show that the specific mixture of agonistic and mutualistic interactions between species is likely to contribute to stabilizing populations in ecological networks. Real ecosystems contain a rich mixture of these types of interactions, meaning that community network structure may affect the dynamics of individual populations. Moreover, stability and controllability of networks also depend on how tightly the key nodes in these networks are coupled (*4*, *5*). These results suggest that some species within ecosystems are especially important to ecological stability, which is consistent with the empirical evidence of the relative importance of different species (*7*).

Forty years ago, May's (*8*) suggestion that complexity does not necessarily beget stability in ecological networks began a debate about a possible trade-off between complexity and stability in ecosystems. The recent results (*3*–*6*) indicate that complexity does beget stability—but only in the presence of certain species and types of interaction between them.

If only a small subset of all possible ecological networks with certain species abundances and types of interactions is stable, this result may explain the characteristic frequency distribution of species abundance observed in ecological communities (*9*). It may also help to predict the consequences for

Scottish Oceans Institute, University of St Andrews, St Andrews KY16 8LB, UK. E-mail: ilb@st-andrews.ac.uk

ecosystem stability of weakening key nodes in these networks through biodiversity loss as a result of selective exploitation or destruction of species (*10*), or because of the effects of climate change on the relative strength of interactions between species (*11*).

However, if we are to have any hope of managing ecological systems, we require a mechanism to identify which disturbances are likely to lead to instability. Using cultured yeast populations, Dai *et al*. (*3*) recently reported the presence of telltale signs of tipping points, or bifurcations in the language of chaos theory, when the system state can change rapidly and unpredictably. Predicting bifurcations in chaotic systems has many of the characteristics of playing roulette, and some have rightly cautioned against optimism about their predictability (*12*). However, it appears that perturbed populations take longer to return to their original state in advance of a bifurcation. This supports the observation of changing dynamics within food webs up to a year in advance of an experimentally induced regime shift in a real ecosystem (*13*). In practice, this effect can be detected statistically (*14*, *15*), suggesting the possibility of establishing indicators of future system status.

These results need to be translated into operational uses. Standard models used to manage biological resources rarely have the capacity to model the dynamics typically associated with bifurcations. The main models are general population models (*16*) and data-driven, heuristic, ecosystem models (*17*, *18*), which are rarely validated and often overparameterized. They are grounded in the concept of linear (predictable) rather than nonlinear (unpredictable) systems and thus fail to capture the underlying complexity of ecological processes.

These model limitations must be kept in mind when reporting results, especially for use in decision-making. It may be tempting to ignore model uncertainty in the name of pragmatism, but this will not lead to better decisions. Indeed, this type of systemic misapplication of ecological models may underlie some cases of natural resource depletion. For example, fisheries models typically assume linear dynamics and rarely consider the implications of wider community interactions for the validity of their predictions (*10*, *19*).

CREDIT: RICH CAREY/SHUTTERSTOCK

Ecosystem dynamics. Models show that the mixture of agonistic and mutualistic interactions in ecological networks is important for the stability of communities. These complex interactions are typically not captured by models used to manage ecological resources.

Predicting the dynamics of real ecosystems—or even of components of these ecosystems—will remain beyond the reach of even the best ecosystem models for the foreseeable future (see the figure). However, the emerging body of evidence (*3*–*6*), suggests that ecological network models can be used to describe ecosystem characteristics and general behavior, including providing indicators of when ecosystems are being stressed. Successful management of ecological processes will come down to being able to identify and measure the dynamics of influential network components, probably in the form of key species (*7*). These species need not be the most common or those that are exploited (*7*, *20*).

In future, the rational management of exploited species will probably depend increasingly on the status of these key species in ecological networks. The legal designation of protected species, together with an obligation on authorities to monitor their status, presents an opportunity to establish ecologically meaningful system indicators that are also relevant to public policy.

References

1. S. A. Levin, *Ecosystems* **1**, 431 (1998).
2. M. Maslin, P. Austin, *Nature* **486**, 183 (2012).
3. L. Dai *et al*., *Science* **336**, 1175 (2012).
4. S. Allesina, S. Tang, *Nature* **483**, 205 (2012).
5. Y. Y. Liu *et al*., *Nature* **473**, 167 (2011).
6. A. Mougi, M. Kondoh, *Science* **337**, 349 (2012).
7. D. U. Hooper *et al*., *Ecol. Monogr.* **75**, 3 (2005).
8. R. M. May, *Nature* **238**, 413 (1972).
9. F. W. Preston, *Ecology* **43**, 185 (1962).
10. A. O. Shelton, M. Mangel, *Proc. Natl. Acad. Sci. U.S.A.* **108**, 7075 (2011).
11. P. L. Zarnetske *et al*., *Science* **336**, 1516 (2012).
12. A. Hastings, D. B. Wysham, *Ecol. Lett.* **13**, 464 (2010).
13. S. R. Carpenter *et al*., *Science* **332**, 1079 (2011).
14. A. J. Veraart *et al*., *Nature* **481**, 357 (2012).
15. M. Scheffer *et al*., *Nature* **461**, 53 (2009).
16. R. Hilborn, *Nat. Resour. Model.* **25**, 122 (2012).
17. V. Christensen *et al*., *Ecol. Modell.* **220**, 1984 (2009).
18. A. D. M. Smith *et al*., *Science* **333**, 1147 (2011).
19. G. Sugihara *et al*., *Proc. Natl. Acad. Sci. U.S.A.* **108**, E1224 (2011).
20. P. M. Cury *et al*., *Science* **334**, 1703 (2011).

10.1126/science.1225049

APPLIED PHYSICS

Spin Twists in a Transistor

Igor Žutić and Jeongsu Lee

By using electron spin in a transistor, researchers have developed a new approach for transferring and processing information.

Transistors are the centerpiece of conventional electronics, with two key features of switching and amplification. However, transistors relying on electron charge are oblivious to another property of electrons: their spin. In a simple picture, these spins are compass needles, aligned by a magnetic field. With different orientations, "up" and "down," spin lends itself to encoding binary information as ones and zeroes, as explored in the field of spintronics (*1*, *2*). Whereas harnessing spin for robust information storage in computer hard drives and magnetic random access memories has been very successful, delivering a spin transistor has been challenging (*1*). On page 324 of this issue, Betthausen *et al*. (*3*) describe a newly discovered spin-transistor action. Considering that the pioneering work on another spin transistor (*4*) waited two decades for experimental realization (*5*), it is a remarkable feat that the work of Betthausen *et al*. presents the experiment and theory for their spin transistor.

Department of Physics, University at Buffalo, The State University at New York, Buffalo, NY 14260, USA. E-mail: zigor@buffalo.edu; jl376@buffalo.edu

Published by AAAS

ecosystem stability of weakening key nodes in these networks through biodiversity loss as a result of selective exploitation or destruction of species (*10*), or because of the effects of climate change on the relative strength of interactions between species (*11*).

However, if we are to have any hope of managing ecological systems, we require a mechanism to identify which disturbances are likely to lead to instability. Using cultured yeast populations, Dai *et al*. (*3*) recently reported the presence of telltale signs of tipping points, or bifurcations in the language of chaos theory, when the system state can change rapidly and unpredictably. Predicting bifurcations in chaotic systems has many of the characteristics of playing roulette, and some have rightly cautioned against optimism about their predictability (*12*). However, it appears that perturbed populations take longer to return to their original state in advance of a bifurcation. This supports the observation of changing dynamics within food webs up to a year in advance of an experimentally induced regime shift in a real ecosystem (*13*). In practice, this effect can be detected statistically (*14*, *15*), suggesting the possibility of establishing indicators of future system status.

These results need to be translated into operational uses. Standard models used to manage biological resources rarely have the capacity to model the dynamics typically associated with bifurcations. The main models are general population models (*16*) and data-driven, heuristic, ecosystem models (*17*, *18*), which are rarely validated and often overparameterized. They are grounded in the concept of linear (predictable) rather than nonlinear (unpredictable) systems and thus fail to capture the underlying complexity of ecological processes.

These model limitations must be kept in mind when reporting results, especially for use in decision-making. It may be tempting to ignore model uncertainty in the name of pragmatism, but this will not lead to better decisions. Indeed, this type of systemic misapplication of ecological models may underlie some cases of natural resource depletion. For example, fisheries models typically assume linear dynamics and rarely consider the implications of wider community interactions for the validity of their predictions (*10*, *19*).

CREDIT: RICH CAREY/SHUTTERSTOCK

Ecosystem dynamics. Models show that the mixture of agonistic and mutualistic interactions in ecological networks is important for the stability of communities. These complex interactions are typically not captured by models used to manage ecological resources.

Predicting the dynamics of real ecosystems—or even of components of these ecosystems—will remain beyond the reach of even the best ecosystem models for the foreseeable future (see the figure). However, the emerging body of evidence (*3*–*6*), suggests that ecological network models can be used to describe ecosystem characteristics and general behavior, including providing indicators of when ecosystems are being stressed. Successful management of ecological processes will come down to being able to identify and measure the dynamics of influential network components, probably in the form of key species (*7*). These species need not be the most common or those that are exploited (*7*, *20*).

In future, the rational management of exploited species will probably depend increasingly on the status of these key species in ecological networks. The legal designation of protected species, together with an obligation on authorities to monitor their status, presents an opportunity to establish ecologically meaningful system indicators that are also relevant to public policy.

References

1. S. A. Levin, *Ecosystems* **1**, 431 (1998).
2. M. Maslin, P. Austin, *Nature* **486**, 183 (2012).
3. L. Dai *et al*., *Science* **336**, 1175 (2012).
4. S. Allesina, S. Tang, *Nature* **483**, 205 (2012).
5. Y. Y. Liu *et al*., *Nature* **473**, 167 (2011).
6. A. Mougi, M. Kondoh, *Science* **337**, 349 (2012).
7. D. U. Hooper *et al*., *Ecol. Monogr.* **75**, 3 (2005).
8. R. M. May, *Nature* **238**, 413 (1972).
9. F. W. Preston, *Ecology* **43**, 185 (1962).
10. A. O. Shelton, M. Mangel, *Proc. Natl. Acad. Sci. U.S.A.* **108**, 7075 (2011).
11. P. L. Zarnetske *et al*., *Science* **336**, 1516 (2012).
12. A. Hastings, D. B. Wysham, *Ecol. Lett.* **13**, 464 (2010).
13. S. R. Carpenter *et al*., *Science* **332**, 1079 (2011).
14. A. J. Veraart *et al*., *Nature* **481**, 357 (2012).
15. M. Scheffer *et al*., *Nature* **461**, 53 (2009).
16. R. Hilborn, *Nat. Resour. Model.* **25**, 122 (2012).
17. V. Christensen *et al*., *Ecol. Modell.* **220**, 1984 (2009).
18. A. D. M. Smith *et al*., *Science* **333**, 1147 (2011).
19. G. Sugihara *et al*., *Proc. Natl. Acad. Sci. U.S.A.* **108**, E1224 (2011).
20. P. M. Cury *et al*., *Science* **334**, 1703 (2011).

10.1126/science.1225049

APPLIED PHYSICS

Spin Twists in a Transistor

Igor Žutić and Jeongsu Lee

By using electron spin in a transistor, researchers have developed a new approach for transferring and processing information.

Transistors are the centerpiece of conventional electronics, with two key features of switching and amplification. However, transistors relying on electron charge are oblivious to another property of electrons: their spin. In a simple picture, these spins are compass needles, aligned by a magnetic field. With different orientations, "up" and "down," spin lends itself to encoding binary information as ones and zeroes, as explored in the field of spintronics (*1*, *2*). Whereas harnessing spin for robust information storage in computer hard drives and magnetic random access memories has been very successful, delivering a spin transistor has been challenging (*1*). On page 324 of this issue, Betthausen *et al*. (*3*) describe a newly discovered spin-transistor action. Considering that the pioneering work on another spin transistor (*4*) waited two decades for experimental realization (*5*), it is a remarkable feat that the work of Betthausen *et al*. presents the experiment and theory for their spin transistor.

Department of Physics, University at Buffalo, The State University at New York, Buffalo, NY 14260, USA. E-mail: zigor@buffalo.edu; jl376@buffalo.edu

Published by AAAS

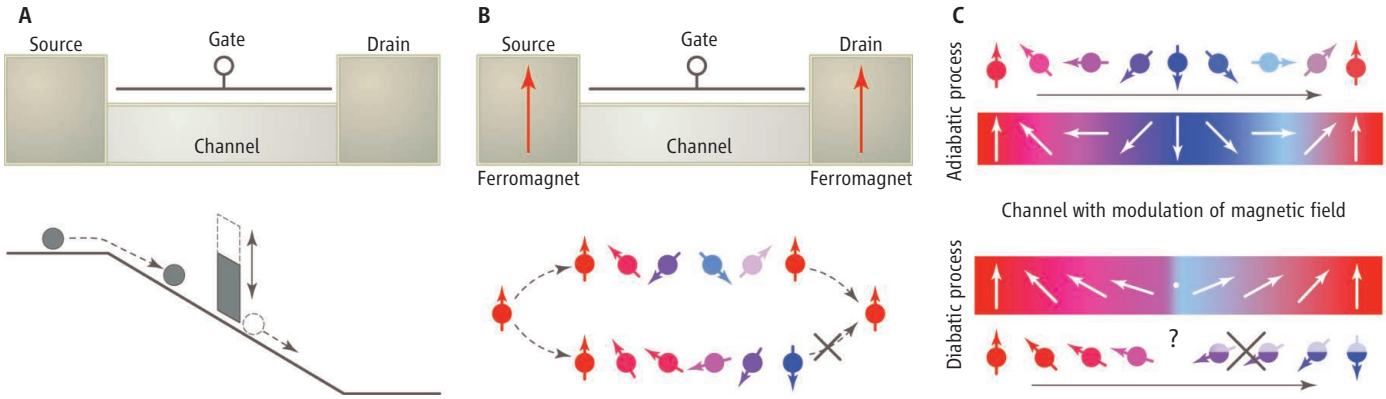

Transistor switching. (**A**) In conventional transistors, the electron flow from source to drain is controlled by the gate voltage, V_G. (**B**) In a spin transistor, V_G alters the spin-orbit coupling, which rotates the electron spin direction in the channel. A ferromagnetic source initializes the spin alignment, and a ferromagnetic drain determines whether the flow is permitted (restricted), depending on the spin alignment (misalignment) between the electron exiting the channel and the drain. (**C**) In adiabatic spin transistors, the "on" state is realized by the gradual (adiabatic) change of the magnetic field (white arrows). The spins have time to respond to the direction dictated by the field, and electrons flow smoothly across the channel. For the "off" state, there is an abrupt (diabatic) change of the magnetic field. Electrons unable to align their spin along the field are scattered back and their flow is impeded.

Conventional transistors (*6*) are three-terminal devices relying on classical charge transfer (see the figure, panel A). Describing spin transistors (panels B and C), however, is more elusive because it requires quirky probabilistic laws of quantum mechanics. Similar to tossing a coin, we cannot say whether the tails or heads will be next, but we can only calculate the likelihood for either outcome to happen. In a spin transistor, the relevant outcomes are different spin orientations. By using spin twists, Betthausen *et al*. have implemented transistor switching action between the low- and high-resistance states ("on" and "off," respectively). For the compass-needle analogy, we can have two extreme cases for spin twists: For a magnet slowly rotating above a compass, the needle will follow the magnet, as expected for an adiabatic transition. However, if we rotate the magnet too quickly, the compass needle will not have time to react and its orientation will stay put, a sign that the transition is diabatic.

Betthausen *et al*. have shown how adiabatic processes effectively shelter spin information, propagating undisturbed and without scattering at distances 10 to 100 times greater than the characteristic distance for charge scattering. Although such a distance of spin-information transfer is still small, it dwarfs what is currently available in other type of spin transistors (*5*, *7*, *8*) and even the characteristic dimensions of ever-shrinking conventional transistors. These results were made possible by tailoring materials properties and adding magnetic (Mn) impurities in a two-dimensional channel material (Cd,Mn)Te (*9*). This choice enables both a large spin splitting (energy difference between spin-up and spin-down orientation), and a high electron mobility, while the strong magnetic field keeps their spins in check. Careful design of the magnetic field profile combines a helical pattern along the channel (see the figure, panel C), which results in a twisting of the spins, and a constant, but tunable, external field that selects the transition mechanism.

The new spin transistor gives the field of spintronics a major boost, opening unexplored directions of not just storing but also transferring and processing spin-based information (*10*–*12*). At present, however, the spin transistor is unlikely to compete with its conventional counterpart. The adiabatic spin transistor is only realized at temperatures below 1 K, and the reliance on an external magnetic field is not very practical. Furthermore, the amplification in the transistor action has yet to be demonstrated. However, none of these current limitations are fundamental obstacles.

A higher operation temperature could be realized by adding more Mn impurities to increase the spin splitting. Alternatively, one could consider other two-dimensional magnetic channels—for example, magnetic semiconductors (*13*) or oxides (*14*)—showing a permanent magnetism with a large spin splitting. Some caution is needed because additional magnetic impurities typically reduce the mobility and thus shorten the range of spin-information transfer. If an important functionality can be identified for the spin transistor, the low temperature alone would not be the deal breaker. With either voltage-tunable permanent magnets (*1*, *15*, *16*) or spin-orbit coupling (*1*, *2*, *5*) the need for an external magnetic field could be removed because the spin splitting would be electrically controlled. This possibility would allow revisiting amplification, as it is known in conventional transistors (*6*), where the change in the gate voltage controls the source-drain current (see the figure, panel A). Demonstrating the amplification in adiabatic spin transistors could also come with additional benefits of a versatile spin control and a robust performance with respect to slight variations, inevitable in fabrication of different devices.

At the heart of spintronics lies the quest to elucidate physical phenomena and possible applications emerging from microscopic spins. Although spin twists are limited to small distances, they may offer a giant leap for effectively taming the spin transistor.

References

1. I. Žutić, J. Fabian, S. Das Sarma, *Rev. Mod. Phys.* **76**, 323 (2004).
2. J. Fabian *et al*., *Acta Phys. Slov.* **57**, 565 (2007).
3. C. Betthausen *et al*., *Science* **337**, 324 (2012).
4. S. Datta, B. Das, *Appl. Phys. Lett.* **56**, 665 (1990).
5. H. C. Koo *et al*., *Science* **325**, 1515 (2009).
6. P. Horowitz, W. Hill, *The Art of Electronics* (Cambridge, New York, 1989).
7. J. Wunderlich *et al*., *Science* **330**, 1801 (2010).
8. N. Rangaraju, J. A. Peters, B. W. Wessels, *Phys. Rev. Lett.* **105**, 117202 (2010).
9. J. K. Furdyna, *J. Appl. Phys.* **64**, R29 (1988).
10. S. Sugahara, *IEE Proc., Circ. Devices Syst.* **152**, 355 (2005).
11. H. Dery, Y. Song, P. Li, I. Žutić, *Appl. Phys. Lett.* **99**, 082502 (2011).
12. H. Dery *et al*., *IEEE Trans. Electron. Dev.* **59**, 259 (2012).
13. T. Jungwirth, J. Sinova, J. Mašek, J. Kučera, A. H. MacDonald, *Rev. Mod. Phys.* **78**, 809 (2006).
14. L. Li, C. Richter, J. Mannhart, R. C. Ashoori, *Nat. Phys.* **7**, 762 (2011).
15. H. Ohno *et al*., *Nature* **408**, 944 (2000).
16. Y. Yamada *et al*., *Science* **332**, 1065 (2011).

10.1126/science.1225219

Published by AAAS

RETROSPECTIVE

Aaron Shatkin (1934–2012)

A virologist discovered the eukaryotic mRNA 5′-terminal cap structure and revealed its role in gene expression.

Nahum Sonenberg[1] and Witold Filipowicz[2]

Aaron Shatkin died of cancer at his home in Scotch Plains, New Jersey, on 4 June, at the age of 77. When asked last year by the Bowdoin College (where he majored in chemistry) magazine, what was the most rewarding part of his job, he responded: "Seeing students and others I've mentored at CABM (Center for Advanced Biotechnology and Medicine at Rutgers University and the University of Medicine and Dentistry of New Jersey) and elsewhere become independent, accomplished researchers and leaders in their fields in many different countries." His graciousness and passion for science were among his finest attributes. Both of us, like all his trainees, owe our progress in science largely to his extraordinary mentorship.

Aaron did his graduate studies with Edward Tatum, Nobel laureate, at the Rockefeller University, investigating the morphology of the filamentous fungus *Neurospora crassa*. However, the work coauthored with Edward Reich and Richard Franklin, demonstrating that the antibiotic actinomycin D blocks cellular messenger RNA (mRNA) synthesis, had the most impact on his future career and started his lifelong adventure with animal viruses. The availability of actinomycin D allowed Aaron and others to investigate virus gene expression in the absence of host mRNA synthesis, which greatly facilitated the study of virus-encoded proteins. Following the move to the laboratory of Norman Salzman at the National Institutes of Health in 1963, Aaron studied several human viruses including vaccinia virus and poliovirus, providing early insights into viral RNA and protein synthesis. From the mid-1960s, he focused almost entirely on the life cycle of reovirus, studied also independently by Wolfgang Joklik and Bernard Fields. After moving to the Roche Institute of Molecular Biology in Nutley, New Jersey, in 1968, Aaron showed that the segmented genome of the reovirus consists of 10 separate double-stranded RNA "chromosomes," which are copied by a viral RNA polymerase, and that the resulting transcripts function both as mRNAs and templates for synthesis of progeny segments. The work with reovirus led Aaron and his associate Yasuhiro Furuichi to discover the 5′-terminal m^7GpppN cap structure in 1975.

The discovery that viral mRNAs have their termini modified with m^7GpppN caps (made together with Bernard Moss working on vaccinia virus) had far-reaching consequences. Caps are present on all nuclear-transcribed cellular mRNAs and mRNAs of many viruses, and are involved in almost every aspect of mRNA metabolism. In 1975, Aaron and James Darnell showed that long heterogeneous nuclear RNAs too harbor m^7GpppN caps in addition to being polyadenylated at the 3′ end. How both these terminal structures could be preserved in much shorter mature mRNAs became evident only upon the discovery of mRNA splicing.

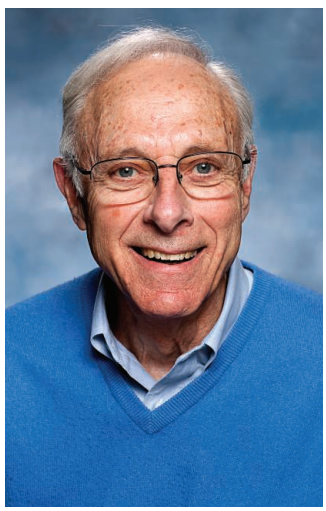

Aaron's laboratory further led the field in conducting a comprehensive analysis of the mechanism by which the m^7GpppN cap facilitates translation initiation. This entailed the discovery of new translation factors and promulgation of the scanning mechanism by which the mammalian 40*S* ribosome selects the AUG initiation codon. His laboratory also documented the importance of the cap for mRNA stability. More recently, Aaron pursued his favorite topic of the capping mechanism and enzymes involved. His last paper in 2011 described the x-ray structure of the carboxyl-terminal capping domain of the human capping enzyme. Although focused on mRNA capping, Aaron was always open to other ideas. His laboratory discovered the pathway leading to RNA ligation and transfer RNA (tRNA) splicing in animal cells in the early 1980s.

Aaron was loved by his peers, students, and collaborators. He was a person of exceptional integrity, and his warm character and radiating optimism (and smile) were infectious. He was an excellent mentor, always fostering openness, collaboration, and friendly dispute. Most of his former students and collaborators remained in close contact with Aaron, very often seeking his support and advice. Over 40 of us, from all over the world, gathered in September 2011 for the "Shatkin Reunion"—sadly the last one—to show our appreciation for his mentorship and friendship. The day of the reunion was full of recollections, short stories, and news from the lives of our families, which Aaron followed very closely. What moved us most strongly on that day was Aaron's engaging presentation, delivered already in frail health, describing his current research and reminiscing about the happy days with his students and colleagues.

Aaron was a recipient of many awards and honors, including the Steel award from the U.S. National Academy of Sciences (1977) and the Association of American Medical Colleges Award (2003). He was elected to the U.S. National Academy of Sciences in 1981 and the American Academy of Arts and Sciences in 1997. In addition to his illustrious career as a researcher, Aaron greatly contributed to other aspects of science. He was a founding editor-in-chief of the journal *Molecular and Cellular Biology*. In 1986, he became the founding director of CABM in Piscataway, New Jersey. Under Aaron's leadership, CABM has grown into a world-class research institution. In recognition of Aaron's extraordinary leadership, an endowed annual lectureship was established in his name at CABM, with Harold Varmus, director of the National Cancer Institute, giving the inaugural lecture in April 2012. Aaron arrived a few minutes late for the lecture, straight from Boston where he was undergoing experimental therapy. He passed away a month later. He worked until a few weeks before he died, a testament to his devotion to science and his work. Aaron is survived by his son Greg. Joan, his beloved wife for 51 years, passed away in 2009. Till his last days, Aaron stopped daily for a moment of silence in front of her grave.

10.1126/science.1226820

PHOTO CREDIT: UNIVERSITY OF MEDICINE AND DENTISTRY OF NEW JERSEY

[1]Department of Biochemistry, McGill University, Goodman Cancer Research Center, Montreal, Quebec H3A 1A3, Canada. [2]Friedrich Miescher Institute for Biomedical Research, Maulbeerstrasse 66, 4058 Basel, Switzerland. E-mail: nahum.sonenberg@mcgill.ca; witold.filipowicz@fmi.ch

The Exploration of Hot Nuclear Matter

Barbara V. Jacak[1] and Berndt Müller[2]*

When nuclear matter is heated beyond 2 trillion degrees, it becomes a strongly coupled plasma of quarks and gluons. Experiments using highly energetic collisions between heavy nuclei have revealed that this new state of matter is a nearly ideal, highly opaque liquid. A description based on string theory and black holes in five dimensions has made the quark-gluon plasma an archetypical strongly coupled quantum system. Open questions about the structure and theory of the quark-gluon plasma are under active investigation. Many of the insights are also relevant to ultracold fermionic atoms and strongly correlated condensed matter.

Nuclear matter in today's universe hides inside atomic nuclei and neutron stars. The nucleons (neutrons and protons) are the building blocks of such matter and consist, in turn, of quarks. Quarks are bound together by the strong interaction, which is mediated by the exchange of gluons. Unlike the uncharged photons, which mediate electromagnetic interactions but do not interact with one another, gluons have color, which is the strong interaction's analog of charge. Colored gluons interact among themselves, as well as with the quarks, making the theory of the strong interaction, known as quantum chromodynamics (QCD), rich in structure and at the same time extremely difficult to solve.

Remarkably, the strong interaction weakens at short distances—a property known as "asymptotic freedom" (*1*, *2*). Conversely, it is exceedingly strong at distances similar to the size of a nucleon (10^{-15} m), confining quarks inside nucleons and other quark-containing particles, known as hadrons. Asymptotic freedom suggests that nucleons can be "boiled" into a plasma of their constituent quarks and gluons when the strong interaction among them is weakened by increasing the density or temperature of the matter. Today, quarks are confined in nuclei and neutron stars, which are cold objects, but the early universe was extremely hot (*3*). Its temperature exceeded 150 MeV (about 2×10^{12} K) until about 10 μs after the Big Bang, and QCD predicts that such conditions are sufficient for the quark-gluon plasma (QGP), to exist (Fig. 1).

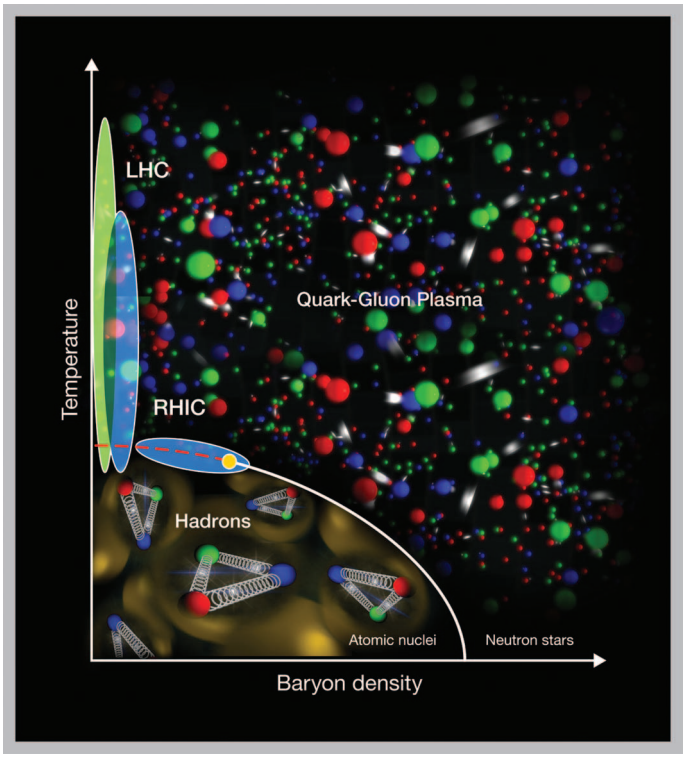

Fig. 1. Phase diagram of QCD matter in the temperature–baryon density plane. Baryons are hadrons containing three valence quarks; the most common are protons and neutrons, shown at the lower left. Colored spheres indicate individual quarks, which are not bound together in the quark-gluon plasma. RHIC (blue ovals) and LHC (green oval) explore matter with almost equal numbers of quarks and antiquarks. At lower beam energies, RHIC produces matter with a surplus of quarks, corresponding to high net baryon density. There may be a critical point (yellow circle) in the phase diagram, at the end of a line indicating a first-order phase transition. [Credit: Brookhaven National Laboratory]

Understanding the evolution of our universe thus requires knowledge of the structure and dynamics of the QGP. Although numerical ab initio simulations of the thermodynamic properties of hot QCD matter in equilibrium have made much progress over the past 30 years (*4*), the dynamical properties of the QGP remain out of reach. Experimental study of hot QCD matter can fill this gap by colliding heavy nuclei at high energies and generating the enormous temperatures required to produce QGP in the laboratory, if only for a brief moment.

Discoveries of the Past Decade

The Relativistic Heavy Ion Collider (RHIC) at Brookhaven National Laboratory has explored the QGP since 2000. RHIC collides two beams of heavy ions, each with an energy up to 100 GeV per nucleon. Proton-proton (p+p) and deuteron-gold (d+Au) collisions provide control measurements without QGP formation. At top energy, the initial temperature reached in collisions between two gold nuclei is inferred to lie between 300 and 600 MeV (*5*), well above the QCD phase-transition temperature of ~150 MeV (*6*). RHIC is a flexible, dedicated facility colliding a wide range of nuclei at various energies. This allows exploration of the phase diagram of QCD matter to experimentally pinpoint the conditions for the phase transition into QGP.

Today, two large experiments built and maintained by international collaborations of scientists, PHENIX and STAR (Fig. 2), continue to operate whereas two smaller experiments, BRAHMS and PHOBOS, have completed data taking. Each experiment was optimized for a different set of experimental observables, but common capabilities allow crucial cross checks. Together, PHENIX and STAR use two kinds of plasma probes (*7*–*11*). Internal probes are particles emitted from the plasma itself. "External" probes are not external in the usual sense; they are energetic particles generated in the first stage of the collision, which traverse the plasma and interact with it on their way to the detectors.

Most of the observed particles are hadrons. Their spectra are well described by a thermal distribution blue-shifted by radial expansion of the plasma. Particle correlations reflect an anisotropic collective flow, known as "elliptic flow." They exhibit a $\cos(2\phi)$ modulation in their azimuthal angular distribution with respect to the direction of the impact-parameter vector between the two colliding ions (*12*). The amplitude of elliptic flow grows with increasing impact parameter because the overlap region of the incoming nuclei becomes more asymmetric (Fig. 3, left). The dynamics within the plasma as it expands translate the spatial asymmetry of the initial state into a final-state anisotropy in momentum space. Higher Fourier components of the angular distribution are also observed in the correlation data; these arise primarily from fluctua-

[1]Department of Physics and Astronomy, State University of New York, Stony Brook, NY 11794, USA. [2]Department of Physics and Center for Theoretical and Mathematical Sciences, Duke University, Durham, NC 27708, USA.

*To whom correspondence should be addressed. E-mail: mueller@phy.duke.edu

tions in the initial positions of the nucleons within the nucleus (Fig. 3, right).

The behavior of gases or liquids is often simulated using hydrodynamics. Indeed, hydrodynamics successfully reproduces the magnitude and impact parameter dependence of elliptic flow (*13*, *14*). Surprisingly, the most faithful match to the data requires a nearly vanishing ratio of the shear viscosity (the resistance to flow or the inability of matter to transport momentum) to the entropy density, implying that the QGP is an almost ideal or "perfect" liquid. Including density fluctuations in the initial conditions of the hydrodynamical simulations also reproduces the higher harmonics with the same low shear viscosity (*15*–*17*).

Quantum mechanics imposes a lower limit of the shear viscosity η for a given particle density by virtue of the uncertainty relation. For relativistic fluids like the QGP, which do not conserve particle number, the appropriate measure of density is the entropy density *s*. Constraining hydrodynamics calculations with the full suite of flow data (*18*) shows that $\eta/s = (1-2)\hbar/4\pi k_B$, close to the quantum limit $\hbar/4\pi k_B$ (*19*–*21*). Low shear viscosity per particle indicates correlations or coordination within the QGP. Gases have very weakly correlated constituents, whereas the molecules in crystals move in a highly coordinated manner. Liquids fall in between the two, exhibiting the lowest shear viscosities and flowing freely, as does the QGP.

The opacity of the QGP is measured with external probes. During initial interpenetration of the two nuclei, quark and gluon constituents (partons) can scatter with a large momentum transfer, deflecting the struck quarks or gluons by a large angle. These transit the plasma, losing energy to it. As partons cannot exist in isolation, they ultimately radiate multiple gluons, and the resulting parton cluster forms a spray of hadrons known as a "jet." In the absence of QGP, this process is calculable and can be measured in p+p collisions. RHIC experiments with Au+Au showed that energetic hadrons in the jet are suppressed relative to the production rate in p+p collisions (*22*, *23*). Back-to-back jets of moderate energy disappear entirely (*24*). Photons do not experience the strong interaction (Fig. 4A) and are observed to exit the plasma unscathed (*25*). The success of hydrodynamics with vanishingly small η/s, together with the observed high opacity, show that QGP cannot be the weakly coupled gas naïvely expected from asymptotic freedom. Kinetic theory associates a small shear viscosity with a short mean free path, implying high opacity. A short mean free path also requires strong coupling, because the scattering cross section is proportional to the coupling strength.

First results from Pb+Pb collisions at nearly 14 times higher energy at the Large Hadron Collider (LHC) confirm the physics picture derived from RHIC data (*26*). The initial temperature at LHC is ~30% higher. Hydrodynamical model fits indicate nearly the same η/s ratio as at RHIC (*27*); the hotter QGP produced at LHC is also strongly coupled. Jet quenching measurements at LHC extend the kinematic range by a factor of 5. They are consistent with a linear, or slightly slower, gowth of the opacity with matter density. The LHC's higher energy produces higher-energy jets, which simplifies reconstruction of complete jet observables. Clusters of energy corresponding to back-to-back jets are clearly visible in Fig. 4B (*28*). The data reveal that even very energetic jets lose a sizable fraction of their energy to the medium, where it appears to thermalize rapidly. Analysis of jet shapes and particle content help constrain the mechanism of the parton-QGP interaction. The yields of D and B mesons, which contain heavy quarks, are also much larger at LHC. Furthermore, the Z boson becomes available as a new electroweak probe of the QGP. First, statistically limited, results for these "external" probes can be reproduced reasonably well by extrapolation from RHIC.

Theoretical Tools

Key theoretical tools to describe QGP properties and predict experimental observables are lattice gauge theory and transport theory. Lattice gauge theory is an ab initio formalism that simulates the partition function of QCD on a space-time lattice. Advances in algorithms and computer hardware now permit simulations with physical quark masses on lattices that are simultaneously large and fine enough to be safely extrapolated

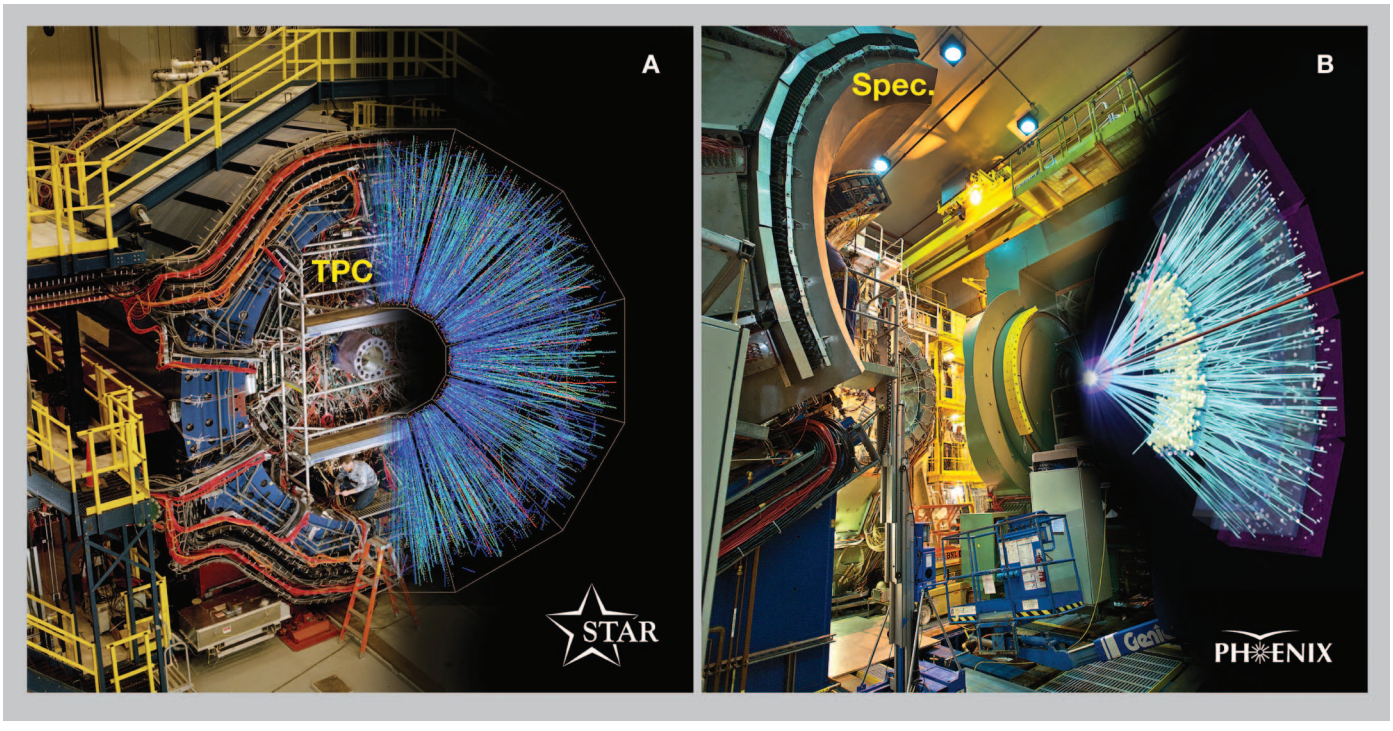

Fig. 2. (**A**) The STAR detector has a time-projection chamber (TPC), which is essentially a three-dimensional digital camera to record trajectories of particles produced in each collision. Surrounding detectors identify hadrons and tag high-momentum electrons. STAR has large acceptance and is thus well suited to study multiparticle correlations and collisions at lower energies. (**B**) The PHENIX detector has two spectrometers to measure photons, electrons, and hadrons at angles near 90°; one is visible at left (Spec.). There are also two muon spectrometers in the beam direction; these detect decays of hadrons containing charm and bottom quarks. A sample event display is shown on the right side of each detector. [Credit: Brookhaven National Laboratory]

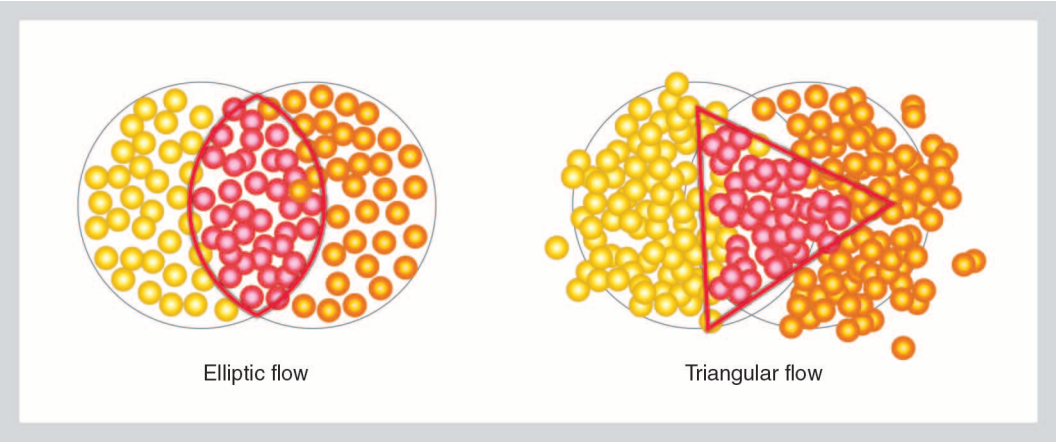

Fig. 3. Elliptic (left) and triangular (right) flow patterns arise from the locations of individual nucleons at the instant when two nuclei interpenetrate. The nucleons of one nucleus are shown in yellow and the other in orange. Red indicates those nucleons in the overlap region, which actually collide. (Left) Adapted with permission from figure 1 in (*56*) [Copyrighted by the American Physical Society]. (Right) Adapted with permission from figure 3 in (*57*). [Copyrighted by the American Physical Society]

to the thermodynamic and continuum limits (*29*). The equation of state of hot QCD matter and correlation functions, such as the screening distance of the color force, are now within reach. However, reliable calculations in lattice QCD are still limited to static properties, severely restricting our ability to address transport properties of the QGP.

Transport theory describes the conversion of the gluon fields in the incoming nuclei into thermal QCD matter, the explosive expansion of the QGP, and finally its disassembly into hadrons. A standard scenario of distinct reaction stages has emerged (*30*). In the first stage, gluons are liberated and form a dense system of nonlinearly coupled fields, known as the glasma. The second stage, the rapid expansion of the hot QGP, is effectively described by relativistic hydrodynamics with small viscous effects. After the matter cools below 150 MeV, its final expansion and freeze-out can be described by kinetic theory for hadrons. Whereas the experimental data provide solid evidence for the validity of the description of stages 2 and 3, experimental exploration of the glasma phase is just beginning.

Physicists were astounded to find that an entirely different approach, using dualities that relate QCD at strong coupling with weakly coupled gravitational theories, can yield insights into the dynamical properties of quantum inviscid liquids. The duality of string theory in anti-de Sitter (AdS) space with conformal quantum field theory (CFT) provides an exact description of some strongly coupled systems. The formalism, known as AdS/CFT correspondence (*31*, *32*), holographically maps the intractable strongly coupled quantum field theory onto a solvable classical gravity theory in five dimensions. Thermalization of the quantum field appears as formation of a black hole in the gravity dual theory. Although the formalism is exact only in the limit of an infinite number of colors and at strong coupling, it is believed that for many quantities of interest the three colors of QCD can be considered as a large number. Lattice gauge theory (*33*, *34*) provides compelling evidence for this conjecture. The gravity dual description offers an explanation of how a strongly coupled plasma of gauge fields can reach thermal equilibrium so rapidly and why hydrodynamics furnishes a reliable description even at strong coupling, when kinetic theory fails. Unfortunately, the coupling of true QCD is not as strong as would be required for rigorous application of the AdS/CFT duality. At the moment no gravity dual for true QCD is known, and it is unknown whether one exists.

Interconnections

Understanding strongly coupled or strongly correlated systems is at the intellectual forefront of multiple subfields of physics. One example is ultracold fermionic atoms, such as ^{6}Li, where application of a magnetic field excites a strong resonance. When confined in an atomic trap, these atoms form a degenerate Fermi liquid, which can be manipulated and studied in detail (*35*). At temperatures below ~0.1 μK, the atoms interacting via the resonance form a superfluid (*36*). The shear viscosity η and the entropy density s for this system can be measured separately, showing that η/s falls with decreasing temperature. At very low temperatures, it approaches about four times the universal quantum limit (*37*), only twice as large as the value deduced for the QGP.

Strongly correlated electron systems in condensed matter provide an example of strong coupling where the elementary interaction is not strong, but its role is amplified by the large number of interacting particles and their ability to dynamically correlate their quantum wave functions. Surprisingly, holographic gravity duals have also helped to provide simple descriptions of such complex systems (*38*, *39*).

Strongly coupled systems in conventional plasma physics include warm, dense matter and dusty plasmas (*40*) residing in astrophysical environments, such as the rings of Saturn, and in thermonuclear fusion. In these plasmas, the ratio r of potential to kinetic energy is large, implying strong coupling; at sufficiently large r, such plasmas can even crystallize. The shear viscosity exhibits a minimum at a certain value of r, where the dominant mechanism of momentum transport changes from ballistic quasiparticle motion to some form of collective transport.

An advantage of QCD matter over other strongly coupled systems is that the interaction is well defined. The QGP thus offers a chance to understand how a strongly coupled fluid emerges from a microscopic theory that is precisely known. The strongly coupled QGP is also the only known relativistic liquid. Its structure is not dominated by repulsive interactions, so it challenges the traditional concept of a liquid. However, the high temperature of the QGP, combined with the fundamental nature of the QCD interaction, permits ab initio techniques to address equilibrium properties of hot QCD matter without any model assumptions or approximations. The rapidly expanding capabilities to perform definitive calculations of this kind enable newly rigorous comparisons between the theory of strongly coupled systems and experiment.

Open Questions and Challenges

The surprising experimental results present an entirely new set of questions about the QGP. Roughly following the time development of heavy ion collisions, one must now ask: What is the nature of QCD matter at low temperature but high density, and how does it affect plasma formation? How can the plasma thermalize so rapidly? Does it exhibit novel symmetry properties along the way? The QCD plasma is strongly coupled, but at what scales? Does it contain quasiparticles, or does the strong coupling completely wipe out long-lived collective excitations? What impact does the coupling have on color screening? Is there a characteristic screening length, and if so, what is it? What is the mechanism for parton-plasma interactions, and how does the plasma respond to energy deposited in it?

Gravity dual calculations show that thermalization propagates at the speed of light and all anisotropies disappear quickly in the strong coupling limit (*41*, *42*). Plasma instabilities may play a role. The microscopic structure of the strongly coupled QGP is still poorly understood; in the gravity dual picture, no quasiparticles exist except phonons. Lattice simulations confirm that the quantum numbers associated with quarks—baryon number, electric charge, and flavor—are carried by elementary, quarklike constituents at temperatures above the critical temperature for QGP formation, T_c. However, they are unable to

address the dynamic response of the plasma and provide no information about the presence or absence of propagating quasiparticles. Energy loss of heavy quarks is sensitive to the spectrum of excitations of the QGP and may provide a handle on quasiparticles and their properties. Photons and leptons should preserve imprints of the early stages of the collision.

Shear viscosity and speed of sound are two important indicators of the microscopic structure of any material. The viscosity probes how the constituents of the material are coupled, whereas the speed of sound is sensitive to both the mass of the constituents and the strength of their interaction. Because strongly coupled theories do not allow particle-like excitations, the very nature of the plasma constituents is a question. A promising way to measure both quantities in the QGP is by systematic studies of the response of the matter to initial density fluctuations.

contain bottom quarks. The small size of these mesons enables their existence in QGP because screening occurs only at larger distance scales. Quarkonia have different excited states with varying binding energies; loosely bound, larger states are easier for the QGP to screen. Indeed, suppression of charm quarkonia (charmonia) in QGP, compared to p+p collisions, has already been observed (*47*–*51*). It should be possible to infer the color screening scale with spectroscopy of different quarkonium states as a function of beam energy, meson momentum, and the emission angle with respect to the beam. Untangling initial state effects on heavy quark production and final state effects, which can re-form bound states, requires control measurements in (p or d)+nucleus collisions, along with theoretical study of color screening in an expanding plasma.

Highly energetic partons created in the initial phase of the collision lose energy as they pass

discriminate between radiative and collisional energy loss. Because little difference has been found in the suppression of light and heavy (mostly charm) quarks (*52*), separating the charm quark from the even heavier bottom quark is a key experimental goal.

The Look Ahead at RHIC and LHC

Recent RHIC upgrades have increased both the luminosity and the range of particle species available. Higher luminosity makes rare probes, such as jets and hadrons containing c and b quarks, more accessible. PHENIX and STAR are being upgraded with state-of-the-art silicon microvertex detectors to enable precise measurements of heavy quarks by tagging their decays. These will allow separation of the charm quark from the bottom quark, which is three times heavier and should sail right through the QGP. A new ion source at RHIC provides additional beam species, such as

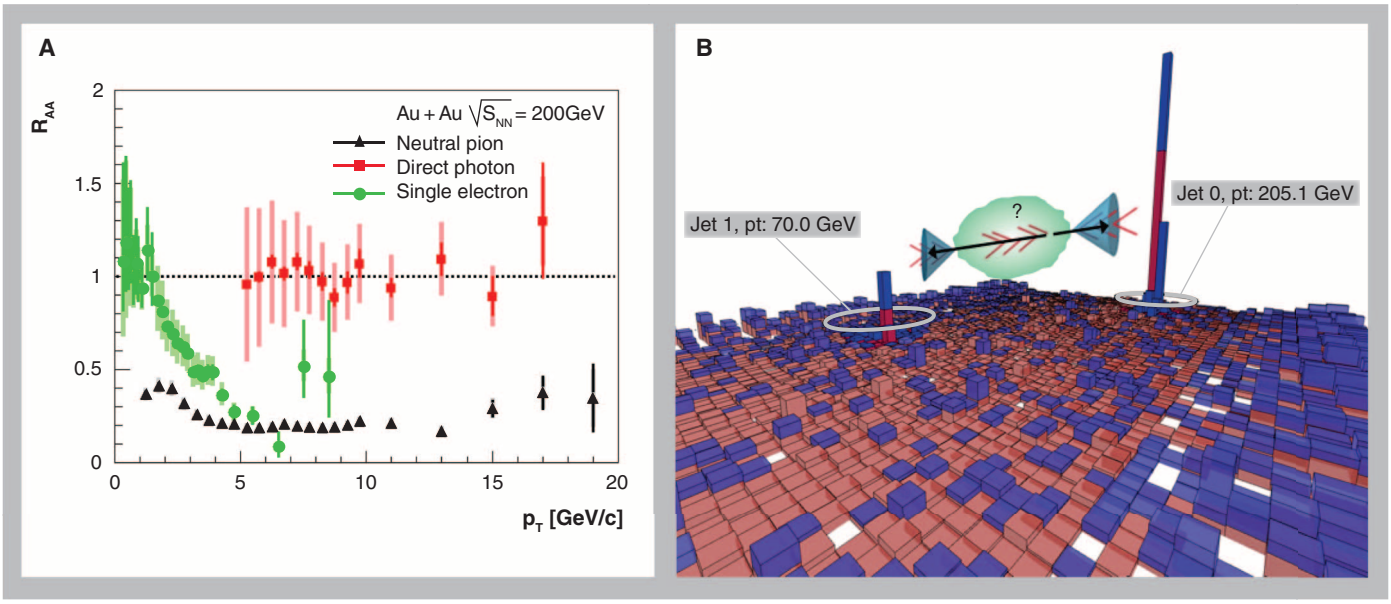

Fig. 4. (**A**) Ratio of particle yield in Au+Au to p+p collisions by PHENIX at RHIC, as a function of particle momentum transverse to the beam direction. Data from (*25*) and adapted with permission from (*52*, *58*) [Copyrighted by the American Physical Society]. The emission of pions and electrons from the decay of heavy quarks is strongly suppressed in Au+Au, whereas photon emission is not suppressed. The suppression of hadrons is a measure of the color opacity of the QGP. (**B**) The cartoon illustrates energy measured in the jet cone on each side of a dijet, along with energy deposit into the QGP, shown as a green shape. The black arrows indicate the path of the energetic partons that create the two jets. The rest of the figure depicts a Pb+Pb event display at LHC from the Compact Muon Solenoid (CMS) (*28*) [Credit: CMS Collaboration; reprinted with permission from https://twiki.cern.ch/twiki/bin/view/CMSPublic/HIEventDisplays]. The angular distribution of energy emitted has been unfolded onto a plane; the height of the peaks is proportional to the amount of energy observed. The Pb beams enter perpendicular to the page. This event was triggered by the jet on the right, and a large energy loss by the jet on the left is seen.

In the QGP, color is screened, akin to the electromagnetic Debye screening observed in conventional plasmas. Lattice QCD shows that above T_c, screening of color is incomplete (*43*–*45*); partial screening is characteristic of strongly coupled plasmas (*46*). Screening in the QGP can be probed experimentally by measuring the survival rate of heavy quark bound states. Charm or bottom quarks are produced in pairs, which sometimes remain bound and are detected as heavy mesons called quarkonia. The mesons called J/ψ and ψ' are composed of charm quarks, the Upsilon mesons (Υ)

through by exciting modes of the medium (collisional energy loss) or by radiating off gluons (radiative energy loss). The second mechanism, akin to bremsstrahlung of photons by electrons passing through matter, becomes less effective as the mass of the parton increases. In a weakly coupled medium, thermalization of deposited energy occurs through a cascade of collisions among quarks and gluons in the plasma; in a strongly coupled medium, the energy is dissipated directly into thermal excitations and sound waves. Measurements of quarks with different mass should

the highly deformed uranium nucleus. U+U collisions, along with asymmetric beam combinations, offer novel ways to control the nuclear geometry, and thus the path length, for probes transiting the QGP. Excitation functions for rare probes can now be used to study predicted features of the QCD matter phase diagram. These measurements, along with RHIC's polarized proton-proton collisions, will systematically test theoretical models, provide benchmarks to isolate the effects of hot QCD matter on observables, and map the parton structure of nuclei in the relevant kinematic range.

The wide range of beam energies available at RHIC also makes it possible to explore the phase diagram of QCD matter at higher baryon densities, because nucleons are partially stopped in collisions at lower energies (*53*). According to some predictions, the transition between hadron and quark matter becomes of first order beyond a critical point in the phase diagram. The results from an exploratory beam energy scan, which hopes to locate this critical point by searching for the signatures of critical fluctuations, are expected soon. Higher beam luminosities will greatly increase the sensitivity of future searches.

The upgrades already under way at RHIC will answer some of the questions posed in the preceding section. Fully exploiting the versatility and luminosity of RHIC requires further detector capabilities. Accessing the early dynamics calls for measuring photons over a larger range of angles, as well as the flow patterns of those photons. Quantifying the color screening length entails precise measurements of heavy quarkonia over a large acceptance, as a function of the mass, momentum, binding energy, path length through the plasma, and initial temperature of the system. Disentangling initial- and final-state effects on bound-state formation implies comparably sized sets of nucleon-nucleus collision data. To pin down the role of gluons in the nuclear wave function (*54*), forward angle detectors for photons, leptons, and hadrons are necessary. To determine the jet energy loss mechanism, full reconstruction of moderate energy jets, which radiate partons near the QGP scale, will be indispensable. Measurement of the energy redistribution in the medium-modified jets coupled with modeling of energy and particle flow will help tease the different mechanisms apart. RHIC is the ideal facility to do this, whereas the higher-energy jets at LHC yield the parton energy dependence of the jet-QGP interaction.

The LHC data will provide stringent tests of jet quenching theory complementary to those at RHIC—for example, via the momentum dependence of heavy quark energy loss, which is predicted to be different in strongly and weakly coupled regimes of the QGP. The higher beam energy at LHC makes the rate of rare probes much higher than at RHIC. This opens a larger kinematic range for hadrons, photons, and b quarks and accesses new probes such as the Z boson. Study of hadrons inside jets energy is determined by an opposing Z boson will provide new constraints on the parton-medium interaction.

The higher energy density reached at LHC should lead to stronger color screening and thus to larger suppression of heavy quark bound states. This effect may be overwhelmed by coalescence of heavy quarks into such states when the QGP converts back into hadrons; coalescence should be more prominent at LHC than at RHIC because more heavy quark pairs are produced in each collision. High statistics spectroscopy of the Υ states will allow comparison of color screening in QGP at different temperatures.

Challenging theoretical advances, including higher-order jet calculations and effective theories for heavy quarks that connect lattice simulations with transport processes, are needed to extract reliable values for the energy loss parameters and the color screening length in the plasma from high-precision data. Major numerical advances will be required to solve the transport equations describing rapid formation of an equilibrated QGP. Development of an exact gravity dual of QCD would enable realistic calculations of dynamical processes in the strong coupling limit. So-called "stringy" corrections for finite numbers of colors would allow bracketing the real-world regime of intermediate coupling from both sides. Such advances will not only elucidate the physics of the QGP but also address intellectual challenges of strong coupling in many areas of physics. The successes and limitations of the string theory–based approach suggest opportunities for the development of novel mathematical techniques applicable to strongly coupled systems.

Exploration of hot QCD matter has made enormous progress during the past decade. Experiments have discovered a new high-temperature phase, the strongly coupled QGP, which persists to the highest temperature probed. Surprising features of the QGP include near-perfect fluidity and extreme opaqueness to all colored probes. The rapid development of theoretical and experimental tools promises quantitative insights into the still mysterious properties of the QGP during the coming decade. These will also inform the study of other strongly coupled systems in nature and in the laboratory.

References and Notes

1. D. J. Gross, F. Wilczek, *Phys. Rev. Lett.* **30**, 1343 (1973).
2. H. D. Politzer, *Phys. Rev. Lett.* **30**, 1346 (1973).
3. E. W. Kolb, M. S. Turner, *The Early Universe* (Redwood City, Addison-Wesley, 1988).
4. P. Petreczky, *Nucl. Phys. A.* **830**, 11c (2009).
5. A. Adare *et al.*; PHENIX Collaboration, *Phys. Rev. C Nucl. Phys.* **81**, 034911 (2010).
6. S. Borsányi *et al.*, *J. High Energy Phys.* **2010**, 77 (2010).
7. I. Arsene *et al.*; BRAHMS Collaboration, *Nucl. Phys. A.* **757**, 1 (2005).
8. K. Adcox *et al.*; PHENIX Collaboration, *Nucl. Phys. A.* **757**, 184 (2005).
9. B. B. Back *et al.*; PHOBOS Collaboration, *Nucl. Phys. A.* **757**, 28 (2005).
10. J. Adams *et al.*; STAR Collaboration, *Nucl. Phys. A.* **757**, 102 (2005).
11. B. Müller, J. L. Nagle, *Annu. Rev. Nucl. Part. Sci.* **56**, 93 (2006).
12. K. H. Ackermann *et al.*, *Phys. Rev. Lett.* **86**, 402 (2001).
13. P. F. Kolb, P. Huovinen, U. Heinz, H. Heiselberg, *Phys. Lett. B* **500**, 232 (2001).
14. D. Teaney, J. Lauret, E. V. Shuryak, *Phys. Rev. Lett.* **86**, 4783 (2001).
15. B. Schenke, S. Jeon, C. Gale, *Phys. Rev. C Nucl. Phys.* **85**, 024901 (2012).
16. M. Luzum, *J. Phys. G* **38**, 124026 (2011).
17. A. Adare *et al.*; PHENIX Collaboration, *Phys. Rev. Lett.* **107**, 252301 (2011).
18. H. Song, S. A. Bass, U. Heinz, T. Hirano, C. Shen, *Phys. Rev. Lett.* **106**, 192301 (2011).
19. P. Danielewicz, M. Gyulassy, *Phys. Rev. D Part. Fields* **31**, 53 (1985).
20. P. K. Kovtun, D. T. Son, A. O. Starinets, *Phys. Rev. Lett.* **94**, 111601 (2005).
21. The Kovtun-Son-Starinets bound (*20*) has been found to be violated in certain strong coupled gauge theories [see (*55*)]. It would be interesting to determine whether the quark-gluon plasma produced in experiments violates this bound.
22. K. Adcox *et al.*; PHENIX Collaboration, *Phys. Rev. Lett.* **88**, 022301 (2002).
23. J. Adams *et al.*; STAR Collaboration, *Phys. Rev. Lett.* **91**, 172302 (2003).
24. C. Adler *et al.*, *Phys. Rev. Lett.* **90**, 082302 (2003).
25. S. Afanasiev *et al.*, PHENIX Collaboration, Measurement of direct photons in Au + Au collisions at $\sqrt{S_{NN}}$ = 200 GeV, arXiv:1205.5759 [nucl-ex]
26. B. Müller, J. Schukraft, B. Wyslouch, First Results from Pb+Pb collisions at the LHC, arXiv:1202.3233 [hep-ex].
27. H. Song, S. A. Bass, U. Heinz, *Phys. Rev. C Nucl. Phys.* **83**, 054912 (2011).
28. S. Chatrchyan *et al.*; CMS Collaboration, *Phys. Rev. C Nucl. Phys.* **84**, 024906 (2011).
29. S. Borsányi *et al.*; Wuppertal-Budapest Collaboration, *J. High Energy Phys.* **2010**, 73 (2010).
30. H. Petersen, J. Steinheimer, G. Burau, M. Bleicher, H. Stöcker, *Phys. Rev. C Nucl. Phys.* **78**, 044901 (2008).
31. J. M. Maldacena, *Adv. Theor. Math. Phys.* **2**, 231 (1998).
32. O. Aharony, S. S. Gubser, J. M. Maldacena, H. Ooguri, Y. Oz, *Phys. Rep.* **323**, 183 (2000).
33. M. Panero, *Phys. Rev. Lett.* **103**, 232001 (2009).
34. S. Datta, S. Gupta, *Phys. Rev. D Part. Fields Gravit. Cosmol.* **82**, 114505 (2010).
35. K. M. O'Hara, S. L. Hemmer, M. E. Gehm, S. R. Granade, J. E. Thomas, *Science* **298**, 2179 (2002).
36. J. Kinast, S. L. Hemmer, M. E. Gehm, A. Turlapov, J. E. Thomas, *Phys. Rev. Lett.* **92**, 150402 (2004).
37. C. Cao *et al.*, *Science* **331**, 58 (2011).
38. S. Sachdev, *Annu. Rev. Con. Mat. Phys.* **3**, 9 (2012).
39. S. Hartnoll, *Science* **322**, 1639 (2008).
40. C. L. Chan *et al.*, Dusty plasma liquids, arXiv:physics/0410042 [physics.plasm-ph].
41. V. Balasubramanian *et al.*, *Phys. Rev. Lett.* **106**, 191601 (2011).
42. P. M. Chesler, L. G. Yaffe, *Phys. Rev. Lett.* **106**, 021601 (2011).
43. M. Asakawa, T. Hatsuda, *Phys. Rev. Lett.* **92**, 012001 (2004).
44. S. Datta, F. Karsch, P. Petreczky, I. Wetzorke, *Phys. Rev. D Part. Fields Gravit. Cosmol.* **69**, 094507 (2004).
45. H.-T. Ding *et al.*, *Proc. Sci. LATTICE* **2010**, 180 (2010); http://pos.sissa.it/archive/conferences/105/180/Lattice%202010_180.pdf.
46. D. Sarmah, M. Tessarotto, M. Salimullah, *Phys. Scr.* **74**, 288 (2006).
47. B. Alessandro *et al.*; NA50 Collaboration, *Eur. Phys. J. C* **39**, 335 (2005).
48. A. Adare *et al.*; PHENIX Collaboration, *Phys. Rev. C Nucl. Phys.* **84**, 054912 (2011).
49. G. Aad *et al.*; ATLAS Collaboration, *Phys. Lett. B* **697**, 294 (2011).
50. S. Chatrchyan *et al.*, CMS Collaboration, *J. High Energy Phys.* **1205**, 063 (2012).
51. B. Abelev *et al.*, ALICE Collaboration, J/ψ production at low transverse momentum in Pb-Pb collisions at $\sqrt{S_{NN}}$ = 2.76 TeV, arXiv:1202.1383 [hep-ex].
52. A. Adare *et al.*; PHENIX Collaboration, *Phys. Rev. Lett.* **98**, 172301 (2007).
53. B. I. Abelev *et al.*; STAR Collaboration, *Phys. Rev. C Nucl. Phys.* **81**, 024911 (2010).
54. L. McLerran, *Nucl. Phys. A.* **752**, 355 (2005).
55. Y. Kats, P. Petrov, *J. High Energy Phys.* **2009**, 044 (2009).
56. B. Alver *et al.*, *Phys. Rev. C Nucl. Phys.* **77**, 014906 (2008).
57. B. Alver, G. Roland, *Phys. Rev. C Nucl. Phys.* **81**, 054905 (2010).
58. A. Adare *et al.*; PHENIX Collaboration, *Phys. Rev. Lett.* **101**, 232301 (2008).

Acknowledgments: This work was supported by grants from the U.S. Department of Energy.

10.1126/science.1215901

2.8 Million Years of Arctic Climate Change from Lake El'gygytgyn, NE Russia

Martin Melles,[1]* Julie Brigham-Grette,[2] Pavel S. Minyuk,[3] Norbert R. Nowaczyk,[4] Volker Wennrich,[1] Robert M. DeConto,[2] Patricia M. Anderson,[5] Andrei A. Andreev,[1] Anthony Coletti,[2] Timothy L. Cook,[2]† Eeva Haltia-Hovi,[4]‡ Maaret Kukkonen,[1] Anatoli V. Lozhkin,[3] Peter Rosén,[6] Pavel Tarasov,[7] Hendrik Vogel,[1] Bernd Wagner[1]

The reliability of Arctic climate predictions is currently hampered by insufficient knowledge of natural climate variability in the past. A sediment core from Lake El'gygytgyn in northeastern (NE) Russia provides a continuous, high-resolution record from the Arctic, spanning the past 2.8 million years. This core reveals numerous "super interglacials" during the Quaternary; for marine benthic isotope stages (MIS) 11c and 31, maximum summer temperatures and annual precipitation values are ~4° to 5°C and ~300 millimeters higher than those of MIS 1 and 5e. Climate simulations show that these extreme warm conditions are difficult to explain with greenhouse gas and astronomical forcing alone, implying the importance of amplifying feedbacks and far field influences. The timing of Arctic warming relative to West Antarctic Ice Sheet retreats implies strong interhemispheric climate connectivity.

The effects of global warming are documented and predicted to be most pronounced in the Arctic, a region that plays a crucial, but not yet well-understood role within the global climate system (*1*). Reliable climate projections for high northern latitudes are, however, hampered by the complexity of the underlying natural variability and feedback mechanisms (*2*, *3*). To date, information concerning the natural climate variability in the Arctic is widely restricted to the last glacial/interglacial cycle, the period covered by the longest ice-core records from the Greenland ice cap (*4*). A limited number of records extend deeper in time, from both the marine realm (*5*) and the Arctic borderland (*6*), but these records are restricted in terms of age control and temporal resolution.

Here, we present a time-continuous and high-resolution record of environmental history from the Arctic spanning the past 2.8 million years (My) from Lake El'gygytgyn, located ~100 km to the north of the Arctic Circle in northeastern Russia (67.5°N, 172°E) (Fig. 1). The length, temporal continuity, and centennial- to millennial-scale temporal resolution (Fig. 2 and supplementary materials) provide a detailed view of natural climatic and environmental variability in the terrestrial Arctic, a better understanding of the representative nature of the last climate cycle for the Quaternary, and insight into how sensitively the terrestrial Arctic reacts to a range of forcing mechanisms.

Lake setting, drilling, and core analyses. Lake El'gygytgyn is located in a meteorite impact crater formed 3.58 million years ago (Ma) (*7*). The 170-m-deep lake has a bowl-shaped morphology with a diameter of ~12 km, a surface area of 110 km^2, and a relatively small catchment of 293 km^2 (*8*). The modern continental Arctic climate produces herb-dominated tundra in the catchment, 9 months per year of lake-ice cover, and oligotrophic to ultra-oligotrophic conditions in the lake. Low productivity in combination with complete overturning of the water column during the ice-free period in summer leads to well-oxygenated bottom waters throughout the year.

Scientific deep drilling was performed in the El'gygytgyn Crater in winter 2008/2009 (*9*). We used advanced high-resolution (logging/scanning) technologies and standard techniques to investigate the core composite from site 5011-1 (Fig. 1) of the International Continental Scientific Drilling Program (ICDP) for lithology as well as selected physical, chemical, and biological proxies (*10*). According to the age model (Fig. 2), which is based on magnetostratigraphy and tuning of proxy data to the regional insolation and global marine isotope stratigraphy (fig. S1), the upper 135.2 m of the sediment record continuously represents the environmental history of the past 2.8 My. To display the obtained data versus time (Fig. 3) we removed volcanic ashes and other event layers caused by mass movement deposits (*10*). Though highly varied in nature, the resultant record of pelagic sedimentation consists of three dominant lithofacies (see supplementary materials). Climate and environmental interpretation of the pelagic sedimentation record is based on complementary biological and geochemical indicators, which show that distinct facies reflect end-member glacial/interglacial climatic conditions (*9*, *11*).

Glacial variability and proxies. Facies A is characterized by dark gray to black finely laminated (<5 mm) silt and clay and may contain

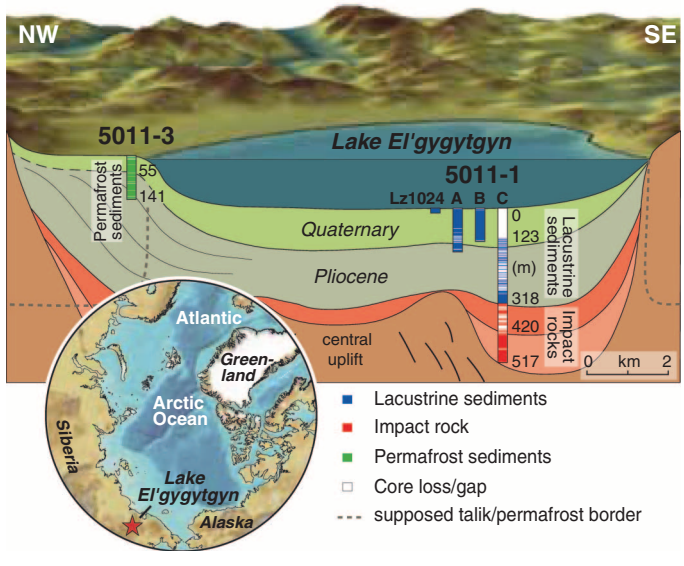

Fig. 1. Location of Lake El'gygytgyn in northeastern Russia (inserted map) and schematic cross-section of the El'gygytgyn basin stratigraphy showing the location of ICDP sites 5011-1 and 5011-3. At site 5011-1, three holes (1A, 1B, and 1C) were drilled to replicate the Quaternary and uppermost Pliocene sections. Hole 1C further penetrated through the remaining lacustrine sequence down to a 318-m depth and then ~200 m into the impact rock sequence underneath. Lz1024 is a 16-m-long percussion piston core taken in 2003 that fills the stratigraphic gap between the lake sediment surface and the top of drill cores 1A and 1B.

[1]Institute of Geology and Mineralogy, University of Cologne, Zuelpicher Strasse 49a, D-50674 Cologne, Germany. [2]Department of Geosciences, University of Massachusetts, 611 North Pleasant Street, Amherst, MA 01003, USA. [3]Far East Branch Russian Academy of Sciences, North-East Interdisciplinary Scientific Research Institute, 16 Portovaya Street, 685000 Magadan, Russia. [4]Helmholtz Centre Potsdam, GFZ German Research Centre for Geosciences, Telegrafenberg C321, D-14473 Potsdam, Germany. [5]Department of Earth and Space Sciences, University of Washington, Box 351310, Seattle, WA 98195–1310, USA. [6]Climate Impacts Research Centre, Umeå University, SE-981 07 Abisko, Sweden. [7]Institute of Geological Sciences, Free University Berlin, Malteserstrasse 74-100, Haus D, D-12249 Berlin, Germany.

*To whom correspondence should be addressed. E-mail: mmelles@uni-koeln.de

†Present address: Department of Physical and Earth Sciences, Worcester State University, Worcester, MA 01602, USA.

‡Present address: Department of Geology, Lund University, Sölvegatan 12, S-223 62 Lund, Sweden.

elongated sediment clasts of coarser grain sizes (fig. S2). This facies was deposited during times of heavy global marine isotopic values (*12*) and low regional July insolation (Fig. 3, A, B, and D) (*13*). Facies A represents peak glacial conditions, when perennial lake ice persisted, requiring mean annual air temperatures at least 4 (± 0.5)°C lower than today (*14*). This resulted in a stagnant water column with oxygen-depleted bottom waters, as reflected by low Mn/Fe ratios (Fig. 3G) and minima in magnetic susceptibility (MS) (Fig. 3E), indicating reducing conditions with magnetite dissolution (see supplementary materials). Dark laminations along with maxima in the content of total organic carbon (TOC) (Fig. 3F) reflect the absence of bioturbation and enhanced preservation of organic matter. Low Si/Ti ratios (Fig. 3H) and a robust correlation between Si/Ti ratios and biogenic silica contents (see supplementary materials), however, suggest relatively low primary production.

Facies A first appears 2.602 to 2.598 Ma, during marine isotope stage (MIS) 104 (Fig. 3D), corresponding with pollen assemblages that indicate substantial cooling at the Pliocene/Pleistocene boundary (see supplementary materials). This cooling coincides with distinct climatic deterioration at Lake Baikal (*15*) and may be associated with the poorly dated Okanaanean Glaciation in eastern Chukotka at the beginning of the Pleistocene (*16*). On the other hand, the first occurrence of facies A at Lake El'gygytgyn clearly postdates the onset of stratification across the western subarctic Pacific Ocean at 2.73 Ma, an event believed to have triggered the intensification of Northern Hemispheric glaciation (*17*). Hence, the onset of full glacial cycles in central Chukotka cannot directly be linked to changes in thermohaline circulation in the Pacific.

From the long-term succession of facies A (Fig. 3D) and Mn/Fe ratios (Fig. 3G), pervasive glacial episodes at Lake El'gygytgyn gradually increase in frequency from ~2.3 to ~1.8 Ma, eventually concurring with all glacials and several stadials reflected globally in stacked marine isotope records (*12*). The full establishment of glacial/interglacial cycles by ~1.8 Ma at Lake El'gygytgyn coincides well with enhanced glacial erosion in British Columbia (*18*) and the onset of subpolar cooling in both hemispheres with an average bipolar temperature drop of 4° to 5°C due to the emergence of the tropical Pacific cold tongue (*19*). Nevertheless, this event clearly predates the mid-Pleistocene transition, when the dominance of 41 thousand years (ky) of obliquity was globally replaced by the 100-ky cycle between 1.25 and 0.7 Ma (*20*).

Interglacial variability and proxies. Facies B is characterized by massive to faintly banded silt that is olive gray to brownish in color (fig. S2). This facies comprises the majority of sediment that accumulated in Lake El'gygytgyn during the past 2.8 My, representing 79% of the Quaternary history (Fig. 3D). Facies B reflects a wide range of glacial to interglacial settings and includes the style of modern sedimentation. As such, a seasonal ice cover promotes higher diatom productivity, as indicated by high Si/Ti ratios (Fig. 3H and supplementary materials). In contrast, TOC content is low (Fig. 3F), suggesting high organic matter decomposition due to oxygenation of bottom waters as a consequence of wind- and density-driven mixing. Complete water-column ventilation is also indicated in the sediment colors, maxima in MS (Fig. 3E), and high Mn/Fe ratios (Fig. 3G). In addition, the lack of stratification indicates minor sediment homogenization by bioturbation.

Facies C consists of reddish-brown silt-sized sediment with distinct fine laminations (<5 mm) (fig. S2). This facies is irregularly distributed in the record compared with facies A and B (Fig. 3D). Facies C coincides with some periods of light values in the global marine isotope record and high regional July insolation (Fig. 3, A and B). The characteristics of facies C suggest that it represents particularly warm interglacials. High Mn/Fe ratios (Fig. 3G) along with reddish-brown sediment colors imply well-oxygenated bottom waters. In contrast with facies B, however, the sediments are distinctly laminated. This is traced back to a combination of factors, including a particularly high primary production in spring and summer and anoxic bottom water conditions during winter stratification under a seasonal ice cover, which excludes bioturbation despite annual oxygenation. High primary production, presumably caused by a longer ice-free season and enhanced nutrient supply from the catchment relative to other interglacials, is indicated by exceptionally high Si/Ti ratios (Fig. 3H). Anoxic bottom water

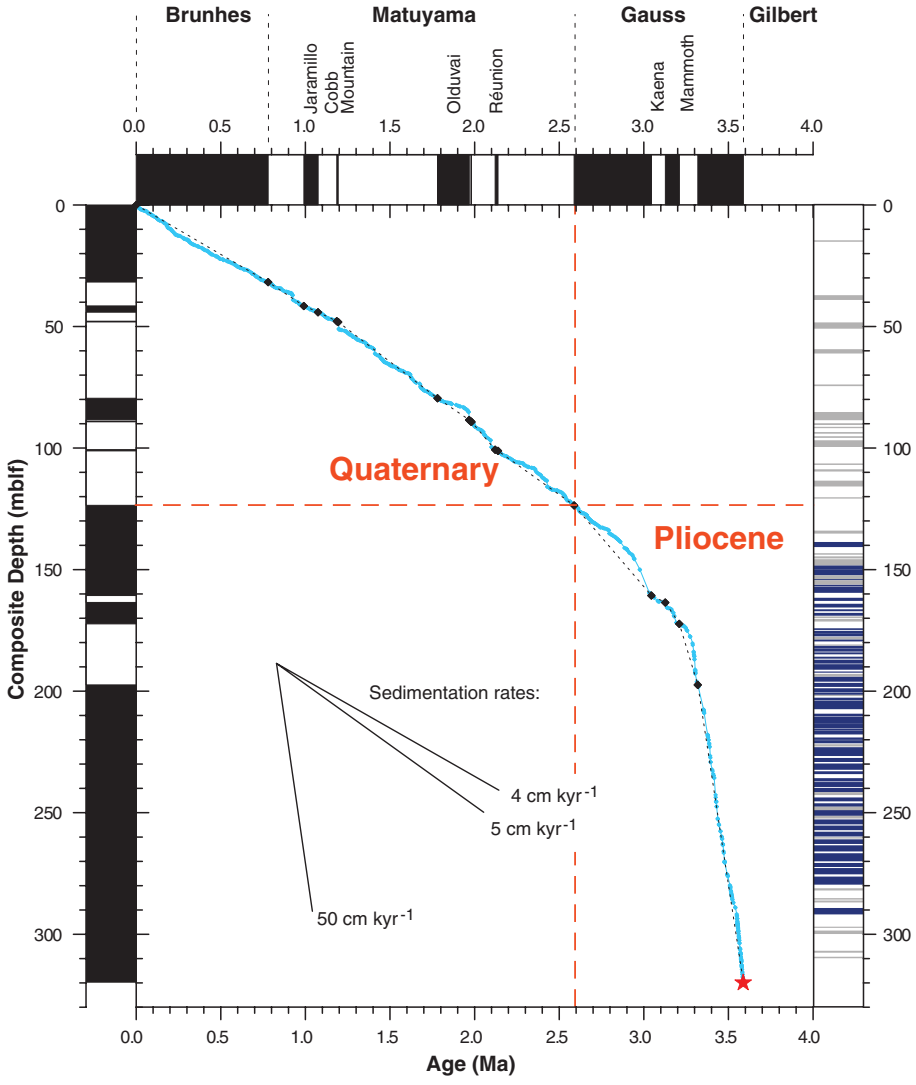

Fig. 2. Age/depth model with resulting sedimentation rates for the ICDP 5011-1 core composite based on magnetostratigraphy and correlation between sediment proxy data, the LR04 marine isotope stack (*12*), and regional spring and summer insolation (*13*). Initial first-order tie points are indicated by black diamonds; second- and third-order tie points are denoted by the blue curve. The red star marks the time of the impact inferred from $^{40}Ar/^{39}Ar$ dating (*7*) at 3.58 (±0.04) Ma. Black and white bars denote normal and reversed polarity, respectively. Mass movement deposits and core gaps greater than 50 cm in thickness are indicated on the right *y* axis in gray and blue, respectively. mblf, meters below lake floor.

conditions during winter are implied by high TOC contents (Fig. 3F), reflecting high primary production and incomplete decomposition compared with facies B, and variable MS values (Fig. 3E), reflecting partial dissolution of magnetite.

The described characteristics of facies C are most pronounced for MIS 11c, 31, 49, 55, 77, 87, 91, and 93 (red bars in Fig. 3), suggesting that these interglacials represent unusual "super interglacials" in the Arctic throughout the Quaternary. The exceptional character of these interglacial conditions becomes evident based on a comparison of MIS 1 and 5e (facies B) with MIS 11c and 31 (super interglacials of facies C), using additional biological proxies and pollen-based climate reconstructions (Fig. 3, I to L).

Sediments formed in Lake El'gygytgyn during MIS 1 and 5e have Si/Ti ratios only slightly higher than those formed during glacial and stadial conditions of MIS 2, 5d, and 6 (Fig. 3K). Pollen data show distinct increases in tree and

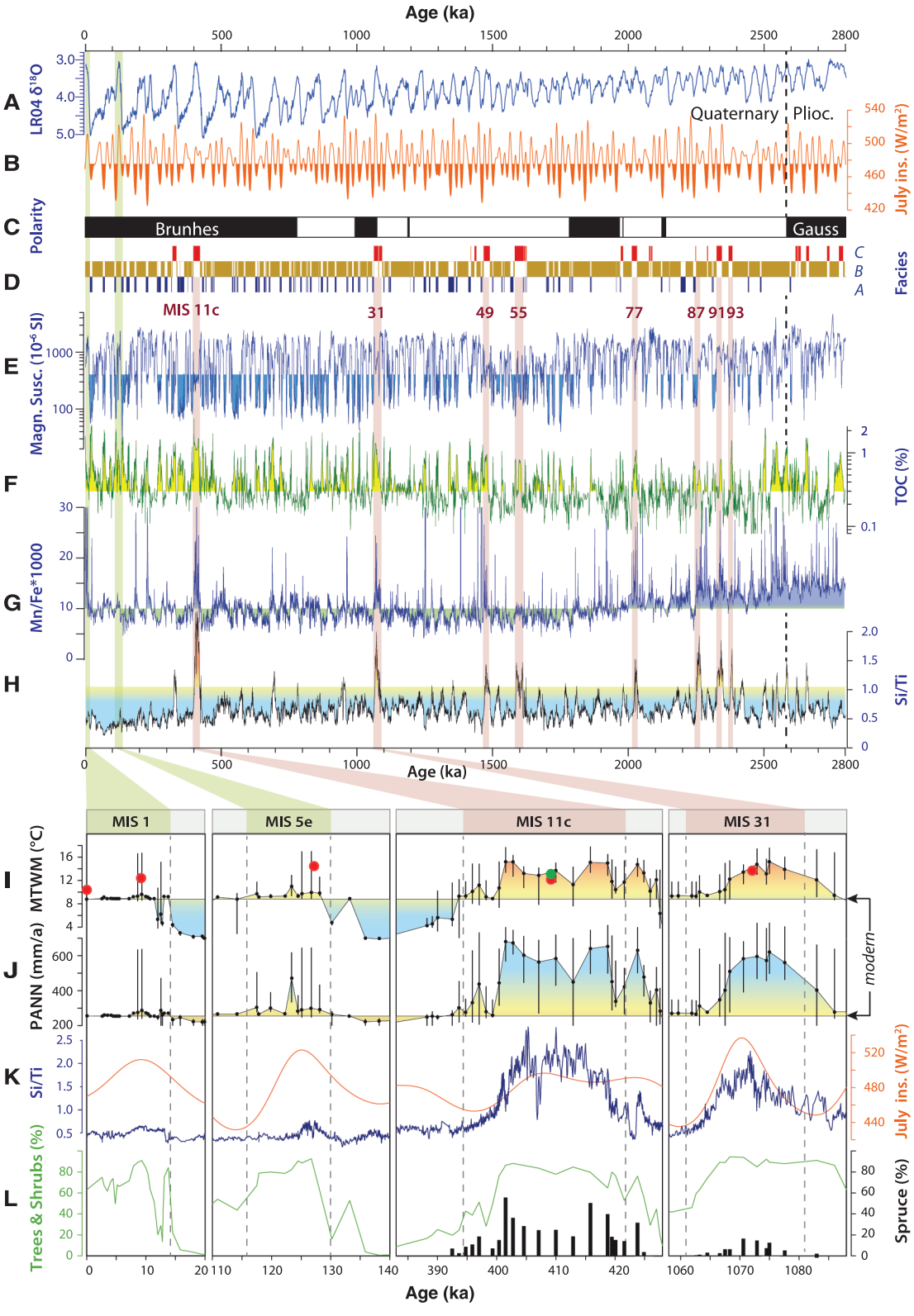

Fig. 3. (**A** to **H**) (A) LR04 global marine isotope stack (*12*) and (B) mean July insolation for 67.5°N (*13*) for the past 2.8 My compared with (C) magnetostratigraphy, (D) facies, (E) magnetic susceptibility, (F) TOC contents, (G) Mn/Fe ratios, and (H) Si/Ti ratios in the sediment record from Lake El'gygytgyn (magnetic susceptibility and x-ray fluorescence data are smoothed using a 500-year weighted running mean to improve the signal-to-noise ratio). Super interglacials at Lake El'gygytgyn are highlighted with red bars. (**I** to **L**) Expanded views into the interglacials MIS 1, 5e, 11c, and 31 and adjoining glacials/stadials. (I) Reconstructed MTWM and (J) PANN based on the pollen spectra and best modern analog approach [modern values from (*56*)]. (K) Mean July insolation for 67.5°N (*13*) compared with El'gygytgyn Si/Ti ratios, smoothed by five-point weighted running mean. (L) Tree and shrub pollen percentages compared with spruce pollen content. Simulated July surface air temperatures (red and green dots) at the location of the lake are shown for comparison. The location of the dots relative to the *x* axis corresponds with the GHG and orbital forcing used in each interglacial simulation (see supplementary materials). Simulated modern and preindustrial temperatures are close to observed values, so model temperatures are not corrected for bias. The green dot indicates the results derived with a deglaciated Greenland and increased heat flux under Arctic Ocean sea ice by 8 W m^{-2}.

shrub pollen (Fig. 3L) and suggest that birch and alder shrubs dominated the vegetation (fig. S4). Pollen-based climate reconstructions (see supplementary materials) suggest that the mean temperature of the warmest month (MTWM; i.e., July) and the annual precipitation (PANN) during the peak of MIS 1 and 5e were only ~1° to 2°C and, with one exception, ~50 mm higher than today, respectively (Fig. 3, I and J).

This observation is consistent with temperature reconstructions for the Holocene thermal maximum, which indicate +1.6 (±0.8)°C warming in the western Arctic (*21*) and +1.7 (±0.8)°C across the entire Arctic (*3*) relative to modern, confirming that Lake El'gygytgyn records regional rather than just local climate change (*14*). In contrast, temperature reconstructions for the MIS 5e thermal maximum are more variable, indicating +5 (±1)°C across the entire Arctic, albeit with smaller anomalies reconstructed for the Pacific sector (*3*, *22*). The warmer climate across the Arctic during MIS 5e compared with MIS 1 is thought to have caused a size reduction of the Greenland Ice Sheet equivalent to 1.6 to 2.2 m in global sea-level rise (*23*).

Strongly enhanced primary productivity during the super interglacials MIS 11c and 31 compared with MIS 1 and 5e, as inferred from higher Si/Ti ratios (Fig. 3K), is associated with comparable maxima in tree and shrub pollen but is marked by distinct differences in pollen composition (Fig. 3L and supplementary materials). For instance, substantial spruce pollen is present during MIS 11c and 31 but is missing during shrub-dominated MIS 1 and 5e interglacials. According to the best modern analog (BMA; see supplementary materials) climate reconstruction, maximum MTWM and PANN were up to 4° to 5°C and ~300 mm higher than those of MIS 1 and 5e, respectively (Fig. 3, I and J).

Sediment records of MIS 11 are rare in the Arctic, and their reconstructed temperature signals are inconclusive (*22*). However, there are indications that the Greenland Ice Sheet was much smaller or even absent (*24*, *25*), with forests covering at least South Greenland (*26*). Relative sea level may have been significantly higher than today (*25*, *27*). Particularly warm conditions are also suggested by records from Lake Biwa (*28*), Lake Baikal (*29*), the mid-latitude Atlantic (*30*), and the Belize Reef (*31*) and may have been associated with megadroughts in the southwestern United States (*32*).

As yet, MIS 31 is not unambiguously recorded in the Arctic, but it is known for substantial changes in and around Antarctica, including a southward shift of the subtropical front and warmer waters in the Southern Ocean (*33*, *34*) and the collapse of the West Antarctic Ice Sheet (WAIS) (*35*). In the Northern Hemisphere, the Plio/Pleistocene Gubik Formation of northern Alaska includes at least five sea-level high stands associated with episodes of warm climate and reduced sea ice (*36*). One of these episodes, the Fishcreekian transgression, is now thought to have occurred ~1.2 Ma (*37*) and thus may be correlative with MIS 31. Another possibly correlative site is at Fosheim Dome on Ellesmere Island. This site includes terrestrial deposits dated to ~1.1 Ma, which enclose fossil beetle (Coleoptera) assemblages, suggesting temperatures 8° to 14°C above modern values (*38*).

Other Arctic sites potentially correlative with one or more of the older Early Pleistocene super interglacials recorded in Lake El'gygytgyn (Fig. 3) include the Kap København Formation in northern Greenland, currently dated to ~2.4 Ma. At this time, sea ice was strongly reduced and forests reached the Arctic Ocean about 1000 km further to the north than today (*39*). Another candidate is the balmy Bigbendian Transgression of the Gubik Formation dated to ~2.6 Ma (*36*).

Interglacial forcings and feedbacks. Comparing the relative warmth of the Pleistocene interglacials recorded at Lake El'gygytgyn (Fig. 3I) in the context of orbital and greenhouse gas (GHG) forcing (*40*), we find that peak summer warmth during MIS 5e and 31 corresponds to the congruence of high obliquity, high eccentricity, and precession aligning perihelion with boreal summer. The net effect of this orbital configuration produces high-intensity summer insolation at the lake, >50 Wm^{-2} greater than today (Fig. 3K). Similarly, peak warmth during MIS 1 and 11c also coincides with perihelion during boreal summer, but lower eccentricity (and lower obliquity at MIS 11c) attenuates the effect of precession relative to MIS 5e and 31, making summer insolation forcing less intense, albeit longer in duration.

GHG radiative forcing from a combination of CO_2, CH_4, and N_2O atmospheric mixing ratios determined from ice cores (see supplementary materials) is similar during MIS 5e and 11c (+0.16 and +0.19 Wm^{-2} relative to preindustrial GHG concentrations, respectively). Early MIS 1 is clearly an exception, with substantially lower CO_2 levels [~260 parts per million by volume (ppmv)] around the time of peak Holocene warmth [~9 thousand years ago (ka)] producing −0.44 Wm^{-2} less radiative forcing relative to preindustrial levels. MIS 31 (~1.072 Ma) lies beyond the oldest ice cores, so no direct information on atmospheric composition is available. However, a proxy-based reconstruction of mid-Pleistocene partial pressure of CO_2 based on boron isotopes in plank-

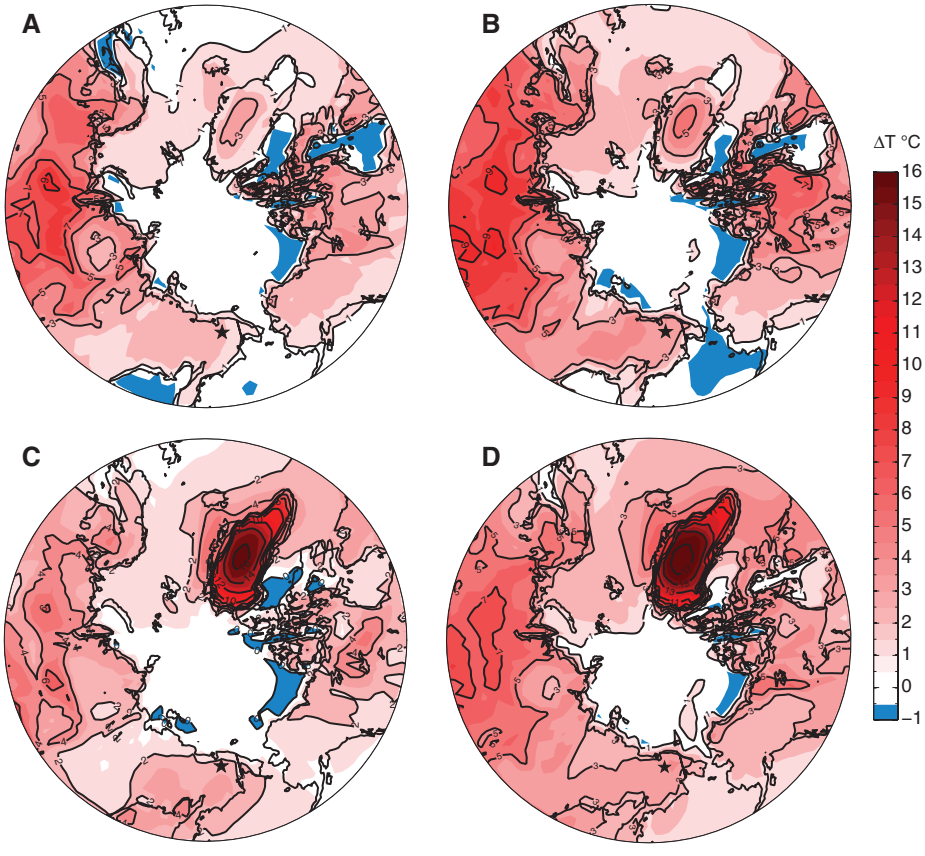

Fig. 4. Simulated interglacial warming (2-m surface temperature in degrees Celsius) relative to preindustrial levels. (**A**) MIS 1 (9-ky orbit and GHGs). (**B**) MIS 5e (127-ky orbit and GHGs). (**C**) MIS 11c (409-ky orbit, GHGs, no Greenland Ice Sheet, and 8 W m^{-2} enhanced oceanic heat convergence under Arctic sea ice). (**D**) MIS 31 (1072-ky orbit, GHGs, and no Greenland Ice Sheet). Orbital and GHG forcing for MIS 5e and 11c follow that used by Yin and Berger (*40*). Forcing for MIS 31 follows that used by DeConto *et al.* (*42*). The location of Lake El'gygytgyn is shown with a star near the bottom-center of each panel. Areas of no shading (white) roughly correspond to statistically insignificant anomalies at the 95% confidence interval.

tonic foraminifera (*41*) indicates that the highest mid-Pleistocene CO_2 levels (~325 ppmv) occurred around 1 Ma, roughly coinciding with the exceptional warmth of MIS 31. Though uncertain, these reconstructed CO_2 levels at MIS 31 would have added ~0.84 Wm^{-2} of radiative forcing, even if CH_4 and N_2O mixing levels remained close to preindustrial values, which is unlikely considering the ubiquitous correlation of elevated CH_4 and N_2O during late Pleistocene interglacials. In sum, much of the warmth during MIS 31 can be explained by elevated greenhouse gas levels (*42*).

To investigate potential reasons for the super interglacials at Lake El'gygytgyn, we tested the equilibrated response of a Global Climate Model (GCM) with an interactive vegetation component (see supplementary materials) to the orbital and GHG forcing corresponding to the timing of peak summer warmth at MIS 1, 5e, 11c, and 31. Comparisons with a preindustrial control simulation (Fig. 4) show that differences in MTWM maxima at Lake El'gygytgyn during MIS 1 and 5e (+2.1° and +4.2°C) were in the same range as those during MIS 11c and 31 (+2.2° and +3.5°C) (Fig. 3I, red dots, Fig. 4, and supplementary materials). The same holds true for the modeled differences in PANN (0 and –37 mm/a and +38 and 0 mm/a, respectively). The results are similar to previous interglacial simulations using an intermediate complexity model (*40*), with the combined effect of orbital and GHG forcing at MIS 5e producing the greatest summer warming among the four interglacials modeled here. Our simulated summer warming (4.2°C) over the Beringian interior at MIS 5e also closely matches the warming simulated by a coupled atmosphere-ocean GCM (*43*). Consequently, the distinctly higher observed values of MTWM and PANN at MIS 11c cannot readily be explained by the local summer orbital forcing or GHG concentrations alone and suggest that other processes and feedbacks contributed to the extraordinary warmth at this interglacial and the relatively muted response to the strongest forcing at MIS 5e.

Vegetation-land surface feedbacks are accounted for in our model, and the simulated poleward advance of evergreen needle-leaf forest during the interglacials provides a good match with our reconstructions (see supplementary materials), yet the warming effect of boreal forest expansion does not provide a satisfactory explanation for the warmth of MIS 11c. A deglaciated Greenland has been shown to have important regional effects on surrounding sea surface temperatures (SSTs) and sea-ice conditions, but widespread warming in the circum-Arctic (and Beringia in particular) has been shown to be minimal (*43*, *44*). This observation is supported by our simulations, showing that the loss of the Greenland Ice Sheet at MIS 11c raises summer temperatures at Lake El'gygytgyn by only 0.3°C. Furthermore, Greenland was likely reduced in size during MIS 5e and perhaps other interglacials, offering little help in differentiating Beringia's response from one interglacial to the next. Meltwater impacts on ocean overturning (ignored in our simulations) generally have a cooling effect on the Northern Hemisphere, adding to the difficulty in explaining the exceptional warmth at MIS 11c relative to MIS 1 and 5e.

The super interglacials at Lake El'gygytgyn coincide remarkably with diatomite layers in the Antarctic ANDRILL 1B record (see supplementary materials), which reflect periods of a diminished WAIS and open water in the Ross Embayment (*35*, *45*). The higher number of events at Lake El'gygytgyn does not necessarily reflect a higher frequency, but it may also reflect the discontinuity of the ANDRILL 1B record (*46*).

Linkages between extraordinary warmth at Lake El'gygytgyn and Antarctic ice volume imply strong intrahemispheric climate coupling that could be related to reductions in Antarctic Bottom Water (AABW) formation (*47*) during times of ice sheet/shelf retreat and elevated fresh water input into the Southern Ocean. This is supported by distinct minima in AABW inflows into the southwest Pacific during MIS 11 and 31 (*48*). As a consequence, changes in thermohaline circulation during MIS 11 and 31 might have reduced upwelling in the northern North Pacific (*49*), as indicated by distinctly lower BSi concentrations compared with other interglacials at Ocean Drilling Program site 882 (*50*, *51*). A stratified water column during the super interglacials would have resulted in higher SSTs in the northern North Pacific, with the potential to raise air temperatures and precipitation rates over adjacent land masses via effects on the dominant pressure patterns (Siberian high and Aleutian low) that dominate the modern climatology at the lake (*52*).

An alternative mechanism linking Lake El'gygytgyn with Antarctica could be related to higher relative sea level due to the combined retreats of the WAIS (*44*) and the Greenland Ice Sheet (*24*), resulting in enhanced warm-water intrusion into the Arctic Ocean. Potential gateways are the Denmark Strait and Barents Sea from the Atlantic Ocean and the Bering Strait from the Pacific Ocean. In the northeastern Atlantic, however, SSTs, at least during MIS 11, were lower than during MIS 9, 5e, and 1 (*53*). Today, Bering Strait throughflow is restricted by shallow waters of only ~50 m in depth, resulting in an average northward transport of ~0.8 sverdrups (1 sverdrup = 10^6 m^3 s^{-1}) (*54*). Substantial interannual variability in flow rate can produce elevated heat fluxes (5 to 6 × 10^{20} J/year in 2007), which can be amplified in the Arctic by internal-feedback mechanisms (*3*). No evidence as yet exists for substantial changes in temperature or flow rates during super interglacials; however, as a first exploration of this idea, we increased the heat flux convergence under Arctic sea ice in our interglacial climate model simulations by 8 W m^{-2} (reflecting an extreme ~fourfold increase in warmer Bering Strait throughflow). The additional heat flux results in substantial reductions in seasonal sea ice and warmer Arctic SSTs but contributes little additional warming (<0.7°C) (Figs. 3I and 4C) in the Beringian interior.

Fully testing these ideas will require additional climate-ocean modeling, explicitly accounting for glacial/interglacial changes in regional sea level (paleobathymetry and gateways), changes in land-ice distributions, and melt-water inputs in both polar regions, as well as contemporaneous sediment records from the Arctic and North Pacific Oceans.

The paleoclimatic record from Lake El'gygytgyn provides a benchmark of Arctic change from an area that has otherwise been a data desert for time-continuous terrestrial records of the Pliocene and Pleistocene. The sediments provide a fresh window into the environmental dynamics of the Arctic from a terrestrial high-latitude site for comparison with other Arctic records. Marine cores from the Arctic basin, such as those from the ACEX/Lomonosov Ridge or HOTRAX expeditions (*55*), still lack the comparable resolution and length to test for perennial versus seasonal sea-ice conditions during interglacials over the past 2.8 My. The attenuated response of Arctic SSTs in model simulations of the interglacials (Fig. 4) (*43*) relative to surrounding continents hints that deep Arctic Ocean cores might not provide a complete perspective of the pacing or magnitude of climate change in the Arctic borderlands. The observed response of the region's climate and terrestrial ecosystems to a range of interglacial forcing provides a challenge for modeling and important constraints on climate sensitivity and polar amplification. The marked coherence of interglacial warmth across the western Arctic with repeated deglaciation events in West Antarctica supports the notion of strong teleconnections between the polar regions over the past 2.8 My.

References and Notes

1. ACIA, *Arctic Climate Impact Assessment* (Cambridge Univ. Press, Cambridge, 2005).
2. J. Christensen *et al.*, in *Fourth Assessment Report of the Intergovernmental Panel on Climate Change* (Cambridge Univ. Press, Cambridge, 2007), pp. 847–940.
3. G. H. Miller *et al.*, *Quat. Sci. Rev.* **29**, 1779 (2010).
4. North Greenland Ice Core Project members, *Nature* **431**, 147 (2004).
5. M. O'Regan, C. J. Williams, K. E. Frey, M. Jakobsson, *Oceanography* **24**, 66 (2011).
6. CAPE Last Interglacial Project Members, *Quat. Sci. Rev.* **25**, 1383 (2006).
7. P. Layer, *Meteorit. Planet. Sci.* **35**, 591 (2000).
8. M. Nolan, J. Brigham-Grette, *J. Paleolimnol.* **37**, 17 (2007).
9. M. Melles *et al.*, *Sci. Drill.* **11**, 29 (2011).
10. Materials and methods are available as supplementary materials on *Science* Online.
11. M. Melles *et al.*, *J. Paleolimnol.* **37**, 89 (2007).
12. L. E. Lisiecki, M. E. Raymo, *Paleoceanography* **20**, PA1003 (2005).
13. J. Laskar *et al.*, *Astron. Astrophys.* **428**, 261 (2004).
14. M. Nolan, *Clim. Past Disc.* **8**, 1443 (2012).
15. D. Demske, B. Mohr, H. Oberhänsli, *Palaeogeogr. Palaeoclimatol. Palaeoecol.* **184**, 107 (2002).
16. A. F. Fradkina *et al.*, *Geol. Soc. Am. Spec. Pap. 382* (2005).
17. G. H. Haug *et al.*, *Nature* **433**, 821 (2005).
18. D. L. Shuster, T. A. Ehlers, M. E. Rusmoren, K. A. Farley, *Science* **310**, 1668 (2005).
19. A. Martínez-Garcia, A. Rosell-Melé, E. L. McClymont, R. Gersonde, G. H. Haug, *Science* **328**, 1550 (2010).

20. P. U. Clark *et al*., *Quat. Sci. Rev.* **25**, 3150 (2006).
21. D. S. Kaufman, J. Brigham-Grette, *Quat. Sci. Rev.* **12**, 21 (1993).
22. G. H. Miller *et al*., *Quat. Sci. Rev.* **29**, 1679 (2010).
23. E. J. Colville *et al*., *Science* **333**, 620 (2011).
24. E. Willerslev *et al*., *Science* **317**, 111 (2007).
25. M. E. Raymo, J. X. Mitrovica, *Nature* **483**, 453 (2012).
26. A. de Vernal, C. Hillaire-Marcel, *Science* **320**, 1622 (2008).
27. G. A. Milne, J. X. Mitrovica, *Quat. Sci. Rev.* **27**, 2292 (2008).
28. P. E. Tarasov *et al*., *Earth Sci. Rev.* **108**, 64 (2011).
29. A. A. Prokopenko *et al*., *Clim. Past* **6**, 31 (2010).
30. R. Stein, J. Hefter, J. Grützner, A. Voelker, B. D. A. Naafs, *Paleoceanography* **24**, PA2203 (2009).
31. E. Gischler, R. N. Ginsburg, J. O. Herrle, S. Prasad, *Sedimentology* **57**, 1049 (2010).
32. P. J. Fawcett *et al*., *Nature* **470**, 518 (2011).
33. R. P. Scherer *et al*., *Geophys. Res. Lett.* **35**, L03505 (2008).
34. P. Maiorano, M. Marino,].-A. Flores, *Mar. Micropaleontol.* **71**, 166 (2009).
35. T. Naish *et al*., *Nature* **458**, 322 (2009).
36. J. Brigham-Grette, L. D. Carter, *Arctic* **43**, 74 (1992).
37. G. A. Goodfriend, J. Brigham-Grette, G. H. Miller, *Quat. Res.* **45**, 176 (1996).
38. S. A. Elias, J. V. Matthews Jr., *Can. J. Earth Sci.* **39**, 911 (2002).
39. S. Funder *et al*., *Bull. Geol. Soc. Den.* **48**, 177 (2001).
40. Q. Z. Yin, A. Berger, *Clim. Dyn.* **36**, 1 (2011).
41. B. Hönisch, N. G. Hemming, D. Archer, M. Siddall, J. F. McManus, *Science* **324**, 1551 (2009).
42. R. M. DeConto, D. Pollard, D. Kowalewski, *Global Planet. Change* **88-89**, 45 (2012).
43. B. L. Otto-Bliesner *et al*., *Science* **311**, 1751 (2006).
44. S. J. Koenig, R. M. DeConto, D. Pollard, *Clim. Dyn.* **37**, 1247 (2011).
45. D. Pollard, R. M. DeConto, *Nature* **458**, 329 (2009).
46. R. McKay *et al*., *Quat. Sci. Rev.* **34**, 93 (2012).
47. A. Foldvik, *J. Geophys. Res.* **109**, C02015 (2004).
48. I. R. Hall, I. N. McCave, N. J. Shackleton, G. P. Weedon, S. E. Harris, *Nature* **412**, 809 (2001).
49. E. D. Galbraith *et al*., *Nature* **449**, 890 (2007).
50. G. H. Haug, M. A. Maslin, M. Sarnthein, R. Stax, R. Tiedemann, *Proc. ODP Sci. Results* **145**, 293 (1995).
51. S. L. Jaccard, E. D. Galbraith, D. M. Sigman, G. H. Haug, *Quat. Sci. Rev.* **29**, 206 (2010).
52. C. J. Mock, P. J. Bartlein, P. A. Anderson, *Int. J. Climatol.* **18**, 1085 (1998).
53. J. P. Helmke, H. A. Bauch, *Paleoceanography* **18**, 1036 (2003).
54. R. A. Woodgate, T. Weingartner, R. Lindsay, *Geophys. Res. Lett.* **37**, L01602 (2010).
55. L. Polyak, M. Jakobsson, *Oceanography* **24**, 52 (2011) and references therein.
56. M. New, D. Lister, M. Hulme, I. Makin, *Clim. Res.* **21**, 1 (2002).

Acknowledgments: Drilling operations were funded by the ICDP, the NSF, the German Federal Ministry of Education and Research (BMBF), Alfred Wegener Institute and Helmholtz Centre Potsdam (GFZ), the Russian Academy of Sciences Far East Branch, the Russian Foundation for Basic Research, and the Austrian Federal Ministry of Science and Research. The Russian Global Lake Drilling 800 drilling system was developed and operated by DOSECC. We thank all participants of the expedition for their engagement during recovery of the ICDP 5011-1 cores. Funding of core analyses was provided by BMBF (grant 03G0642), German Research Foundation (Deutsche Forschungsgemeinschaft, grants ME 1169/21 and ME 1169/24), the NSF (grant 0602471), Vetenskapsrådet, The Swedish Research Council, the Kempe Foundation, and the Civilian Research and Development Foundation (grant RUG1-2987-MA-10). We thank N. Mantke, A. Shahnazarian, and numerous students (Univ. of Cologne) for their competent help in core processing; T. Matrosova for contributing modern surface pollen data; and R. McKay for providing a modified lithological log of the ANDRILL 1B record. We also thank four anonymous reviewers for supportive and constructive comments that greatly improved the manuscript. The data reported in this paper are available in the databases of PANGAEA via www.pangaea.de (DOI: 10.1594/PANGAEA.783305) and of the U.S. National Climatic Data Center via www.ncdc.noaa.gov/paleo/paleolim/paleolim_data.html.

Supplementary Materials

www.sciencemag.org/cgi/content/full/science.1222135/DC1
Materials and Methods
Supplementary Text
Figs. S1 to S6
Tables S1 to S5
References (*57*–*106*)

19 March 2012; accepted 1 June 2012
Published online 21 June 2012;
10.1126/science.1222135

REPORTS

Imaging the Impact of Single Oxygen Atoms on Superconducting $Bi_{2+y}Sr_{2-y}CaCu_2O_{8+x}$

Ilija Zeljkovic,[1] Zhijun Xu,[2] Jinsheng Wen,[2] Genda Gu,[2] Robert S. Markiewicz,[3] Jennifer E. Hoffman[1]*

High-temperature cuprate superconductors display unexpected nanoscale inhomogeneity in essential properties such as pseudogap energy, Fermi surface, and even superconducting critical temperature. Theoretical explanations for this inhomogeneity have ranged from chemical disorder to spontaneous electronic phase separation. We extend the energy range of scanning tunneling spectroscopy on $Bi_{2+y}Sr_{2-y}CaCu_2O_{8+x}$, allowing a complete mapping of two types of interstitial oxygen dopants and vacancies at the apical oxygen site. We show that the nanoscale spatial variations in the pseudogap states are correlated with disorder in these dopant concentrations, particularly that of apical oxygen vacancies.

Many of today's prominent materials, such as high–transition temperature (T_c) superconductors, doped semiconductors, and colossal magnetoresistance materials, are nonstoichiometric and electronically inhomogeneous at the nanoscale (*1*). Both desirable and undesirable electronic properties may arise from chemical inhomogeneity. To fully understand and harness these materials, and to drive the discovery of new materials, it is crucial to understand the impact of single atoms on these inhomogeneous electronic states.

Cuprate superconductors are quasi–two-dimensional (2D) materials that arise from off-stoichiometric doping of a Mott insulator by oxygen intercalation and/or cation substitution. Nanoscale electronic inhomogeneity in the cuprates has been predicted (*2*, *3*) and detected (*4*–*7*), but the roles of spontaneous electronic phase separation (*2*) and chemical disorder (*3*) are unresolved. Scanning tunneling microscopy (STM) has thus far lacked the necessary energy range to image the full set of relevant dopants. We present atomically resolved STM spectroscopy on $Bi_{2+y}Sr_{2-y}CaCu_2O_{8+x}$ (BSCCO) that doubles the energy range of previous work (*8*) and demonstrates the impact of single dopant atoms on electronic states.

In BSCCO, a prominent gap in the density of states shows energy variation of ~100%, on a 2- to 3-nm length scale, across a wide range of doping (*9*). Recent studies (*10*, *11*) suggest that this spectral inhomogeneity results primarily from variations in the pseudogap (PG), a depression in the density of states near the Fermi level ε_F that persists far above the superconducting T_c, most dominantly on the underdoped side of the phase diagram. Nanoscale variation in the PG offers the opportunity to uncover the variable(s) determining its local strength, thus setting the stage for control of this mysterious phase, whose energy scale anticorrelates with superconductivity (*12*, *13*) and which many believe is a competitor to superconductivity (*11*, *14*).

Several previous studies searched for chemical origins of spectral gap variation in BSCCO. Kinoda *et al*. observed atomic defects in Pb-doped BSCCO with resonance energy +1.7 eV, identified as Bi^{3+} substitutions at the Sr^{2+} site (*15*). These defects may correlate weakly with regions of large PG, but no quantitative analysis was presented (*16*). McElroy *et al*. observed localized conductance signatures in BSCCO at −0.96V, identified as interstitial oxygen dopants (*8*), but several mysteries were left unresolved. First, the counted oxygen fell ~50% short of the expected density for each T_c (*17*). Second, the correlation

[1]Department of Physics, Harvard University, 17 Oxford Street, Cambridge, MA 02138, USA. [2]Condensed Matter Physics and Materials Science Department, Brookhaven National Laboratory, Upton, NY 11973–5000, USA. [3]Department of Physics, Northeastern University, 360 Huntington Avenue, Boston, MA 02115, USA.

*To whom correspondence should be addressed: jhoffman@physics.harvard.edu

between oxygen locations and PG was weak and of unexpected sign: Although it is well established that globally increasing oxygen content correlates with decreasing PG (*12*, *13*), McElroy found that the oxygen dopant locations were weakly correlated with regions of increased gap.

To resolve the latter issue, one carefully tuned theory suggested that the dominant local effect of interstitial oxygens may be strain, which increases the local pairing strength (*18*, *19*). A second proposal by Zhou *et al*. (*20*) explained both the missing oxygen and the counterintuitive correlation by postulating the existence of two types of interstitial oxygen dopants: "type-B" oxygens observed by McElroy, which live around the BiO plane and contribute only delocalized charge, and "type-A" oxygens, which live around the SrO plane and have an immediate electrostatic effect, locally hole-doping the adjacent CuO_2 layer. Therefore, Zhou *et al*. predicted that the type-A oxygens would follow the expected global trend: a strong anticorrelation with the PG. The weak correlation observed between McElroy's type-B oxygens and the PG could be explained as a side effect of slight repulsion between type-B and type-A oxygens. (See additional discussion in supplementary materials, section I.) However, the type-A oxygens were predicted to have resonances even farther below ε_F than the –0.96-V type Bs. This experimental challenge has prevented their observation to date.

We set out to observe the high-energy dopants and elucidate their role in cuprate inhomogeneity. BSCCO was grown with a floating zone technique. As is common to facilitate the growth process, the starting composition for all crystals studied here contained Bi:Sr in a ratio 2.1:1.9. By some combination of cation substitution and oxygen intercalation, as-grown crystals tended to be optimally doped with $T_c \sim 91$ K. Some samples were then annealed at 550°C in vacuum to remove oxygen and reduce T_c toward the underdoped side of the phase diagram. We present STM data from four samples with decreasing oxygen content and $T_c = 91$, 82, 68, and 55 K. The samples were cleaved in cryogenic ultra-high vacuum and immediately inserted into our home-built STM, where they were imaged at $T = 6$ K.

Figure 1A shows a topography of the BiO surface of BSCCO with $T_c = 55$ K, demonstrating atomic resolution at +1 V bias. Figure 1B shows the local differential tunneling conductance $g(\vec{r}, V = -1\text{V})$ (where r is the local position and V is voltage), approximately proportional to the local density of states at –1 eV, acquired over the same area as Fig. 1A, containing atomic-scale features of similar form and concentration to the previously observed type-B oxygen dopants (*8*). Figure 1C extends the energy range down to show $g(\vec{r}, V = -1.5\text{ V})$, resolving a second set of atomic-scale features presumed to be the predicted type-A interstitial oxygen dopants (*20*). Figure 1D extends the energy range up to show $g(\vec{r}, V = +1\text{V})$, revealing a third set of atomic-scale features. We observe no other distinct atomic-scale features in $g(\vec{r}, V)$ images at biases between –2 V and +1.6 V.

To clarify the identity of these three features, we repeat the same measurements on four different samples and show the density of each type of dopant versus T_c in Fig. 1E. As expected, we observe a monotonic decrease in the number of both types of interstitial oxygen dopants with falling T_c. However, the +1 V features increase from virtually zero for optimally doped BSCCO to almost 1% per CuO_2 plaquette for the $T_c = 55$ K sample. Previous studies detected no change in cation concentration on annealing up to 840°C (*21*), so our observed increasing concentration after 550°C vacuum annealing suggests oxygen-site vacancies instead. There are three distinct oxygen lattice sites, but because the +1 V features

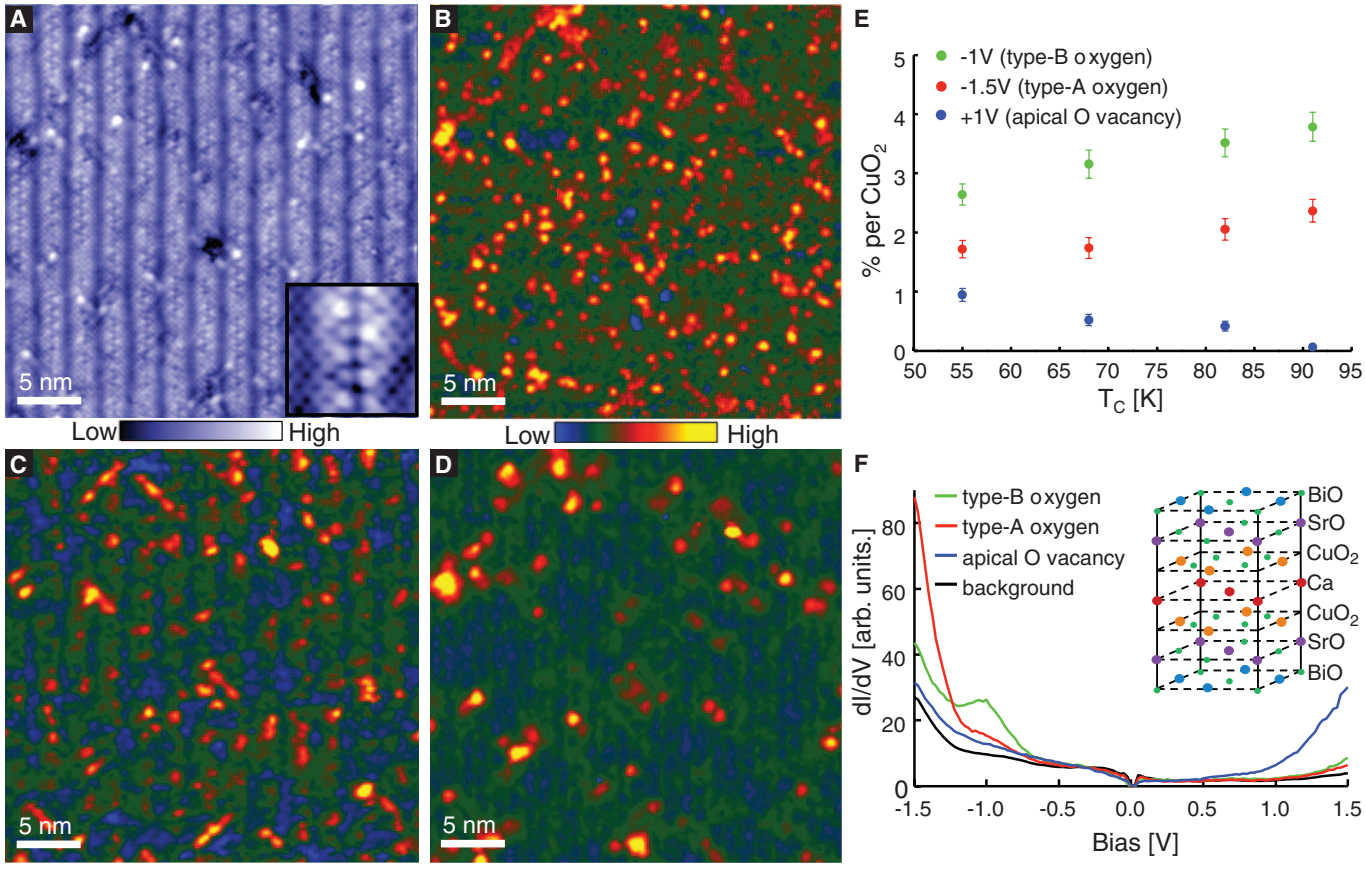

Fig. 1. (**A**) Atomically resolved topographic image of BSCCO with T_c = 55 K, acquired at V_{sample} = +1 V and setpoint current I = 150 pA over a 35-nm area (inset, 3× magnification). (**B** to **D**) Differential conductance (dI/dV) images in the same area as (A), acquired at V_{sample} = –1, –1.5, and +1 V, respectively. (**E**) Density of each type of dopant imaged within the four samples studied. (**F**) dI/dV spectra over each dopant type, from the T_c = 82 K sample. Each colored spectrum is the average of all imaged dopants of its type within a 30-nm field of view; the black trace shows the average spectrum far from dopants. (Inset) Top half of the BSCCO unit cell.

are laterally aligned with the Bi site, we identify them as missing apical oxygen atoms in the SrO layer (see supplementary materials, section II).

Typical differential conductance spectra at each of the three types of dopants, and the background, are shown in Fig. 1F. The defining features used to identify the impurities, such as the peak around –1 V for a type-B oxygen, and the sudden changes of the slope around –1.2 V and +0.8 V for type-A oxygen and apical oxygen vacancy, respectively, are robust for different set-up conditions, locations, and samples (fig. S4).

We investigated the relationship of these dopants to the inhomogeneous PG. Figure 2, A to C shows the three types of dopants (two interstitials and one vacancy), superimposed on a PG map acquired for the T_c = 55 K sample (see supplementary materials, section IV for details of PG determination). Any correlation between type-B oxygens and PG is too weak to be seen by the naked eye. In contrast to Zhou's prediction, the type-A oxygens are correlated with regions of large PG. One immediately sees the strongest correlation between apical oxygen vacancies and PG. Figure 2D shows the cross-correlations between the positions of the dopant atoms and the corresponding gap map. Figure 2E shows the average PG as a function of distance from the nearest dopant. This behavior is consistent across the three underdoped samples studied (see supplementary materials, section V).

We examined more carefully the surprising departure from Zhou's prediction in Fig. 3, which plots the local PG energy versus the local concentration of each dopant type. For the type-B interstitial oxygens in Fig. 3A, the local trend within each sample shows correlation between increased local oxygen concentration and increased local PG; the global trend between samples shows anticorrelation between global oxygen concentration and global PG. In contrast to Zhou's prediction, Fig. 3B shows that a qualitatively similar juxtaposition of local and global trends holds for the type-A interstitial oxygens in the three underdoped samples. However, Fig. 3C shows excellent alignment of local and global trends for the correlation between apical oxygen vacancy density and PG. This suggests that, in underdoped samples, variations in the local hole concentration, and thus the local PG, are governed primarily by the local removal of holes by apical oxygen vacancies, rather than the strain or the donation of localized holes from the interstitial oxygens.

The interstitial oxygens, previously predicted (*3*) to determine the local gap, do contribute de-

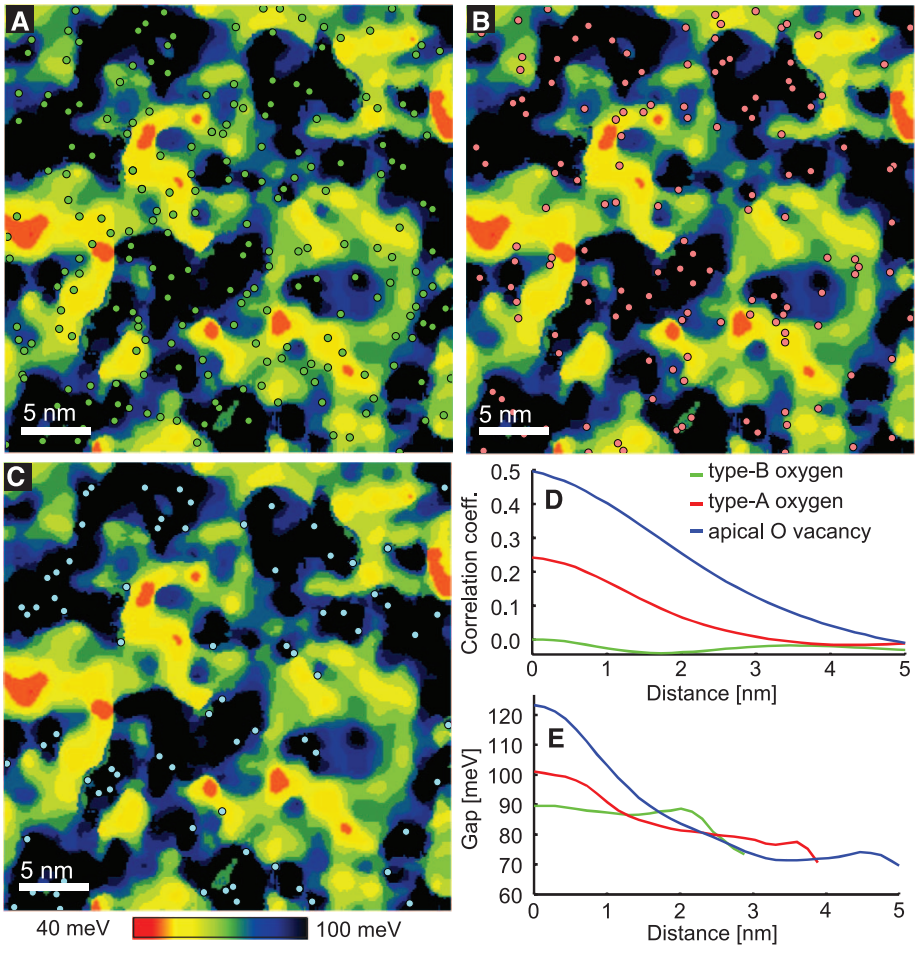

Fig. 2. Comparison of dopant locations and PG map. Locations of (**A**) type-B interstitial oxygens (green circles), (**B**) type-A interstitial oxygens (red circles), and (**C**) apical oxygen vacancies (blue circles) superimposed on top of the PG map of the T_c = 55 K sample. (**D**) Cross-correlation coefficient relating the PG to the distance to the nearest dopant. (**E**) Average PG versus distance from the nearest dopant of each type. In (D) and (E), green, red, and blue lines represent type-B oxygens, type-A oxygens, and apical oxygen vacancies, respectively.

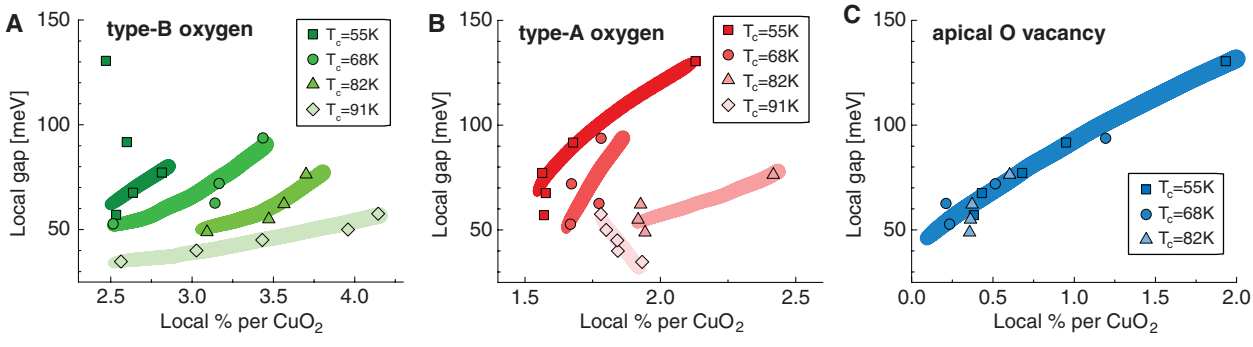

Fig. 3. Local PG versus local dopant density. For each sample, we create a local density map of the number of a given dopant type per region of radius ξ ~ 2 nm. The values in the density map are then binned based on the PG value at the corresponding pixel. The average PG value in each bin is then plotted versus the average dopant density value within each bin. (**A**) Local PG versus local density of type-B interstitial oxygen dopants, from the four different samples used in this study. (**B**) Local PG versus local density of type-A interstitial oxygen dopants, from the four different samples used in this study. (**C**) Local PG versus local density of apical oxygen vacancies, from the three underdoped samples used in this study. Trend lines in (A) to (C) are guides to the eye.

localized holes, but in underdoped samples even the type-A interstitial oxygen positions remain correlated to regions of decreased local hole concentration, likely due to a tendency to remain close to the apical oxygen vacancies. In the optimally doped sample, the apical oxygen vacancy concentration is negligible, so the local hole concentration may be set by the next-closest dopant to the CuO_2 plane, the type-A interstitial oxygen, as predicted by Zhou *et al*. (*20*). Indeed, Fig. 3B shows that the local PG decreases with increasing local type-A concentration in the $T_c = 91$ K sample. We therefore reconcile the apparent contradiction between the global (*12*, *13*) and local (*7*, *8*) doping trends for both types of interstitial oxygens.

Does dopant inhomogeneity cause PG inhomogeneity or merely pin intrinsic inhomogeneity, caused perhaps by strong correlations? Because the 2- to 3-nm length scale of PG inhomogeneity remains the same across a wide range of dopant concentrations (fig. S7A, inset), intrinsic PG inhomogeneity seems plausible. However, our experiment shows clearly that the dopant locations that are fixed at high T, particularly the apical oxygen vacancies, do govern the local PG strength that is subsequently determined on cooling through the PG transition temperature T^*.

Our experiment directly measures the strong correlation between apical oxygen vacancies and the PG, but is there a relationship between apical oxygens and superconductivity itself? In fact, apical oxygen effects may be credited for the discovery of high-T_c superconductivity, as Müller was originally driven to explore the LaBaCuO system by the expectation of strong electron-phonon coupling due to the Jahn-Teller effect in the CuO_6 octahedral environment, specifically the displacement of the Cu-apical-O bond (*22*). However, subsequent isotope effect measurements suggested that any phonon contribution to superconductivity is dominated by CuO_2 plane oxygen (*23*). We conjecture that the apical oxygen vacancies influence the superconductivity indirectly in underdoped samples by reducing the local hole concentration, which locally strengthens the PG, tying up antinodal states (*11*, *14*), and locally decreasing the Fermi level carriers that would otherwise be available for coherent pairing. Calculations also showed a correlation between T_c and apical oxygen height and emphasized the importance of the axial orbital for the hopping and phase coherence necessary for superconductivity (*24*, *25*). Thus, apical oxygen vacancies may lower the local superconducting T_c and/or critical current J_c.

Another manifestation of electronic inhomogeneity is a disordered "checkerboard" (CB) modulation of the spectral weight that is static but most noticeable at energies within and near the PG energy. Field (*26*), doping (*9*), and temperature (*27*) dependence suggest that the CB is in fact the electronic ordered phase associated with the PG. The CB wave vector tracks the antinodal nesting wave vector across a wide range of doping (*28*). A closely related disordered periodic inhomogeneity arises from elastic scattering between degenerate states; this dispersing quasiparticle interference (QPI) may exist at similar wave vectors to the static CB, but only at a limited range of energies within the superconducting gap (*29*).

It was previously claimed that type-B oxygen dopants are found in the minima of the QPI patterns (*8*), at both positive and negative energies. However, QPI has opposite spatial phase for filled and empty states (*30*), suggesting that the previously observed correlation (*8*) relates instead to the CB. Figure 4A shows the distribution of the three types of observed atomic dopants on top of a filtered $g(\vec{r}, V = 36\ \mathrm{mV})$ image (figs. S10 to S12). A histogram of the distance from each dopant to the center of the nearest "checker" (Fig. 4B) demonstrates the strong tendency of apical oxygen vacancies to lie in the peaks of the imaged CB and weaker tendency for interstitial oxygen dopants to lie in the troughs. We therefore conclude that the apical oxygen vacancies play the primary role in pinning the CB.

Our high-bias atomically resolved STM results suggest a possible route to increase T_c in BSCCO: underdope to increase the pairing potential (*31*) but explore different annealing recipes to allow interstitial oxygen removal without creating apical oxygen vacancies, the defects most favorable to the PG and possibly competitive to superconductivity. Recently, a ~15% increase in maximum T_c has been predicted from alternate dopant arrangements (*32*). Our spectroscopy methods may also prove useful in future studies of the effects of single-atom impurities in other fragile quasi-2D materials.

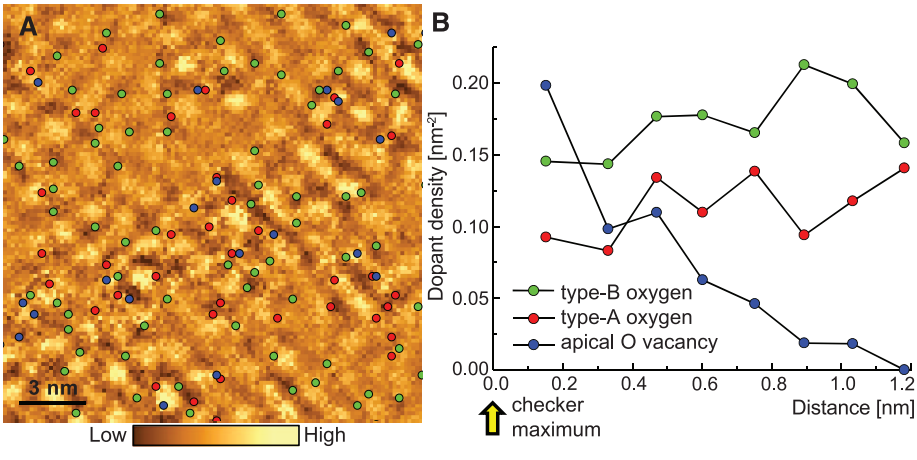

Fig. 4. Comparison of dopant locations and the checkerboard. (**A**) Fourier-filtered dI/dV image of the T_c = 55 K sample at +36 mV, showing a clear CB (setup: $V_{sample} = -150$ mV; $I = 800$ pA). Type-B oxygens, type-A oxygens, and apical oxygen vacancies are superimposed as green, red, and blue circles, respectively. (**B**) Dopant density of each type versus distance from the center of the nearest CB maximum.

References and Notes

1. E. Dagotto, *Science* **309**, 257 (2005).
2. V. J. Emery, S. A. Kivelson, O. Zachar, *Phys. Rev. B* **56**, 6120 (1997).
3. I. Martin, A. Balatsky, *Physica C* **357-360**, 46 (2001).
4. S.-H. Pan *et al*., *Nature* **413**, 282 (2001).
5. K. M. Lang *et al*., *Nature* **415**, 412 (2002).
6. K. K. Gomes *et al*., *Nature* **447**, 569 (2007).
7. W. D. Wise *et al*., *Nat. Phys.* **5**, 213 (2009).
8. K. McElroy *et al*., *Science* **309**, 1048 (2005).
9. K. McElroy *et al*., *Phys. Rev. Lett.* **94**, 197005 (2005).
10. M. C. Boyer *et al*., *Nat. Phys.* **3**, 802 (2007).
11. A. Pushp *et al*., *Science* **324**, 1689 (2009).
12. G. Deutscher, *Nature* **397**, 410 (1999).
13. S. Hüfner, M. A. Hossain, A. Damascelli, G. A. Sawatzky, *Rep. Prog. Phys.* **71**, 062501 (2008).
14. T. Kondo, R. Khasanov, T. Takeuchi, J. Schmalian, A. Kaminski, *Nature* **457**, 296 (2009).
15. G. Kinoda *et al*., *Phys. Rev. B* **71**, 020502 (2005).
16. G. Kinoda, T. Hasegawa, *Phys. Rev. B* **67**, 224509 (2003).
17. M. Presland, J. Tallon, R. Buckley, R. Liu, N. Flower, *Physica C* **176**, 95 (1991).
18. T. S. Nunner, B. M. Andersen, A. Melikyan, P. J. Hirschfeld, *Phys. Rev. Lett.* **95**, 177003 (2005).
19. W. Chen, M. Gabay, P. J. Hirschfeld, *New J. Phys.* **14**, 033004 (2012).
20. S. Zhou, H. Ding, Z. Wang, *Phys. Rev. Lett.* **98**, 076401 (2007).
21. D. B. Mitzi, L. W. Lombardo, A. Kapitulnik, S. S. Laderman, R. D. Jacowitz, *Phys. Rev. B Condens. Matter* **41**, 6564 (1990).
22. J. G. Bednorz, K. A. Müller, *Zeitschrift für Physik B* **64**, 189 (1986).
23. D. Zech *et al*., *Nature* **371**, 681 (1994).
24. Y. Ohta, T. Tohyama, S. Maekawa, *Phys. Rev. B Condens. Matter* **43**, 2968 (1991).
25. E. Pavarini, I. Dasgupta, T. Saha-Dasgupta, O. Jepsen, O. K. Andersen, *Phys. Rev. Lett.* **87**, 047003 (2001).
26. J. E. Hoffman *et al*., *Science* **295**, 466 (2002).
27. C. V. Parker *et al*., *Nature* **468**, 677 (2010).
28. Y. Kohsaka *et al*., *Nature* **454**, 1072 (2008).
29. J. E. Hoffman *et al*., *Science* **297**, 1148 (2002).
30. T. Hanaguri *et al*., *Nat. Phys.* **3**, 865 (2007).
31. E. Berg, D. Orgad, S. Kivelson, *Phys. Rev. B* **78**, 094509 (2008).
32. L. Goren, E. Altman, *Phys. Rev. B* **84**, 094508 (2011).

Acknowledgments: We thank A. Bansil, I. Bozovic, S. Davis, E. Hudson, P. Hirschfeld, A. Kapitulnik, D.-H. Lee, and J. Nieminen for useful discussions. J.E.H. acknowledges support from the NSF CAREER grant DMR-0847433 and AFOSR PECASE grant FA9550-06-1-0531. G.D.G. acknowledges support from the U.S. Department of Energy (DOE) under contract DE-AC02-98CH10886. R.S.M. acknowledges support from the DOE under contract DE-FG02-07ER46352.

Supplementary Materials

www.sciencemag.org/cgi/content/full/337/6092/320/DC1
Materials and Methods
Supplementary Text
Figs. S1 to S12
References (*33*–*52*)

3 January 2012; accepted 29 May 2012
10.1126/science.1218648

Spin-Transistor Action via Tunable Landau-Zener Transitions

C. Betthausen,[1] T. Dollinger,[2] H. Saarikoski,[2] V. Kolkovsky,[3] G. Karczewski,[3] T. Wojtowicz,[3] K. Richter,[2] D. Weiss[1]*

Spin-transistor designs relying on spin-orbit interaction suffer from low signal levels resulting from low spin-injection efficiency and fast spin decay. Here, we present an alternative approach in which spin information is protected by propagating this information adiabatically. We demonstrate the validity of our approach in a cadmium manganese telluride diluted magnetic semiconductor quantum well structure in which efficient spin transport is observed over device distances of 50 micrometers. The device is turned "off" by introducing diabatic Landau-Zener transitions that lead to a backscattering of spins, which are controlled by a combination of a helical and a homogeneous magnetic field. In contrast to other spin-transistor designs, we find that our concept is tolerant against disorder.

The use of electron spin to store and process information calls for the ability to inject, propagate, and manipulate spin with high efficiency (*1*, *2*). Much of the recent research in the field has been motivated by attempts to realize the seminal spin transistor proposed by Datta and Das (*3*). Their original concept requires spin injection from ferromagnetic contacts into a narrow channel of a two-dimensional electron gas (2DEG), where transport is ballistic and spins precess in a gate-controlled spin-orbit field into "on" or "off" orientations. Even though such spin manipulation in a spin-orbit field has been demonstrated in a nonlocal measurement (*4*), signal levels remain small as a result of low spin-injection efficiency and limited spin lifetime. The latter can be enhanced if spin polarization is protected against scattering processes by an SU(2) symmetry that emerges when the Rashba spin-orbit interaction strength is equal to the Dresselhaus term (*5*, *6*). This creates a persistent spin-helix state (*6*) that has been observed in optical measurements (*7*). Aside from 2D systems, spin-transistor action was also explored in bulk bipolar semiconductors (*8*, *9*).

Here, we present an alternative efficient spin-transistor design that uses adiabatic spin propagation to protect spin information and tunable diabatic Landau-Zener transitions between spin eigenstates for spin-transmission control (Fig. 1). According to the adiabatic theorem of quantum mechanics (*10*), a spin that is initially in an eigenstate will remain in its instantaneous eigenstate during transport if external perturbations act on it slowly. Spin information is hence protected against decay, allowing spin to propagate over device distances of several micrometers. For rapidly changing perturbations, spin cannot adapt its state, which becomes a superposition of eigenstates. This causes diabatic Landau-Zener transitions between the spin eigenstates (*11*, *12*), which can be used to selectively backscatter spin-polarized charge carriers, thus giving rise to transistor action.

We demonstrate the validity of our approach in a (Cd,Mn)Te diluted magnetic semiconductor quantum-well (QW) structure in which the giant Zeeman splitting, attributed to *s-d* exchange interaction between electronic states and the localized Mn spins (*13*), gives rise to intrinsic spin polarization. We modulate the diabatic spin-backscattering probability by a combination of a spatially rotating magnetic field $\mathbf{B}_s$ and a homogenous magnetic field $\mathbf{B}$. $\mathbf{B}_s$ is created by premagnetized ferromagnetic stripes placed above the device (Fig. 2, A and D). In the absence of the homogeneous field, eigenfunctions change slowly, leading to adiabatic spin transport and a helical spin wave resulting from U(1) symmetry. If scattering is spin-independent, spin orientation depends only on the position along the transport direction and not on the specific path of the spin: the device is in its on state. However, if the helical field component is equal in amplitude to the homogeneous component, diabatic transitions and backscattering of spin occur. Consequently, the device is in the off state. As in the original Datta-Das concept, we measure the source-drain resistance, which intensifies as the spin-backscattering rate is increased. The degree of adiabaticity is therefore monitored electrically in the channel resistance, in contrast to interference measurements (*14*, *15*) of geometrical (Berry) phases (*16*), associated with adiabatic spin evolution only.

Our setup consists of three building blocks: (i) a high-mobility 2DEG with a giant Zeeman splitting, (ii) a grating of ferromagnetic stripes on top of the sample (Fig. 2, A and D), and (iii) a homogeneous B field generated by a superconducting coil. A modulation doped (Cd,Mn)Te quantum-well structure (*17*, *18*) is used to confine electrons to two dimensions. The ferromagnetic grating is made of 75-nm-thick dysprosium stripes patterned to periods a ranging from 0.5 to 8 μm. The stripes are premagnetized in a field of 8 T, which gives rise to a remnant magnetization of 0.7×10^6 A/m, determined by superconducting quantum interference device (SQUID) measurements. In the plane of the 2DEG, the stray field of the periodic grating of magnets is approximately helical with an amplitude of ~50 mT (Fig. 2B). The magnetic field texture translates to a helical spin polarization via the giant Zeeman coupling. In our devices, we use the beating pattern of the Shubnikov–de Haas oscillations at low fields (Fig. 2E) to estimate a Zeeman splitting of 1 meV for a 50-mT stray field at 25 mK (*18*, *19*). The Zeeman energy E_Z is the largest spin-dependent energy scale; Rashba and Dresselhaus spin-orbit splittings are more than one order of magnitude smaller (*20*). Spin polarization $p = (n_\downarrow - n_\uparrow)/(n_\uparrow + n_\downarrow) \approx E_Z/2E_F$ in the 2DEG ranges from 8 to 15% in a 50-mT stray field for our samples (Fig. 2, C and D). Here, $n_{\uparrow,\downarrow}$ denotes the density of spin-up/down electrons; E_F is the Fermi energy.

To measure the longitudinal resistance $\rho_{xx}(B)$ in a Hall bar geometry, the magnetic field is first ramped up to 8 T under an angle θ (Fig. 2A) to magnetize the stripes, and then data are taken on the sweep back to –0.5 T. In the presence of a helical stray field, $\rho_{xx}(B)$ shows distinct peaks at about ±50 mT (Fig. 2, E and F) for the studied devices A, B, and C (fig. S1). The samples differ in QW thickness, carrier density, electron mobility, and Mn concentration (table S1), but the results are independent of such details. The peaks do not appear in unmodulated reference samples. Apart from a small dip near $B = 0$, reminiscent of weak antilocalization (black traces in Fig. 2F), these samples do not show any notable

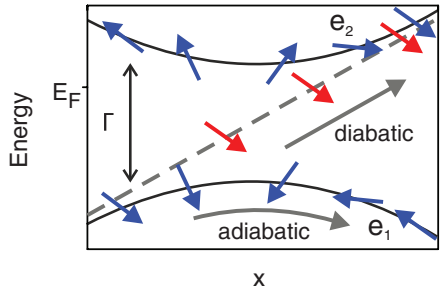

Fig. 1. Spin-transistor action via tunable diabatic transitions in a system of two orthogonal spin-eigenstates e_1 and e_2 (blue arrows) with energy separation Γ at the closest approach. A spin that is transported along a spatial coordinate x through the system, starting from e_1, will remain in this instantaneous eigenstate if evolution (here defined as rotation of eigenstate spin orientation) is slow in the reference frame of the spin (small dx/dt). In a fast evolution (large dx/dt), spin cannot adapt to the changing environment, leading to a diabatic evolution (red arrows) corresponding to a Landau-Zener transition to e_2. The e_2 state lies above E_F, causing wave-function decay and spin backscattering. Spin-transistor action involves either tuning Γ or dx/dt.

[1]Department of Experimental and Applied Physics, Regensburg University, 93040 Regensburg, Germany. [2]Department of Theoretical Physics, Regensburg University, 93040 Regensburg, Germany. [3]Institute of Physics, Polish Academy of Sciences, 02668 Warsaw, Poland.

*To whom correspondence should be addressed. E-mail: dieter.weiss@physik.uni-regensburg.de

features at low B. The ρ_{xx} peaks in the modulated samples vanish rapidly with increasing temperature T and are no longer recognizable above ~0.6 K (Fig. 3A). This behavior, confirmed by full numerical transport calculations in Fig. 3B (*18*), is expected for the spin polarization of (Cd,Mn)Te, as the dominant *s-d* exchange part in the g factor contributes appreciably only at low T. Because of their orbital nature, magnetic commensurability effects persist to much higher T (~40 K) (*21*) and can therefore be excluded. Hence, the T dependence of the peaks confirms a spin-related effect.

The ρ_{xx} peaks reflect reduced spin transmission through the 2DEG channel, which can be intuitively explained within the following model: Due to the high mobility of our samples, let us assume that the spin transport is ballistic on the scale of the period of the Dy grating. Figure 2C shows the Zeeman-split subbands of a 2DEG. At E_F there is an imbalance of spin states moving in the x direction because some of the occupied spin-split modes exhibit unoccupied counterparts above E_F. For a Zeeman-split state pair close to E_F, the upper state (solid blue line in Fig. 2C) is unoccupied, whereas the lower state (solid red line) is occupied and carries spin. Assuming a helical stray field (*22*, *23*) with amplitude B_s, the total magnetic field, $\mathbf{B} + \mathbf{B_s(x)}$, gives rise to a Zeeman splitting $E_{Z,\pm(x)} = \pm\frac{1}{2} g_{\mathrm{eff}} \mu_B B_s \sqrt{1 + \gamma^2 + 2\gamma\cos(2\pi x/a)}$, where $\gamma = B/B_s$, g_{eff} is the (giant) effective g factor of (Cd,Mn)Te, and μ_B is Bohr's magneton.

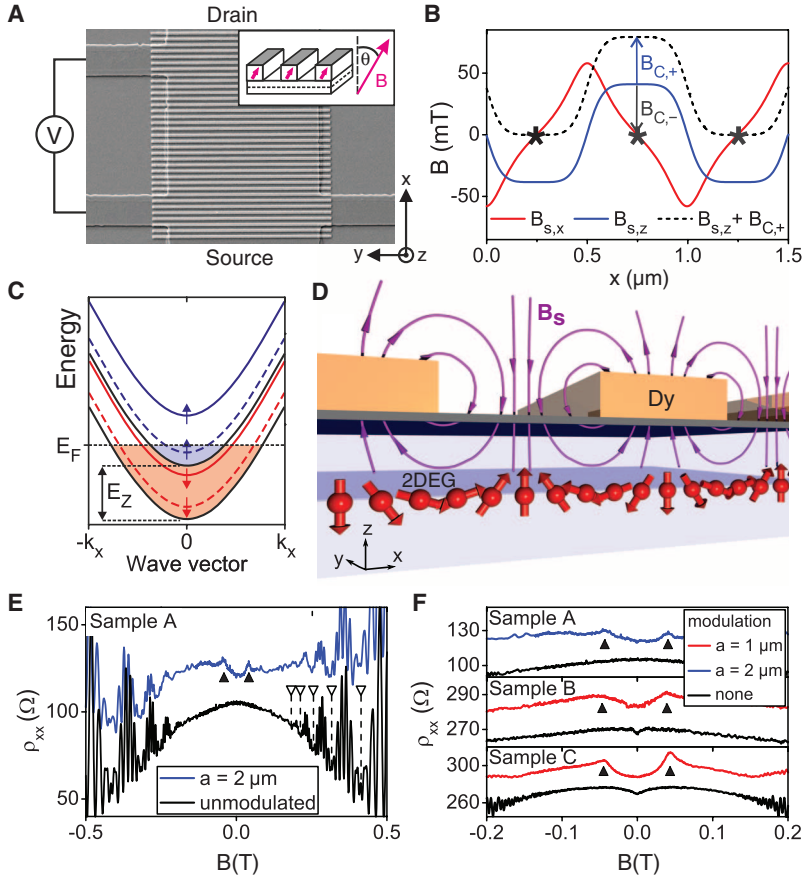

Fig. 2. (**A**) Electron micrograph of a Hall-bar segment covered with Dy stripes. (Inset) Orientations of the external homogeneous B field and the magnetic moments of the premagnetized stripes (magenta arrows), defined by the tilt angle θ with respect to the z axis in the xz plane. (**B**) Calculated magnetic stray-field components $B_{s,x}$ (red) and $B_{s,z}$ (blue) in the plane of the 2DEG for sample C with a grating of a = 1 μm. $B = B_{C,+}$ and $B = B_{C,-}$ denote the external field needed to generate points of vanishing total magnetic field (marked by asterisks) if the external field is applied in positive or negative z direction, respectively. (**C**) Schematic band structure of the (Cd,Mn)Te QW. Black solid lines, Zeeman-split spin-up and spin-down subbands for wave vectors in the y direction, $k_y = 0$; dashed lines, spin-split subbands for $k_y \neq 0$, but with spin-up and spin-down states occupied at E_F; colored solid lines, spin-split subbands for $k_y \neq 0$, but with an empty upper band. Only Landau-Zener transitions between filled and empty subbands contribute to spin backscattering. Spin-up and spin-down densities $n_\uparrow$ and $n_\downarrow$ are represented by blue and red areas, respectively. (**D**) In the adiabatic transport regime at $B = 0$, electron spins in the 2DEG (spheres with arrows) keep anti-aligned with the stray-field B_s of the stripes, and a spin-helix forms. (**E** and **F**) ρ_{xx} with and without modulation at T = 25 mK and θ = 0° (upper curves, shifted for clarity). Mn ions in the QW cause a distinct beating pattern with nodes (open triangles) at higher B (E). Resistance peaks (black triangles) are associated with blocking of spin transmission.

For one pair of spin-polarized states (that is, for fixed wave vector k_y), the total magnetic field, Zeeman-split energy levels, spin directions, and local energy bands are depicted in Fig. 3E (case $B = B_s/2$) and Fig. 3F ($B = B_s$). Because of the large Zeeman splitting associated with the stray field at $B = 0$, the Larmor frequency $\omega_L = g_{\mathrm{eff}}\mu_B B_s/\hbar$ (where $\hbar$ is Planck's constant h divided by 2π) is higher than the frequency of stripe modulation in a ballistic flight through the device $\omega_f = 2\pi v_{F,x}/a$ (where $v_{F,x} = \hbar k_x/m^*$ is the component of the Fermi velocity parallel to the transport direction, m^* is the effective mass of CdTe, and k_x is the wave vector in x direction). This keeps spin transport predominantly in the adiabatic regime, as expressed by the condition $Q = \omega_L/\omega_f > 1$, where Q is a measure of the degree of adiabaticity in ballistic systems (*16*, *24*, *25*). For $B = B_s$, a degeneracy point emerges in the energy bands midway between adjacent stripes, because the total magnetic field vanishes at those points (Figs. 2B and 3F). In the reference frame of the spin, the direction of the magnetic field first rotates continuously as it approaches the degeneracy point adiabatically, but then the field reverses direction. This violates the conditions for adiabaticity, because an instant 180° spin-rotation would be needed to stay on the lower band. Hence, a transition to the upper Zeeman band occurs close to the degeneracy. On the upper band the spin is parallel to the magnetic field, giving rise to a tunneling barrier because the potential energy rises above E_F; this leads to backscattering, and spin-transport is blocked, increasing the resistance of the sample. Only spin-polarized modes are affected by this blocking, because both spin bands of spin-compensated modes remain everywhere below E_F.

The probability of a diabatic transition to the upper Zeeman band is finite, even if there are no degeneracy points. Using Landau-Zener formalism, we show (*18*) that the spin-backscattering probability associated with a diabatic transition becomes increasingly probable as the distance between the Zeeman-split levels at the closest approach decreases or transport velocity $v_{F,x}$ increases (*11*, *12*, *26*). The periodic stripe grating forms a spatially repeating sequence of potential transition points that enhances the probability of a diabatic transition.

The actual stray-field profile of the magnetized stripes is anisotropic and only approximately helical (Fig. 2B). This provides an additional means to confirm that the ρ_{xx} peaks stem from spin-transmission blocking. To do that, we studied samples with different stripe periodicities a ranging from 0.5 to 8 μm (shown for θ = 45° in Fig. 3C) and measured $\rho_{xx}(B)$ at different tilt angles θ for a given value of a (shown for a = 1 μm in Fig. 3D). We calculated the stray field of the stripes within the dipole approximation for different values of θ and a, which gives the positions of the spin-blocking peaks as field values where zeros form in the total field. Our theoretical data are compared with the corresponding values

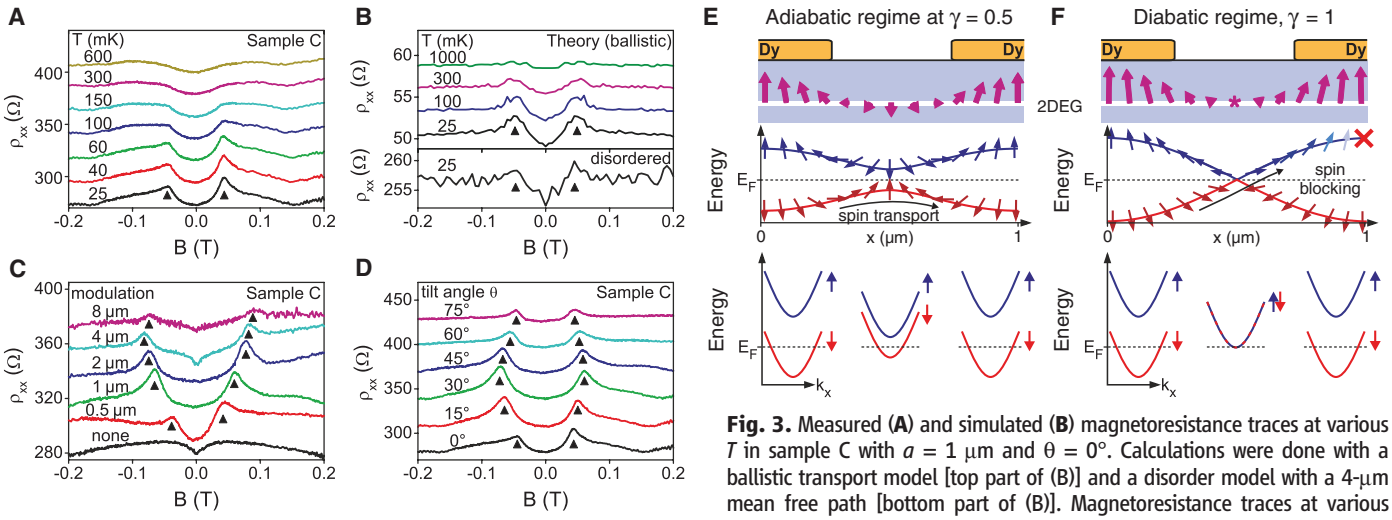

Fig. 3. Measured (**A**) and simulated (**B**) magnetoresistance traces at various T in sample C with a = 1 μm and θ = 0°. Calculations were done with a ballistic transport model [top part of (B)] and a disorder model with a 4-μm mean free path [bottom part of (B)]. Magnetoresistance traces at various periods a (**C**) and tilt angles θ (**D**) at 25 mK, θ = 45° in (C), and a = 1 μm in (D). All curves, except the lowest ones, in (A) to (D) are shifted for clarity. (**E** and **F**) Total magnetic field acting on an electron (top panels) and Zeeman-split energy-bands of a polarized state (middle panels) with spin-orientations (arrows) in the (E) adiabatic transport regime at $\gamma = B/B_s = {}^1/_2$ and in the (F) diabatic regime $\gamma = 1$. The x component of magnetic field reverses direction in the center at $\gamma = 1$, which leads to spin backscattering. (Bottom panels) Corresponding local Zeeman-split energy bands.

extracted for sample C in Fig. 4A (and for sample B in fig. S3) and show the expected anisotropy. Note that no fit parameters were used in the calculations.

In the ballistic model, all spin-polarized transport modes are blocked at $B = B_s$, increasing the resistance of the sample. A single degeneracy point in the Zeeman bands is sufficient to block all spin transmission; hence, the peak height does not depend on the number of modulations, which is in line with the measurements of different modulation periods at a fixed device length of 50 μm (Fig. 3C). Only the 8-μm modulation shows a reduced peak height, which is probably due to the highly anisotropic stray field.

The ballistic model gives an estimate $E_Z(T,2B_s)/(4E_F)$ for the relative magnetoresistance peak height $\Delta\rho_{xx}/\rho_{xx}$ (black line in Fig. 4B). In the presence of disorder, diabatic transitions are perturbed and, hence, peak heights are reduced. However, we found that disorder does not strongly affect the measured peak heights in sample C. The experimental values in Fig. 4B are comparable to our disorder model at an electron mean free path of l_e = 4 μm (blue triangles in Fig. 4B). The peaks disappear in the calculations at l_e = 0.65 μm, which equals the measured mean free path in sample C. Orbital effects may enhance spin effects and contribute to a better-than-expected device performance at low T (*18*). Nevertheless, experiments indicate that adiabatically transported spin is stable over device distances of 50 μm, which are much longer than electron mean free paths in the samples (between 0.47 and 1.39 μm).

Our results demonstrate the concept of an adiabatic spin transistor: Adiabatic transport protects spin information, whereas diabatic transitions lead to spin backscattering (thus depolarizing the current) and allow for switching between on and off states. In contrast to the Datta-Das concept, our approach is tolerant against disorder. Our proof of concept device shows source-drain resistance modulation of up to ~10%, which is expected to be considerably enhanced in materials with high spin polarization (*18*). Furthermore, the homogeneous B field, provided here by coils, might be replaced with a magnetic gate that is switched by spin torque, discussed in (*18*). This would enable the device to be controlled purely by electric fields. As we use a paramagnetic material, our device operates only at low T. However, we stress that the design concepts are not restricted to a particular choice of materials, temperature, methods of spin injection, manipulation, or detection. Transferring our concept to higher T requires employing exchange or spin-orbit splitting rather than Zeeman splitting. Possible material systems in which exchange interaction can be tuned by means of an electric field involve, for instance, magnetic semiconductors (*27*).

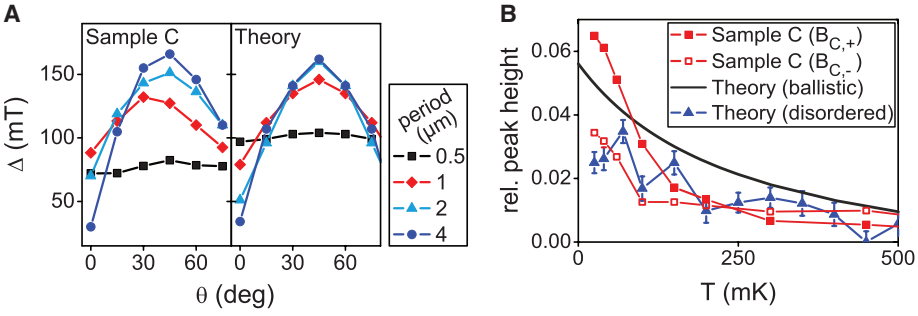

Fig. 4. (**A**) Measured and calculated anisotropy of the stray field, as reflected by the resistance peak separation $\Delta = B_{C,+} - B_{C,-}$. (**B**) Relative resistance peak height $\Delta\rho_{xx}/\rho_{xx}$ as a function of temperature in sample C (solid and open squares for $B_{C,+}$ and $B_{C,-}$, respectively), in the ballistic theoretical model (solid line), and in a model that includes disorder (triangles). In the latter case, the mean free path is 4 μm, and the device length is 18 μm. The stray-field modulation period is 1 μm. The corresponding reference values of the spin-compensated limit are estimated from the resistances at 1 K. Error bars denote the uncertainty in the disorder-averaged values.

References and Notes

1. D. D. Awschalom, D. Loss, N. Samarth, Eds., *Semiconductor Spintronics and Quantum Computation* (Springer, Berlin, 2009).
2. I. Žutić, J. Fabian, S. Das Sarma, *Rev. Mod. Phys.* **76**, 323 (2004).
3. S. Datta, B. Das, *Appl. Phys. Lett.* **56**, 665 (1990).
4. H. C. Koo *et al.*, *Science* **325**, 1515 (2009).
5. J. Schliemann, J. C. Egues, D. Loss, *Phys. Rev. Lett.* **90**, 146801 (2003).
6. B. A. Bernevig, J. Orenstein, S.-C. Zhang, *Phys. Rev. Lett.* **97**, 236601 (2006).
7. J. D. Koralek *et al.*, *Nature* **458**, 610 (2009).
8. J. Fabian, I. Žutić, S. Das Sarma, *Appl. Phys. Lett.* **84**, 85 (2004).
9. N. Rangaraju, J. A. Peters, B. W. Wessels, *Phys. Rev. Lett.* **105**, 117202 (2010).
10. M. Born, V. Fock, *Z. Phys. A* **51**, 165 (1928).

11. L. Landau, *Phys. Sov. Union* **2**, 46 (1932).
12. C. Zener, *Proc. R. Soc. London Ser. A* **137**, 696 (1932).
13. J. K. Furdyna, *J. Appl. Phys.* **64**, R29 (1988).
14. M. König *et al.*, *Phys. Rev. Lett.* **96**, 076804 (2006).
15. T. Koga, Y. Sekine, J. Nitta, *Phys. Rev. B* **74**, 041302(R) (2006).
16. M. V. Berry, *Proc. R. Soc. London Ser. A* **392**, 45 (1984).
17. B. A. Piot *et al.*, *Phys. Rev. B* **82**, 081307 (2010).
18. Materials and methods are available as supplementary materials on *Science* Online.
19. F. J. Teran *et al.*, *Phys. Rev. Lett.* **88**, 186803 (2002).
20. M. Cardona, N. E. Christensen, G. Fasol, *Phys. Rev. B* **38**, 1806 (1988).
21. P. H. Beton *et al.*, *Phys. Rev. B* **42**, 9689 (1990).
22. C. Jia, J. Berakdar, *Phys. Rev. B* **81**, 052406 (2010).
23. M. Calvo, *Phys. Rev. B* **18**, 5073 (1978).
24. O. Zaitsev, D. Frustaglia, K. Richter, *Phys. Rev. B* **72**, 155325 (2005).
25. M. Popp, D. Frustaglia, K. Richter, *Phys. Rev. B* **68**, 041303(R) (2003).
26. J. P. Davis, P. Pechukas, *J. Chem. Phys.* **64**, 3129 (1976).
27. H. Ohno *et al.*, *Nature* **408**, 944 (2000).

Acknowledgments: We thank M. Wimmer for useful discussions and providing the code for the transport equation solver; M. Kiessling for SQUID measurements; M. Wiater for technical assistance in molecular beam epitaxy growth; and C. Back, G. E. W. Bauer, J. Fabian, V. I. Falko, C. Strunk, and G. Woltersdorf for fruitful discussions. We acknowledge financial support from the Deutsche Forschungsgemeinschaft through SFB 689, WE 247618, FOR 1483, and Elitennetzwerk Bayern. Our research in Poland (V.K., G.K., T.W.) was partially supported by the European Union within the European Regional Development Fund, through Innovative Economy grant POIG.01.01.02-00-008/08.

Supplementary Materials

www.sciencemag.org/cgi/content/full/337/6092/324/DC1
Materials and Methods
Supplementary Text
Figs. S1 to S8
Table S1
References (*28*–*39*)

1 March 2012; accepted 14 June 2012
10.1126/science.1221350

A Paramagnetic Bonding Mechanism for Diatomics in Strong Magnetic Fields

Kai K. Lange,[1] E. I. Tellgren,[1] M. R. Hoffmann,[1,2] T. Helgaker[1]*

Elementary chemistry distinguishes two kinds of strong bonds between atoms in molecules: the covalent bond, where bonding arises from valence electron pairs shared between neighboring atoms, and the ionic bond, where transfer of electrons from one atom to another leads to Coulombic attraction between the resulting ions. We present a third, distinct bonding mechanism: perpendicular paramagnetic bonding, generated by the stabilization of antibonding orbitals in their perpendicular orientation relative to an external magnetic field. In strong fields such as those present in the atmospheres of white dwarfs (on the order of 10^5 teslas) and other stellar objects, our calculations suggest that this mechanism underlies the strong bonding of H_2 in the $^3\Sigma_u^+(1\sigma_g 1\sigma_u^*)$ triplet state and of He_2 in the $^1\Sigma_g^+(1\sigma_g^2 1\sigma_u^{*2})$ singlet state, as well as their preferred perpendicular orientation in the external field.

Chemical bonding mechanisms are not only well understood phenomenologically and theoretically, but are also accurately described by the methods of modern quantum chemistry. Molecular atomization energies, for example, are today routinely calculated to an accuracy of a few kilojoules per mole—the "chemical accuracy" characteristic of modern measurements (*1*). However, nearly all our knowledge about chemical bonding pertains to Earth-like conditions, where magnetic interactions are weak relative to the Coulomb interactions responsible for bonding. By contrast, in the atmospheres of rapidly rotating compact stellar objects, magnetic fields are orders of magnitude stronger than those that can be generated in laboratories. In particular, some white dwarfs have fields as strong as 10^5 T, and fields up to 10^{10} T exist on neutron stars and magnetars. Under these conditions, magnetism strongly affects the chemistry and physics of molecules, playing a role as important as that of Coulomb interactions (*2*). To understand this unfamiliar chemistry, we cannot be guided solely by the behavior of molecules under Earth-like conditions. In the absence of direct measurements and observations, ab initio (as opposed to semiempirical) quantum mechanical simulations play a crucial role in unraveling the behavior of molecules in strong magnetic fields and may be useful in the interpretation of white dwarf spectra (*3*, *4*).

Over the years, many quantum chemical studies have been performed on one- and two-electron molecules in strong magnetic fields (*5*). Some of these demonstrate how certain otherwise unbound one-electron molecules become bound in strong fields. Intriguingly, Hartree-Fock calculations by Žaucer and Ažman in 1978 (*6*) and by Kubo in 2007 (*7*) suggest that the otherwise dissociative lowest triplet state $^3\Sigma_u^+(1\sigma_g 1\sigma_u^*)$ of H_2 becomes bound in the perpendicular orientation of the molecule relative to the field. The binding has also been noted in simple model calculations and rationalized in terms of van der Waals binding (dispersion) (*8*) and a shift of electronic charge density toward the molecular center (*9*). Bearing in mind that the uncorrelated Hartree-Fock model often strongly overestimates the binding energy in the absence of magnetic fields, these findings must be confirmed by more advanced quantum chemical simulations.

Here, we report highly accurate calculations on H_2 in strong magnetic fields, taking advantage of our recently developed LONDON code, which is capable of treating molecular systems accurately in all field orientations. Our studies not only confirm the bonding of triplet H_2 but also provide an elementary molecular orbital (MO) explanation that involves neither charge displacement nor dispersion: Nonbonding molecular electronic states are stabilized by the reduction of the paramagnetic kinetic energy of antibonding MOs when these are oriented perpendicular to the magnetic field. The generality of the proposed bonding mechanism is confirmed by calculations on He_2, previously not studied in strong magnetic fields.

To represent the molecular electronic states in magnetic fields, we use the full configuration-interaction (FCI) method [implemented using string-based techniques (*10*–*12*)], where the N-electron wave function is expanded linearly in Slater determinants,

$$|\mathrm{FCI}\rangle = \sum_n C_n \det|\phi_{p_{1n}}, \phi_{p_{2n}}, \ldots \phi_{p_{Nn}}| \qquad (1)$$

whose coefficients C_n are determined by the Rayleigh-Ritz variation principle (*13*). Each determinant is an antisymmetrized product of N orthonormal spin MOs ϕ_p; the summation is over all determinants that may be generated from a given set of MOs. The exact solution to the Schrödinger equation is reached in the limit of a complete set of MOs, making it possible to approach this solution in a systematic manner.

The FCI model makes no assumptions about the structure of the electronic system; in particular, it makes no assumptions regarding the dominance of one Slater determinant (assumed in Hartree-Fock and coupled-cluster theories). This model is therefore capable of describing all bonding situations and dissociation processes in an unbiased manner, which is essential when unfamiliar phenomena are studied. Equally important, the FCI model provides a uniform description of different electronic states and is therefore able to describe the complicated evolution of such states that occurs with increasing field strength.

The FCI method is a standard technique of quantum chemistry, often used to benchmark less expensive and less accurate methods, and was previously used by Schmelcher and Cederbaum in their study of H_2 in strong parallel magnetic fields (*14*). Our FCI implementation differs from

[1]Centre for Theoretical and Computational Chemistry, Department of Chemistry, University of Oslo, N-0315 Oslo, Norway. [2]Chemistry Department, University of North Dakota, Grand Forks, ND 58202, USA.

*To whom correspondence should be addressed. E-mail: trygve.helgaker@kjemi.uio.no

theirs in being invariant with respect to gauge origin and hence capable of describing all orientations of the molecule in a field equally well. To understand this point, we recall that the kinetic energy operator (including the spin-Zeeman term) in the magnetic field **B** is given, in atomic units, by

$$T = \frac{1}{2}\sum_i \pi_i^2 + \mathbf{B}\cdot\sum_i \mathbf{s}_i, \qquad \pi_i = -i\nabla_i + \frac{1}{2}\mathbf{B}\times(\mathbf{r}_i - \mathbf{O}) \quad (2)$$

where i is the imaginary unit, and π_i and $\mathbf{s}_i$ are the kinetic momentum and spin operators of electron i, respectively. The kinetic energy operator depends parametrically on the gauge origin **O**, an arbitrary point in space where the field contribution to the operator vanishes. In exact theory, all choices of **O** yield the same energy and other properties of the system; in approximate calculations (except in parallel orientations with the gauge origin on the molecular axis), the calculated results depend on **O** unless gauge origin invariance is carefully imposed. For the results to be reliable, it is essential that the calculations be rigorously invariant with respect to gauge origin in all molecular orientations. The kinetic energy operator in Eq. 2 depends quadratically on π_i and therefore both linearly and quadratically on **B**. For the field strengths considered here, on the order of $B_0 = 2.35 \times 10^5$ T (one atomic unit), the linear and quadratic field contributions to the Hamiltonian are equally important, resulting in a complicated chemistry in this regime.

To ensure gauge origin invariance, we expand the MOs linearly in a set of field-dependent atom-fixed Cartesian Gaussian atomic orbitals (AOs) of the form

$$\chi_{ijk}(\mathbf{r},\mathbf{K},\mathbf{B},\mathbf{O}) = N_{ijk}x_K^i y_K^j z_K^k \times \exp\left[\frac{1}{2}i\mathbf{B}\times(\mathbf{O}-\mathbf{K})\cdot\mathbf{r}\right]\exp(-ar_K^2) \quad (3)$$

where **r** is the position of the electron relative to the origin of the coordinate system, $\mathbf{r}_K$ is its position relative to the center of the Gaussian **K** (here an atomic center), $a > 0$ is the Gaussian exponent, and N_{ijk} is the normalization constant. These AOs depend on the field **B** and on the gauge origin **O** in a physically reasonable manner, being correct to first order in the external magnetic field and ensuring gauge origin invariance of all computed expectation values. The use of such field-dependent orbitals, introduced by London in 1937 (*15*), is a standard technique in perturbative treatments of molecular magnetic phenomena (*16*–*19*). The use of London orbitals in nonperturbative studies is technically more complicated and therefore uncommon. Indeed, London orbitals have previously been used only in calculations on the one-electron H_2^+ molecule (*20*–*22*), on the two-electron H_2 molecule (*6*, *7*), and on larger molecules by our group (*23*, *24*), all at the uncorrelated Hartree-Fock level of theory [see also the Heitler-London model of Basile *et al*. (*9*)]. Our gauge origin–invariant FCI code allows us to study molecules in different electronic states and arbitrary orientations in a reliable

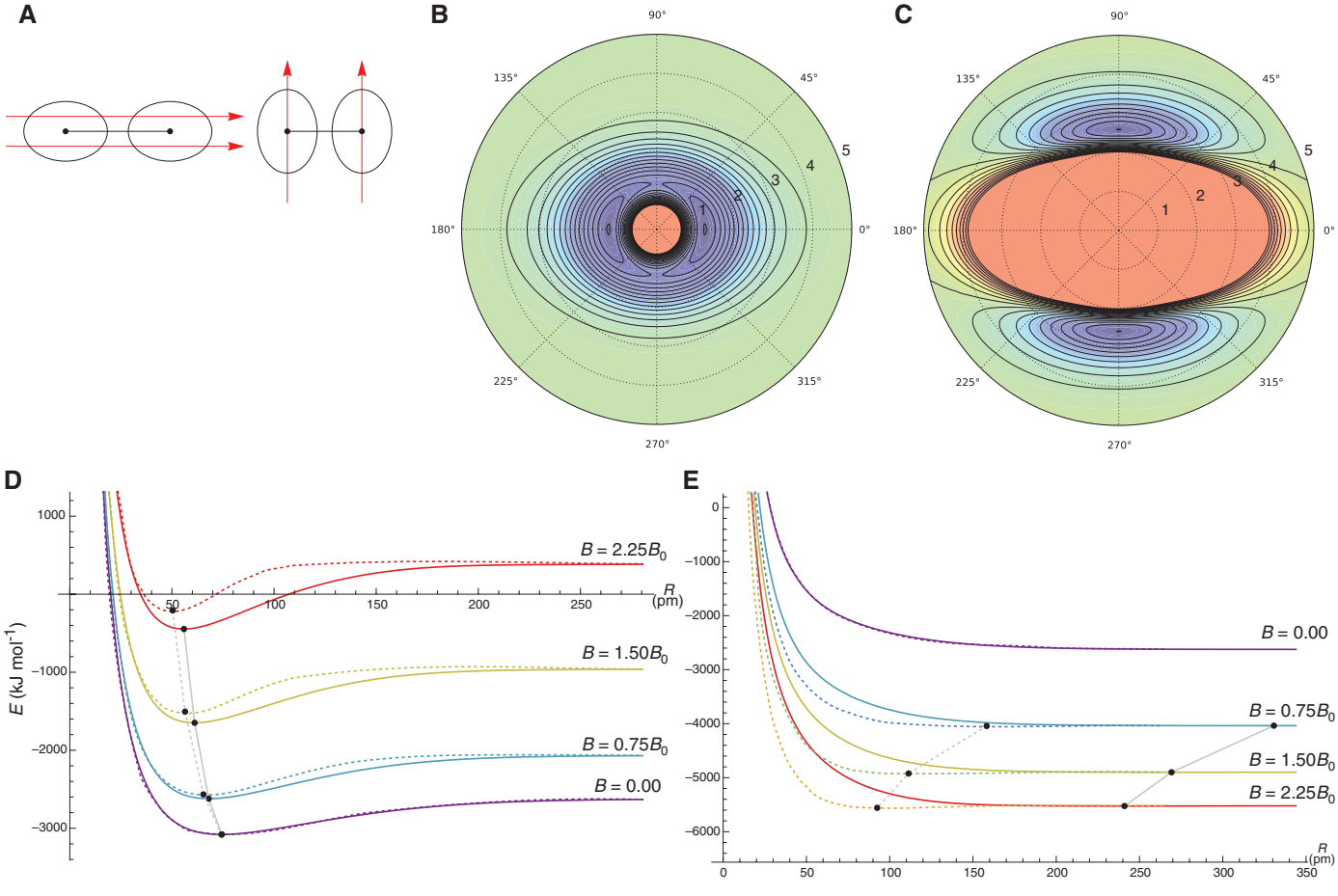

Fig. 1. The H_2 molecule in an external magnetic field. (**A**) Schematic illustration of the chemical bonding in parallel orientation (left) and perpendicular orientation (right) relative to the magnetic field, represented by red arrows. (**B** and **C**) Potential energy surfaces $E(R, \theta)$ of H_2 in the $^1\Sigma_g^+(1\sigma_g^2)$ state (B) and the $^3\Sigma_u^+(1\sigma_g 1\sigma_u^*)$ state (C) calculated at the FCI/un-aug-cc-pVTZ level of theory in a field of strength $B = 1.0B_0$, using a polar coordinate system where R is the internuclear separation and θ is the angle of the molecular axis relative to the field (high values in red, low values in blue). (**D** and **E**) Potential energy curves $E(R, \theta)$ of the $^1\Sigma_g^+(1\sigma_g^2)$ state (D) and the $^3\Sigma_u^+(1\sigma_g 1\sigma_u^*)$ state (E) calculated at different field strengths in parallel orientation ($\theta = 0°$, solid lines) and perpendicular orientation ($\theta = 90°$, dashed lines). The areas between the full and dashed lines represent the energy for intermediate (skew) orientations in the field. The minimum of each curve is marked with a black dot.

and unbiased manner. A more flexible but computationally demanding scheme has been proposed by Kennedy and Kobe, who equipped the wave function with a variationally optimized phase factor (*25*).

In all calculations reported here, we use the correlation-consistent aug-cc-pVTZ basis set (*26*, *27*) in uncontracted form (denoted un-aug-cc-pVTZ). For B on the order of or greater than B_0, the anisotropic distortion of the electronic distribution by the magnetic field is most economically described using anisotropic AOs, with different Gaussian exponents in the parallel and perpendicular directions relative to the field (*28*, *29*). The isotropic un-aug-cc-pVTZ basis that we use is sufficient for an accurate description of electronic systems in fields up to B_0 but becomes progressively less suited in stronger fields, as the systems become more compact and anisotropic. Selected FCI calculations carried out in the larger un-aug-cc-pVQZ basis and in the un-aug-cc-pVTZ basis with extra orbitals added confirm that the un-aug-cc-pVTZ basis provides a qualitatively correct description of the systems studied here.

Because of the shrinking prolate shape of the constituent atoms, diatomic molecules become smaller and develop an energy dependence on their orientation in a magnetic field, as illustrated for the parallel and perpendicular orientations in Fig. 1A. In the covalently bound singlet state, the electronic energy of H_2 increases diamagnetically with increasing field strength (Fig. 1D). Moreover, the molecule becomes shorter and more strongly bound, reflecting a more pronounced diamagnetic behavior in the dissociation limit than in the united-atom limit. As expected for a covalently bound state, the energy is lower in the parallel orientation than in the perpendicular orientation (Fig. 1A), owing to the greater interatomic overlap in this orientation. In the polar plot for $B = B_0$ (Fig. 1B), we therefore observe global minima at inclination angles $\theta = 0°$, 180° connected by saddle points at $\theta = 90°$, 270°. As the field increases from 0 to $2.25B_0$ (the strongest field considered here), the bond distance R_e decreases by 24% from 74 to 56 pm, while the dissociation energy D_e (without the zero-point vibrational contribution) increases by 83%, from 455 kJ mol^{-1} to 834 kJ mol^{-1}. Because of the prolate shape of the atoms, the saddle points for rotation occur at a slightly shorter distance of 50 pm, with a barrier to rotation of 239 kJ mol^{-1}.

The triplet state $^3\Sigma_u^+(1\sigma_g 1\sigma_u^*)$ behaves very differently from the singlet state. With increasing field strength, the energy of the ββ triplet component in Fig. 1E (the ground state for all finite fields considered here) is lowered paramagnetically and the system becomes more compact, as expected from the shrinking atomic size. The molecule thereby becomes bound, with a preferred perpendicular orientation in the field. At $B = 2.25B_0$, for instance, the bond distance is 92 pm and the dissociation energy 38 kJ mol^{-1}. The barrier to rotation is only slightly lower, 34 kJ mol^{-1}, with saddle points at a large internuclear separation of 241 pm. The other two triplet components behave in the same manner but with the energy shifted upward by the Zeeman interaction. The different shapes of the H_2 singlet and triplet surfaces are immediately apparent from the polar plots in Fig. 1, B and C. Although both surfaces are distinctively prolate in the field direction, the plots reveal two very different states: a fairly isotropic, compact singlet state with parallel global minima connected by perpendicular saddle points, contrasted with a more anisotropic, diffuse triplet state with a larger inaccessible inner region and perpendicular minima connected by parallel saddle points.

To understand the mechanism responsible for the field-induced perpendicular bonding, we examine the behavior of the bonding $1\sigma_g$ and antibonding $1\sigma_u^*$ orbitals in an external magnetic

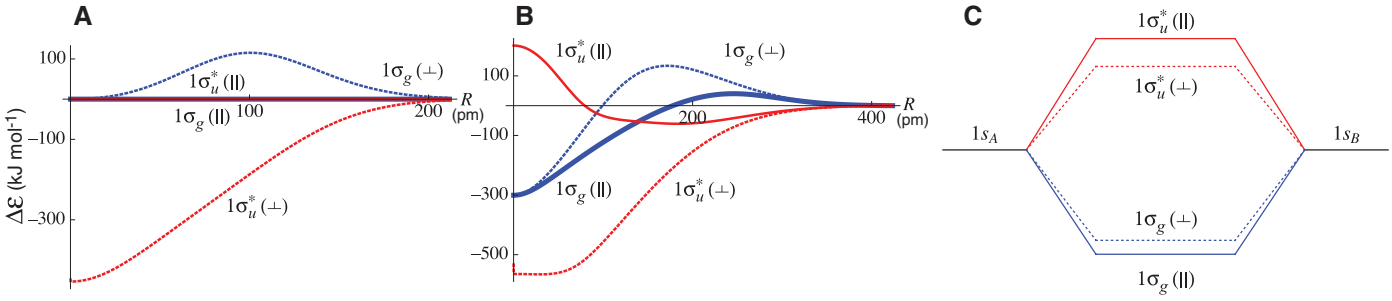

Fig. 2. Orbital energies of the bonding $1\sigma_g$ (blue) and antibonding $1\sigma_u^*$ (red) H_2 orbitals in parallel orientation (solid lines) and perpendicular orientation (dashed lines) relative to an external magnetic field. (**A**) The field-induced change in the orbital bonding energy $\Delta\mathcal{E}_p(R, \theta, B_0)$ calculated with a fixed exponent $a = 1$ for different internuclear separations R. (**B**) The field-induced change in the orbital bonding energy $\Delta\mathcal{E}_p(R, \theta, B_0)$ calculated with an optimized exponent for different internuclear separations R. (**C**) The MO energy level diagram in a magnetic field.

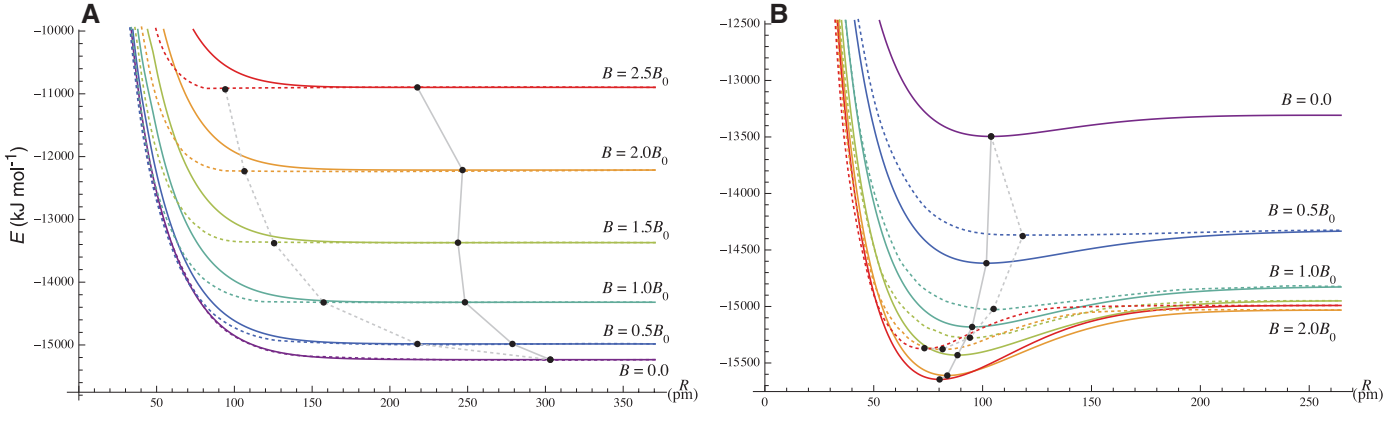

Fig. 3. (**A**) Potential energy curve of He_2 in the $^1\Sigma_g^+(1\sigma_g^2 1\sigma_u^{*2})$ state calculated using FCI/un-aug-cc-pVTZ theory in parallel orientation (solid lines) and perpendicular orientation (dashed lines) for $0 \le B \le 2.5B_0$. (**B**) Same as (A) for He_2 in the $^3\Sigma_u^+(1\sigma_g^2 1\sigma_u^* 2\sigma_g)$ state. The energy minimum of each curve is marked with a black dot.

field. In a minimal basis consisting of two 1s Gaussian orbitals of the form given in Eq. 3 with $i = j = k = 0$, the normalized bonding and antibonding MOs of H_2 located on the z axis in an external field **B** of arbitrary orientation are given by

$$1\sigma_{g/u} = \left\{2 \pm 2\,\exp\left[-\frac{a}{2}(1 + \tilde{B}_x^2 + \tilde{B}_y^2)R^2\right]\right\}^{-1/2} \times (1s_A \pm 1s_B) \quad (4)$$

where $1s_A$ and $1s_B$ are 1s orbitals with exponent a on the two atoms, R is the internuclear separation, and $\tilde{B}_x = B_x/4a$ and $\tilde{B}_y = B_y/4a$ are scaled perpendicular field components. There is no contribution from B_z to the MOs. When R tends to zero, these MOs transform smoothly into helium AOs of the same exponent:

$$\lim_{R\to 0} 1\sigma_g = 1s \quad (5)$$

$$\lim_{R\to 0} 1\sigma_u^* = (1 + \tilde{B}_x^2 + \tilde{B}_y^2)^{-1/2} \times (2p_z + i\tilde{B}_x 2p_y - i\tilde{B}_y 2p_x) \quad (6)$$

Whereas $1\sigma_g$ transforms into an 1s orbital, $1\sigma_u^*$ transforms into a combination of 2p orbitals. In particular, for $\tilde{B} = 1$, $1\sigma_u^*$ becomes $2p_0$ in the parallel orientation and $2p_{-1}$ in the perpendicular orientation. In a magnetic field, the $2p_{-1}$ orbital has a lower energy than the $2p_0$ orbital (by the orbital-Zeeman interaction); therefore, $1\sigma_u^*$ favors a perpendicular orientation relative to the magnetic field. No such orientational preference is observed for $1\sigma_g$, which transforms into the same 1s orbital in all orientations. By this argument, H_2 adopts a perpendicular orientation in the triplet state, with its singly occupied bonding and antibonding orbitals.

Let $\mathcal{E}_p(R, \theta, B)$ be the orbital energy of ϕ_p at configuration (R, θ) and in the field B, and consider the quantity

$$\Delta\mathcal{E}_p(R,\theta,B) = [\mathcal{E}_p(R,\theta,B) - \mathcal{E}_p(R,\theta,0)] - [\mathcal{E}_p(\infty,\theta,B) - \mathcal{E}_p(\infty,\theta,0)] \quad (7)$$

which represents the field-induced change in the orbital energy $\mathcal{E}_p(R, \theta, B) - \mathcal{E}_p(R, \theta, 0)$ at the molecular configuration (R, θ) relative to the change observed in the dissociation limit. With a fixed orbital exponent $a = 1$, we observe the expected stabilization of $1\sigma_u^*$ in the perpendicular orientation (and a smaller $1\sigma_g$ destabilization in the bonding region), and neither stabilization nor destabilization in the parallel orientation (Fig. 2A). However, when the exponent a is variationally optimized for each (R, θ) (Fig. 2B), $1\sigma_g$ is stabilized in the united atom (where the orientation no longer matters for this orbital), whereas $1\sigma_u^*$ (for which the orientation in the united atom matters) is destabilized in the parallel orientation but further stabilized in the perpendicular orientation. These changes lead to the modified MO energy level diagram shown in Fig. 2C and to the following energy ordering of the lowest H_2 states in a magnetic field:

$$E_\parallel(1\sigma_g^2) \le E_\perp(1\sigma_g^2) \le E_\perp(1\sigma_g 1\sigma_u^*) \le E_\parallel(1\sigma_g 1\sigma_u^*) \quad (8)$$

The field-induced bonding of H_2 in the perpendicular orientation is thus not covalent in nature, nor does it depend on dispersion. Instead, it arises from a lowering (relative to the atomic limit) of the kinetic energy associated with the induced paramagnetic rotation of the electron in the antibonding orbital. The pivotal role of the kinetic energy is confirmed by FCI calculations on H_2; although the field-induced changes in the FCI kinetic and electrostatic energies at a given (R, θ) are of the same order of magnitude, the appearance of a minimum in the dissociation curve is almost entirely due to the lowering of the kinetic energy.

As shown in Fig. 2, the bonding $1\sigma_g$ orbital favors a perpendicular orientation in a magnetic field for intermediate bond distances. In general, therefore, the orientation of H_2 in the triplet state depends on a balance between the preference of $1\sigma_g$ for a parallel orientation and the preference of $1\sigma_u^*$ for a perpendicular orientation. Indeed, for $B = 2.25B_0$, the H_2 minimum shifts slightly away from the perpendicular orientation. Eventually, the H_2 ground state changes from $^3\Sigma_u^+(1\sigma_g 1\sigma_u^*)$ to $^3\Pi_u(1\sigma_g 1\pi_u)$, which is covalently bound with a preferred parallel field orientation, as observed by Kubo using Hartree-Fock theory (*7*).

To demonstrate that the behavior observed for H_2 is a general phenomenon, we have calculated the potential energy curves of He_2 in its lowest $^1\Sigma_g^+(1\sigma_g^2 1\sigma_u^{*2})$ singlet (Fig. 3A) and $^3\Sigma_u^+(1\sigma_g^2 1\sigma_u^* 2\sigma_g)$ triplet (Fig. 3B) states. Without a field, the He_2 singlet ground state is weakly bound by dispersion, with $R_e = 297$ pm and $D_e = 0.092$ kJ mol^{-1} (*30*). In the field, the energy increases diamagnetically. Moreover, He_2 assumes a perpendicular orientation, becoming smaller and more strongly bound, with a bond distance of 94 pm and a dissociation energy of 31 kJ mol^{-1} at $B = 2.5B_0$. The nonmonotonic variation of the saddle point (in the parallel orientation) may be an artifact arising from basis set incompleteness. In the triplet state, the covalently bound He_2 molecule behaves similarly to H_2 in the singlet state. As the field increases to $2.5B_0$, the molecule aligns with the field and shortens from 104 pm to 80 pm while the dissociation energy increases from 178 kJ mol^{-1} to 655 kJ mol^{-1}. In the ββ component of the triplet, He_2 becomes diamagnetic at $B \approx 2.2B_0$.

We have presented advanced FCI calculations on H_2 and He_2 in strong magnetic fields and explained their behavior in terms of elementary concepts of MO theory. To examine the role of electron correlation, we compare the FCI and Hartree-Fock potential energy curves of triplet H_2 (Fig. 4A) and singlet He_2 (Fig. 4B). These plots demonstrate that the paramagnetic perpendicular bonding discussed above does not require electron correlation for its qualitative description; Hartree-Fock theory, in which electronic interactions are described in an averaged, mean-field manner, recovers all the main effects of paramagnetic bonding, underestimating the bond distance slightly and the dissociation energy more strongly. The bonding is clearly not van der Waals in nature, although electron correlation is necessary for its quantitative description. In short, we have identified a distinct mechanism for chemical bonding in strong magnetic fields, arising from the stabilization of antibonding orbitals in a perpendicular orientation relative to the magnetic field. This stabilization leads to the bonding of

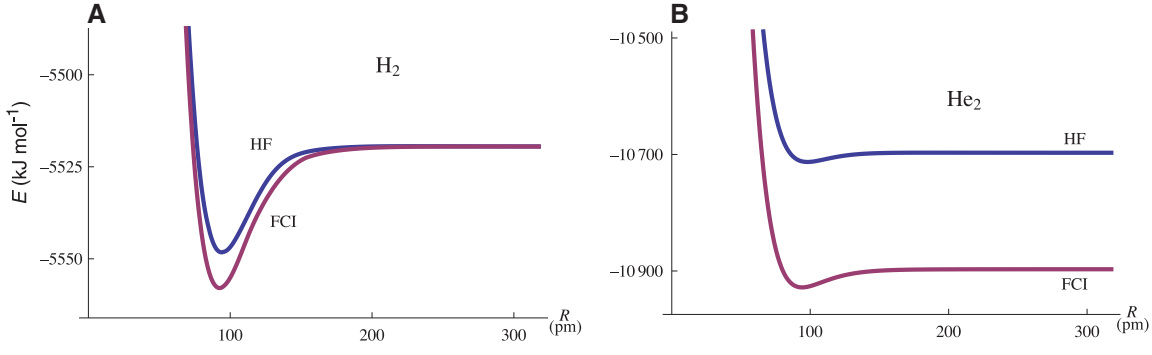

Fig. 4. (**A**) The FCI and unrestricted Hartree-Fock (HF) dissociation curves of H_2 in the $^3\Sigma_u^+(1\sigma_g 1\sigma_u^*)$ state for $B_\perp = 2.25B_0$ calculated in the un-aug-cc-pVTZ basis set. (**B**) Same as (A) for He_2 in the $^1\Sigma_g^+(1\sigma_g^2 1\sigma_u^{*2})$ state for $B_\perp = 2.5B_0$. The Hartree-Fock model overestimates the bond distances of H_2 and He_2 by 1.5 and 4.1%, respectively, whereas the dissociation energies are underestimated by 25 and 49%. The counterpoise corrections for the basis-set superposition error (not added to the plotted curves) are 4 kJ mol^{-1} and 2 kJ mol^{-1}, respectively, for H_2 and He_2 at the equilibrium distances.

species of zero bond order, which are either unbound or bound by dispersion in the absence of a magnetic field. This bonding is sufficiently strong to affect the chemistry of molecules in strong magnetic fields.

References and Notes

1. T. Helgaker, W. Klopper, D. P. Tew, *Mol. Phys.* **106**, 2107 (2008).
2. R. H. Garstang, *Rep. Prog. Phys.* **40**, 105 (1977).
3. S. Jordan, P. Schmelcher, W. Becken, W. Schweizer, *Astron. Astrophys.* **336**, L33 (1998).
4. S. Jordan, P. Schmelcher, W. Becken, *Astron. Astrophys.* **376**, 614 (2001).
5. D. Lai, *Rev. Mod. Phys.* **73**, 629 (2001).
6. M. Žaucer, A. Ažman, *Phys. Rev. A* **18**, 1320 (1978).
7. A. Kubo, *J. Phys. Chem. A* **111**, 5572 (2007).
8. Y. E. Lozovik, A. V. Klyuchnik, *Phys. Lett. A* **66**, 282 (1978).
9. S. Basile, F. Trombetta, G. Ferrante, *Nuovo Cim.* **9**, 457 (1987).
10. P. J. Knowles, N. C. Handy, *Chem. Phys. Lett.* **111**, 315 (1984).
11. W. Duch, *GRMS or Graphical Representation of Model Spaces I: Basics* (Springer-Verlag, New York, 1986).
12. J. Olsen, B. O. Roos, P. Jørgensen, H. J. A. Jensen, *J. Chem. Phys.* **89**, 2185 (1988).
13. T. Helgaker, P. Jørgensen, J. Olsen, *Molecular Electronic-Structure Theory* (Wiley, Chichester, UK, 2000).
14. P. Schmelcher, L. S. Cederbaum, *Phys. Rev. A* **41**, 4936 (1990).
15. F. London, *J. Phys. Radium* **8**, 397 (1937).
16. R. Ditchfield, *J. Chem. Phys.* **56**, 5688 (1972).
17. K. Wolinski, J. F. Hinton, P. Pulay, *J. Am. Chem. Phys. Soc.* **112**, 8251 (1990).
18. W. Kutzelnigg, *Isr. J. Chem.* **19**, 193 (1980).
19. M. Schindler, W. Kutzelnigg, *J. Chem. Phys.* **76**, 1919 (1982).
20. U. Kappes, P. Schmelcher, *Phys. Lett. A* **210**, 409 (1996).
21. U. Kappes, P. Schmelcher, *Phys. Rev. A* **53**, 3869 (1996).
22. U. Kappes, P. Schmelcher, *Phys. Rev. A* **54**, 1313 (1996).
23. E. I. Tellgren, A. Soncini, T. Helgaker, *J. Chem. Phys.* **129**, 154114 (2008).
24. E. I. Tellgren, T. Helgaker, A. Soncini, *Phys. Chem. Chem. Phys.* **11**, 5489 (2009).
25. P. K. Kennedy, D. H. Kobe, *Phys. Rev. A* **30**, 51 (1984).
26. T. H. Dunning, *J. Chem. Phys.* **90**, 1007 (1989).
27. D. E. Woon, T. H. Dunning, *J. Chem. Phys.* **100**, 2975 (1994).
28. P. Schmelcher, L. S. Cederbaum, *Phys. Rev. A* **37**, 672 (1988).
29. U. Kappes, P. Schmelcher, *J. Chem. Phys.* **100**, 2878 (1994).
30. M. Jeziorska, W. Cencek, K. Patkowski, B. Jeziorski, K. Szalewicz, *J. Chem. Phys.* **127**, 124303 (2007).

Acknowledgments: Supported by the Norwegian Research Council through Centre for Theoretical and Computational Chemistry (CTCC) grant 179568/V30 and through grant 197446/V30 and by the European Research Council (ERC) under the European Union's Seventh Framework Program through the advanced grant ABACUS, ERC grant agreement 267683. M.R.H. acknowledges support from the CTCC during a sabbatical stay at the University of Oslo in 2010.

26 January 2012; accepted 25 May 2012
10.1126/science.1219703

Sulfate Burial Constraints on the Phanerozoic Sulfur Cycle

Itay Halevy,[1,2]* Shanan E. Peters,[3] Woodward W. Fischer[2]

The sulfur cycle influences the respiration of sedimentary organic matter, the oxidation state of the atmosphere and oceans, and the composition of seawater. However, the factors governing the major sulfur fluxes between seawater and sedimentary reservoirs remain incompletely understood. Using macrostratigraphic data, we quantified sulfate evaporite burial fluxes through Phanerozoic time. Approximately half of the modern riverine sulfate flux comes from weathering of recently deposited evaporites. Rates of sulfate burial are unsteady and linked to changes in the area of marine environments suitable for evaporite formation and preservation. By contrast, rates of pyrite burial and weathering are higher, less variable, and largely balanced, highlighting a greater role of the sulfur cycle in regulating atmospheric oxygen.

Sulfate (SO_4^{2-}) is the fourth most abundant ion in modern seawater and a major component of the alkalinity budget, which governs the pH of seawater (*1*). Bacterial sulfate reduction accounts for ~50% of sedimentary organic matter respiration (*2*), and precipitation of pyrite (FeS_2) is one of the major exit channels of sulfur from the ocean (*3*). Because reduction of riverine sulfate and burial of the sulfide leave oxidized products in the ocean-atmosphere system, pyrite burial is considered a major indirect source of oxygen to the atmosphere (*4*, *5*).

Several time series data sets constrain aspects of the Phanerozoic sulfur cycle (Fig. 1A). The sulfur isotope composition, $\delta^{34}S$, of carbonate-associated sulfate, sulfate evaporites, and barite ($BaSO_4$) records the $\delta^{34}S$ of seawater sulfate, whereas the $\delta^{34}S$ of sedimentary pyrite captures the products of microbial sulfate reduction (*6*–*8*). The chemical composition of fluid inclusions in halite constrains the concentration of major ions in seawater, including sulfate (*9*, *10*).

Variability in the $\delta^{34}S$ records of seawater sulfate and sedimentary pyrite is typically interpreted to reflect changes in the fraction of sulfur removed from the oceans as pyrite, f_{pyr}. Because pyrite is depleted in ^{34}S by several percent relative to the sulfate reservoir from which it formed, times of high seawater sulfate $\delta^{34}S$ are interpreted as times of high rates of pyrite burial. By assuming a steady state and constant input magnitude and $\delta^{34}S$, or by scaling inputs and outputs to modern values, models of the Phanerozoic sulfur cycle explain long-term trends in $\delta^{34}S$ values by changes in f_{pyr} between ~0.2 and ~0.6 (*4*, *11*–*13*). Recognizing that the magnitude and $\delta^{34}S$ of the influxes to the ocean have likely varied in time, thereby influencing the isotopic record, some models included parameterized influxes and solved mass balance equations for the outfluxes and the value of f_{pyr} (*4*, *13*). The parameterizations are uncertain, however, because they are largely based on a scaling of modern influxes by debated factors, such as the relative rates of seafloor spreading and continental runoff (*14*, *15*).

It is possible to measure the sink of sulfate evaporites from seawater and obtain estimates of the influx magnitude and $\delta^{34}S$ by mass balance, though previous volume estimates of Phanerozoic evaporites (mostly halite, but some sulfate) have been considered too coarse or uncertain to accurately constrain past rates of sulfate burial (*16*–*18*). We quantified sulfate burial over Phanerozoic time, using a comprehensive macrostratigraphic database (*19*, *20*), which includes 23,843 lithostratigraphic rock units in 949 geographic locations across North America and the Caribbean (NAC). Data were binned by age, and sulfate burial rates were obtained by dividing evaporite volume by bin duration. Macrostratigraphy-based estimates of sulfate burial rates are higher than those derived from other compilations. This is due to the improved spatial and lithological resolution of this data set, which includes sedimentary rocks in the surface and subsurface, and many comparatively thin but widespread deposits not included in previous compilations. Notably, the NAC burial rates are highly variable, with values 2 to 14 times the average occurring mainly in Paleozoic intervals (Fig. 1C).

The macrostratigraphic database currently provides comprehensive coverage only in NAC, but can be scaled globally (Fig. 1D) by using mechanistic relationships between the observations and environmental controls on sulfate evaporite deposition (*20*). The volume-weighted average ratio of global to North American sulfate deposit volumes is ~8 (*16*, *17*). In comparison, the area-weighted ratio of global to NAC submerged continental area in latitudes of net evaporation, estimated from paleogeographic reconstructions (*20*, *21*), is ~7. This close agreement reflects a primary requirement for massive sulfate evaporite deposition—hydrographic isolation of large, marine-fed basins at latitudes of net evaporation (*22*). Such basins are created by rifting, small changes in sea level or the development of a barrier to circulation (*22*), often at the shoreward edge of submerged continental shelves. Indeed,

[1]Environmental Sciences and Energy Research, Weizmann Institute of Science, Rehovot 76100, Israel. [2]Geological and Planetary Sciences, California Institute of Technology, Pasadena, CA 91125, USA. [3]Geoscience, University of Wisconsin-Madison, Madison, WI 53706, USA.

*To whom correspondence should be addressed. E-mail: itay.halevy@weizmann.ac.il

the long time-scale variability in the burial rate data is well explained by the estimated NAC submerged continental area at latitudes ±10° to 50° (linear product moment correlation coefficient of 0.47 at the temporal resolution of the paleogeographic reconstructions), and we use this relationship to derive average global burial rates. We add shorter time scale variability to this average using correlations between NAC fluxes and the rate of change in eustatic sea level (*20*, *23*). Additional factors that influence evaporite deposition, such as geodynamic controls on basin subsidence and climate patterns at the regional-to-local scale (*22*), are not explicitly represented by this scaling methodology. They are, however, implicitly included in the scaling because they have contributed to the observed NAC sulfate burial rates (*20*).

Intervals of rapid sulfate evaporite burial (NAC and global) occur with equal frequency during times of high and low marine sulfate concentrations (Fig. 1). This reveals that sulfate burial rates were disconnected from changes in the activity product of calcium and sulfate [$aCa^{2+}aSO_4^{2-}$; e.g., (*13*)], which have varied by up to ~15% (*9*, *10*). We suggest, instead, that the first-order control on sulfate burial was the episodic availability of suitable environments in which evaporation of seawater could lead to saturation, precipitation, accumulation, and long-term preservation of sulfate evaporites. Unsteady sulfate burial rates, governed by the interactions between sea level, tectonics, and paleogeography, suggest that the critical statistic derived from isotope mass balance studies, f_{pyr}, convolves information regarding the relative activity of sulfate-reducing microbiota with the availability of environments suitable for sulfate burial. For example, a decrease in the area of shallow seas due to a drop in sea level or continental migrations could decrease sulfate burial rates and increase f_{pyr}. The rate of pyrite burial itself need not change. Scaled globally and corrected for the decay of surviving rock with time (*20*), the macrostratigraphic data reveal an average Phanerozoic sulfate evaporite burial rate of ~3.3×10^{11} to 4.5×10^{11} mol $year^{-1}$, depending on bin duration. This is only ~10 to 30% of the estimated riverine influx of sulfate to the oceans [~1.5×10^{12} to 3.5×10^{12} mol $year^{-1}$; (*12*, *24*)], implying that the value of f_{pyr} has been ~0.7 to 0.9 if the sulfur cycle operated close to steady state.

The macrostratigraphic data motivated us to reevaluate models of the sulfur cycle by integrating constraints from sulfur isotope measurements and sulfate concentration data from fluid inclusions. In any isotope mass balance model, the time-dependent concentration and $\delta^{34}S$ of seawater sulfate can be expressed by two equations

$$\frac{dM}{dt} = J_{in} - J_e - J_p \quad (1)$$

$$\frac{dM\delta}{dt} = J_{in}\delta_{in} - J_e\delta - J_p(\delta - \Delta) \quad (2)$$

Here, M is the concentration of seawater sulfate and δ is its $\delta^{34}S$ value. J_{in} is the total influx of sulfur to the oceans, with contributions from evaporite weathering, oxidative weathering of sedimentary and igneous sulfide minerals, and volcanic outgassing of sulfur volatiles. The $\delta^{34}S$ of this influx, δ_{in}, depends on the relative contributions of these three components. J_e and J_p are the burial fluxes of sulfate evaporites and pyrite, respectively, and Δ is the average difference (in permil) between the $\delta^{34}S$ of contemporaneous sulfate evaporite and pyrite sedimentary sinks. The values of M, δ, and Δ can be constrained by $\delta^{34}S$ and fluid inclusion data, and J_e, by macrostratigraphic data.

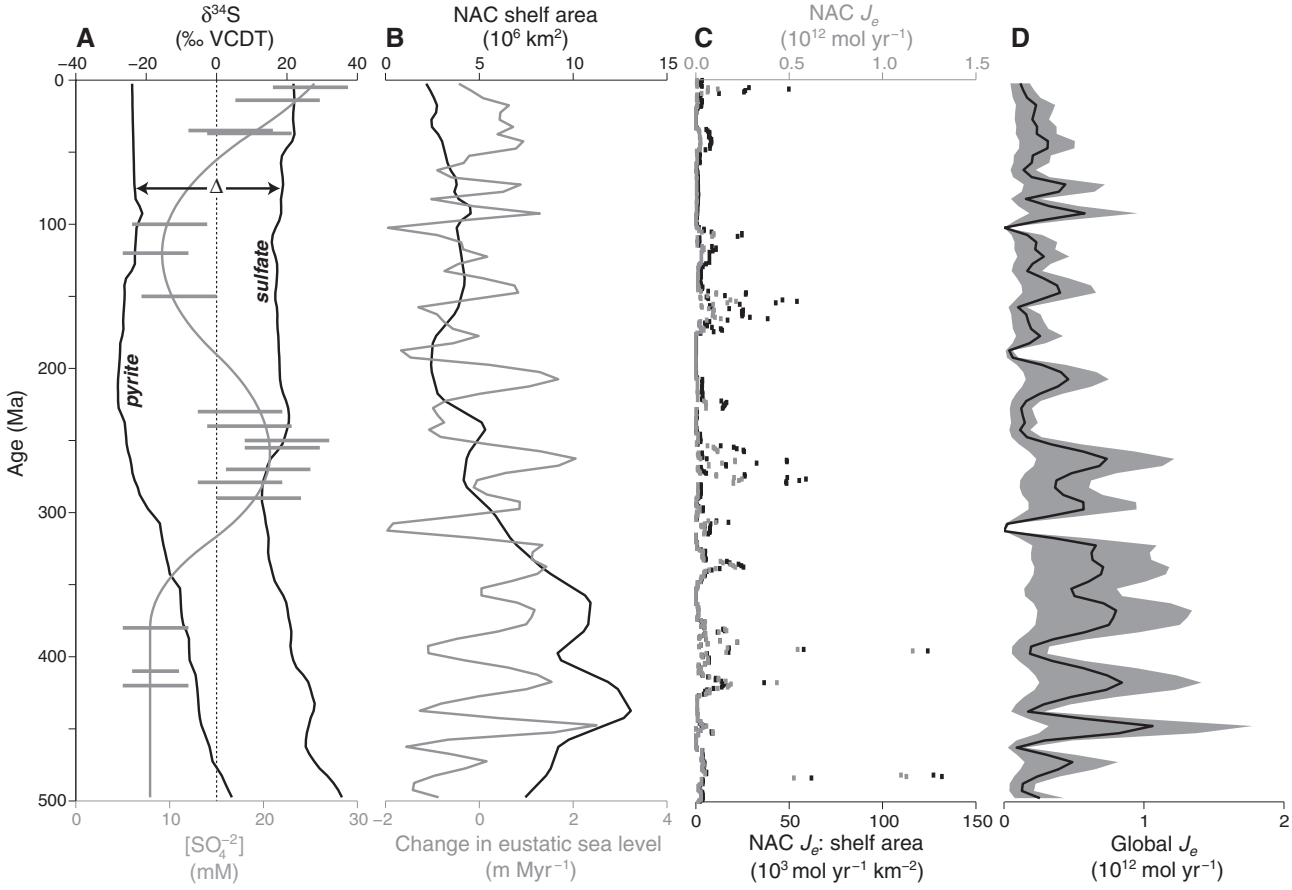

Fig. 1. Observational constraints on the Phanerozoic sulfur cycle. (**A**) Sulfur isotope composition of seawater sulfate and sedimentary pyrite (*8*), and seawater sulfate concentration from fluid inclusions in halite (*9*, *10*). Isotope compositions are reported relative to the standard VCDT (Vienna Canyon Diablo Troilite). (**B**) North America and the Caribbean (NAC) submerged continental area estimates and the rate of change of global mean sea level (*23*). (**C**) Estimates of NAC total and per-area sulfate evaporite burial rates. (**D**) NAC sulfate evaporite burial rates scaled to global fluxes and corrected for decay of the surviving record (*20*), including uncertainty (shaded envelope).

It is possible to solve Eqs. 1 and 2 for the outputs using the inputs ("parameterized input") or for the inputs using the outputs ("parameterized output"), and the solutions can be evaluated with independent physical understanding of the sulfur cycle. We examined three variants of the parameterized input model (*20*). The first assumed constant values of J_{in}, δ_{in}, and Δ (*11*, *12*, *24*) and either a steady state or a dynamic mass balance. In the second and third models, we used influx parameterizations similar to those of (*18*) and (*13*). We examined three variants of the parameterized output model (*20*). The first is a model of constant f_{pyr}. The second, motivated by the observation that pyrite burial is common in shallow, organic-rich sediments (*25*), is a model in which J_p scales with normalized global submerged continental area. This scaling may be weak because although high submerged areas may lead to high bacterial sulfate reduction rates, inefficient delivery of reactive iron across the shelf could limit pyrite burial to near-shore environments (*26*). We therefore considered a third model of constant J_p. Using the macrostratigraphy-based sulfate burial rates as additional constraints, we solved Eqs. 1 and 2 for the time-dependent values of J_{in} and δ_{in}.

Of the parameterized output models (Fig. 2, A to C), the models of constant f_{pyr} yield unrealistically low values of J_{in} (often lower than estimates of the volcanic influx and occasionally negative) and wildly varying values of δ_{in}. The latter is related to the former; if J_{in} is small, then the change in δ_{in} required to drive an observed change in seawater sulfate $\delta^{34}S$ must be large. The models of submerged continental area-dependent or constant J_p yield reasonable values of J_{in} and low values of δ_{in} (near the average sedimentary pyrite $\delta^{34}S$) that become higher during times of increased J_e. This is consistent with the idea of rapid sediment recycling (*4*), where low values of δ_{in} closely follow high relative rates of pyrite burial due to oxidative weathering of recently deposited pyrite; high δ_{in} values result from weathering of newly deposited sulfates. Notably, dynamic and steady-state solutions diverge only during short intervals of rapid change in seawater sulfate concentrations, implying that the system operates much of the time close to steady state. All three parameterized output models, when constrained by the macrostratigraphic data, indicate high average values of f_{pyr} (~0.7 to 0.9).

The parameterized input models yield values of f_{pyr} similar to those in previous modeling studies of the Phanerozoic sulfur cycle (Fig. 2, D and F). However, the model of constant δ_{in} at steady state occasionally requires unrealistically low values of J_{in} to reproduce the $\delta^{34}S$ records [Fig. 2E; e.g., 200 Ma (millions of years ago)], supporting the notion that the $\delta^{34}S$ value of inputs has varied with time. The values of J_e required for mass balance under the other parameterizations are ~three times as large as our burial rate estimates (Fig. 2, E and G, and fig. S1). We hypothesize that this is because parameterizations for the sulfate influx into the ocean are calibrated to modern riverine fluxes, which are higher than the expected long-term average due to the exposure and weathering of recently deposited evaporites (supplementary text). This notion is supported by anomalously high per-area sulfate deposition rates obtained from the NAC macrostratigraphic compilation during the last 10 million years (Fig. 1C); by widespread massive Neogene-age (~23 to 2.6 Ma) evaporites in Europe, Asia, and Africa (*22*, *27*–*31*); and by the recognition that deposition rates decrease with increasing observation time scale to constant, long-term values (*32*). This implies that the high abundance of Neogene-age sulfate evaporites represents gross deposition. Ultimately much of this material will not be preserved, and net deposition rates will converge to long-term Phanerozoic rates (*33*).

The results presented here describe a Phanerozoic sulfur cycle in which the majority of net inputs and outputs are oxidative weathering and burial of sedimentary pyrite, respectively. Over the time intervals resolved by our macrostratigraphic data, the long-term value we estimate for f_{pyr} is generally high, and large downward excursions in its value are associated with high rates of sulfate evaporite burial, rather than times of less pyrite burial. Although spatial heterogeneity and short–time scale variability in the value of J_p have likely occurred (*34*), global models of constant or slowly varying J_p (in response to changes in sub-

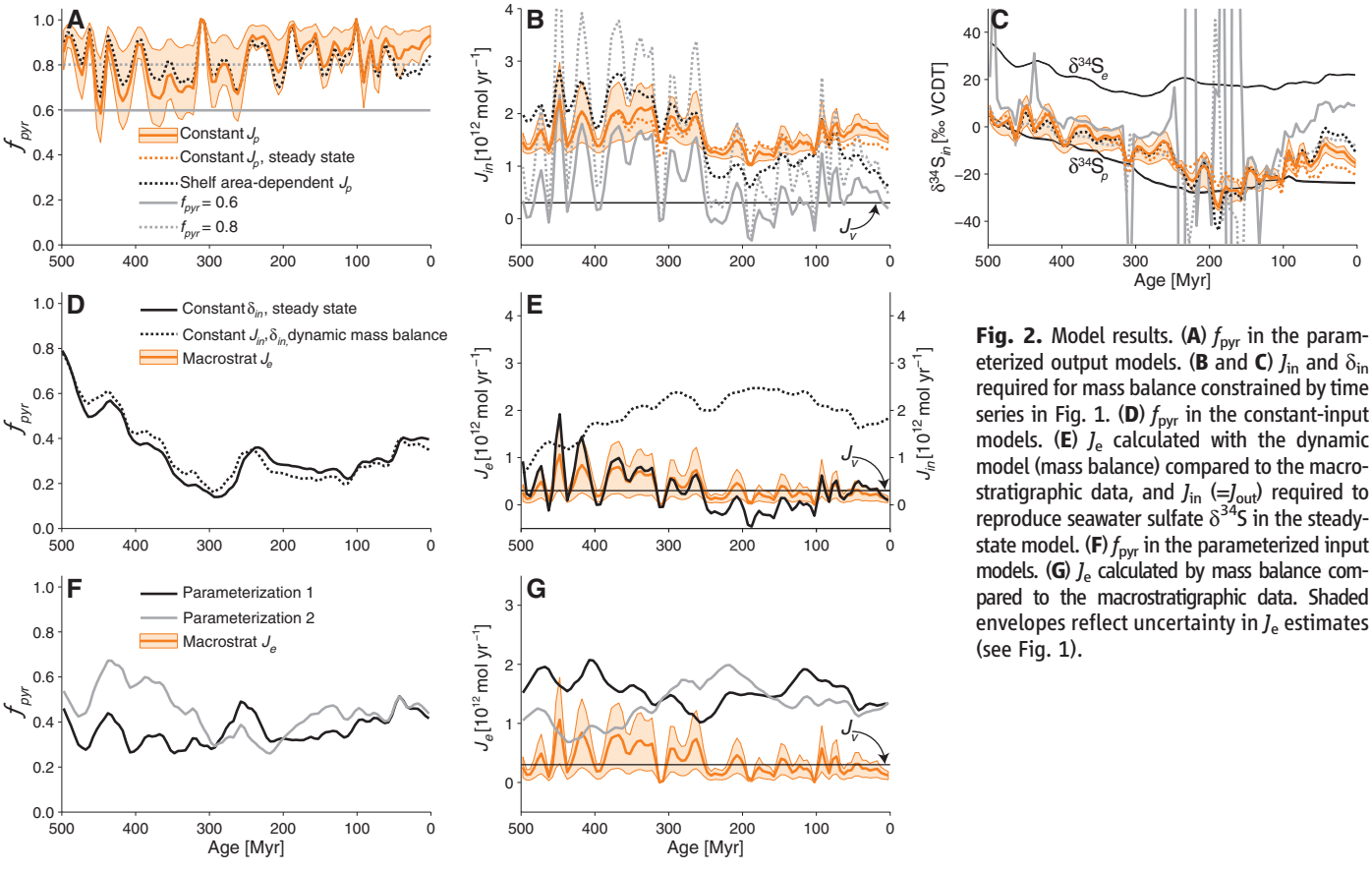

Fig. 2. Model results. (**A**) f_{pyr} in the parameterized output models. (**B** and **C**) J_{in} and δ_{in} required for mass balance constrained by time series in Fig. 1. (**D**) f_{pyr} in the constant-input models. (**E**) J_e calculated with the dynamic model (mass balance) compared to the macrostratigraphic data, and J_{in} (=J_{out}) required to reproduce seawater sulfate $\delta^{34}S$ in the steady-state model. (**F**) f_{pyr} in the parameterized input models. (**G**) J_e calculated by mass balance compared to the macrostratigraphic data. Shaded envelopes reflect uncertainty in J_e estimates (see Fig. 1).

merged continental area) yield results that are consistent both internally and with existing observations of seawater sulfate concentration and $\delta^{34}S$. Large and stable pyrite weathering and burial fluxes highlight the importance of oxidation-reduction feedbacks between carbon, iron, and sulfur (*24*) and imply a greater role for the sulfur cycle in regulating Phanerozoic atmospheric oxygen.

References and Notes

1. F. M. M. Morel, J. G. Hering, *Principles and Applications of Aquatic Chemistry* (Wiley, New York, 1993).
2. B. B. Jørgensen, *Nature* **296**, 643 (1982).
3. R. A. Berner, *Geochim. Cosmochim. Acta* **48**, 605 (1984).
4. R. A. Berner, *Am. J. Sci.* **287**, 177 (1987).
5. D. E. Canfield, *Annu. Rev. Earth Planet. Sci.* **33**, 1 (2005).
6. $\delta^{34}S = ({}^{34}R_{sam}/{}^{34}R_{ref} - 1) \times 1000$, where ${}^{34}R$ is the ratio of ${}^{34}S$ to ${}^{32}S$.
7. H. Strauss, *Palaeogeogr. Palaeocl.* **132**, 97 (1997).
8. N. P. Wu, J. Farquhar, H. Strauss, S. T. Kim, D. E. Canfield, *Geochim. Cosmochim. Acta* **74**, 2053 (2010).
9. T. K. Lowenstein, M. N. Timofeeff, S. T. Brennan, L. A. Hardie, R. V. Demicco, *Science* **294**, 1086 (2001).
10. J. Horita, H. Zimmermann, H. D. Holland, *Geochim. Cosmochim. Acta* **66**, 3733 (2002).
11. R. M. Garrels, A. Lerman, *Am. J. Sci.* **284**, 989 (1984).
12. D. E. Canfield, *Am. J. Sci.* **304**, 839 (2004).
13. A. Kampschulte, H. Strauss, *Chem. Geol.* **204**, 255 (2004).
14. D. B. Rowley, *Geol. Soc. Am. Bull.* **114**, 927 (2002).
15. J. M. Edmond, Y. Huh, in *Tectonic Uplift and Climate Change*, W. F. Ruddiman, W. Prell, Eds. (Plenum, New York, 1997), pp. 329–351.
16. A. B. Ronov, *Int. Geol. Rev.* **24**, 1313 (1982).
17. M. A. Zharkov, *History of Paleozoic Salt Accumulation*, A. L. Yanshin, Ed. (Springer, New York, 1981).
18. R. A. Berner, *Am. J. Sci.* **304**, 438 (2004).
19. S. E. Peters, N. A. Heim, *Paleobiology* **36**, 61 (2010).
20. Methods are available on *Science* Online.
21. C. R. Scotese, *Atlas of Earth History* (PALEOMAP Project, Arlington, TX, 2001).
22. J. K. Warren, *Earth Sci. Rev.* **98**, 217 (2010).
23. B. U. Haq, A. M. Al-Qahtani, *GeoArabia* **10**, 127 (2005).
24. L. R. Kump, R. M. Garrels, *Am. J. Sci.* **286**, 337 (1986).
25. D. E. Canfield, R. Raiswell, *Am. J. Sci.* **299**, 697 (1999).
26. R. Raiswell, *Elements* **7**, 101 (2011).
27. J. M. Rouchy, D. Noel, A. M. A. Wali, M. A. M. Aref, *Sediment. Geol.* **94**, 277 (1995).
28. T. M. Peryt, *Sediment. Geol.* **188–189**, 379 (2006).
29. W. Krijgsman, F. J. Hilgen, I. Raffi, F. J. Sierro, D. S. Wilson, *Nature* **400**, 652 (1999).
30. J. M. Rouchy, A. Caruso, *Sediment. Geol.* **188–189**, 35 (2006).
31. H. Rahimpour-Bonab, Z. Shariatinia, M. G. Siemann, *Geol. J.* **42**, 37 (2007).
32. P. M. Sadler, *GeoResearch Forum* **5**, 15 (1999).
33. S. E. Peters, *J. Geol.* **114**, 391 (2006).
34. B. C. Gill *et al.*, *Nature* **469**, 80 (2011).

Acknowledgments: We thank D. Canfield and J. Adkins for helpful discussion, and C. Scotese for help with the paleogeographic reconstructions. I.H. acknowledges support from a Texaco Postdoctoral Fellowship in Geological and Planetary Sciences at the California Institute of Technology and a Sir Charles Clore Prize for Outstanding Appointment in the Experimental Sciences at the Weizmann Institute of Science. S.E.P. was funded by NSF grant EAR-0819931. W.W.F. acknowledges support from the Agouron Institute and a David and Lucile Packard Foundation Fellowship for Science and Engineering. The binned macrostratigraphic data are available as a supplementary table on *Science* Online.

Supplementary Materials

www.sciencemag.org/cgi/content/full/337/6092/331/DC1
Materials and Methods
Supplementary Text
Figs. S1 to S5
References (*35–46*)
Database S1

7 February 2012; accepted 5 June 2012
10.1126/science.1220224

Rapid Variability of Seawater Chemistry Over the Past 130 Million Years

Ulrich G. Wortmann[1]* and Adina Paytan[2]*

Fluid inclusion data suggest that the composition of major elements in seawater changes slowly over geological time scales. This view contrasts with high-resolution isotope data that imply more rapid fluctuations of seawater chemistry. We used a non–steady-state box model of the global sulfur cycle to show that the global $\delta^{34}S$ record can be explained by variable marine sulfate concentrations triggered by basin-scale evaporite precipitation and dissolution. The record is characterized by long phases of stasis, punctuated by short intervals of rapid change. Sulfate concentrations affect several important biological processes, including carbonate mineralogy, microbially mediated organic matter remineralization, sedimentary phosphorous regeneration, nitrogen fixation, and sulfate aerosol formation. These changes are likely to affect ocean productivity, the global carbon cycle, and climate.

The chemical composition and mineralogy of skeletal limestones and biogenic carbonates vary systematically through time, indicating that the Mg/Ca ratio as well as other constituents of seawater have also changed (*1*). Fluid inclusion studies are also consistent with variable magnesium, calcium, sodium, and sulfate concentrations through time (*2*, *3*). Several hypotheses have been proposed to explain these secular trends, including changes in global weathering patterns (*4*), sea-floor spreading rates (*5*), or burial rates of these elements (*6*).

Evaporites play an important role in the latter process because their precipitation/dissolution rates exceed those of other sediments by three orders of magnitude (*7*, *8*). Halite is the dominant evaporite phase, but the effect of halite precipitation/dissolution on seawater chemistry is limited because the marine Na^+ and Cl^- reservoirs are large ($\approx 6.47 \times 10^{20}$ and 7.5×10^{20} mol respectively). Sulfur-bearing evaporites (such as $CaSO_4$) comprise on average 20% of an evaporite sequence (*9*) but have a 20 times smaller marine reservoir size than that of Cl^-.

The role of sulfur-bearing salts in controlling seawater chemistry is often overlooked. In the modern ocean, pyrite burial is not limited by sulfate availability (*10*), and the strong link between pyrite burial rates and sulfate concentration has just recently been recognized (*11*). Furthermore, basin-scale evaporites (BSEs) occur only sporadically in the geologic record and are not always visible, and the chemical composition of seawater does not depend on the mass of existing evaporites (Fig. 1A) but on the amount of salts that have already been eroded (Fig. 1B) and/or were originally extracted (Fig. 1C). The past 130 million years saw only two BSE events (Fig. 1C): one caused by the desiccation of the Mediterranean during the Messinian (*12*), and the second related to the Early Cretaceous opening of the South Atlantic (*11*, *12*).

Until recently, all available data supported the assumption of slow secular changes to major seawater constituents and their related biogeochemical fluxes. However, as the temporal resolution of proxy data increases, it becomes evident that the rate of change is often faster than expected from the residence time of major species.

High-resolution data sets of seawater $\delta^{34}S$ record two major events, at 130 to 120 million years ago (Ma) and 55 to 45 Ma, that require large changes to the S-fluxes and/or their isotopic composition. Previous interpretations of the $\delta^{34}S$ record called for changes in the planetary degassing flux and/or S burial rates (*6*). Clearly, volcanic activity and pyrite burial are major parameters, but we propose to broaden the discourse by including the effects of evaporite precipitation and dissolution. If these processes occur on a basin-wide scale, they will modify the flux and $\delta^{34}S$ of the sulfur input/output and change the marine sulfate concentration, which in turn affects pyrite burial in a nonlinear way (*11*), further affecting seawater isotopic composition. Under modern conditions, this effect is negligible. However, with decreasing sulfate concentrations, the importance of sulfate availability increases until it becomes the dominant parameter controlling pyrite burial (*11*).

[1]Geobiology Isotope Laboratory, Department of Geology, University of Toronto, Toronto, ON M5S 3B1, Canada. [2]Institute of Marine Sciences University of California Santa Cruz, Santa Cruz, CA 95064, USA.

*To whom correspondence should be addressed. E-mail: uli.wortmann@utoronto.ca (U.G.W.); apaytan@ucsc.edu (A.P.)

Here, we evaluate the effect of basin-scale precipitation/dissolution events, consider the evidence for such a scenario, and discuss alternative explanations for the existing data.

We used a non–steady-state box model of the global S-cycle to investigate how precipitation/dissolution events affect the weathering fluxes of ^{32}S, ^{34}S, and the sulfate concentration of the ocean, which in turn controls the burial fluxes of ^{32}S and ^{34}S (*13*). Our model demonstrates that we can match the first-order shape of the marine $\delta^{34}S$ record (Fig. 2) with two events: the deposition of a BSE between 122 and 120 Ma and the dissolution of a BSE between 51 and 47 Ma (1.02×10^{19} mol and 1.97×10^{19} mol $CaSO_4$, respectively) (fig. S2), which are well within existing estimates of known BSE deposits (Fig. 1).

The timing and magnitude of the evaporite sequences in the South Atlantic are well documented (*14*, *15*), and the decrease in seawater sulfate concentration is supported by geochemical data that suggest decoupling between iron and sulfur burial during the Early Aptian (*11*). BSEs affecting seawater $\delta^{34}S$ at this time is consistent with multiple lines of evidence, although increased volcanic activity also may have contributed to the trend (*16*, *17*).

For an Eocene dissolution event, much of the direct evidence has been literally dissolved; however, large swaths of the Paleotethys margins are lined with massive evaporite deposits of latest Neoproterozoic to Early Cambrian (LNPEC) age, likely formed during the breakup of Rodinia and/or Pannotia. The known outcrops stretch from Oman to Iran, to Afghanistan, to Pakistan, and into western India (*9*). This area is the most extensive evaporite belt on Earth and contains large amounts of sulfate (*9*), the erosion of which could explain the Eocene event.

However, evaporite erosion is usually treated as a continuous process—an assumption that is problematic because the long-term preservation of salt requires burial below the regolith-forming zone, and reactivation does not occur before renewed exhumation. More specifically, studies on modern dissolution processes suggest that the highest dissolution rates are achieved if evaporites act as aquifer with an active flow regime (*18*). Accordingly, the reactivation of old evaporites requires gentle tilting, sufficient precipitation, and efficient drainage. It is unlikely that such conditions persist over geological time scales in convergent margin settings. Therefore, the BSE deposits presently found along the Paleotethys margin probably experienced a window of drastically increased weathering rates during the initial phases of the India Eurasia collision, which occurred between 53.7 to 50.6 Ma (*19*, *20*). These ages are in agreement with the age range predicted by our model for evaporite dissolution and input into the ocean (51 to 47 Ma). If we accept the idea of BSE dissolution/precipitation events, this implies that marine sulfate concentrations changed considerably during the Early Cretaceous and the Early Eocene. The predicted sulfate concentrations are within the range of values derived from fluid inclusion studies (Fig. 2). Furthermore, the increased number of Eocene formations that contain gas-hydrate–related seep carbonates can be explained by the sudden availability of sulfate—a prerequisite for anaerobic methane oxidation and the subsequent precipitation of seep carbonates.

A prior model to explain the rapid Eocene 5 per mil (‰) raise in seawater $\delta^{34}S$ proposed that global pyrite burial rates increased fourfold as a result of euxinic conditions in the wake of the Eocene sea-level rise (*6*). The sedimentary evidence for increased pyrite burial is, however, controversial (*21*).

If the formation and dissolution of large-scale evaporite deposits is episodic as we suggest, this has several important consequences. Specifically, the salinity estimates (*12*) for much of the Phanerozoic have to be revised because large amounts of the LNPEC evaporites remained stored until the Eocene collision of India and Eurasia, and we need to recognize that the major ion composition of seawater varies considerably faster than previously thought. In addition, the dissolution and precipitation of large evaporite sequences affects the distribution of coprecipitating elements (such as strontium) and exerts a major control on the skeletal chemistry of calcifying organisms, possibly controlling the transition from calcite to aragonite seas (*22*). Furthermore, low sulfate concentrations imply reduced rates of organic matter remineralization, which affects the bioavailability of phosphorous, whereas sulfate concentrations above 8 mM may inhibit nitrogen fixation (*23*). Accordingly, variable sulfate concentrations are likely to modulate

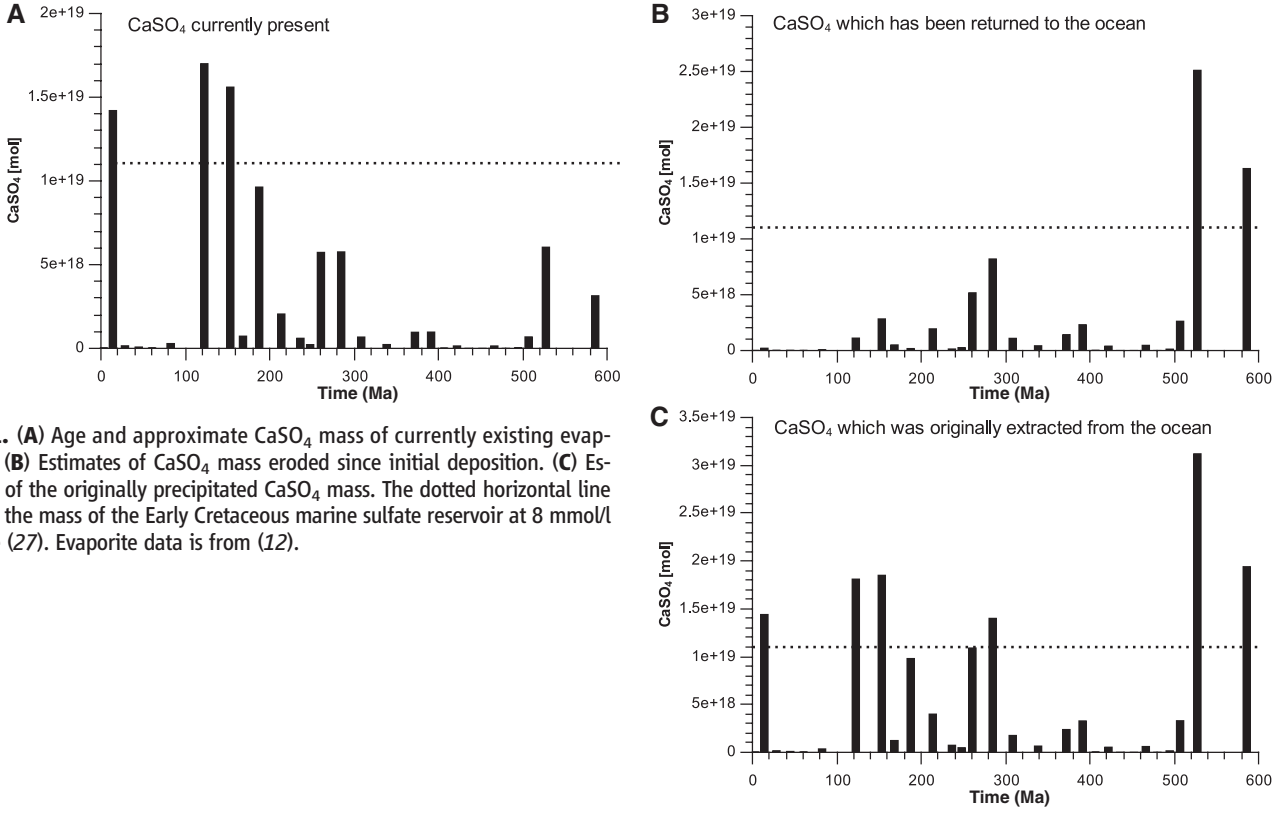

Fig. 1. (**A**) Age and approximate $CaSO_4$ mass of currently existing evaporites. (**B**) Estimates of $CaSO_4$ mass eroded since initial deposition. (**C**) Estimate of the originally precipitated $CaSO_4$ mass. The dotted horizontal line equals the mass of the Early Cretaceous marine sulfate reservoir at 8 mmol/l sulfate (*27*). Evaporite data is from (*12*).

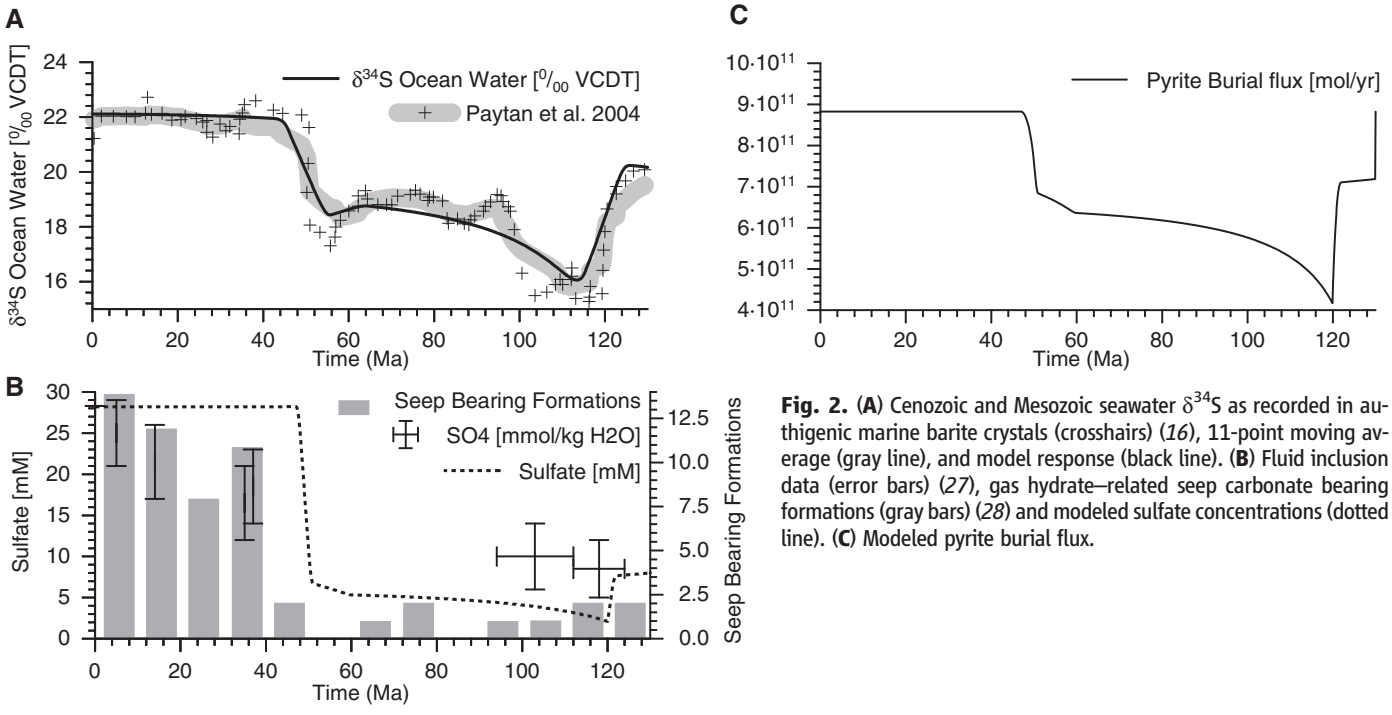

Fig. 2. (**A**) Cenozoic and Mesozoic seawater $\delta^{34}S$ as recorded in authigenic marine barite crystals (crosshairs) (*16*), 11-point moving average (gray line), and model response (black line). (**B**) Fluid inclusion data (error bars) (*27*), gas hydrate–related seep carbonate bearing formations (gray bars) (*28*) and modeled sulfate concentrations (dotted line). (**C**) Modeled pyrite burial flux.

long-term trends in marine ecology and ocean fertility (*24*). Indeed, the low sulfate concentration throughout the Mesozoic (*11*) may have been the very condition that enabled widespread episodes of black-shale formation (*25*) and probably resulted in higher methane fluxes across the benthic boundary layer (*11*). Moreover, because the ocean is a major source for sulfate aerosols, lower marine sulfate concentrations could have affected atmospheric aerosol chemistry, as well (*26*). Thus, times of high sulfate concentrations correlate with an increased aerosol load and global cooling, whereas times of low marine sulfate concentrations correspond with greenhouse periods. Specifically, the rapid rise of the marine sulfate concentrations during the Early Eocene probably increased the aerosol load in the atmosphere, which may have contributed to the demise of the Eocene Climatic Optimum and the onset of the long-term Cenozoic cooling trend.

Much remains to be learned about the contribution of BSEs to the evolution of ocean chemistry. It is evident, however, that the sheer size of these deposits as well as their dissolution/precipitation kinetics must have affected marine sulfate concentrations and thus the biogeochemical cycling of carbon, oxygen, and phosphorous. Most importantly, the assumption of slow secular seawater chemistry changes is neither necessary nor likely. Rather, sulfate concentrations remained stable over long periods of time but changed rapidly when continental breakup or collision events resulted in the creation or destruction of BSE deposits. This provides an explanation of the existing seawater S-isotope data, as well as exciting linkages between sulfur and other biogeochemical cycles, long-term trends in evolution, ocean fertility, and climate. Although this study focuses on the past 130 million years, similar interactions have likely occurred throughout the Phanerozoic.

References and Notes

1. B. H. Wilkinson, *Geology* **7**, 524 (1979).
2. T. K. Lowenstein, M. N. Timofeeff, S. T. Brennan, L. A. Hardie, R. V. Demicco, *Science* **294**, 1086 (2001).
3. J. Horita, H. Zimmermann, H. D. Holland, *Geochim. Cosmochim. Acta* **66**, 3733 (2002).
4. M. E. Raymo, W. F. Ruddiman, P. N. Froelich, *Geology* **16**, 649 (1988).
5. R. A. Spencer, L. A. Hardie, *Fluid-Mineral Interactions: A Tribute to H.P. Eugster*, R. J. Spencer, I.-M. Cho, Eds. (Geochemical Society, St. Louis, MO, 1990), vol. 2 of *Spec. Pub.*, pp. 409–419.
6. A. C. Kurtz, L. R. Kump, M. A. Arthur, J. C. Zachos, A. Paytan, *Paleoceanography* **18**, 1090 (2003).
7. G. Einsele, *Sedimentary Basins: Evolution, Facies, and Sediment Budget* (Springer Verlag, New York, 1992).
8. G. Nichols, E. W. C. Paola, in *Sedimentary Processes, Environments and Basins: A Tribute to Peter Friend*, F. J. G. van den Belt, P. L. de Boer, Eds. (Blackwell Publishing Ltd., Oxford, UK., 2009), pp. 242–252.
9. M. A. Zharkov, *History of Paleozoic Salt Accumulation* (Springer, Berlin, Heidelberg, New York, 1981).
10. R. A. Berner, R. Raiswell, *Geochim. Cosmochim. Acta* **47**, 855 (1983).
11. U. G. Wortmann, B. M. Chernyavsky, *Nature* **446**, 654 (2007).
12. W. W. Hay *et al.*, *Palaeogeogr. Palaeoclimatol. Palaeoecol.* **240**, 3 (2006).
13. Materials and methods are available as Supplementary materials on *Science* Online.
14. K. Burke, C. Şengör, *Mar. Geol.* **83**, 309 (1988).
15. J. R. Southam, W. W. Hay, *The Oceanic Lithosphere*, E. Emiliani, Ed. (Wiley-Interscience, New York, 1981), vol. 7 of *The Sea*, pp. 1617–1684.
16. A. Paytan, M. Kastner, D. Campbell, M. H. Thiemens, *Science* **304**, 1663 (2004).
17. N. DeBond, R. L. Oakes, A. Paytan, U. G. Wortmann, *Isotopes Environ. Health Stud.* **48**, 180 (2012).
18. T. C. Gustavson, W. W. Simpkins, A. Alhades, A. Hoadley, *Earth Surf. Process. Landf.* **7**, 545 (1982).
19. Y. Najman *et al.*, *J. Geophys. Res.* **115**, (B12), B12416 (2010).
20. M. Clementz *et al.*, *Geology* **39**, 15 (2011).
21. P. A. Allison, *Palaeontology* **31**, 1079 (1988).
22. P. Bots, L. G. Benning, R. E. M. Rickaby, S. Shaw, *Geology* **39**, 331 (2011).
23. R. Marino, R. W. Howarth, F. Chan, J. J. Cole, G. E. Likens, *Aquatic Biodiversity*, K. Martens, H. J. Dumont, Eds. (Springer Netherlands, 2003), vol. 171 of *Dev. Hydrobiol.*, pp. 277–293.
24. A. L. Cárdenas, P. J. Harries, *Nat. Geosci.* **3**, 430 (2010).
25. D. D. Adams, M. T. Hurtgen, B. B. Sageman, *Nat. Geosci.* **3**, 201 (2010).
26. V. W. Ribas, L. F. A. Ferrão, O. Roberto-Neto, F. B. Machado, *Chem. Phys. Lett.* **492**, 19 (2010).
27. T. K. Lowenstein, L. A. Hardie, M. N. Timofeef, R. V. Demicco, *Geology* **31**, 857 (2003).
28. S. Kiel, *Terra Nova* **21**, 279 (2009).

Acknowledgments: We thank B. Brunner, M. Kastner, and T. Lowenstein for discussions and their comments on an early draft of this manuscript. We also thank the three anonymous reviewers for their thoughtful comments, which helped clarify and improve the manuscript. This research was support by a Natural Sciences and Engineering Research Council of Canada Discovery Grant to U.G.W. and a NSF CAREER award to A.P. Model Data and Code are available as supplementary materials on *Science* Online.

Supplementary Materials

www.sciencemag.org/cgi/content/full/337/6092/334/DC1
Materials and Methods
Figs. S1 and S2
References (*29*–*37*)
Model Data and Code

16 February 2012; accepted 30 May 2012
10.1126/science.1220656

Identifying Influential and Susceptible Members of Social Networks

Sinan Aral* and Dylan Walker*

Identifying social influence in networks is critical to understanding how behaviors spread. We present a method that uses in vivo randomized experimentation to identify influence and susceptibility in networks while avoiding the biases inherent in traditional estimates of social contagion. Estimation in a representative sample of 1.3 million Facebook users showed that younger users are more susceptible to influence than older users, men are more influential than women, women influence men more than they influence other women, and married individuals are the least susceptible to influence in the decision to adopt the product offered. Analysis of influence and susceptibility together with network structure revealed that influential individuals are less susceptible to influence than noninfluential individuals and that they cluster in the network while susceptible individuals do not, which suggests that influential people with influential friends may be instrumental in the spread of this product in the network.

Peer effects are empirically elusive in the social sciences. Scholars in disciplines as diverse as economics, sociology, psychology, finance, and management are interested in whether children's peers influence their education; whether workers' colleagues influence their productivity; whether happiness, obesity, and smoking are "contagious"; and whether risky behaviors spread via peer influence. Answers to these questions are critical to policy because the success of intervention strategies in these domains depends on the robustness of estimates of the degree to which contagion is at work during a social epidemic (*1*, *2*). Robust estimation of peer effects is also critical to understanding whether new social media technologies magnify peer influence in product demand, voter turnout, and political mobilization or protest.

The recent availability of population-scale networked data sets generated by e-mail, instant messaging, mobile phone communications, and online social networks enables novel investigations of the diffusion of information and influence in networks (*3*–*9*). Unfortunately, identifying influence in these networks is difficult because estimation is confounded by homophily [the tendency for individuals to choose friends with similar tastes and preferences (*10*, *11*), and thus for preferences to be correlated among friends], confounding effects (the tendency for connected individuals to be exposed to the same external stimuli), and simultaneity (the tendency for connected individuals to co-influence each other and to behave similarly at approximately the same time), among other factors (*1*, *2*, *10*, *12*–*17*). Although some new methods separate peer influence from homophily and confounding factors in observational data (*11*), controlling for unobservable factors such as latent homophily (correlation among unobserved drivers of preferences among friends) remains difficult without exogenous variation in adoption probabilities across individuals (*18*). Fortunately, randomized experiments provide a more robust means of identifying causal peer effects in networks (*19*–*22*).

One particularly controversial argument in the peer effects literature is the "influentials" hypothesis—the idea that influential individuals catalyze the diffusion of opinions, behaviors, innovations, and products in society (*23*, *24*). Despite the popular appeal of this argument, a variety of theoretical models suggest that susceptibility, not influence, is the key trait that drives social contagions (*25*–*29*). Little empirical evidence exists to adjudicate these claims. Understanding whether influence, susceptibility to influence, or a combination of the two drives social contagions, and accurately identifying influential and susceptible individuals in networks, could enable new behavioral interventions to affect obesity, smoking, exercise, fraud, and the adoption of new products and services.

We conducted a randomized experiment to measure influence and susceptibility to influence in the product adoption decisions of a representative sample of 1.3 million Facebook users. The experiment involved the random manipulation of influence-mediating messages sent from a commercial Facebook application that lets users share information and opinions about movies, actors, directors, and the film industry. As users adopted and used the product, automated notifications of their activities were delivered to randomly selected peers in their local social networks. For example, when a user rated a movie on the application, a randomly selected subset of the user's Facebook friends were sent a message notifying them of the rating with a link to the canvas page describing the application and instructions on how to adopt it. Because message recipients were randomly selected, treated and untreated peers of the application user differed only by the number of randomized messages they received. Estimates of influence and susceptibility were obtained by modeling time to peer adoption as a function of the peer's treatment status—whether influence-mediating messages had been received, and if so, how many. An influence-mediating message generally refers to any communication between peers that could conduct influence (*19*, *30*), such as wearing a logo advertising a brand or recommending a product to a friend.

The experiment was conducted over 44 days during which 7730 product adopters sent 41,686 automated notifications to randomly chosen targets among their 1.3 million friends. This resulted in 976 unique peer adoptions, or a 13% increase in demand for the product relative to the number of initial adopters (see tables S1 to S4 and figs. S1 to S4).

Our method avoids several known sources of bias in influence identification by randomly manipulating who receives influence-mediating messages. First, we avoid selection bias by randomizing whether and to whom influence-mediating messages are sent (table S5). In uncontrolled environments, users may choose to send messages to peers who are more likely to like the product or to listen to their advice, which confounds estimates of susceptibility to influence by oversampling recipients who are more likely to respond positively. Second, our method eliminates bias created by homophily or assortativity in networks by randomizing the receipt of influence-mediating messages. Even latent homophily is controlled because similarity in unobserved attributes is equally represented across treatment groups. Third, the method controls for unobserved confounding factors, because randomly chosen peers are equally likely to be exposed to external stimuli that affect adoption (such as advertising campaigns or promotions). Fourth, the automatically generated messages include identical information, eliminating heterogeneity in message content and valence, which are known to affect responses to social influence (*31*). Differences in adoption between treatment groups can then be attributed solely to the number of influence-mediating messages they received.

Our statistical approach used hazard modeling, which is the standard technique for estimating social contagion in economics, marketing, and sociology [e.g., (*32*)]. However, we extended existing techniques to distinguish two types of peer adoption: (i) spontaneous adoption, which occurs in the absence of influence, and (ii) influence-driven adoption, which occurs in response to persuasive messages. This extension is important because even in the absence of influence, adoption outcomes cluster among peers as a consequence of homophily, assortativity, simultaneity, and correlated effects (*11*, *12*). We estimate the average treatment effects of notifications by aggregating many individual experiments in which messages were randomized within the local networks of the original adopting users (tables S6 and S7).

To estimate the moderating effects of an individual *i*'s attributes on the influence exerted

Stern School of Business, New York University, New York, NY 10012, USA.

*To whom correspondence should be addressed. E-mail: sinan@stern.nyu.edu (S.A.); dwalker@stern.nyu.edu (D.W.)

by i on peer j (and to distinguish them from the moderating effects of j's attributes on j's susceptibility to influence), we use a continuous-time single-failure proportional hazards model. Survival models provide information about how quickly peers respond (rather than simply whether they respond) and also correct for censoring of peer responses that may occur beyond the experiment's observation window. We specify the following model:

$$\lambda_j(t,X_i,X_j,N_j) = \lambda_0(t)\ \exp[N_j(t)\beta_N + X_i\beta^i_{\text{spont}} + X_j\beta^j_{\text{spont}} + N_j(t)X_i\beta_{\text{infl}} + N_j(t)X_j\beta_{\text{susc}}] \quad (1)$$

where λ_j is the hazard of peer j of application user i adopting the application (each peer j is associated with one and only one application user i), $\lambda_0(t)$ represents the baseline hazard, X_i represents a set of individual attributes of an application user i, X_j represents a set of individual attributes of peer j, $N_j(t)$ represents the number of notifications received by peer j of application user i as a function of time, $N_j(t)$ reflects the extent to which j has been exposed to influence-mediating messages from user i, β_N estimates the effect of receiving a notification on the likelihood of peer adoption (holding sender and potential recipient attributes constant), β^i_{spont} estimates the propensity for peers of user i with attributes X_i to spontaneously adopt in the absence of influence ($N_j = 0$), β^j_{spont} estimates the propensity for peer j with attributes X_j to spontaneously adopt in the absence of influence ($N_j = 0$), β_{infl} estimates the impact of user i's attributes on i's ability to influence peer j to adopt the application above and beyond j's propensity to adopt spontaneously, and β_{susc} estimates the impact of j's attributes on j's likelihood to adopt as a result of influence above and beyond j's propensity to adopt spontaneously (for alternative specifications, robustness, and goodness of fit, see table S8 and figs. S5 to S12).

Models of dyadic (two-party) relationships between influencers and potential susceptibles test whether influence depends on characteristics of the relationship between a given pair—for example, whether women are more influential over men than men are over women. To estimate the effect of dyadic relationships, we use the following continuous-time single-failure proportional hazards model:

$$\lambda_j(t,X_i,X_j,N_j) = \lambda_0(t)\ \exp[N_j(t)\beta_N + S(X_i,X_j)\beta^{i-j}_{\text{spont}} + N_j(t)S(X_i,X_j)\beta^{i\to j}_{\text{infl}}] \quad (2)$$

where X_i represents a set of the individual attributes of the sender, X_j represents a set of the individual attributes of peer j (the potential recipient), and $S(X_i, X_j)$ represents a set of dyadic covariates that characterize the joint attributes of the sender-recipient pair. Dyadic covariates estimate, for example, whether influence is stronger when the sender and recipient are the same or different genders. β_{spont} estimates the effect of a dyadic relationship between application user i and peer j on the tendency for j to adopt spontaneously. For example, when the dyadic relationship variable is an indicator of similarity (such as "same age"), β_{spont} captures the extent to which similarity on that dimension predicts the likelihood to spontaneously adopt, and represents the propensity to adopt as a result of preference similarity and other explanations for correlations in adoption likelihoods between peers that are not a result of influence. β_{infl} estimates the effect of the dyadic attribute (e.g., "same age") on the degree to which i influences j to adopt, above and beyond j's likelihood to spontaneously adopt.

On average, susceptibility decreases with age (Fig. 1). People over the age of 31 are the least susceptible to influence; relative to people who do not declare their age, they have an 18% lower hazard of adopting the application upon receiving a notification ($P < 0.05$; the statistical significance of all estimates is derived from χ^2 tests). However, people in this same age quartile (>31) are significantly more influential than people in the lowest age quartile (<18). Relative to people younger than 18, people over 31 have a 51% greater instantaneous likelihood of influencing their peers to adopt with an influence-mediating message ($P < 0.05$).

Men are 49% more influential than women ($P < 0.05$), but women are 12% less susceptible to influence than men ($P < 0.05$). Single and married individuals are the most influential. Single individuals are significantly more influential than those who are in a relationship (113% more influential, $P < 0.05$) and those who report their relationship status as "It's complicated" (128% more influential, $P < 0.05$). Married individuals are 140% more influential than those in a relationship ($P < 0.01$) and 158% more influential than those who report that "It's complicated" ($P < 0.01$). Susceptibility increases with increasing relationship commitment until the point of marriage. People who are engaged to be married are 53% more susceptible to influence than single people ($P < 0.05$), whereas married individuals are the least susceptible to influence ($P = 0.93$, n.s.). The engaged and those who report that "It's complicated" are the most susceptible to influence. Those who report that "It's complicated" are 111% more susceptible to influence than baseline users who do not report their relationship status on Facebook ($P < 0.05$), and those who are engaged are 117% more susceptible than baseline users ($P < 0.001$).

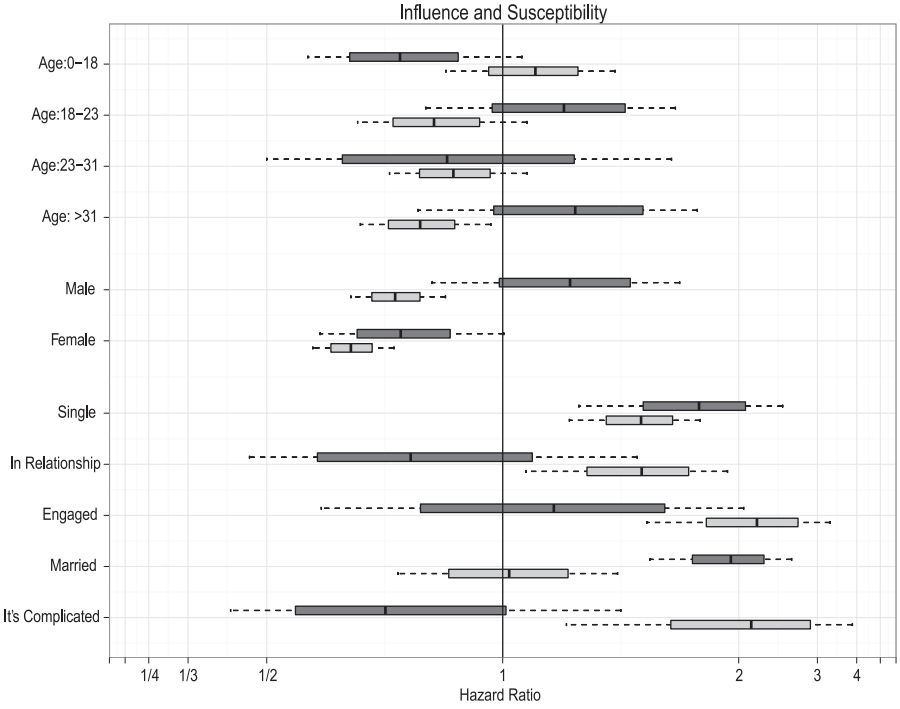

Fig. 1. Effects of age, gender, and relationship status on influence and susceptibility. Influence (dark gray) and susceptibility to influence (light gray) are shown with SEs (boxes) and 95% confidence intervals (whiskers). The figure displays hazard ratios (HRs) representing the percent increase (HR > 1) or decrease (HR < 1) in adoption hazards associated with each attribute. Age is binned by quartiles. Each attribute is shown as a pair of estimates, one reflecting influence (dark gray) and the other susceptibility (light gray). Personal relationship status reflects the status of an individual's current romantic relationship and is specified on Facebook as Single, In a Relationship, Engaged, Married, or It's Complicated. Estimates are shown relative to the baseline case for each attribute, which is the average for individuals who do not display that attribute in their online profile.

People exert the most influence on peers of the same age [97% more influence than baseline ($P < 0.01$)] (Fig. 2). They also seem to exert more influence on younger peers than on older peers, although this difference is not significant. In nondyadic susceptibility models, we found that women were less susceptible to influence than men (Fig. 1). Dyadic models (Fig. 2) further revealed that women exert 46% more influence over men than over other women ($P = 0.01$). Finally, individuals in equally (and more) committed relationships relative to their peers (e.g., those who are married versus those who are engaged, in a relationship, or single) are significantly more influential [equally committed, 70% more influential than baseline ($P < 0.05$); more committed, 101% more influential than baseline ($P < 0.05$)], although future work will be needed to determine whether there is something "different" about people who do not provide some information (e.g., age) (table S1).

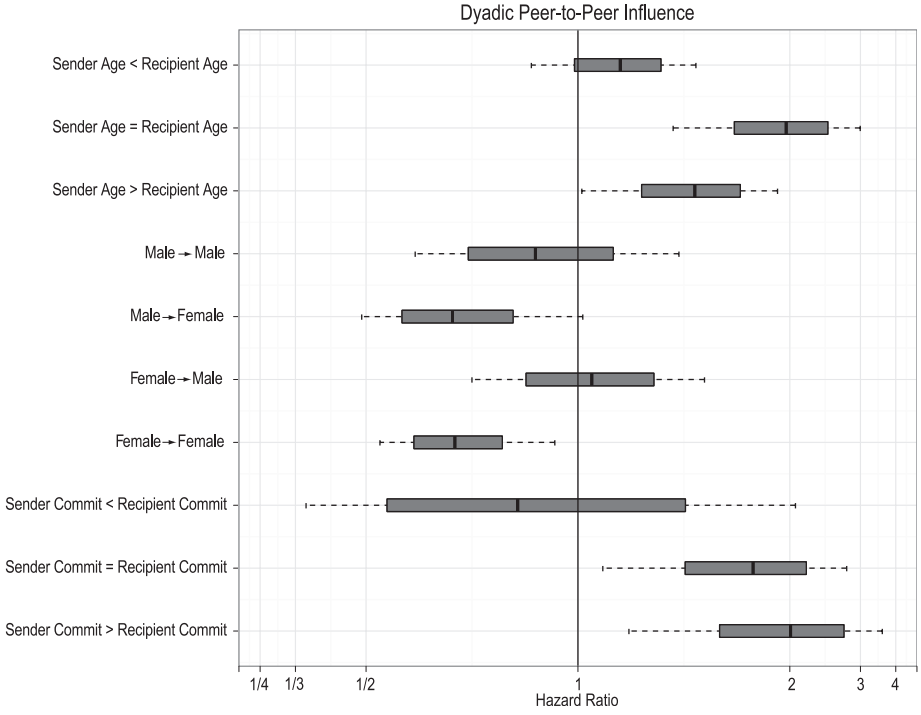

Fig. 2. Dyadic influence models involving age, gender, and relationship status. The results include the relative age, gender similarity, and commitment level of the relationship status of senders and recipients, with SEs (boxes) and 95% confidence intervals (whiskers). The figure displays hazard ratios representing the percent increase (HR > 1) or decrease (HR < 1) in adoption hazards associated with each attribute. The baseline case represents dyads in which the attribute being examined is unreported in the Facebook profile of one or both peers.

Comparing spontaneous adoption hazards to influenced adoption hazards reveals the potential roles that different individuals play in the diffusion of a behavior (Fig. 3). For example, in the case of the movie product we studied, both single and married individuals adopt spontaneously more often than baseline users [single, 31% more often ($P < 0.05$); married, 36% more often ($P = 0.06$)], are more influential than baseline users [single, 71% more influential ($P < 0.01$); married, 94% more influential ($P < 0.001$); Fig. 1], and have peers who are no more likely to adopt spontaneously than baseline users ($P = 0.39$ and 0.08; n.s.). This suggests that influence exerted by single and married individuals positively contributes to this product's diffusion without any need to target their peers. On the other hand, women are poor candidates for targeted advertising because they are likely to adopt spontaneously and are 22% less influential on their peers than baseline users ($P < 0.05$). Those who claim that their relationship status is complicated are easily influenced by their peers to adopt [35% more susceptible than baseline ($P < 0.05$)] but are not influential enough to spread the product further ($P = 0.49$; n.s.). These results have implications for policies designed to promote or inhibit diffusion, and they illustrate the general utility of our method for informing intervention strategies, targeted advertising, and policy-making.

Figure 4 shows the joint distributions of influence and susceptibility in a network, reveal-

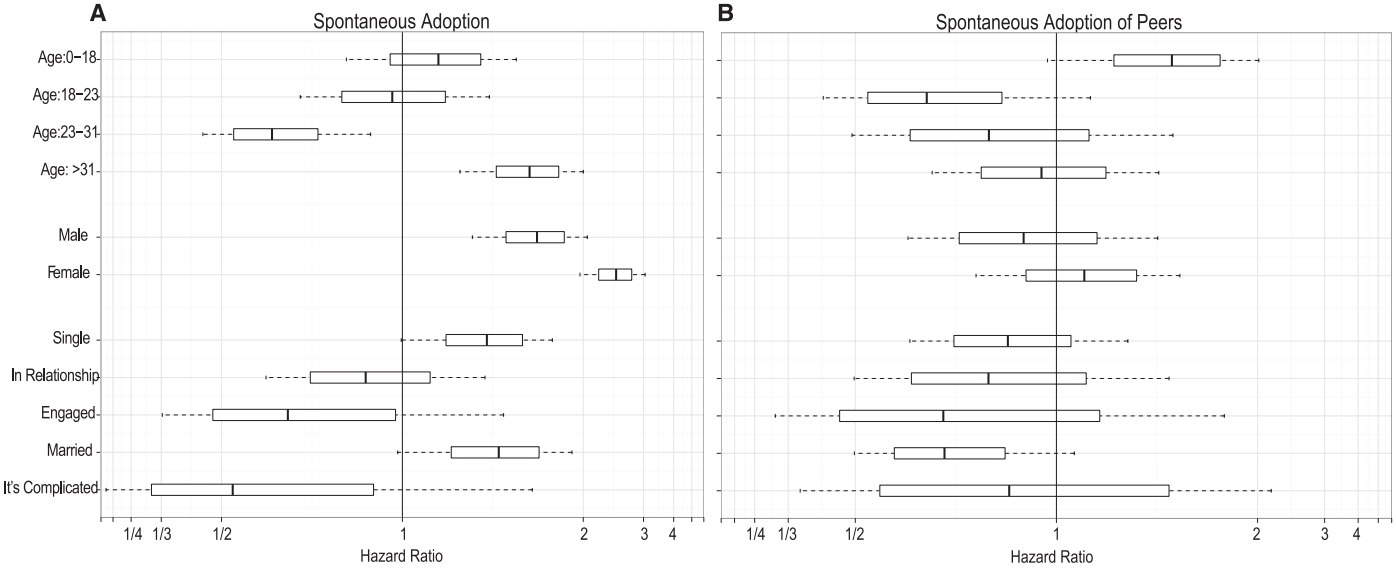

Fig. 3. (**A**) Hazard ratios for individuals to adopt spontaneously as a function of their attributes, with SEs (boxes) and 95% confidence intervals (whiskers). (**B**) Hazard ratios for individuals to have peers who adopt spontaneously as function of their attributes. The figure displays hazard ratios representing the percent increase (HR > 1) or decrease (HR < 1) in adoption hazards associated with each attribute.

ing the correlation of influence and susceptibility across all individuals and the assortativity of influence and susceptibility across all individuals and their peers in the network. We calculated individual influence and susceptibility scores as the product of the estimated hazard ratios of individuals' attributes for a broader sample of 12 million users with 85 million relationships. The analysis combines the estimated impact of each demographic attribute on influence and susceptibility to calculate individuals' overall influence and susceptibility scores. For example, a 35-year-old single female has an influence score equal to $\exp(\beta_{\text{infl, }>31} + \beta_{\text{infl, single}} + \beta_{\text{infl, female}})$. The following inferences can be drawn from our results:

1) Highly influential individuals tend not to be susceptible, highly susceptible individuals tend not to be influential, and almost no one is both highly influential and highly susceptible to influence (Fig. 4, panel I). This implies that influential individuals are less likely to adopt the product as a consequence of natural influence processes (i.e., in the absence of targeting); hence, targeting influentials with low propensities to spontaneously adopt would be a potentially viable promotion strategy.

2) The "influentials" and "susceptibles" hypotheses are orthogonal claims. Both influential individuals and noninfluential individuals have approximately the same distribution of susceptibility to influence among their peers; hence, being influential is not simply a consequence of having susceptible peers (Fig. 4, panel II). Both influence and susceptibility play a role in the peer-to-peer diffusion of the product. Combining studies of influence with studies of susceptibility will therefore likely improve our understanding of the diffusion of behavioral contagions.

3) There are more people with high influence scores than high susceptibility scores (Fig. 4, panel I), which suggests that, in our context, targeting should focus on the attributes of current adopters (e.g., giving individuals incentives to influence their peers) rather than attributes of their peers (e.g., giving individuals with susceptible peers incentives to adopt).

4) Influentials cluster in the network. As shown in Fig. 4, panel III, influential individuals connected to other influential peers are approximately twice as influential as baseline users. In contrast, we find a tendency for less susceptible users to cluster together and no clusters of highly susceptible users (Fig. 4, panel IV). The clustering of influentials suggests the existence of a multiplier effect of infecting a highly influential individual. However, such individuals also tend to have peers with only average susceptibility, making predictions about which effect would dominate difficult without more evidence. Additional empirical and simulation studies should therefore examine the effects of the assortativity of influence and susceptibility on the diffusion of behaviors, products, and diseases.

Analyzing the heat maps in Fig. 4 is not sufficient to identify optimal intervention targets, because more information is needed about the network structure around candidate targets in each region. For example, an individual with high influence and high peer susceptibility in the upper right quadrant of in Fig. 4, panel II, may seem like a good target, but may be of low degree or may be isolated. The network diagrams to the left of the heat maps show the assortativity of influence and susceptibility in ego networks from different regions combined with information on their network structures, such as network degree and the distribution of influence and susceptibility across peers in the network. Analyzing networks in different regions of the

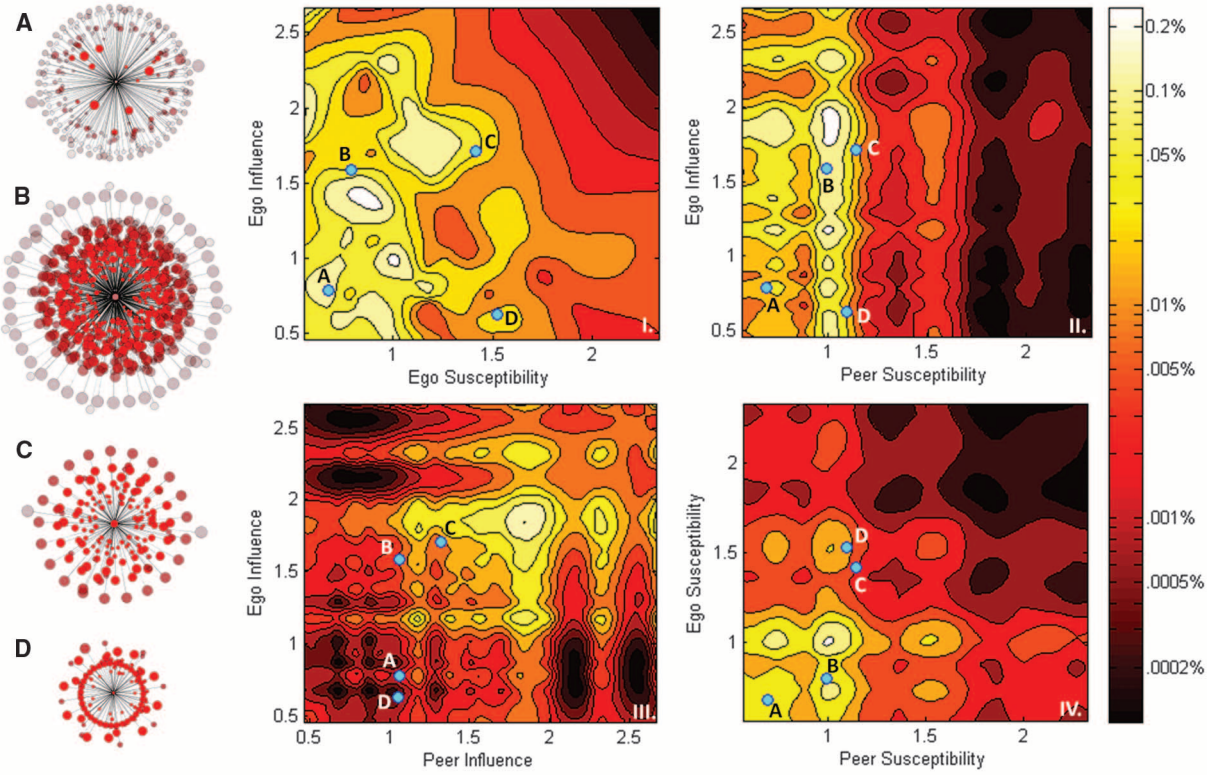

Fig. 4. Scores for 12 million Facebook users (collected from users who installed one of several other Facebook applications developed by the company) with 85 million relationships are calculated by means of hazard rate estimates relative to the baseline hazard in the influence and susceptibility model described in the text. The resulting heat maps are shown at the right. Panel I displays the percentage of people (ego) with predicted influence (*y* axis) and predicted susceptibility (*x* axis). Panels II to IV display the percentage of ego-peer relationships: panel II, ego influence (*y* axis) and peer susceptibility (*x* axis); panel III, ego influence (*y* axis) and peer influence (*x* axis); and panel IV, ego susceptibility (*y* axis) and peer susceptibility (*x* axis). The heat maps do not provide information on network structure, which can be important for informing targeting decisions. The diagrams to the left of the heat maps show the assortativity of influence and susceptibility in ego networks drawn from the regions of the heat maps labeled A, B, C, and D. Nodes in the networks are sized in proportion to their predicted influence (larger nodes are more influential) and are shaded and placed relative to their predicted susceptibility (redder nodes and nodes closer to ego are more susceptible; grayer nodes and nodes farther from ego are less susceptible).

heat maps, such as those displayed in Fig. 4, can suggest optimal targets. For example, node C is not only highly influential, highly susceptible, and has peers who are themselves influential and susceptible, but is also of above average degree in its region and has many peers who are susceptible rather than one highly susceptible peer driving the average susceptibility in its network. These characteristics in combination make C a good target.

Our method uses randomized experiments to identify influential and susceptible individuals in large social networks; however, the work does have limitations. Although we avoid bias by randomizing message recipient selection and holding message content constant, recipient selection and message content may be important aspects of influence and should therefore be estimated in future experiments. Furthermore, it is still not clear whether influence and susceptibility are generalized characteristics of individuals or instead depend on which product, behavior, or idea is diffusing. Although our estimates should generalize to the diffusion of similar products, they are not conclusions about who is more or less influential in general. Our experimental methods for influence identification, however, are generalizable and can be used to measure influence and susceptibility in the diffusion of other products and behaviors in a variety of settings.

Previous research has taken an individualistic view of influence—that someone's importance to the diffusion of a behavior depends only on his or her individual attributes or personal network characteristics. In contrast, our results show that the joint distributions of influence, susceptibility, and the likelihood of spontaneous adoption in the local network around individuals together determine their importance to the propagation of behaviors. Future research should therefore examine how the codistribution of influence, susceptibility, and dyadic induction in networks affects the diffusion of behaviors, the development of social contagions, and the effects of policies intended to promote or contain behavior change. More generally, our results show the potential of methods based on large-scale in vivo randomized experiments to robustly estimate peer effects and identify influential and susceptible members of social networks.

References and Notes

1. S. Aral, *Mark. Sci.* **30**, 217 (2011).
2. S. Aral, D. Walker, *IEEE Intell. Syst.* **26**, 91 (2011).
3. G. Kossinets, D. J. Watts, *Science* **311**, 88 (2006).
4. D. Lazer *et al.*, *Science* **323**, 721 (2009).
5. N. Eagle, M. Macy, R. Claxton, *Science* **328**, 1029 (2010).
6. S. A. Golder, M. W. Macy, *Science* **333**, 1878 (2011).
7. S. Aral, M. W. Van Alstyne, *Am. J. Sociol.* **117**, 90 (2011).
8. E. Sun, I. Rosenn, C. Marlow, T. Lento, in *Proceedings of the Third International Conference on Weblogs and Social Media* (AAAI Press, Menlo Park, CA, 2009).
9. J. Leskovec, L. A. Adamic, B. A. Huberman, *ACM Trans. Web* 10.1145/1232722.1232727 (2007).
10. M. McPherson, L. Smith-Lovin, J. M. Cook, *Annu. Rev. Sociol.* **27**, 415 (2001).
11. S. Aral, L. Muchnik, A. Sundararajan, *Proc. Natl. Acad. Sci. U.S.A.* **106**, 21544 (2009).
12. C. F. Manski, *Soc. Methodol.* **23**, 1 (1993).
13. S. Currarini, M. O. Jackson, P. Pin, *Proc. Natl. Acad. Sci. U.S.A.* **107**, 4857 (2010).
14. H. Noel, B. Nyhan, *Soc. Networks* **33**, 211 (2011).
15. W. Hartmann *et al.*, *Mark. Lett.* **19**, 287 (2008).
16. N. A. Christakis, J. H. Fowler, *N. Engl. J. Med.* **357**, 370 (2007).
17. R. Lyons, *Stat. Polit. Policy* 10.2202/2151-7509.1024 (2011).
18. C. R. Shalizi, A. C. Thomas, *Sociol. Methods Res.* **40**, 211 (2011).
19. S. Aral, D. Walker, *Manage. Sci.* **57**, 1623 (2011).
20. D. Centola, *Science* **329**, 1194 (2010).
21. S. Leider, M. M. Möbius, T. Rosenblat, Q.-A. Do, *Q. J. Econ.* **124**, 1815 (2009).
22. E. Bakshy, I. Rosenn, C. Marlow, L. Adamic, in *WWW '12 Proceedings of the 21st International Conference on World Wide Web* (ACM, New York, 2012), pp. 519–528.
23. E. Katz, *Public Opin. Q.* **21**, 61 (1957).
24. T. W. Valente, *Network Models of the Diffusion of Innovations* (Hampton, Cresskill, NJ, 1995).
25. D. Kempe, J. Kleinberg, É. Tardos, in *Proceedings of the Ninth ACM SIGKDD International Conference on Knowledge Discovery and Data Mining* (Association for Computing Machinery, New York, 2003), pp. 137–146.
26. M. Granovetter, *Am. J. Sociol.* **83**, 1420 (1978).
27. D. J. Watts, P. S. Dodds, *J. Consum. Res.* **34**, 441 (2007).
28. P. S. Dodds, D. J. Watts, *Phys. Rev. Lett.* **92**, 218701 (2004).
29. D. Centola, M. Macy, *Am. J. Sociol.* **113**, 702 (2007).
30. D. Godes *et al.*, *Mark. Lett.* **16**, 415 (2005).
31. C. Heath, C. Bell, E. Sternberg, *J. Pers. Soc. Psychol.* **81**, 1028 (2001).
32. R. Iyengar, C. Van den Bulte, T. W. Valente, *Marketing Sci.* **30**, 195 (2011).

Acknowledgments: We thank S. Aral, H. Frydman, C. Hurvich, P. Perry, J. Simonoff, and M. Sternberg for invaluable discussions. Supported by a Microsoft research faculty fellowship (S.A.) and by NSF Career Award 0953832 (S.A.). The research was approved by the NYU institutional review board. There are legal obstacles to making the data available, but code is available upon request. The requests for data and randomization of message targets we used are standard ways in which applications request and use user data on Facebook. They are covered by the Facebook privacy policy and terms of service. Opt-in permissions were granted by the user to the application developer on a per-application basis when the user installed the application, via Facebook application authentication dialogs. In the dialogs we asked for all the categories of data we used in the study, and all of these requests were in line with the Facebook terms of service. Users saw these requests and opted in to them before installing the app.

Supplementary Materials

www.sciencemag.org/cgi/content/full/science.1215842/DC1
Materials and Methods
Figs. S1 to S12
Tables S1 to S9

26 October 2011; accepted 30 May 2012
Published online 21 June 2012;
10.1126/science.1215842

Sex-Specific Adaptation Drives Early Sex Chromosome Evolution in *Drosophila*

Qi Zhou and Doris Bachtrog*

Most species' sex chromosomes are derived from ancient autosomes and show few signatures of their origins. We studied the sex chromosomes of *Drosophila miranda*, where a neo-Y chromosome originated only approximately 1 million years ago. Whole-genome and transcriptome analysis reveals massive degeneration of the neo-Y, that male-beneficial genes on the neo-Y are more likely to undergo accelerated protein evolution, and that neo-Y genes evolve biased expression toward male-specific tissues—the shrinking gene content of the neo-Y becomes masculinized. In contrast, although older X chromosomes show a paucity of genes expressed in male tissues, neo-X genes highly expressed in male-specific tissues undergo increased rates of protein evolution if haploid in males. Thus, the response to sex-specific selection can shift at different stages of X differentiation, resulting in masculinization or demasculinization of the X-chromosomal gene content.

X and Y chromosomes follow distinctive evolutionary trajectories after recombination becomes suppressed between ancestral homologous autosomes with a sex-determining function (*1*). The lack of recombination greatly impairs natural selection on the Y, which loses most of its original genes and often accumulates repetitive DNA (*2*). However, Y chromosomes are not complete evolutionary dead ends; instead, their male-limited transmission favors the gain of male-related genes ("masculinization"). Low gene density yet enrichment of male-specific genes is shared among many independently evolved ancient Ys (*3*, *4*), but few traces of their evolutionary origins remain, making processes involved in Y degeneration little understood. Conversely, the X still recombines in females, and selection can effectively purge deleterious alleles and incorporate beneficial mutations (*2*). Unlike autosomes, the X is transmitted more often through females than males, favoring an underrepresentation of male-beneficial genes on the X ("demasculinization") (*5*, *6*). Further, almost all X-linked genes are haploid in males (hemizygous) and can fix re-

Department of Integrative Biology, University of California Berkeley, Berkeley, CA 94720, USA.

*To whom correspondence should be addressed. E-mail: dbachtrog@berkeley.edu

cessive male-advantageous alleles more easily than can autosomes (*7*), potentially leading to masculinization. These aspects of X chromosome biology dictate unusual and sometimes opposing patterns of sequence and expression evolution (*8*) but are difficult to distinguish in ancestral systems.

The genome of *Drosophila* fly species can be divided into a set of homologous chromosomal arms called "Muller elements" (*9*). Chromosomal fusions between the ancient sex chromosomes (Muller-A element, referred here as "chrXL" and "chrY") with autosomes have repeatedly generated younger secondary sex chromosomes. Male *Drosophila* lack meiotic recombination (*9*); thus, Y-fused autosomes (neo-Ys) cannot recombine with their homologs (neo-Xs), which sets the stage for sex chromosome differentiation. *D. miranda* harbors two such successive fusions that created sex chromosomes of different ages (Fig. 1A) (*10*). Muller-D became sex-linked before the divergence of *D. miranda* and *D. pseudoobscura* roughly 10 to 18 million years ago and resembles the ancestral sex chromosomes; the non-recombining Muller-D element is almost completely degenerated and now part of the heterochromatic Y (*11*), whereas its recombining counterpart ("chrXR") evolved an architecture typical of an X (*5*, *12*). Another fusion specific to *D. miranda* involves Muller-C element (referred as "neo-X" and "neo-Y") and occurred only about 1 million years ago (*13*). This very young sex-chromosome system is in the process of evolving from a pair of ordinary autosomes to a pair of heteromorphic sex chromosomes. Cytogenetic studies and investigations of individual genes or genomic regions have revealed that the *D. miranda* neo-Y is intermediately degenerate (*10*, *14*–*16*), rendering the neo-X partially hemizygous.

We conducted a whole-genome analysis of the neo-sex chromosomes, integrated with transcriptomes from multiple tissues using next-generation sequencing technology. We sequenced both sexes of an inbred *D. miranda* strain (MSH22), and assembled scaffolds were anchored onto the *D. pseudoobscura* genome (table S1) (*17*). We annotated a total of 14,819 proteins for the *D. miranda* genome, using 16,133 *D. pseudoobscura* proteins as queries. We assessed the quality of our assemblies using bacterial artificial chromosome clone sequences and 454 data (table S3) and validated our chromosomal assignments by comparing male and female mapping coverage along each chromosome (Fig. 1B). Coverage of male and female coincides well along the autosomes, whereas both chrXL and chrXR show only about half as many reads mapped in males as in females (Fig. 1B and table S4), indicating that their homologous ancient Ys are too degenerate to show any significant sequence similarity. In contrast, male coverage along the neo-X is about three quarters that of females, suggesting that parts of the neo-Y are highly diverged from the neo-X. Of the neo-X sequence, 71.8% can be aligned with the neo-Y, with 1.5% (±0.00093%) nucleotide divergence between aligned regions. Coding regions are under stronger selective constraint and exhibit a higher alignment rate (92.6%) and lower divergence between the neo-X and neo-Y (1.1% ± 0.18%).

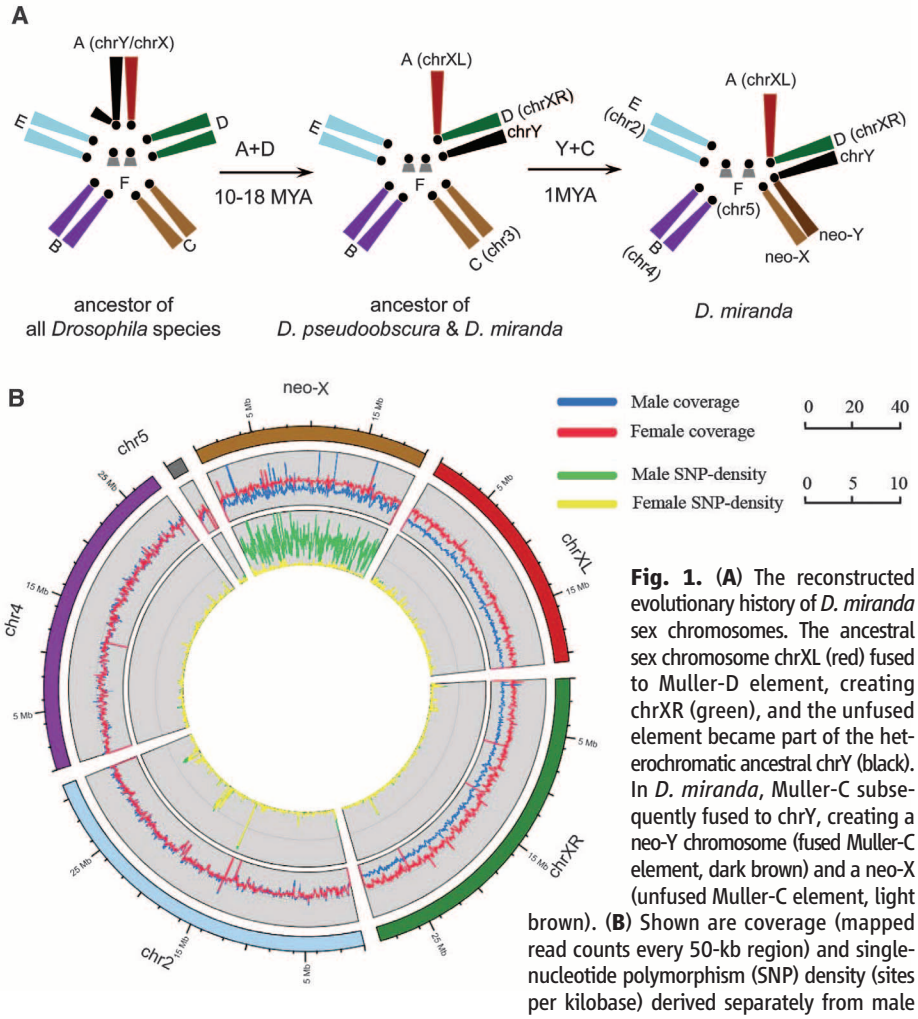

Fig. 1. (**A**) The reconstructed evolutionary history of *D. miranda* sex chromosomes. The ancestral sex chromosome chrXL (red) fused to Muller-D element, creating chrXR (green), and the unfused element became part of the heterochromatic ancestral chrY (black). In *D. miranda*, Muller-C subsequently fused to chrY, creating a neo-Y chromosome (fused Muller-C element, dark brown) and a neo-X (unfused Muller-C element, light brown). (**B**) Shown are coverage (mapped read counts every 50-kb region) and single-nucleotide polymorphism (SNP) density (sites per kilobase) derived separately from male and female genomic reads in a 5-kb sliding window across the *D. miranda* genome. The high male SNP density along the neo-X (male, 3.696 versus female, 0.080 sites per kilobase) reflects divergence between the neo-X and neo-Y chromosomes.

We compared protein-coding regions to gain insights into the process of gene loss of a Y. The neo-X and neo-Y are derived from a gene-rich autosome, with initially identical gene sets (*10*): 2951 genes with intact open reading frames (ORFs) could be annotated on the neo-X, whereas only 1941 intact ORFs were identified on the neo-Y. The remaining 1010 genes that were ancestrally present on the neo-Y (34.2%) are probably nonfunctional: 848 ORFs are disrupted by premature terminal codons (PTC) and/or frame-shift mutations, and 162 genes are partially or completely deleted from the neo-Y (Fig. 2A) (*17*). No spatial clustering of nonfunctional genes was detected on the neo-Y (Fig. 2B).

Severely disabling mutations have also accumulated in regulatory regions on the neo-Y. We compared allelic expression of 2165 neo-sex linked genes in males that were expressed from the neo-X: 883 genes (40.8%) show similar levels of expression from both chromosomes, whereas 947 (43.7%) are expressed at a significantly higher level from the neo-X, and 335 genes (15.5%) are neo-Y–biased (binomial test, $P < 0.05$), whereas 220 genes (10.2%) with a transcribed neo-X copy are completely silenced on the neo-Y. A large fraction of neo-Y genes is still transcribed, despite having disrupted ORFs: 83.0% of all neo-Y genes with nonsense mutations are transcribed, yet at a significantly lower level than that of genes with intact neo-Y ORFs (Wilcoxon test, $P < 2.2 \times 10^{-16}$) (Fig. 2B). This implies that down-regulated genes either tend to acquire nonsense mutations or that pseudogenes become transcriptionally silenced on the neo-Y but could also reflect up-regulation of the neo-X copy at nonfunctional neo-Y genes (dosage compensation) (*12*). Gene loss is nonrandom with regard to gene function. Nonfunctional and down-regulated genes on the neo-Y are significantly enriched for

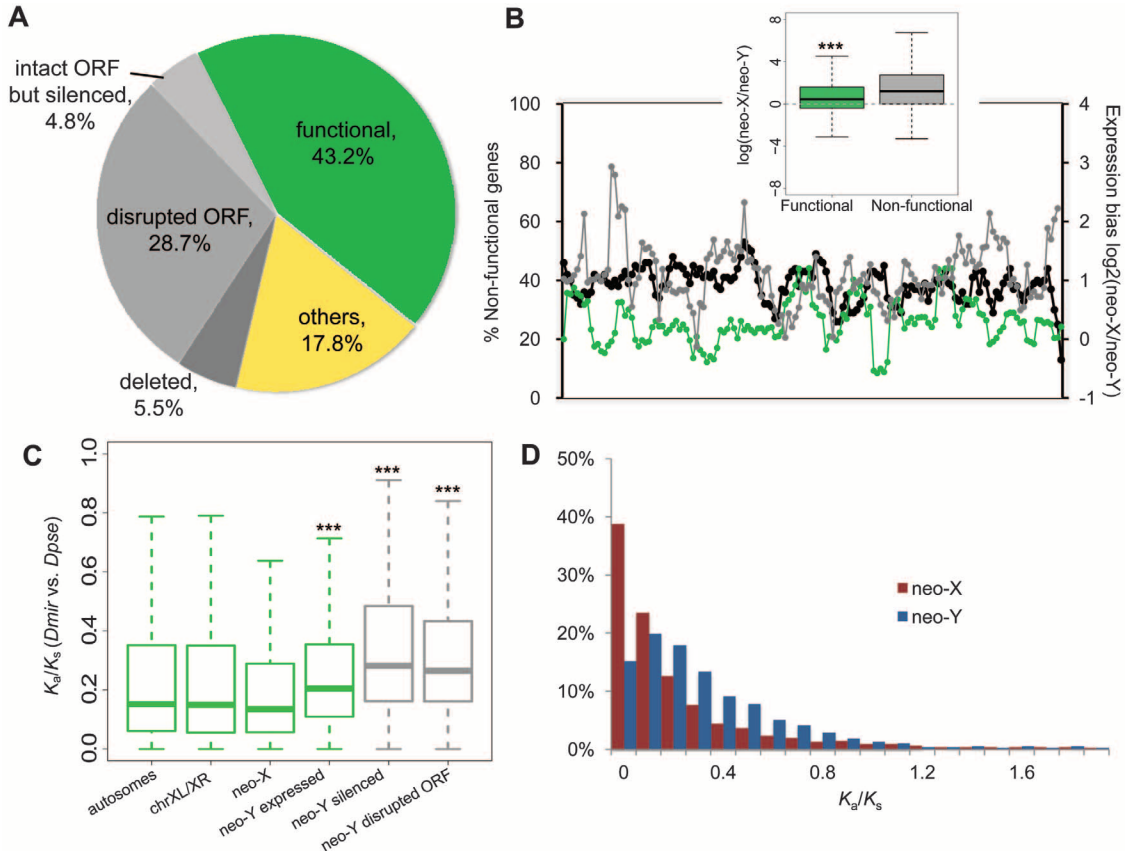

Fig. 2. (**A**) Composition of neo-Y genes with regard to inferred functionality (green, intact ORFs and detectable expression in adult male; gray, disrupted ORF and/or silenced expression; and yellow, genes without neo-X expression or without diagnostic SNPs). (**B**) The chromosomal distribution of nonfunctional genes across a sliding window size of 20 genes (black line). Average neo-X expression bias within the investigated window was calculated from log ratios of neo-X versus neo-Y expression for functional (green) and nonfunctional (gray) genes. Functional neo-Y genes show significantly less neo-X–biased expression than do nonfunctional genes (boxplot, $P < 2.2 \times 10^{-16}$, Wilcoxon test). (**C**) Evolutionary rate comparisons (K_a/K_s ratios relative to *D. pseudoobscura*) among genes on different chromosomes. Wilcoxon tests show significant differences in K_a/K_s ratios between neo-X versus neo-Y genes, genes with intact neo-Y copies with versus without expression ($P = 0.000242$), and disrupted versus intact transcribed neo-Y genes ($P = 2.971 \times 10^{-12}$). Different levels of significance are marked as asterisks. (**D**) The frequency distribution of K_a/K_s ratios of neo-X and neo-Y genes.

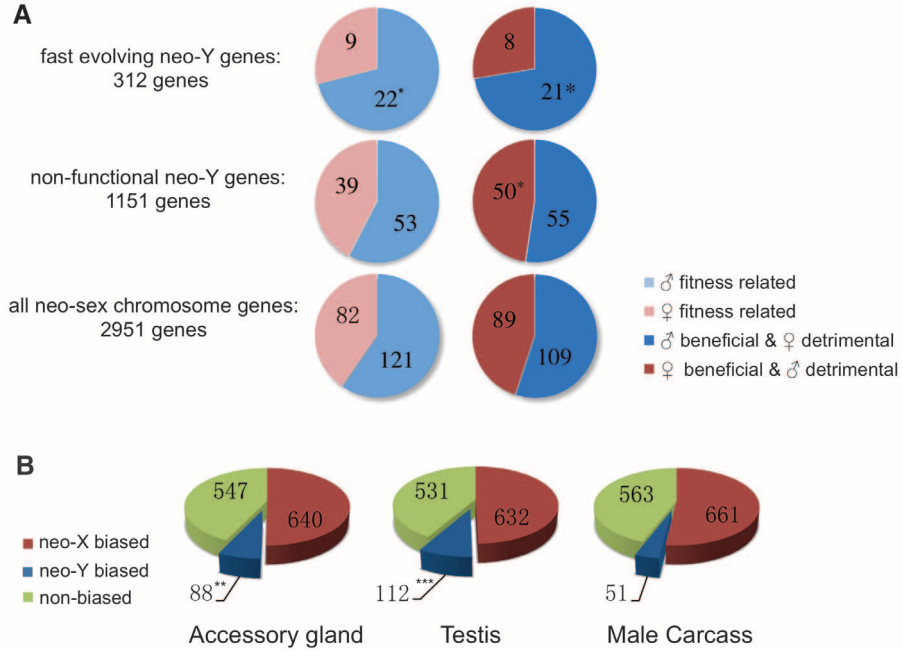

Fig. 3. (**A**) Sex-specific fitness effects and sexual antagonism of neo-sex genes (light blue, male-fitness related; light red, female-fitness related; dark blue, male-beneficial/female-detrimental; dark red, female-beneficial/male-detrimental). Significance is evaluated by comparing all neo-sex genes to either fast evolving or nonfunctional neo-Y genes (*$P < 0.05$, **$P < 0.01$). (**B**) The number of neo-X–biased (red), neo-Y–biased (blue), and nonbiased (green) genes in different tissues of male *D. miranda*.

various gene ontology (GO) categories of primary metabolic processes (such as GO 0046165, 0016042, and 0006094), whereas genes involved in regulatory (GO 0050789 and 0048519) or developmental processes (GO 0032502) tend to maintain nonbiased expression and intact ORFs (one-tailed Fisher's exact test, $P < 0.01$) (tables S5 and S6). Thus, although natural selection is impaired on the neo-Y, it tends to maintain haploinsufficient genes (such as regulatory genes), whereas haplosufficient genes (such as metabolic enzymes) are more prone to degeneration (*18*). Overall, ~40% of the neo-Y genes have lost their functions within 1 million years.

Deleterious mutations with more subtle effects also accumulate on the neo-Y. We calculated pairwise rates of nonsynonymous (K_a) and synonymous changes (K_s), and their ratios (ω), using *D. pseudoobscura* as an outgroup. Genes on the neo-Y evolve significantly faster than do their neo-X homologs or genes on other chromosomes at both synonymous and nonsynonymous sites (Wilcoxon test, $P < 0.01$) (table S7). Selection to maintain codon usage bias is reduced in *D. miranda* (*19*); thus, patterns of synonymous changes (K_s) should largely reflect mutational differences. Although neo-Y genes generally show lower codon bias (table S7), this difference is not statistically significant between

the neo-X and neo-Y or between functional and nonfunctional neo-Y genes (Wilcoxon test, $P > 0.05$). Thus, the contribution of codon bias selection to elevated K_s patterns appears limited and instead may reflect male-driven evolution (*20*). Neo-Y genes with disrupted ORFs evolve significantly faster at the protein level than do those with intact ORFs (Wilcoxon test, $P = 2.97 \times 10^{-12}$) (Fig. 2C), and intact but silenced neo-Y genes evolve significantly faster than do those still expressed from the neo-Y (Wilcoxon test, $P = 2.42 \times 10^{-4}$) (Fig. 2C). This suggests that neo-Y genes with disrupted ORFs or silenced expression are subject to little selective constraint, and we classified all these genes as nonfunctional in subsequent analysis (fig. S4) (*17*). The distribution of ω at neo-Y genes is shifted toward neutral evolution (ω = 1), and the proportion of genes under strong selective constraints (ω < 0.1) is greatly reduced as compared with neo-X genes (15.02 versus 38.78%) (Fig. 2D). This pattern is consistent with an accumulation of mildly deleterious amino acid mutations at many neo-Y loci.

Decay in gene function is the primary but not only force driving early Y evolution. Y chromosomes are limited to males, and genes found on ancient Ys often have male-specific function (*3*, *4*). It is unclear whether male-related genes only accumulate on old, gene-poor Ys, where adaptive mutations experience little interference from segregating deleterious mutations, or whether masculinization accompanies early stages of Y evolution, and thus contributes to degeneration through hitchhiking effects (fixations of deleterious mutations linked to strongly beneficial alleles) (*2*). To explore whether adaptive evolution for male-function is operating on neo-Y genes, we performed maximum-likelihood analysis of the lineage-specific ω ratio of all functional neo-sex genes (*17*). We identified 312 transcribed genes evolving significantly faster on the neo-Y lineage (as compared with 66 genes evolving faster on the neo-X lineage; likelihood ratio test, $P < 0.05$) and evaluated whether this set of functional neo-Y genes shows characteristics of male-specific selection. Recently acquired male-limited inheritance releases sexually antagonistic male-beneficial/female-detrimental mutations from counter selection in females, and such genes may show increased rates of adaptive evolution on the neo-Y. We classified orthologous *D. miranda* genes according to a sexual antagonism scheme proposed for *D. melanogaster* (table S8) (*21*) and found a significant enrichment of male-beneficial/female-detrimental genes or genes correlated with male-specific fitness among the fast-evolving neo-Y genes (Fisher's exact test, $P < 0.05$) (Fig. 3A). These gene categories are not enriched among nonfunctional genes, indicating that male-beneficial genes are under selective constraint on the neo-Y and that male-specific selection is driving adaptive protein evolution at some neo-Y genes. Genes related to male fitness are more likely to be functional on the neo-Y, whereas genes classified as female-beneficial/male-detrimental are enriched for genes with disrupted ORFs or silenced expression (Fig. 3A). This suggests that although selection operates to maintain male-beneficial genes, those harming males are actively removed from the neo-Y. Transcriptome analysis of male-specific organs (testis and accessory gland) versus male somatic carcass tissues (removing these organs) provides additional evidence for masculinization. In all tissues, the majority of genes show neo-X–biased expression. However, testis and accessory glands harbor about twice as many genes with neo-Y–biased expression as compared with that of male somatic carcass (Fisher's exact test, $P < 0.05$) (Fig. 3B), caused by up-regulation of the neo-Y alleles (fig. S5) (*17*). Also, functional neo-Y genes in *D. miranda* have evolved significantly increased expression-specificity in accessory glands (relative to male somatic carcass tissues) as compared with that of their orthologous *D. pseudoobscura* genes (figs. S6 and S7) (*17*). Further, genes with significant neo-Y–biased expression are enriched for male reproductive GO terms, including "insemination," "copulation," and "reproductive process" (GO 0007320, 0007620, and 0022414) (table S11). Thus, although most neo-Y genes undergo degeneration, a subset acquires or improves male-related functions. The absence of sexual conflicts on a male-limited chromosome enables male-specific adaptation and may appreciably contribute to Y degeneration through the hitchhiking effect (*22*).

Evolutionary forces on an evolving X chromosome can operate in opposite directions. Female-biased transmission will favor female-specific genes and disfavor male-beneficial genes. Old X chromosomes in *Drosophila* contain a deficiency of genes expressed in male-specific tissue (*5*, *6*). In *D. miranda*, both chrXL and chrXR show a clear under-representation of testis and accessory gland genes (Fisher's exact test, $P < 0.05$) (Fig. 4A), and ovary expression is higher for genes located on chrXL and chrXR (Wilcoxon test, $P < 0.05$) (Fig. 4B) (*17*). Thus, an X chromosome becomes fully demasculinized and feminized within 10 to 18 million years in *Drosophila* (*5*). No chromosome-wide changes in overall expression patterns in sex tissues are observed on the neo-X (Fig. 4, A and B), and its origin may be too recent for a large turnover of gene content to have taken place. Young X-linked genes in *Drosophila* tend to be male-biased (*23*), possibly because of the fixation of recessive, male-beneficial mutations, and demasculinization appears to happen over longer evolutionary time periods. In *D. miranda*, approximately half of the neo-X genes have no functional neo-Y homologs (they are hemizygous) and might show different evolutionary dynamics than those with functional neo-Y copies (diploid neo-X genes). We find that hemizygous genes evolve significantly faster at their neo-X branch than do diploid ones (median ω ratios of 0.1416 versus 0.0997, Wilcoxon test, $P = 0.0005187$) (Fig. 4C). If male-beneficial

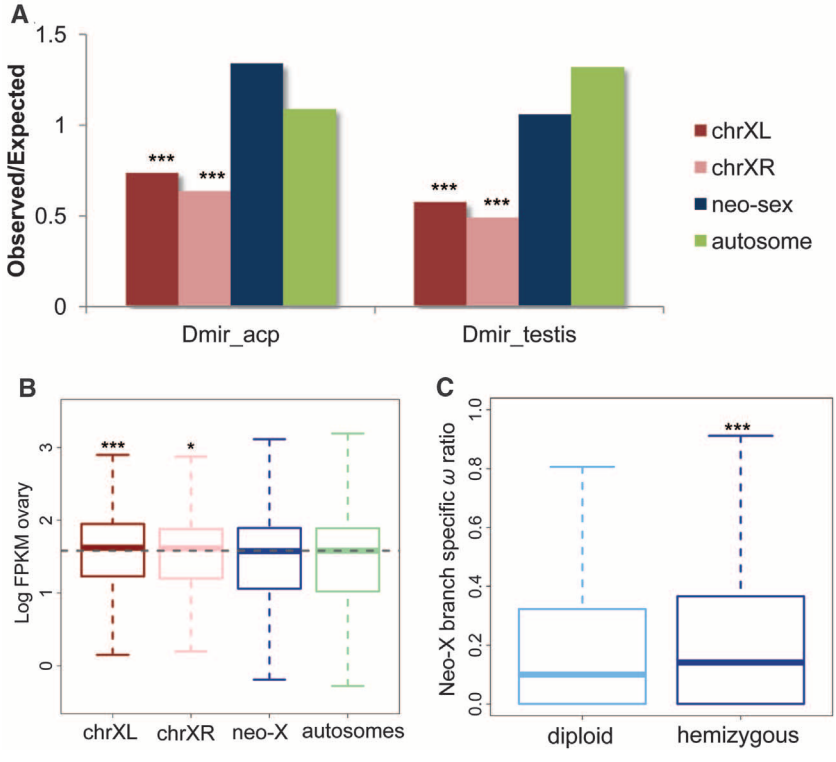

Fig. 4. (**A**) The observed/expected ratio of genes highly expressed (top 500; fig. S7 for different cutoffs) in testis or accessory glands. (**B**) Log-based absolute expression levels [fragments per kilobase of exon per million fragments mapped (FPKM)] from ovary for each chromosome (fig. S7). (**C**) The ω ratio on the neo-X branch at hemizygous and diploid neo-X genes.

adaptation drives elevated protein evolution at hemizygous neo-X genes, this pattern should be more pronounced for genes expressed highly in a male-specific tissue. Indeed, hemizygous (but not diploid) neo-X genes show a significant positive correlation between their absolute expression levels in accessory gland and ω ratios (F-statistic comparing diploid versus hemizygous neo-X genes, $P < 0.05$) (*17*), and a similar trend is observed for expression levels in testis but not somatic genes (fig. S11) (*17*). Thus, masculinization occurs on hemizygous neo-X loci, whereas demasculinization and feminization dominate on chrXL and chrXR. Gene loss, gain, and movement appear as the dominant mechanisms for depleting male genes on the X (*5*), and differences in dominance and rates could contribute to the observed temporal dynamics of masculinization and feminization/demasculinization. Recessive male-beneficial amino acid substitutions might accumulate relatively quickly in hemizgyous neo-X genes, whereas gene content turnover removing male genes might proceed slowly over longer time periods. Also, demasculinization might result from cellular processes that only operate on older X chromosomes, such as dosage compensation or silencing of the X during spermatogenesis (*24*, *25*). Overall, a variety of—and sometimes opposing—evolutionary forces operate on evolving sex chromosomes because of common sexual conflicts.

References and Notes

1. J. J. Bull, *Evolution of Sex Determining Mechanisms* (Benjamin Cummings, Menlo Park, CA, 1983).
2. B. Charlesworth, D. Charlesworth, *Philos. Trans. R. Soc. Lond. B Biol. Sci.* **355**, 1563 (2000).
3. L. B. Koerich, X. Wang, A. G. Clark, A. B. Carvalho, *Nature* **456**, 949 (2008).
4. H. Skaletsky *et al.*, *Nature* **423**, 825 (2003).
5. D. Sturgill, Y. Zhang, M. Parisi, B. Oliver, *Nature* **450**, 238 (2007).
6. E. Betrán, K. Thornton, M. Long, *Genome Res.* **12**, 1854 (2002).
7. B. Charlesworth, J. Coyne, N. Barton, *Am. Nat.* **130**, 113 (1987).
8. B. Vicoso, B. Charlesworth, *Nat. Rev. Genet.* **7**, 645 (2006).
9. H. J. Muller, in *The New Systematics*, J. Huxley, Ed. (Clarendon Press, Oxford, 1940), pp. 185–268.
10. M. Steinemann, S. Steinemann, *Genetica* **102/103**, 409 (1998).
11. A. B. Carvalho, A. G. Clark, *Science* **307**, 108 (2005).
12. I. Marín, A. Franke, G. J. Bashaw, B. S. Baker, *Nature* **383**, 160 (1996).
13. D. Bachtrog, B. Charlesworth, *Nature* **416**, 323 (2002).
14. M. Steinemann, S. Steinemann, F. Lottspeich, *Proc. Natl. Acad. Sci. U.S.A.* **90**, 5737 (1993).
15. D. Bachtrog, *Nat. Genet.* **34**, 215 (2003).
16. D. Bachtrog, E. Hom, K. M. Wong, X. Maside, P. de Jong, *Genome Biol.* **9**, R30 (2008).
17. Materials and methods are available as supplementary materials on *Science* Online.
18. F. A. Kondrashov, E. V. Koonin, *Trends Genet.* **20**, 287 (2004).
19. D. Bachtrog, *Genetics* **165**, 1221 (2003).
20. D. Bachtrog, *Mol. Biol. Evol.* **25**, 617 (2008).
21. P. Innocenti, E. H. Morrow, *PLoS Biol.* **8**, e1000335 (2010).
22. D. Bachtrog, *Nat. Genet.* **36**, 518 (2004).
23. Y. E. Zhang, M. D. Vibranovski, B. H. Krinsky, M. Long, *Genome Res.* **20**, 1526 (2010).
24. D. Bachtrog, N. R. Toda, S. Lockton, *Curr. Biol.* **20**, 1476 (2010).
25. E. Lifschytz, D. L. Lindsley, *Proc. Natl. Acad. Sci. U.S.A.* **69**, 182 (1972).

Acknowledgments: We thank R. Nielsen, M. Eisen, X. Xun, and L. Tian for help and discussion. This work was funded by NIH grants (R01GM076007 and R01GM093182) and a Packard Fellowship to D.B. All DNA/RNA-seq reads are deposited at www.ncbi.nlm.nih.gov/sra under accession no. SRA048115. The genome assembly and annotation is available at the National Center for Biotechnology Information under BioProject ID PRJNA77213.

Supplementary Materials

www.sciencemag.org/cgi/content/full/337/6092/341/DC1
Materials and Methods
Figs. S1 to S11
Tables S1 to S12
References (*26*–*44*)

30 May 2012; accepted 7 June 2012
10.1126/science.1225385

Hypoxia Triggers Meiotic Fate Acquisition in Maize

Timothy Kelliher* and Virginia Walbot*

Evidence from confocal microscopic reconstruction of maize anther development in fertile, *mac1* (excess germ cells), and *msca1* (no germ cells) flowers indicates that the male germ line is multiclonal and uses the MAC1 protein to organize the somatic niche. Furthermore, we identified redox status as a determinant of germ cell fate, defining a mechanism distinct from the animal germ cell lineage. Decreasing oxygen or H_2O_2 increases germ cell numbers, stimulates superficial germ cell formation, and rescues germinal differentiation in *msca1* flowers. Conversely, oxidizing environments inhibit germ cell specification and cause ectopic differentiation in deeper tissues. We propose that hypoxia, arising naturally within growing anther tissue, acts as a positional cue to set germ cell fate.

Most animals sequester germline stem cells during embryogenesis (*1*, *2*), whereas plants are strictly vegetative until intrinsic and environmental cues trigger reproduction (*3*, *4*). The morphogenetic mechanism underlying the somatic-to-germinal switch is a botanical mystery, which if understood would permit tailored manipulations in crop breeding and yield enhancement.

The angiosperm male germ line develops in immature anthers, within each of four lobes surrounding a central vasculature (*5*), viewed transversely as a butterfly shape (fig. S1). We tracked cellular ontogeny in three-dimensional reconstructions of ~1000 fertile anthers by confocal microscopy, finding that anther length is a precise and reliable proxy for developmental stage. In 70- to 120-μm-long anthers, each lobe consisted of 15 to 20 isodiametric L2-d (layer 2–derived, tracing back to the second meristem layer) cells, haphazardly arranged with 3 to 5 cells in transverse view (fig. S2). Starting at 120 μm and continuing for 30 hours to ~220 μm, successive, symmetric divisions in different L2-d progenitors yielded a column of 8 to 12 presumptive germinal cells, initiating centrally where lobes are widest and completing at the tapered tip and base (Fig. 1A and figs. S3 and S4). The majority of these presumptive archesporial cells derived from apical progenitors [63%, 67 out of 106 (67/106)], but 21% were lateral (22/106), and 16% were basal (17/106) (Fig. 1B). Therefore, in a fertile lobe, all L2-d cells can generate presumptive archesporial cells, which are central in transverse view, surrounded by four or five L2-d neighbors. Initially these presumptive germ cells lacked the well-established (*6*) morphological traits of premeiotic cells, but ~12 hours after birth, archesporial cells were distinguished from neighboring L2-d cells by their enlarged and nonrectilinear shape, dimly mottled cytoplasmic stain, and 2-μm-wide unstained boundary. Differentiated archesporial cells contained elevated amounts of MAC1 protein, a molecular marker for fate acquisition (Fig. 1C) (*7*).

Shortly after archesporial cell enlargement in the transverse view, encircling L2-d cells began dividing periclinally, founding the secondary parietal layer and endothecium. This process begins centrally at ~180 μm, and a full somatic bilayer is constituted by ~280 μm. In *multiple archesporial cells 1* (*mac1*) male sterile anthers, the bilayer is replaced by a single faulty layer and excess archesporial cells (*8*). In primordia (<120-μm anther length) and later developmental stages, *mac1* lobes had extra L2-d cells, including supernumerary central cells, all of which differentiated as archesporial (Fig. 1A and fig. S5). The encircling ring of L2-d cells generated additional archesporial cells for 24 hours after normal cessation (Fig. 1, A and D), never forming the somatic bilayer. Once specified, *mac1* archesporial cells proliferated excessively: 30% were EdU+ (5'-ethynyl-2'-deoxyuridine) versus 12% in fertile anthers (fig. S6). When analyzed by quantitative real-time polymerase chain reaction (qRT-PCR), *Mac1* transcripts were low in anther primordia; expression increased 20-fold during germinal specification (anther length, 150 μm) and was highly specific to laser-microdissected archesporial cells both 1 and 3 days after

Department of Biology, Stanford University, Stanford, CA 94305, USA.

*E-mail: tkellih1@stanford.edu (T.K.); walbot@stanford.edu (V.W.)

specification (Fig. 1E). MAC1 is a secreted ligand (*7*); homologs in rice and *Arabidopsis* bind leucine-rich repeat receptor-like kinases (*9*–*11*), defining a signaling module. We conclude that MAC1 has two roles: (i) autonomously limiting the proliferation of multipotent L2-d cells and their archesporial derivatives, and then (ii) directing the L2-d ring to exit multipotency, differentiate as somatic, and make the signature periclinal division to form the somatic bilayer. Distinctive receptors or intracellular events in archesporial and L2-d cells may facilitate differential interpretation of the MAC1 signal from the archesporial source.

Despite excess proliferation and the absence of normal soma, *mac1* archesporial cells followed normal gene expression patterns in preparation for meiosis: of the 297 genes identified by transcriptome profiling as archesporial cell–enriched in fertile anthers (*12*), 96.7% had parallel expression in microdissected *mac1* archesporial cells (table S1). *mac1* archesporial cells started meiosis, but arrested in prophase I (*8*). The normal maturation of *mac1* archesporial cells indicates independence from somatic tissues for specification, multiple mitoses, and meiotic entry (*13*). Germinal independence contrasts with animal spermatogenesis, where meiotic entry depends on a functional somatic niche (*14*).

Having shown that archesporial cells use MAC1 to organize the somatic niche, we considered the preceding step: how multipotent L2-d cells acquire an archesporial fate. In *male sterile converted anther 1* (*msca1*) anthers, centrally positioned presumptive archesporial cells failed to progress and instead made longitudinal divisions and differentiated as vasculature (fig. S7). We conclude that *msca1* is epistatic to *mac1*, because vascular bundles were observed in *mac1 msca1* anthers (fig. S8). Furthermore *Mac1* transcripts were low in *msca1* anthers, confirming that increased expression is an archesporial cell attribute (Fig. 1E). MSCA1, a glutaredoxin, is a redox regulator that uses glutathione to reduce disulfide bridges in target proteins; it is in a plant-specific clade that regulates transcription factor activity (*15*).

Redox status affects many plant developmental processes, including the placement of root transition zones (*16*). During archesporial cell specification, the tassel is tightly encased within a whorl of not–yet-photosynthetic leaves, rapidly growing organs with high metabolic demand. Using a needle-borne O_2 probe inserted into the airspace (~1 cm^3) between the tassel and the innermost leaf (fig. S9), we found 1.2 to 1.4% O_2 hypoxic atmosphere (n = 5 plants) during archesporial cell specification; this condition was transient, because 5 days later O_2 was >5%.

Administering gases through hoses threaded into the leaf whorl modulated O_2 concentration (fig. S9); the probe registered 0% with N_2 and exceeded 30% (maximal capacity) with O_2. After 48 hours, both manipulations resulted in excess cell proliferation (Fig. 2, A and B), but only N_2 increased the representation of central cells (Fig. 2C), all of which differentiated as archesporial, phenocopying early *mac1* (Fig. 2, C and F). The ratio of archesporial to total L2-d cells is informative (Fig. 2D): In N_2, ratios were significantly elevated during late archesporial cell specification (Student's t test, $P < 0.01$) but decreased later, reflecting precocious somatic bilayer formation (Fig. 2E); whereas O_2 depressed ratios and delayed bilayer formation. Results were con-

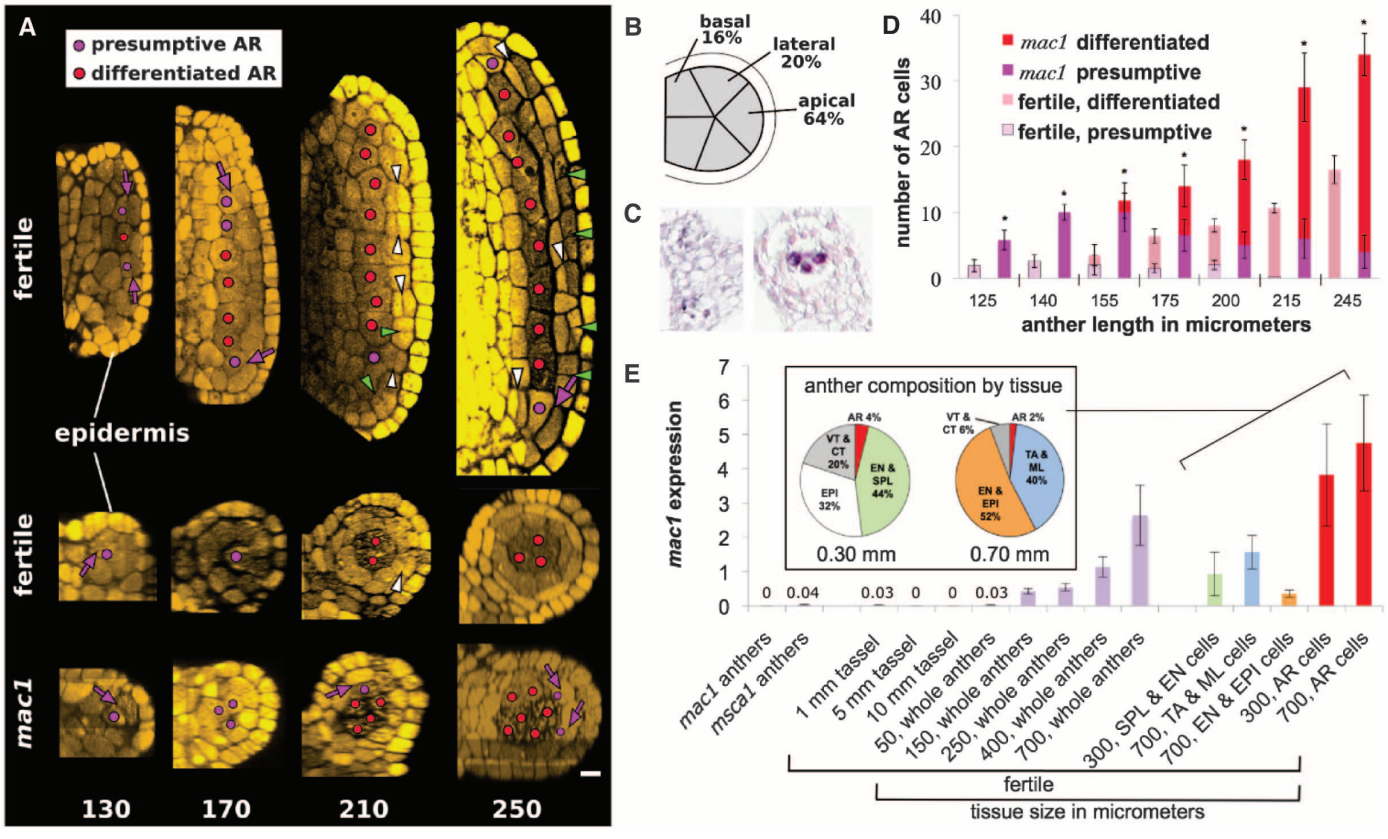

Fig. 1. Anther development in fertile and *mac1* anthers. (**A**) Longitudinal confocal images (top) and transverse *Z*-stack reconstructions (bottom) of fertile and *mac1* male sterile anther development. Numbers indicate anther length in micrometers. (**B**) Lines indicate lobe positions, and percentages represent the frequency of archesporial cell births. (**C**) MAC1 immunohistolocalization shows diffuse protein distribution in L2-d cells of early lobes (left) and enrichment in differentiated archesporial cells (right). (**D**) Presumptive and differentiated archesporial cell counts in *mac1* and fertile anthers (asterisks indicate $P < 0.05$). (**E**) Quantification of *mac1* transcript by qRT-PCR. (Inset) Cellular composition of laser-microdissected anthers. Differentiated archesporial cells are highly enriched in *Mac1* transcripts 1 day (300 μm) and 3 days (700 μm) after specification. AR, archesporial; VT, vasculature; CT, connective tissue; EPI, epidermis; EN, endothecium; TA, tapetum; ML, middle layer; purple arrows, AR-generative divisions; white arrowheads, periclinal divisions generating SPL and EN; green arrowheads, anticlinal divisions. Scale bar, 15 μm.

firmed by gas administration directly via needles (Fig. 2, G and H, and fig. S10) and by injection of hydrogen peroxide (H_2O_2) and the peroxide scavenger potassium iodide (KI) (Fig. 2, I and J, and fig. S12). Compressed air and needle puncture were used as controls, because wounding alone slightly increased total L2-d and archesporial cell counts.

The manipulation of redox status could trigger archesporial cell fate outside of anther lobes, a feature never seen in ~1000 untreated anthers. 4.4% of 1490 treated anthers had ectopic arche-

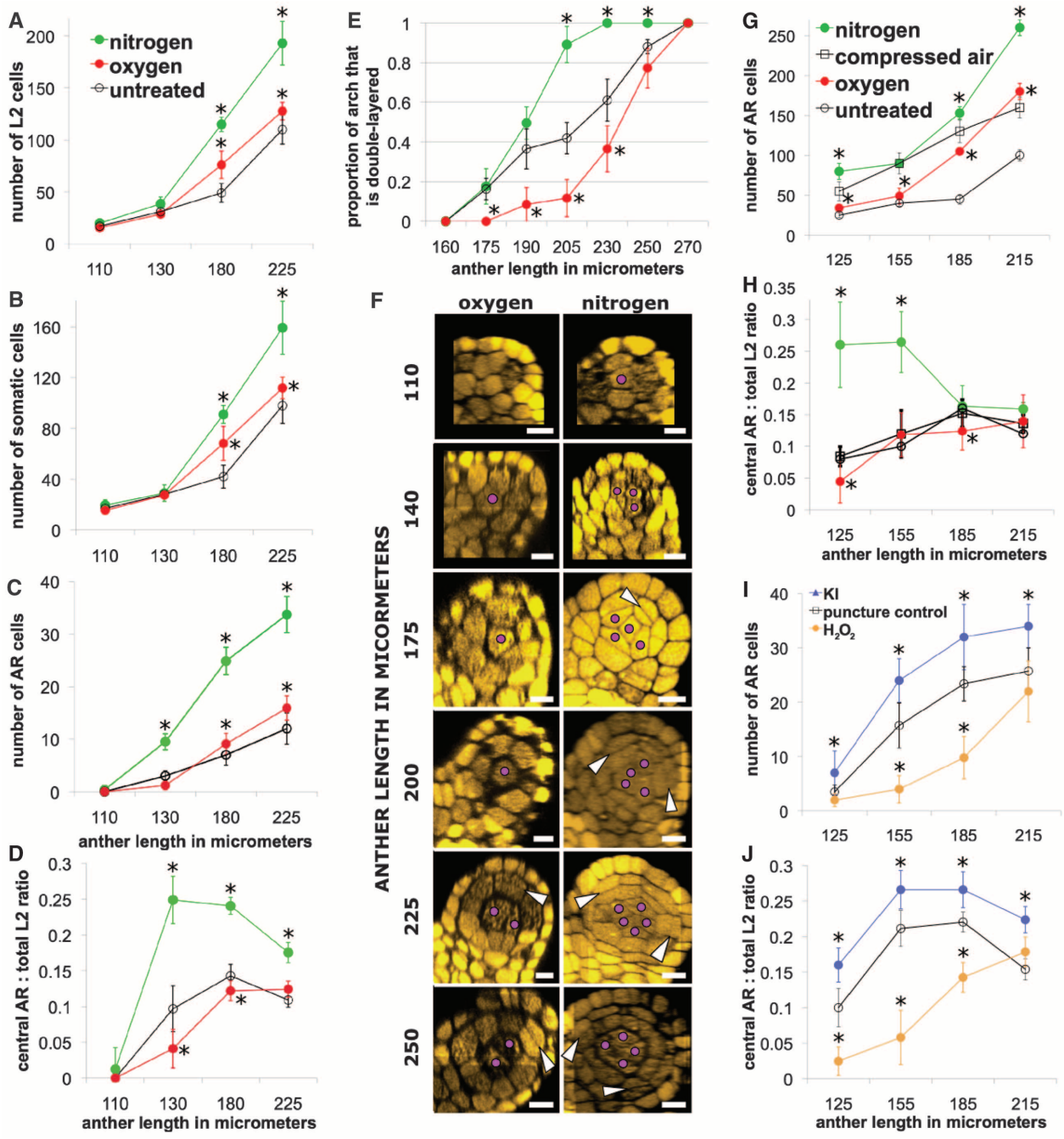

Fig. 2. (**A** to **F**) Internal composition after 48-hour N_2 and O_2 application via hoses. (A) Both gases increased total cell counts, and (B) most cells were somatic. (C) N_2 gas resulted in about a threefold increase in presumptive and differentiated archesporial cells, as compared to O_2 gas and no treatment. (D) The ratio of central archesporial cells to total L2-d cells was lower in O_2-treated anthers than in untreated anthers, whereas N_2-treated anthers had much higher ratios that dropped later during somatic bilayer formation. (E) Bilayer formation was measured as a proportion of L2-d somatic ring cells on the lobe arch that had divided periclinally. (F) Transverse reconstructions of single lobes in gas treatments. White arrowheads, periclinal divisions; purple dots, archesporial cells. Scale bar, 20 μm. (**G** and **H**) Cellular composition after 48-hour gas application via needle. All needle treatments resulted in excess proliferation and excess archesporial cells; thus, compressed air was used as a control. (G) Central presumptive + differentiated archesporial counts were significantly higher in N_2 and slightly lower in O_2 as compared to compressed air. (H) The ratio of central archesporial cells to total L2-d cells is high in N_2 early, dropping later from precocious somatic development. (**I** and **J**) In the chemical injections, needle puncture alone caused proliferation and excess archesporial cells versus untreated anthers, and served as a control. (I) KI promoted and H_2O_2 inhibited central archesporial cell counts at all stages versus control. (J) This led to increased ratios in KI and depressed ratios in H_2O_2, with precocious bilayer formation lowering the ratio in KI in the final size class. Error bars are ± SD (n > 10 plants). Asterisks represent significance compared to control by Student's t test (P < 0.01). See figs. S10 to S13 for additional data.

sporial cells, 3.0% in oxidizing and 6.3% in reducing treatments. Archesporial cell location was significantly biased in oxidizing treatments for the connective and vascular tissues ($\chi^2 = 9.82$, $P < 0.005$) (Fig. 3A and table S3). This preference for internal locations may reflect an intrinsic capacity for deeper tissues to achieve hypoxia during oxidizing treatments. Reducing treatments showed a significant but opposite bias: 17% of ectopic archesporial cells were internal, whereas 83% were epidermal or subepidermal ($\chi^2 = 7.62$, $P < 0.01$) (Fig. 3, B and C, and table S2).

Although single ectopic archesporial cells occurred, more commonly an archesporial cell cluster wove randomly through the anther. Oriented divisions in surrounding cells were reminiscent of somatic bilayer formation. Ectopic archesporial cells were observed in treated *mac1* anthers, but surrounding cells did not organize into bilayers (Fig. 3D), indicating that ectopic archesporial cells require MAC1 to generate a niche. Reductive but not oxidizing treatments rescued archesporial cell specification in *msca1* anthers (Fig. 3E and fig. S14): 9.5% of KI-treated and 37% of sodium nitroprusside (SNP)–treated *msca1* anthers had archesporial cells. Like KI, SNP lowers H_2O_2 levels (*17*), indicating that a reductive environment suffices to modify the unidentified target(s) of MSCA1, causing archesporial cell formation.

Genetic evidence supports a key role for reactive oxygen species (ROS) management to sustain fertility. Loss-of-function mutants of anther-expressed glutaredoxins, including maize *msca1* and rice *microsporeless1*, are male sterile (*18*–*21*), indicating that excessive ROS cause sterility. Transcriptome profiling of microdissected archesporial cells demonstrated preferential expression of genes that lower ROS, support reducing capacity, and contribute to alternative metabolism (table S4). The last set indicates that archesporial cells might bypass the mitochondrial electron transport chain, minimizing damaging ROS (*22*) and reducing mutational load and cellular disruption in the germinal population (*23*).

Collectively, microscopic reconstructions and experimental manipulations of redox refute the prevailing lineage model of anther development that asserts that a monoclonal germinal lineage is founded by a singular asymmetric cell division in each lobe (*3*, *4*). We propose that early anther lobes in maize are composed of equivalent, multipotent L2-d cells expressing MAC1, MSCA1, and its archesporial fate–determining target(s). In this model, MSCA1-mediated events are triggered in central lobe cells by hypoxic conditions, which arise naturally during plant growth. These archesporial cells would then increase MAC1 expression to repress their own proliferation and instruct L2-d neighbors to adopt somatic fates. These events proceed from the center, where lobes are widest, toward the anther base and tip, resulting in a multiclonal archesporial cell column encircled by two somatic rings just 40 hours after the first presumptive archesporial cell birth. Concomitantly, anthers have more than doubled in length from both continual anticlinal division in somatic cells and substantial archesporial cell expansion.

In contrast, vertebrates and ecdysozoa establish germline stem cells before gastrulation through either lineage or inductive mechanisms. Even in basal animals, multipotent cells competent to form both germ-line and somatic niches are sequestered embryonically (*2*). Rarely, an adult germ line can be generated from somatic neoblasts, as in regenerating planaria (*24*). Any of the early anther somatic cells can acquire a premeiotic fate after redox manipulation, illustrating the plasticity of plant development and the capacity to reprogram cell fate based on environmental conditions. As an example, reducing treatments increased proliferation in the L2-d cell pool, placing more cells in the center of lobes, where archesporial cell fate specification normally starts. An emerging theme in studies of mammalian stem cells is that maintenance of a hypoxic niche is critical for stem cell proliferation and function (*25*–*27*), a striking parallel to the specification of anther germinal cells. Multicellularity evolved in a hypoxic aqueous environment, and we speculate that animal and plant stem cells retain a dependence on this physiological status.

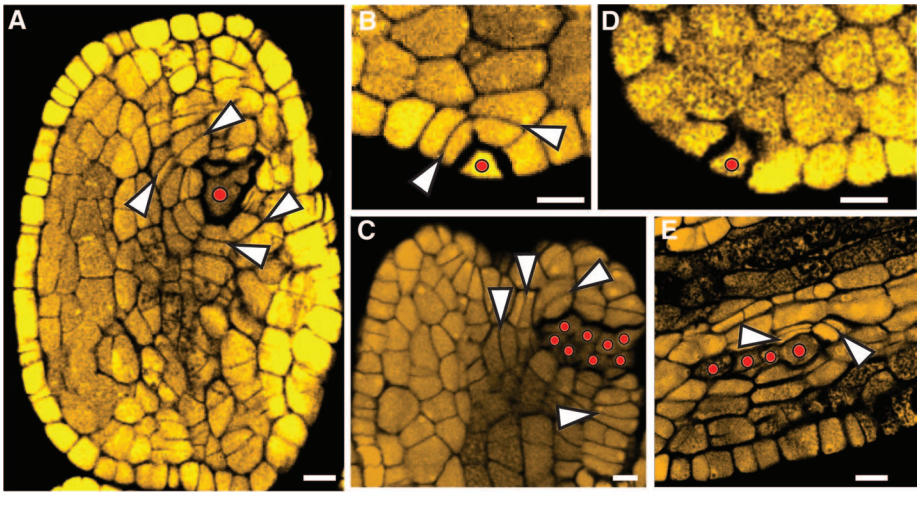

Fig. 3. Ectopic archesporial cell and bilayer formation. (**A**) O_2 needle treatment with archesporial cells near vasculature. (B) to (D) N_2 needle treatment with (**B**) a single epidermal archesporial cell, (**C**) an ectopic archesporial cell cluster, and (**D**) a single ectopic archesporial cell in *mac1*, missing the somatic layer–adding divisions. (**E**) 20 μM SNP injected into *msca1* caused ectopic archesporial cell formation in the lobe vascular bundle. In (A) to (C) and (E), white arrowheads indicate somatic divisions, with new cell walls built to add layers surrounding the archesporial cell(s). In all panels, red dots indicate archesporial cells. Scale bar, 10 μm.

References and Notes

1. C. G. Extavour, M. Akam, *Development* **130**, 5869 (2003).
2. C. Juliano, G. Wessel, *Science* **329**, 640 (2010).
3. C. L. Hord, H. Ma, *Plant Cell Monogr.* **9**, 361 (2008).
4. P. A. Bedinger, J. E. Fowler, in *Handbook of Maize: Its Biology*, J. L. Bennetzen, S. C. Hake, Eds. (Springer, New York, 2009), pp. 57–77.
5. R. B. Goldberg, T. P. Beals, P. M. Sanders, *Plant Cell* **5**, 1217 (1993).
6. L. C. Boavida, J. D. Becker, J. A. Feijó, *Int. J. Dev. Biol.* **49**, 595 (2005).
7. R. C.-J. Wang *et al.*, *Development* **139**, 2594 (2012).
8. W. F. Sheridan, E. A. Golubeva, L. I. Abrhamova, I. N. Golubovskaya, *Genetics* **153**, 933 (1999).
9. X. Feng, H. G. Dickinson, *Dev* **137**, 2409 (2010).
10. C. Albrecht, E. Russinova, V. Hecht, E. Baaijens, S. de Vries, *Plant Cell* **17**, 3337 (2005).
11. X. Feng, H. G. Dickinson, *Trends Genet.* **23**, 503 (2007).
12. G.-L. Nan *et al.*, *BMC Plant Biol.* **11**, 120 (2011).
13. T. Kelliher, V. Walbot, *Dev. Biol.* **350**, 32 (2011).
14. J. L. Leatherman, S. Dinardo, *Nat. Cell Biol.* **12**, 806 (2010).
15. M. C. Albertson *et al.*, U.S. patent 7915478 (2011).
16. H. Tsukagoshi, W. Busch, P. N. Benfey, *Cell* **143**, 606 (2010).
17. J. W. Wang, J. Y. Wu, *Plant Cell Physiol.* **46**, 923 (2005).
18. G. Bertoni, *Plant Cell* **23**, 3562 (2011).
19. S. Li *et al.*, *Plant Cell* **21**, 429 (2009).
20. J. Murmu *et al.*, *Plant Physiol.* **154**, 1492 (2010).
21. L. Hong *et al.*, *Plant Cell* **24**, 577 (2012).
22. Q. Chen, E. J. Vazquez, S. Moghaddas, C. L. Hoppel, E. J. Lesnefsky, *J. Biol. Chem.* **278**, 36027 (2003).
23. G. Miller, V. Shulaev, R. Mittler, *Physiol. Plant.* **133**, 481 (2008).
24. J. Baguñá, E. Saló, C. Auladell, *Development* **107**, 77 (1989).
25. M. V. Gustafsson *et al.*, *Dev. Cell* **9**, 617 (2005).
26. B. Keith, M. C. Simon, *Cell* **129**, 465 (2007).
27. S. J. Morrison *et al.*, *J. Neurosci.* **20**, 7370 (2000).

Acknowledgments: Supplementary figures, tables, and experimental procedures are available on *Science* Online. We thank R. Wang for MAC1 immunohistolocalization, B. Marchant for tassel treatments, D. Tollenor for oxygen measurements, and R. Egger and W. James Nelson for discussions. Transcriptome data were deposited in the Gene Expression Omnibus (accession no. GSE39101). T.K. and V.W. are inventors on a patent application (61/598.544) filed by Stanford University entitled "Method for Modulating the Number of Archesporial Cells in a Developing Anther." Supported by NSF grant PGRP07-01880. T.K. was supported by an NIH Biotechnology Training Grant (5-T32-GM008412-17).

Supplementary Materials

www.sciencemag.org/cgi/content/full/337/6092/345/DC1
Materials and Methods
Figs. S1 to S14
Tables S1 to S4
References (*28*–*33*)

6 February 2012; accepted 2 May 2012
10.1126/science.1220080

Diversity of Interaction Types and Ecological Community Stability

A. Mougi[1] and M. Kondoh[1,2]*

Ecological theory predicts that a complex community formed by a number of species is inherently unstable, guiding ecologists to identify what maintains species diversity in nature. Earlier studies often assumed a community with only one interaction type, either an antagonistic, competitive, or mutualistic interaction, leaving open the question of what the diversity of interaction types contributes to the community maintenance. We show theoretically that the multiple interaction types might hold the key to understanding community dynamics. A moderate mixture of antagonistic and mutualistic interactions can stabilize population dynamics. Furthermore, increasing complexity leads to increased stability in a "hybrid" community. We hypothesize that the diversity of species and interaction types may be the essential element of biodiversity that maintains ecological communities.

In nature, a number of species coexist to form a complex community network of interspecific interactions, contrary to a theoretical prediction that a complex community is inherently unstable (*1*). This paradox has stimulated ecologists to try to identify what maintains species diversity in natural communities (*2*–*8*). An ecological community has been viewed as a network of species connected by interspecific interactions. For example, a food web is the classical representation of "who eats whom" in the community (*9*). A mutualistic network, which represents mutualisms within a community, is another interaction network, the structure and dynamics of which are of particular interest in recent studies of community ecology (*10*). There is no doubt that independently developed studies of these interaction networks have contributed to our understanding of how interspecific interactions are related to population dynamics, what determines community structure, and how species diversity is maintained in nature (*2*–*8*). However, the applicability of these insights to real communities remains equivocal, because real communities are "hybrids"composed of different types of interactions (*11*–*15*). Mixing different types of interspecific interactions may dramatically alter our view of community dynamics and its relevance to community structure, which has been modeled only in small and simple systems [(*16, 17*), but see (*14*, *18*, *19*)]. Although a recent study showed that interaction type may affect community stability and its relationship with complexity (*19*), it has remained unanswered how changing relative frequencies of different interaction types, or the diversity of interaction types, affect community stability and complexity-stability relationships. Here we present a theoretical hybrid community model, which involves both antagonistic and mutualistic interactions in varying proportions, and reveal a role of the multiple interaction types and their composition for the maintenance of complex communities.

Consider an ecological community consisting of N species, in which population dynamics is driven by interspecific interactions. If a Holling type I (linear) functional response is assumed, the population dynamics of species i is described as

$$\frac{dX_i}{dt} = X_i\left(r_i - s_iX_i + \sum_{j=1,\ j\neq i}^{N} a_{ij}X_j\right) \quad (1)$$

where X_i is the abundance of species i, r_i is the intrinsic rate of change in species i, s_i is density-dependent self regulation, and a_{ij} is the interaction coefficient between species i and species j. Of the three different network structures examined, here we describe the results for cascade (*20*) and bipartite (*8*) networks. In the cascade model, for each pair of species $i, j = 1,\ldots, n$ with $i < j$, species i never consumes species j, whereas species j may consume species i (*20*). In the bipartite model, no interactions occur within the same trophic levels (*6*, *8*, *21*), and species numbers in each trophic level are the same. We define the proportion of connected pairs P as the proportion of realized interaction links L in the possible maximum interaction links L_{max} of a given network model ($L = PL_{max}$). In the cascade model, $L_{max} = N(N-1)/2$, and in the bipartite model, $L_{max} = (N/2)^2$. With a biologically feasible assumption that interaction strengths decrease with increasing resource species, due to an allocation of interacting effort, the interaction coefficients a_{ij} ($i \neq j$) are determined as

$a_{ij} = e_{ij}f_M A_{ij} \Big/ \sum_{k\in \text{resource of mutualist } i,\ k\neq i} A_{ik}$ and $a_{ji} = e_{ji}f_M A_{ji} \Big/ \sum_{k\in \text{resource of mutualist } j,\ k\neq j} A_{jk}$ in a mutualistic interaction; $a_{ij} = g_{ij}f_A A_{ij} \Big/ \sum_{k\in \text{resource of predator } i,\ k\neq i} A_{ik}$ and $a_{ji} = -a_{ij}/g_{ij} = -f_A A_{ij} \Big/ \sum_{k\in \text{resource of predator } i,\ k\neq i}$ A_{ik} in an antagonistic interaction between consumer i and resource j, where A_{ij} is the potential preference for the interaction partners; f_M and f_A are the relative strengths of mutualistic and antagonistic interactions, respectively; and e_{ij} and g_{ij} are the conversion efficiency when species i utilizes species j in mutualistic and antagonistic interactions, respectively. For a Holling type II (nonlinear and saturating) functional response, we used $a_{ij} = n_{ij}f_l\left(A_{ij} \Big/ \sum_{k\in \text{resource of sp. } i,\ k\neq i} A_{ik}\right) \Big/ \left\{1 + \sum_k h_{ik}\left(A_{ij} \Big/ \sum_{k\in \text{resource of sp. } i,\ k\neq i} A_{ik}\right)X_k\right\}$, where f_l is f_M or f_A, n_{ij} is e_{ij} or g_{ij}, and h_{ij} is the handling time (*6*, *8*, *21*). Parameters, s_i, e_{ij}, g_{ij}, A_{ij}, and h_{ij} are randomly chosen from a uniform distribution between 0 and 1, and there is no correlation between the pairwise parameters (A_{ij} and A_{ji}, e_{ij} and e_{ji}, g_{ij} and g_{ji}, h_{ij} and h_{ji}). The intrinsic rate of change, r_i, is determined to hold $dX_i/dt = 0$ after imposition of an equilibrium density of each species, X_i*, from a uniform distribution between 0 and 1. Thus, r_i of basal species with no mutualistic interactions should be always positive, whereas that of species with no predators should be negative. Stability analysis is based on a Jacobian community matrix following May's approach (*1*, *19*, *22*, *23*). Stability is defined as the probability of local equilibrium stability, which is estimated as the frequency of locally stable systems across 1000 sample communities.

The analysis depicts a major effect of interaction type-mixing on population stability (Fig. 1; see the supplementary materials text for analytical results). Consider a food web composed of N species, where a proportion P (≤1; the proportion of connected pairs) of all possible species pairs is interacting. Congruent with earlier theoretical studies (*24*), species may show a stable coexistence under broad P or N ranges (Fig. 1). Yet this is no longer true if a small number of mutualistic interactions is added to the food web. Consider the proportion p_M of randomly chosen antagonistic links that are changed to mutualistic links. The model analysis indicates that in the presence of only a few mutualistic interactions (p_M set to 0.1 to 0.3), virtually no community is stable (Fig. 1) (*23*). Therefore, even a slight "contamination" of mutualistic interactions can completely destabilize an otherwise stable predator-prey community, clearly demonstrating the potential major effects of interaction type-mixing on population dynamics.

However, this is just half of the story. A further increase in the proportion of mutualism has

[1]Department of Environmental Solution Technology, Faculty of Science and Technology, Ryukoku University, 1-5 Yokoya, Seta Oe-cho, Otsu 520-2194, Japan. [2]PRESTO, Japanese Science and Technology Agency, 4-1-8 Honcho, Kawaguchi, Japan.

*To whom correspondence should be addressed. E-mail: mkondoh@rins.ryukoku.ac.jp

another intriguing consequence. As mutualism (p_M) increases, the population becomes more stable and reaches its peak stability at a moderate mixture of both interaction types (Fig. 1). The same qualitative pattern is observed when resilience, a stability index for transient dynamics (*20*), is used instead. Although the overall unimodal pattern observed is qualitatively unchanged over a wide range of proportions of connected pairs (Fig. 1), species richness (fig. S2), and parameter variability (fig. S3), the sharp stability peak may not be observed when the dynamics is too strongly stabilized or destabilized at the background so that there is no room for changing p_M to alter stability. For example, with high species richness or strong self-regulation intensity, stability is maximized at a wide range of mutualism proportions (p_M).

The analysis of a hybrid community model provides a different perspective on the ongoing complexity-stability debate (*24*, *25*). Increased complexity (high species richness and more connected pairs) destabilizes, or shows inconsistent effects on, population stability in a nonhybrid community composed of either mutualistic or antagonistic interactions (Fig. 2, A and E). However, positive relationships are consistently observed in hybrid communities with a moderate mixture of interaction types (Fig. 2D) (*23*). Our model demonstrates a positive complexity-stability relationship, irrespective of the network structure choice (random, cascade, or bipartite) or functional response (fig. S4). This suggests that multispecies coexistence in a hybrid community can be maintained, rather than destabilized, by community complexity. The choice of parameters does not change the pattern as long as it is within the parameter ranges that are not extremely stabilizing or destabilizing (figs. S2 and S3). Furthermore, those results do not change qualitatively even if the interspecific competition between basal species in the communities (figs. S5 and S6) or the varying relative strength of antagonistic and mutualistic interactions f_A and f_M is considered (fig. S7). Our analysis also suggests that the negative relationship between the number of interactions and the interaction strength assumed is crucial for the present patterns. In fact, the violation of this assumption does not create the mixing effect on community stability, as shown in fig. S8 (*1*, *19*).

Under a traditional ecological hypothesis, acutely fragile communities are unlikely to persist under disturbance, and therefore a natural community should be structured to support population stability (*26*). Based on this hypothesis, an increasing number of empirical studies have been conducted to examine the structural patterns of community networks, such as food webs and mutualistic networks, and predict the network dynamics-related consequences (*2*–*8*). Our results show that interaction type-mixing and community network structure synergistically affect population dynamics, and they clearly illustrate the limitations of a single–interaction-type approach. The community structure effect on population dynamics may not be correctly evaluated in the absence of interaction type-mixing information. For example, our model indicates that the effect of community complexity on stability can vary largely, depending on interaction types and their diversity. Our study establishes the potential importance of interaction type-mixing in resolving the structure-dynamics relationship. However, empirical data on hybrid community interaction webs are limited. Consequently, additional empirical study of the structure and dynamics of hybrid communities composed of various types of interactions must be pursued. A possible test of our hypothesis is to compare the composition of interaction types between different com-

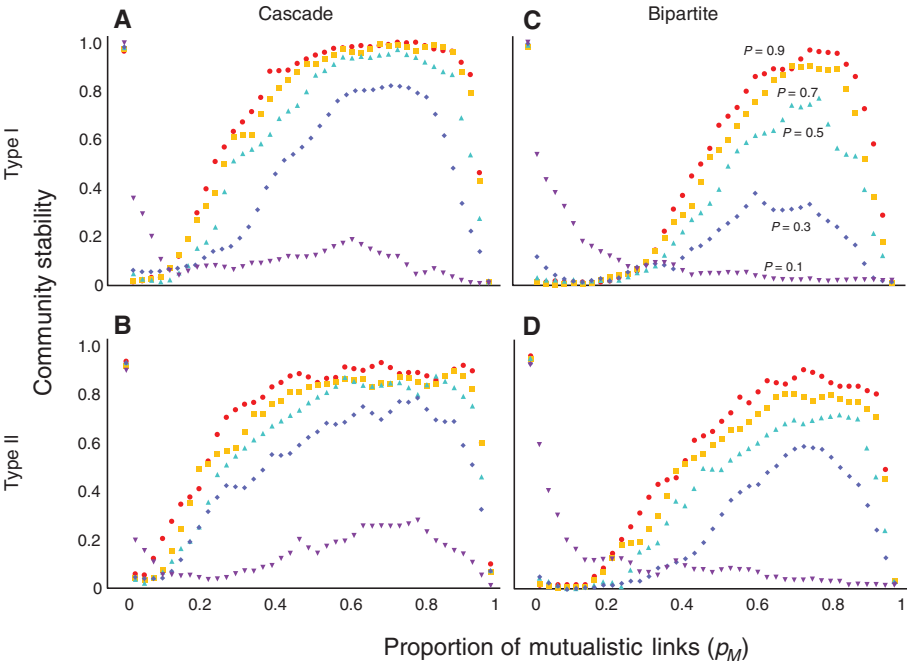

Fig. 1. (**A** to **D**) Relationships between the proportion of mutualistic links (p_M) and stability with varying proportions of connected pairs (P) in four models with different network structures and functional responses. Colors indicate different values of P. We assume N = 50.

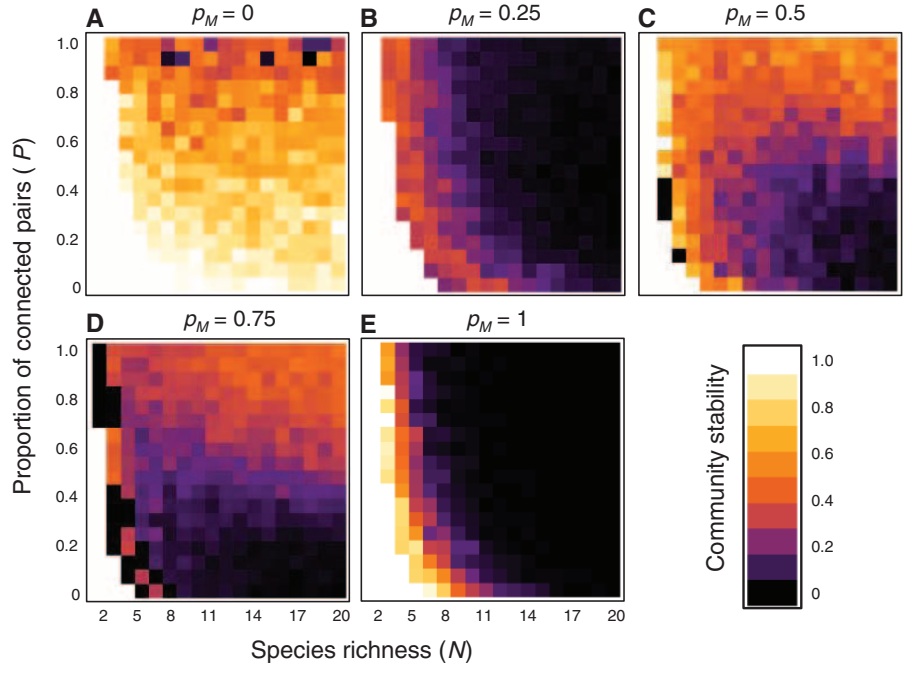

Fig. 2. (**A** to **E**) Complexity-stability relationships with varying proportions of mutualistic links (p_M) in a cascade model with type I functional response.

munities under varying levels of disturbance. An ecosystem under more-intensive disturbance is expected to have a more stabilizing composition of interaction types.

Species diversity has been of primary interest in understanding the role of biodiversity in ecosystem maintenance (*24*, *27*), and a major focus of biodiversity conservation. The present study sheds new light on another aspect of biodiversity: diversity in interaction types. We determined that biodiversity in species and interactions is integral to stabilizing biological communities, which has important implications for biodiversity conservation. Species loss is of vital conservation concern; however, we may also need to identify the interaction types lost or maintained for two primary reasons. First, a complex community may be self-sustaining only in the presence of different interaction types. Therefore, a biased loss of one interaction type may critically destabilize the complex ecosystem. Second, the multiple interaction types can change the complexity-stability effect. The positive complexity-stability relationship of hybrid communities implies that a hybrid community is self-sustaining. However, it should be noted that such a self-sustaining community is more vulnerable to cascading biodiversity losses; a simplified community can destabilize population dynamics and enhance additional species losses.

References and Notes

1. R. M. May, *Nature* **238**, 413 (1972).
2. A.-M. Neutel, J. A. P. Heesterbeek, P. C. De Ruiter, *Science* **296**, 1120 (2002).
3. U. Brose, R. J. Williams, N. D. Martinez, *Ecol. Lett.* **9**, 1228 (2006).
4. N. D. Martinez, R. J. Williams, J. A. Dunne, in *Ecological Networks: Linking Structure to Dynamics in Food Webs*, M. Pascual, J. A. Dunne, Eds. (Oxford Univ. Press, Oxford, 2006), pp. 163–185.
5. J. Bascompte, P. Jordano, J. M. Olesen, *Science* **312**, 431 (2006).
6. T. Okuyama, J. N. Holland, *Ecol. Lett.* **11**, 208 (2008).
7. S. Allesina, D. Alonso, M. Pascual, *Science* **320**, 658 (2008).
8. E. Thébault, C. Fontaine, *Science* **329**, 853 (2010).
9. S. L. Pimm, *Food Webs* (Chapman and Hall, London, 2002).
10. J. N. Thompson, *Science* **312**, 372 (2006).
11. J. M. Chase *et al.*, *Ecol. Lett.* **5**, 302 (2002).
12. S. Y. Strauss, R. E. Irwin, *Annu. Rev. Ecol. Syst.* **35**, 435 (2004).
13. K. D. Lafferty *et al.*, *Ecol. Lett.* **11**, 533 (2008).
14. C. J. Melián *et al.*, *Oikos* **118**, 122 (2009).
15. C. Fontaine *et al.*, *Ecol. Lett.* **14**, 1170 (2011).
16. J. F. Addicott, H. I. Freedman, *Theor. Popul. Biol.* **26**, 320 (1984).
17. M. S. Ringel, H. H. Hu, G. Anderson, M. S. Ringel, *Theor. Popul. Biol.* **50**, 281 (1996).
18. S. Allesina, M. Pascual, *Theor. Ecol.* **1**, 55 (2008).
19. S. Allesina, S. Tang, *Nature* **483**, 205 (2012).
20. X. Chen, J. E. Cohen, *Proc. Biol. Sci.* **268**, 869 (2001).
21. F. Zhang, C. Hui, J. S. Terblanche, *Ecol. Lett.* **14**, 797 (2011).
22. S. E. Townsend, D. T. Haydon, L. Matthews, *J. Theor. Biol.* **267**, 243 (2010).
23. See supplementary materials text on *Science* Online.
24. K. S. McCann, *Nature* **405**, 228 (2000).
25. A. R. Ives, S. R. Carpenter, *Science* **317**, 58 (2007).
26. S. L. Pimm, *The Balance of Nature?* (Univ. of Chicago Press, Chicago, 1991).
27. M. Loreau *et al.*, *Science* **294**, 804 (2001).

Acknowledgments: This work was supported by the Environment Research and Technology Development Fund (grant D-1102) of the Ministry of the Environment, Japan; a Grant-in-Aid for Scientific Research (B) (no. 20370012); and a Grant-in-Aid for Challenging Exploratory Research (no. 23657019, 30388160) of the Japan Society for the Promotion of Science. The authors declare no competing financial interests.

Supplementary Materials

www.sciencemag.org/cgi/content/full/337/6092/349/DC1
Supplementary Text
Figs. S1 to S8

14 February 2012; accepted 25 May 2012
10.1126/science.1220529

LAAT-1 Is the Lysosomal Lysine/Arginine Transporter That Maintains Amino Acid Homeostasis

Bin Liu,[1,4]* Hongwei Du,[2,3,4]* Rachael Rutkowski,[5]† Anton Gartner,[5] Xiaochen Wang[4]‡

Defective catabolite export from lysosomes results in lysosomal storage diseases in humans. Mutations in the cystine transporter gene *CTNS* cause cystinosis, but other lysosomal amino acid transporters are poorly characterized at the molecular level. Here, we identified the *Caenorhabditis elegans* lysosomal lysine/arginine transporter LAAT-1. Loss of *laat-1* caused accumulation of lysine and arginine in enlarged, degradation-defective lysosomes. In mutants of *ctns-1* (*C. elegans* homolog of *CTNS*), LAAT-1 was required to reduce lysosomal cystine levels and suppress lysosome enlargement by cysteamine, a drug that alleviates cystinosis by converting cystine to a lysine analog. LAAT-1 also maintained availability of cytosolic lysine/arginine during embryogenesis. Thus, LAAT-1 is the lysosomal lysine/arginine transporter, which suggests a molecular explanation for how cysteamine alleviates a lysosomal storage disease.

Defects in exporting hydrolytic degradation products from lysosomes cause lysosomal storage diseases such as cystinosis, which is characterized by intralysosomal accumulation of free cystine because of mutations in the lysosomal cystine transporter gene *CTNS* (cystinosin) (*1*–*4*). The most effective therapeutic agent for cystinosis, cysteamine (an aminothiol), converts lysosomal free cystine to cysteine and the mixed disulfide of cysteine-cysteamine, which is thought to be exported from lysosomes as a lysine analog through a lysine/cationic amino acid transporter (*5*–*7*). The molecular identity of the transporter remains unknown. Although biochemically detected, most mammalian lysosomal amino acid transporters have not been molecularly characterized (*1*).

From a forward genetic screen for *Caenorhabditis elegans* mutants with increased embryonic cell corpses, we isolated a recessive mutant *qx42* that accumulated many refractile corpse-like objects and lysotracker-positive puncta, suggestive of abnormal lysosomes (fig. S1, A to G). Using NUC-1::mCherry, which labels lysosomes (*8*, *9*), or lysotracker staining, we found that *qx42* lysosomes were on average twice the volume of wild type (1.3 versus 0.5 μm^3) (Fig. 1, A to F‴, and fig. S1, H to K).

We next examined whether *qx42* affected lysosomal cargo degradation. Apoptotic cells are phagocytosed, then degraded in lysosomes. Cell death and cell corpse engulfment were normal in *qx42* mutants (fig. S2). However, degradation of apoptotic cells in phagolysosomes (indicated by GFP::RAB-7 or NUC-1::mCherry) as measured by loss of HIS-24::GFP or H2B::GFP (which label chromatin in all somatic and germ nuclei, including cell corpses, respectively) was severely affected in *qx42* mutants, with HIS-24::GFP persisting >4 times as long as in wild type (Fig. 2A and fig. S2, L to O). Yolk lipoprotein is degraded throughout embryogenesis to nourish developing cells (*10*, *11*). In *qx42* mutants, intestinal secretion of yolk reporter VIT-2::GFP and uptake by oocytes were normal (fig. S3, A to B′). However, *qx42* embryos accumulated significantly more VIT-2::GFP in enlarged puncta, which overlapped with NUC-1::mCherry, suggesting defective lysosomal yolk degradation (Fig. 2, B to D, and fig. S3, C to H′). Cell surface proteins CAV-1 and RME-2, which are internal-

[1]Graduate Program in Chinese Academy of Medical Sciences and Peking Union Medical College, China. [2]State Key Laboratory of Molecular and Developmental Biology, Institute of Genetics and Developmental Biology, Chinese Academy of Sciences, Beijing 100101, China. [3]Graduate School, Chinese Academy of Sciences, Beijing 100039, China. [4]National Institute of Biological Sciences, No. 7 Science Park Road, Zhongguancun Life Science Park, Beijing 102206, China. [5]Wellcome Trust Centre for Gene Regulation and Expression, College of Life Sciences, University of Dundee, Dundee DD1 5EH, UK.

*These authors contributed equally to this work.
†Present address: Walter and Eliza Hall Institute of Medical Research, 1G Royal Parade, Parkville 3052, Australia.
‡To whom correspondence should be addressed. E-mail: wangxiaochen@nibs.ac.cn

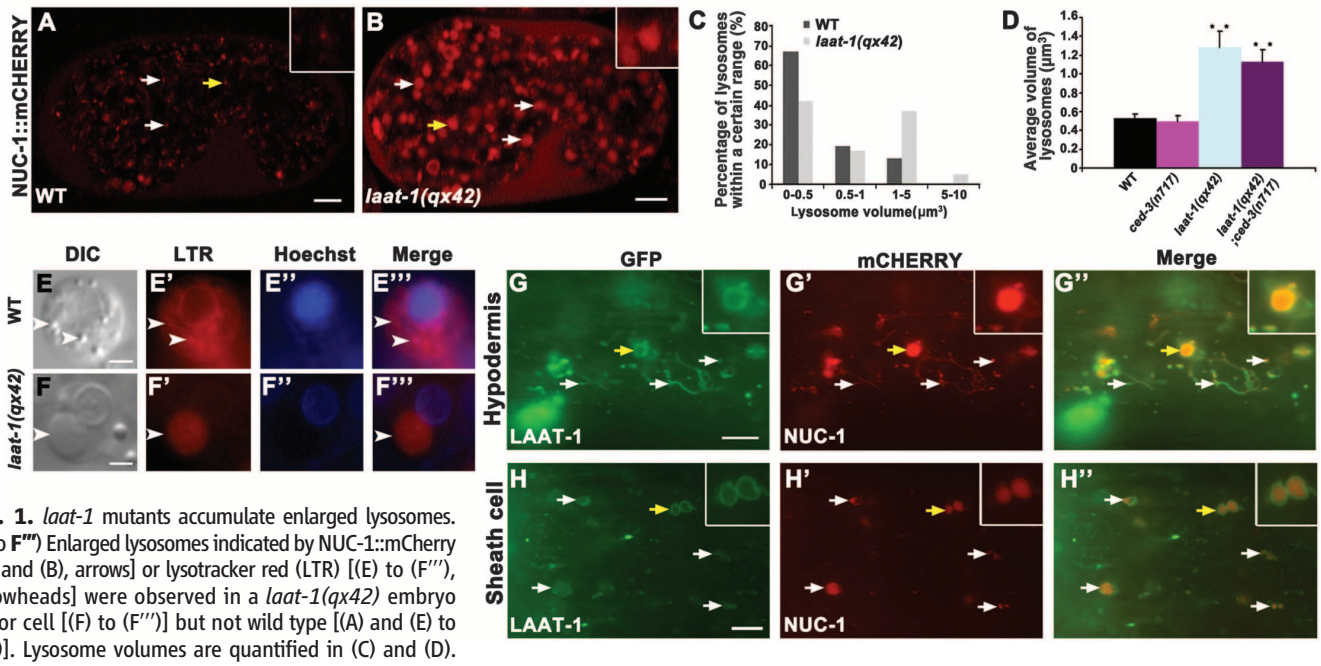

Fig. 1. *laat-1* mutants accumulate enlarged lysosomes. (**A** to **F‴**) Enlarged lysosomes indicated by NUC-1::mCherry [(A) and (B), arrows] or lysotracker red (LTR) [(E) to (F‴), arrowheads] were observed in a *laat-1(qx42)* embryo (B) or cell [(F) to (F‴)] but not wild type [(A) and (E) to (E‴)]. Lysosome volumes are quantified in (C) and (D). Average lysosomal volumes (±SEM, n = 100) in different strains are shown in (D). $^{**}P < 0.0001$. (**G** and **H**) Fluorescent images of hypodermal (G) or sheath (H) cells in wild-type animals expressing LAAT-1::GFP and NUC-1::mCherry. In (A), (B), and (G) to (H″), insets show 4× magnification of lysosomes indicated by yellow arrows. Scale bars: 2 μm in (E) and (F); 5 μm in other panels.

Fig. 2. *laat-1* mutants are defective in lysosomal degradation of various cargoes. (**A**) Fluorescent images of wild-type and *laat-1(qx42)* embryos expressing HIS-24::GFP and GFP::RAB-7 at different time points. Arrows indicate phagolysosomes. Quantification is shown in the right panel, with average duration (±SEM) shown in parentheses. (**B** to **G**) Confocal fluorescent images of wild-type [(B) and (E)] or *laat-1(qx42)* [(C) and (F)] embryos expressing NUC-1::mCherry and VIT-2::GFP [(B) and (C)] or T12G3.1::GFP [(E) and (F)]. Arrows indicate overlapping GFP and mCherry; arrowheads indicate nonoverlapping GFP. Structures indicated by yellow arrows or arrowheads are magnified 4× in the insets. Quantifications are shown in (D) and (G). At least 10 embryos were scored in each strain. Data are shown as mean ± SEM. $^{**}P < 0.0001$. Scale bars, 5 μm.

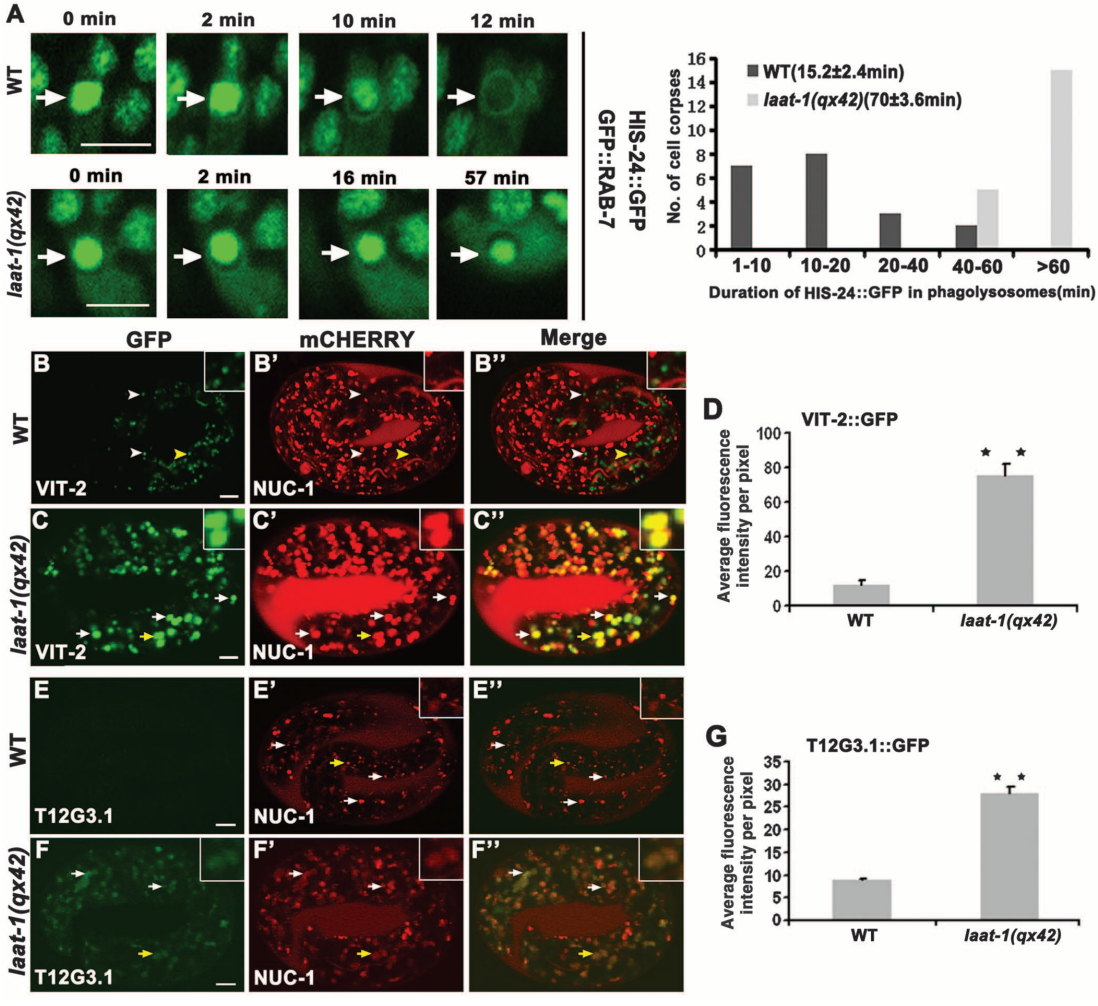

ized and degraded in wild-type embryos, accumulated in enlarged lysosomes in *qx42* embryos (fig. S4) (*12*). Damaged organelles and protein aggregates are delivered via the autophagy pathway to lysosomes for degradation (*13*). Autophagy substrates SEPA-1 and T12G3.1 (the *C. elegans* homolog of mammalian p62) were cleared during embryogenesis in wild type but persisted in late-stage *qx42* mutant embryos and overlapped with NUC-1::mCherry, indicating defective autolysosomal degradation (Fig. 2, E to G, and fig. S5) (*14*, *15*). Thus, *qx42* impairs lysosomal degradation of phagocytic, endocytic, and autophagic cargoes.

The gene affected in *qx42*, *Y43H11AL.2*, encodes a conserved protein containing seven predicted transmembrane domains and two internal PQ (Proline-Glutamine) loop repeats, characteristic of lysosomal cystine transporters (LCTs) (*16*) (fig. S6F). Cystinosin, the archetypal LCT family member, is a lysosomal cystine transporter, the abnormal function of which causes cystinosis (*4*). We named the *Y43H11AL.2* gene *laat-1* (lysosomal amino acid transporter 1) based on similarity with LCT family proteins and cellular functions (see below). *qx42* has an A>T mutation in *laat-1* that creates a premature stop codon after Asn[127]. Other independently isolated *laat-1* mutant alleles also caused enlarged lysosome and persistent cell corpse phenotypes (figs. S1, L to R, and S2K). *laat-1* was expressed in various cell types in embryos, larvae, and adults (fig. S7). GFP or mCherry fusion of LAAT-1, which fully rescued *qx42* defects (fig. S6, A to E), labeled membranes of NUC-1– or lysotracker-positive structures and overlapped with lysosomal membrane protein CTNS-1, the *C. elegans* homolog of human cystinosin (*17*), indicating that LAAT-1 localizes to lysosomal membranes (Fig. 1, G to H″, and fig. S7, A to C″). LAAT-1(Δ299-304)::GFP, which lacks the C-terminal dileucine-based lysosomal sorting motif (*18*), stained plasma membranes instead of lysosomes and failed to rescue *laat-1(qx42)* mutant phenotypes, indicating that LAAT-1 function depends on its lysosomal localization (figs. S6, A to F, and S7, D to E″).

We examined lysosomes purified from *C. elegans* embryos (fig. S8) and found that loss of CTNS-1 caused cystine accumulation, suggesting that CTNS-1 mediates cystine efflux from lysosomes like human cystinosin (Fig. 3A). In *laat-1* mutant lysosomes, cystine levels were normal, but lysine and arginine levels were 16 and 8 times as higher as wild type, respectively, suggesting that LAAT-1 exports lysine and arginine from lysosomes (Fig. 3A and fig. S9A). Macrophage-like coelomocytes from *ctns-1* mutants contained huge granules (>6.5 μm in diameter), which accumulated endocytosed cargo Cherry and were labeled by lysosomal membrane protein CUP-5 but not endosomal protein RME-8, indicating that they are enlarged lysosomes (*19*, *20*) (Fig. 3, B and C, and fig. S9B). Most wild-type and *laat-1(qx42)* coelomocytes contained small lysosomes (<4.5 μm) or 2 to 3 bigger ones (4.5 to 6.5 μm) (Fig. 3C). Cysteamine treatment of *ctns-1* mutants greatly reduced lysosomal cystine accumulation and almost completely suppressed the enlarged lysosome phenotype (Fig. 3, C and D). In *laat-1(qx42) ctns-1(ok813)* double mutants, however, cysteamine failed to deplete lysosomal cystine and suppress enlarged lysosomes, which accumulated high levels of cystine and the lysine analog mixed disulfide of cysteine-cysteamine (Fig. 3, C to E). These data strongly suggest that LAAT-1 transports lysine out of lysosomes.

We investigated whether LAAT-1 or its human counterpart PQLC2 transported lysine and arginine using a whole cell–based transporter assay (*4*). Wild-type PQLC2::GFP localized to lysosomes in COS-7 cells, while PQLC2 (ΔLL)::GFP, which lacks the lysosomal sorting motif, associated with plasma membranes, indicating that PQLC2 is a lysosomal membrane protein like LAAT-1 (fig. S6F and fig. S9, C to H″). Expression of plasma membrane–targeted LAAT-1 [LAAT-1(Δ299-304)::GFP] or PQLC2 [PQLC2(ΔLL)::GFP] caused increased uptake of lysine and arginine,

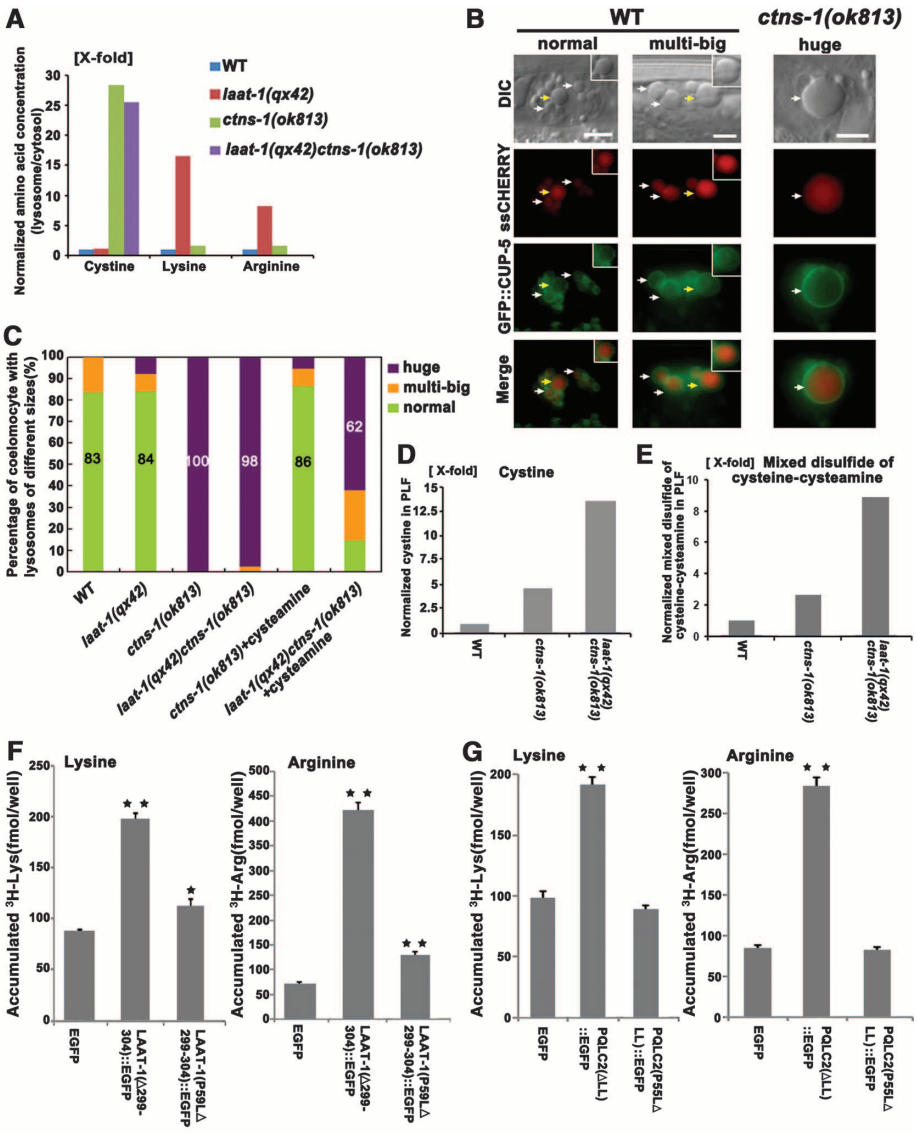

Fig. 3. LAAT-1 is a lysosomal lysine and arginine transporter. (**A**) The ratio of amino acid concentration in lysosomal versus cytosolic fractions prepared from embryonic lysates was determined and normalized as 1 fold in wild type (*y* axis). (**B**) Differential interference contrast (DIC) and fluorescent images of wild-type and *ctns-1(ok813)* coelomocytes expressing secreted Cherry (ssCherry) and the lysosomal marker GFP::CUP-5. Lysosomes are labeled by Cherry and CUP-5 (arrows). Insets show lysosomes indicated by yellow arrows. Scale bars, 5 μm. Quantification is shown in (**C**). (**D** and **E**) Cystine (D) and mixed disulfide of cysteine-cysteamine (E) was determined in purified lysosomal fractions (PLF) after cysteamine treatment and normalized as 1 fold in wild type. (**F** and **G**) Lysine and arginine uptake was determined in (F) LAAT-1- or (G) PQLC-2–expressing COS-7 cells. Data are shown as mean ± SEM. $^{**}P < 0.0001$; $^{*}P < 0.05$; all other points had $P > 0.05$. Data in (A), (D), (E), (F), and (G) are representative of three independent experiments.

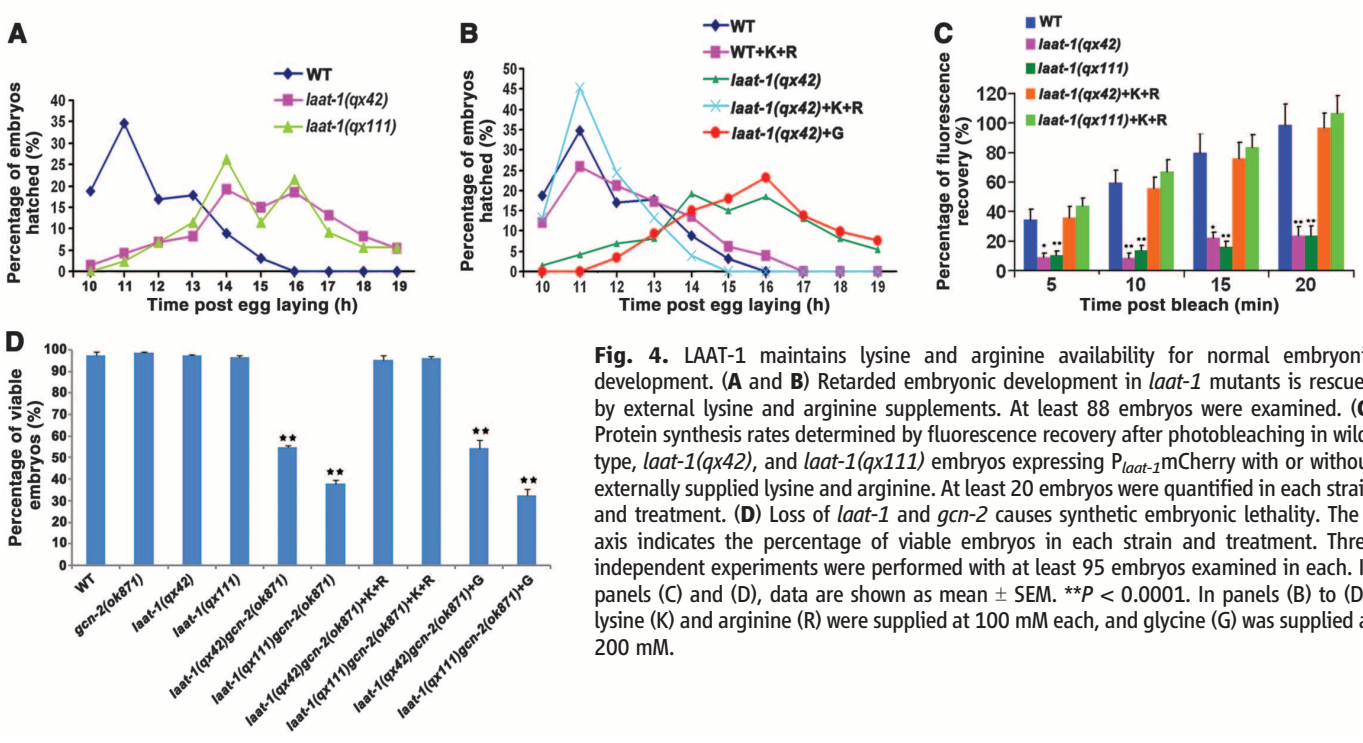

Fig. 4. LAAT-1 maintains lysine and arginine availability for normal embryonic development. (**A** and **B**) Retarded embryonic development in *laat-1* mutants is rescued by external lysine and arginine supplements. At least 88 embryos were examined. (**C**) Protein synthesis rates determined by fluorescence recovery after photobleaching in wild-type, *laat-1(qx42)*, and *laat-1(qx111)* embryos expressing $P_{laat\text{-}1}$mCherry with or without externally supplied lysine and arginine. At least 20 embryos were quantified in each strain and treatment. (**D**) Loss of *laat-1* and *gcn-2* causes synthetic embryonic lethality. The *y* axis indicates the percentage of viable embryos in each strain and treatment. Three independent experiments were performed with at least 95 embryos examined in each. In panels (C) and (D), data are shown as mean ± SEM. $^{**}P < 0.0001$. In panels (B) to (D), lysine (K) and arginine (R) were supplied at 100 mM each, and glycine (G) was supplied at 200 mM.

which was almost completely abolished when the invariant Pro in the first PQ loop was mutated to Leu (Fig. 3, F and G, and fig. S6F). Uptake of histidine, but not alanine, glutamic acid, cystine, or cysteine, was increased in LAAT-1- or PQLC2-expressing cells, suggesting specific transport of cationic amino acids (fig. S10). *laat-1* lysosomes did not significantly accumulate histidine, indicating that LAAT-1 is probably not the major histidine transporter in vivo (fig. S9A).

laat-1 mutants were viable but developed slowly (Fig. 4A). External supplements of both lysine and arginine completely rescued retarded embryonic development (Fig. 4B and fig. S11, A and B) but did not reverse the enlarged lysosome or defective yolk degradation phenotypes in *laat-1* mutants (fig. S11C). Thus, loss of *laat-1* affects lysosomal export of lysine/arginine, which limits their cytoplasmic availability and thereby retards embryonic development. When deprived of amino acids, eukaryotic cells trigger the amino acid response (AAR) pathway through activation of GCN2 protein kinase, leading to repression of global protein synthesis (*21*). Consistent with this, *laat-1* embryos showed reduced protein synthesis, which was efficiently rescued by supplementing lysine and arginine (Fig. 4C and fig. S11D) (*22*). The AAR pathway is essential for survival during amino acid deprivation (*23*, *24*). *gcn-2(ok871)* embryos developed normally but died when *laat-1* was defective. The synthetic lethality was completely rescued by supplying both lysine and arginine but not glycine (Fig. 4D). Thus, loss of *laat-1* limits cytosolic lysine and arginine, causing embryonic lethality when the GCN-2–mediated AAR pathway is impaired (fig. S11E).

We have identified LAAT-1 and its human homolog PQLC2 as the lysosomal lysine/arginine transporter. Cysteamine treatment significantly reduced lysosomal free cystine and efficiently suppressed the enlarged lysosome phenotype in *ctns-1(lf)* single mutants but not *laat-1(lf) ctns-1(lf)* double mutants, which accumulated the lysine analog mixed disulfide of cysteine-cysteamine in lysosomes, suggesting that LAAT-1 (and probably PQLC2) may mediate cystine depletion by cysteamine. It is thus important to examine whether loss of *PQLC2* affects mammalian lysosome function and causes lysosome-related diseases. Our finding that defective lysosomal export of lysine/arginine leads to retarded embryonic development reveals the role of lysosomal amino acid transporters in maintaining cytosolic amino acid availability during embryonic development, providing insights into the pathogenesis of lysosomal transport disorders.

References and Notes

1. C. Sagné, B. Gasnier, *J. Inherit. Metab. Dis.* **31**, 258 (2008).
2. W. A. Gahl, N. Bashan, F. Tietze, I. Bernardini, J. D. Schulman, *Science* **217**, 1263 (1982).
3. A. J. Jonas, A. A. Greene, M. L. Smith, J. A. Schneider, *Proc. Natl. Acad. Sci. U.S.A.* **79**, 4442 (1982).
4. V. Kalatzis, S. Cherqui, C. Antignac, B. Gasnier, *EMBO J.* **20**, 5940 (2001).
5. J. G. Thoene, R. G. Oshima, J. C. Crawhall, D. L. Olson, J. A. Schneider, *J. Clin. Invest.* **58**, 180 (1976).
6. W. A. Gahl, F. Tietze, J. D. Butler, J. D. Schulman, *Biochem. J.* **228**, 545 (1985).
7. R. L. Pisoni, J. G. Thoene, H. N. Christensen, *J. Biol. Chem.* **260**, 4791 (1985).
8. P. Guo, T. Hu, J. Zhang, S. Jiang, X. Wang, *Proc. Natl. Acad. Sci. U.S.A.* **107**, 18016 (2010).
9. Y. C. Wu, G. M. Stanfield, H. R. Horvitz, *Genes Dev.* **14**, 536 (2000).
10. J. Kimble, W. J. Sharrock, *Dev. Biol.* **96**, 189 (1983).
11. B. Grant, D. Hirsh, *Mol. Biol. Cell* **10**, 4311 (1999).
12. A. Audhya, I. X. McLeod, J. R. Yates, K. Oegema, *PLoS ONE* **2**, e956 (2007).
13. N. Mizushima, *Genes Dev.* **21**, 2861 (2007).
14. Y. Zhang *et al.*, *Cell* **136**, 308 (2009).
15. Y. Tian *et al.*, *Cell* **141**, 1042 (2010).
16. Y. Zhai, W. H. Heijne, D. W. Smith, M. H. Saier Jr., *Biochim. Biophys. Acta* **1511**, 206 (2001).
17. P. M. Mangahas, X. Yu, K. G. Miller, Z. Zhou, *J. Cell Biol.* **180**, 357 (2008).
18. T. Braulke, J. S. Bonifacino, *Biochim. Biophys. Acta* **1793**, 605 (2009).
19. S. Treusch *et al.*, *Proc. Natl. Acad. Sci. U.S.A.* **101**, 4483 (2004).
20. Y. Zhang, B. Grant, D. Hirsh, *Mol. Biol. Cell* **12**, 2011 (2001).
21. T. E. Dever *et al.*, *Cell* **68**, 585 (1992).
22. P. Syntichaki, K. Troulinaki, N. Tavernarakis, *Nature* **445**, 922 (2007).
23. S. A. Wek, S. Zhu, R. C. Wek, *Mol. Cell. Biol.* **15**, 4497 (1995).
24. P. Zhang *et al.*, *Mol. Cell. Biol.* **22**, 6681 (2002).

Acknowledgments: We thank B. Zhu and X. Wang for discussion and critical reading of the manuscript; M. Dong for antibodies; B. Grant, H. Fares, D. Xue, H. Zhang, and the *C. elegans* Genetic Center (CGC) for strains; the Moerman laboratory (University of British Columbia) for performing the comparative genomic hybridization array; and I. Hanson for editing services. Data described in the paper are presented in the main text and the supplementary materials. This work was supported by a Ministry of Science and Technology grant (2010CB835201) to X.W. and a CR-UK Career Development Award (C11852/A4500), a CR-UK Project Grant (C11852/A5991), and a Wellcome Trust Senior Research Fellowship (0909444/Z/09/Z) to A.G.

Supplementary Materials

www.sciencemag.org/cgi/content/full/337/6092/351/DC1
Materials and Methods
Figs. S1 to S11
References (*25*–*43*)

8 February 2012; accepted 23 May 2012
10.1126/science.1220281

Deformations Within Moving Kinetochores Reveal Different Sites of Active and Passive Force Generation

Sophie Dumont,[1]*† E. D. Salmon,[2] Timothy J. Mitchison[1]

Kinetochores mediate chromosome segregation at mitosis. They are thought to contain both active, force-producing and passive, frictional interfaces with microtubules whose relative locations have been unclear. We inferred mechanical deformation within single kinetochores during metaphase oscillations by measuring average separations between fluorescently labeled kinetochore subunits in living cells undergoing mitosis. Inter-subunit distances were shorter in kinetochores moving toward poles than in those moving away. Inter-subunit separation decreased abruptly when kinetochores switched to poleward movement and decreased further when pulling force increased, suggesting that active force generation during poleward movement compresses kinetochores. The data revealed an active force-generating interface within kinetochores and a separate passive frictional interface located at least 20 nanometers away poleward. Together, these interfaces allow persistent attachment with intermittent active force generation.

Kinetochores link chromosomes to microtubules in the mitotic spindle and generate forces for chromosome movement (*1*). Mammalian kinetochores consist of more than 80 proteins (*2*), many of whose positions have been mapped with nanometer-level precision (*3*–*9*). Kinetochores are thought to interact both actively and passively with microtubules, but the molecular identity and physical nature of the relevant interfaces are unclear (*10*). Active interfaces generate pulling force by transducing the free energy of microtubule plus-end depolymerization into mechanical work (*11*, *12*) at kinetochores moving poleward (P). Passive interfaces generate molecular friction when kinetochores are forced to slide over the microtubule lattice toward plus-ends (*13*). This occurs when kinetochores moving away from poles (AP) are pulled by P sisters and also when poleward flux pulls microtubules away from stationary kinetochores in some systems (*14*, *15*).

Mechanical compliance (deformation in response to force) should report on the position and direction of forces acting on kinetochores (*6*). We used the separation between red and green probes to measure kinetochore deformation in living Ptk2 cells. The CenpC probe reported on kinetochore subunits near the chromosome, and Cdc20 and Hec1 probes reported on subunits near microtubules. CenpC binds DNA (*16*), Cdc20 reports on microtubule-binding protein KNL1, and Hec1 binds microtubules and is part of the load-bearing Ndc80 complex (Fig. 1A) (*17*). Metaphase oscillations, in which kinetochores switch fairly regularly between P and AP movement, provided natural force fluctuations (*18*, *19*).

A one-dimensional map of kinetochore subunits (Fig. 1A) was generated from light-level measurements in fixed cells and in vitro structural work (*6*). We coexpressed two fluorescent kinetochore protein pairs in Ptk2 cells, either

[1]Department of Systems Biology, Harvard Medical School, Boston, MA 02115, USA. [2]Department of Biology, University of North Carolina at Chapel Hill, Chapel Hill, NC 27599, USA.

*Present address: Department of Cell and Tissue Biology, University of California, San Francisco, San Francisco, CA 94143, USA.

†To whom correspondence should be addressed. E-mail: sophie.dumont@ucsf.edu

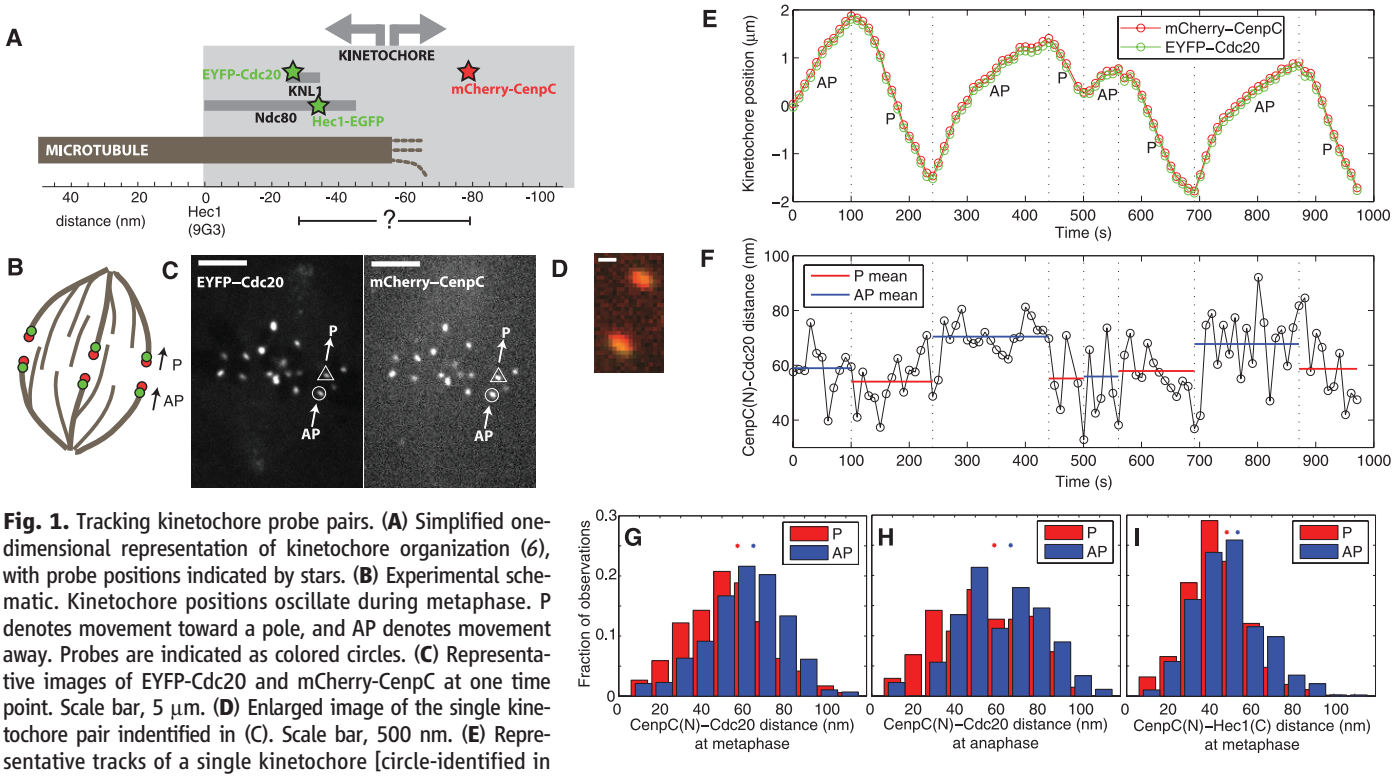

Fig. 1. Tracking kinetochore probe pairs. (**A**) Simplified one-dimensional representation of kinetochore organization (*6*), with probe positions indicated by stars. (**B**) Experimental schematic. Kinetochore positions oscillate during metaphase. P denotes movement toward a pole, and AP denotes movement away. Probes are indicated as colored circles. (**C**) Representative images of EYFP-Cdc20 and mCherry-CenpC at one time point. Scale bar, 5 μm. (**D**) Enlarged image of the single kinetochore pair indentified in (C). Scale bar, 500 nm. (**E**) Representative tracks of a single kinetochore [circle-identified in (C)], with direction indicated. Dashed lines indicate direction reversals. (**F**) Inter-probe distance versus time from the tracks in (E). Dotted lines indicate direction reversals. (**G** and **H**) Histograms of all CenpC(N)–Cdc20 distance measurements during metaphase (G) and anaphase (H). The average of the means of P and AP distributions is consistent with the reported CenpC–KNL1 N-terminal distance in fixed cells (53 to 54 nm) (*6*, *17*). (**I**) Histograms of all CenpC(N)–Hec1(C) distance measurements during metaphase. The noise in single traces and histogram widths [(F) to (I)] stemmed from both experimental noise (such as centroid determination and two-color registration) and biological variation. Stars indicate histogram distribution means.

mCherry-CenpC [N-terminal label, CenpC(N)] and EYFP-Cdc20, or mCherry-CenpC and Hec1-EGFP [C-terminal label, Hec1(C)]. These probes did not perturb metaphase oscillations (*17*). The Cdc20 probe was brighter than the Hec1 probe and was used for most experiments. We imaged red and green probes simultaneously by means of confocal fluorescence microscopy with a dichroic beam splitter and a single camera. Cells were compressed with an agarose pad so as to keep kinetochores in focus (Fig. 1B), and compression did not perturb oscillations (table S1) (*20*). Occasionally, drastic compression was used to induce unusually large forces (*17*). Using a variant (*3*, *6*) of SHREC (single-molecule high-resolution colocalization) (*21*) in vivo (Fig. 1C), we measured the distance between centroids of the probes (Fig. 1D) every 10 s during several oscillation cycles (Fig. 1E and movies S1 and S2) (*17*).

We first asked whether P and AP kinetochores were on average different. Graphs of interprobe distance over time for a single kinetochore (Fig. 1F), and a histogram of many kinetochores (Fig. 1G), revealed CenpC(N)–Cdc20 distances of 47 ± 20 nm in P kinetochores (n = 525 measurements), and 55 ± 19 nm in AP kinetochores (n = 569 measurements). These values differ with high significance ($P = 10^{-10}$) (table S2). Of kinetochores imaged, 93% displayed a greater mean inter-probe distance in AP than in P state (fig. S1A). The 15% shorter CenpC(N)–Cdc20 distance in P as compared with AP kinetochores could stem from either a mechanically compliant CenpC(N)–Cdc20 linkage that responds to force or from biochemical changes that relocalize a probe molecule.

To distinguish mechanical from biochemical causes of inter-probe distance change, we first asked whether it also occurred during anaphase, which drastically changes kinetochore biochemistry (*22*). Anaphase kinetochores are biased toward P motion to segregate chromosomes, but AP transients still occur in Ptk2 cells with similar velocities to metaphase (*18*, *23*), probably because of polar ejection forces (*17*). Inter-probe distances in anaphase were statistically indistinguishable from those at metaphase (P = 0.2 for P, and P = 0.4 for AP). The mean CenpC(N)–Cdc20 distance in anaphase was 49 ± 22 nm in P kinetochores (n = 204 measurements) and 57 ± 20 nm in AP kinetochores (n = 89 measurements) (Fig. 1H and table S2). Just as for metaphase, anaphase P and AP inter-probe distances were statistically different from each other (P = 0.004), and all but one kinetochore displayed a greater mean inter-probe distance in AP than in P state.

Next, we measured the inter-probe distance at metaphase between CenpC(N) and Hec1(C), which is part of the main load-bearing complex, Ndc80. The mean CenpC(N)–Hec1(C) distance was 38 ± 15 nm in P kinetochores (n = 564 measurements) and 43 ± 17 nm in AP kinetochores (n = 487 measurements) (Fig. 1I and table S2). These values differ with high significance ($P = 10^{-5}$), and their average was consistent with the localization of Hec1 in fixed cells (*6*). Here too, the mean behavior was representative of individual kinetochores (fig. S1B). Observing similar changes in distance from CenpC to two different probes reporting on the microtubule-binding KMN network (*2*, *17*) strongly argues that length changes between P and AP are due to mechanical compliance.

In a mechanical model, force changes and deformation changes are expected to be closely correlated in time. To test whether this requirement is met, we tracked sister kinetochores during direction reversals (Fig. 2A) in which forces change abruptly. We measured the distance within one kinetochore and distance between that kinetochore and its sister, where the latter reports on force between kinetochores from centromere stretch, during 40 s of observation (five sequential images) centered on reversals, averaged over all reversals in the data set (Fig. 2, B to D). Kinetochore direction (Fig. 2B) (*19*) and inter-kinetochore distance (Fig. 2C) both changed abruptly at reversals. P-to-AP and AP-to-P reversals occurred at markedly different inter-kinetochore distances ($P = 10^{-13}$) (Fig. 2C and table S3) and times. The leading P kinetochore reversed on average 6 ± 11 s (n = 133 reversals) before the trailing AP one (and in 15% of the cases after the AP one), which was illustrated by a shift on the

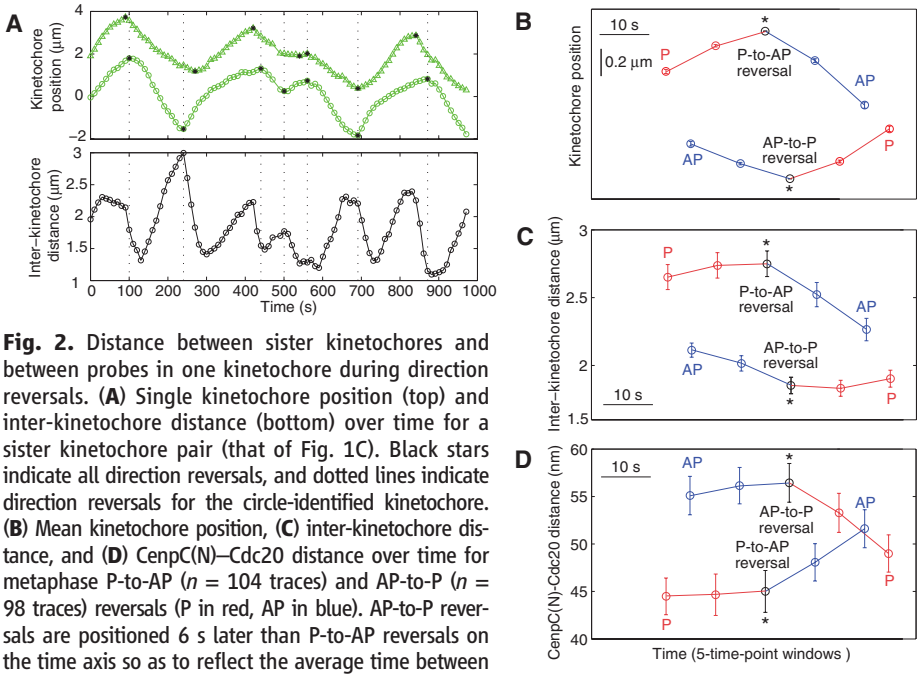

Fig. 2. Distance between sister kinetochores and between probes in one kinetochore during direction reversals. (**A**) Single kinetochore position (top) and inter-kinetochore distance (bottom) over time for a sister kinetochore pair (that of Fig. 1C). Black stars indicate all direction reversals, and dotted lines indicate direction reversals for the circle-identified kinetochore. (**B**) Mean kinetochore position, (**C**) inter-kinetochore distance, and (**D**) CenpC(N)–Cdc20 distance over time for metaphase P-to-AP (n = 104 traces) and AP-to-P (n = 98 traces) reversals (P in red, AP in blue). AP-to-P reversals are positioned 6 s later than P-to-AP reversals on the time axis so as to reflect the average time between them. Bars indicate SEM. Direction reversals cause abrupt changes in inter-probe distance within a kinetochore, which is consistent with a mechanical response to a change in force.

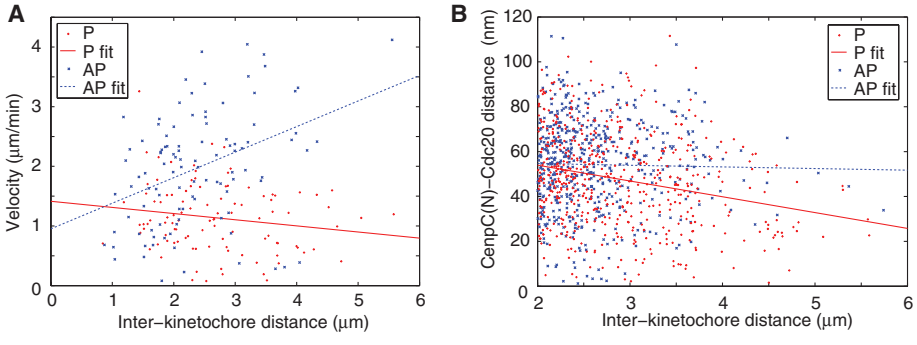

Fig. 3. Kinetochore velocity and CenpC(N)–Cdc20 distance at different inter-kinetochore distances. (**A**) Kinetochore velocity as a function of inter-kinetochore distance during metaphase P (n = 104 traces) and AP (n = 104 traces) movement before and after P-to-AP reversals, respectively, when the highest inter-kinetochore distances are visited. P velocity decreases and AP velocity increases with inter-kinetochore distance, as expected if P kinetochores generate force and inter-kinetochore distance is a metric for force. We include data from drastic spindle compression to probe even higher forces (*17*). (**B**) CenpC(N)–Cdc20 distance as a function of inter-kinetochore distance during metaphase P (n = 547 measurements) and AP (n = 529 measurements) movement. Inter-probe distance decreases with inter-kinetochore distance in P kinetochores, which is consistent with a force-deformation relationship. Lines are best linear fits.

time axis (Fig. 2, B to D). Inter-kinetochore distance tended to increase during coordinated movement because the leading P kinetochore moved slightly faster (on average) than did its trailing AP sister (fig. S2, A to D). P-to-AP reversal occurred on average 7 ± 15 s (n = 151 reversals) after the maximum inter-kinetochore distance had been reached; inter-kinetochore distance was 2.7 ± 1.0 μm at this reversal and decreased abruptly afterward as both sisters transiently moved toward each other (Fig. 2C). AP-to-P reversal occurred after this decrease in inter-kinetochore distance at 1.9 ± 0.6 μm, which is close to the global minimum (Fig. 2C and fig. S2D). The above data are consistent with a mechanical model (*24*) in which high centromere stretch favors P-to-AP reversal and low stretch favors AP-to-P reversal (*14*).

Within our time resolution, changes in movement direction and CenpC(N)–Cdc20 distances coincided (*17*). CenpC(N)–Cdc20 distances increased abruptly after P-to-AP reversals and decreased abruptly after AP-to-P reversals (Fig. 2D; fig. S2, E and F; and tables S3 and S4), which was also true at anaphase (table S3). That change in forces exerted by P and on AP kinetochores—measured through inter-kinetochore stretch—coincides closely with changes in inter-probe distances within kinetochores supports the mechanical interpretation of inter-probe distances and constrains time scales associated with force transitions.

Extent of deformation is expected to correlate with magnitude of force in a mechanical model. To test this, we plotted inter-probe distance against inter-kinetochore distance. Here too, chromosome oscillations provided natural changes in kinetochore forces (fig. S2); to extend the range of forces, we included measurements from drastically compressed cells in which inter-kinetochore stretch was up to 6 μm. Force between kinetochores is due to active force from the P kinetochore opposed largely by friction from the AP kinetochore (*14*, *15*, *24*). Velocity of AP kinetochores increased with inter-kinetochore distance, as expected if AP movement is due to pulling by the P sister opposed by frictional drag at the AP kinetochore ($P = 10^{-4}$) (Fig. 3A and table S5). Consistent with this view, velocity of P kinetochores decreased with inter-kinetochore distance (P = 0.08) (Fig. 3A and table S5) (*13*). Inter-probe distances in P kinetochores decreased with inter-kinetochore distance ($P = 10^{-8}$) (Fig. 3B and table S5). This suggests that P kinetochores that exert more force are more compressed. No correlation between inter-probe and inter-kinetochore distances was detected in AP kinetochores (P = 0.6) (Fig. 3B and table S5). When little active force was generated at low inter-kinetochore distances, both P and AP kinetochores displayed similar inter-probe distances (Fig. 3B).

Because P kinetochores, where active force is generated, are internally compressed relative to AP kinetochores and because the larger the force generated at P kinetochores the more compressed they are, we developed a simple mechanical model in which frictional forces are generated at a more outward position than that of active forces in P kinetochores, leading to internal compression (Fig. 4A, figs. S3 and S4, and tables S6 and S7) (*17*). AP kinetochores, which lack active force generation, are extended by pulling from centromeric chromatin balanced by friction at the kinetochore-microtubule interface. Kinetochore deformation need not vary linearly with force and may either represent changes in length of protein linkages or their reorientation and reorganization. We extended this mechanical model in light of previous mapping data (Fig. 4B) (*6*). The active, force-generating interface for P movement lies internal to the mean position of the Hec1(C) probe, and the passive, frictional interface is at least 20 nm outward of the active interface (Fig. 3B). This makes the microtubule-binding site at the outer end of Hec1 (Fig. 4A, 0 nm mean position) a good candidate for passive force generation (*17*).

Spatially separated passive and active interfaces at kinetochores, whether comprising different molecules or different interactions of the same molecule with microtubules in different locations (*17*), may represent a design principle with important advantages. The passive frictional interface binds persistently to microtubules independently of the microtubule dynamics state or movement direction, ensuring segregation accuracy. The active interface consumes energy to efficiently move kinetochores poleward but can evolve without the constraint of requiring persistent attachment. Together, both interfaces allow the kinetochore to harness force from depolymerizing microtubules without losing grip. That said, kinetochores may be able to function using only the passive interface—for example, in systems without anaphase A (*25*) or where microtubules polymerize continuously at kinetochores, even during anaphase (*26*). In these systems, segregation forces will be generated elsewhere in the spindle and presumably transmitted to chromatin via molecular friction.

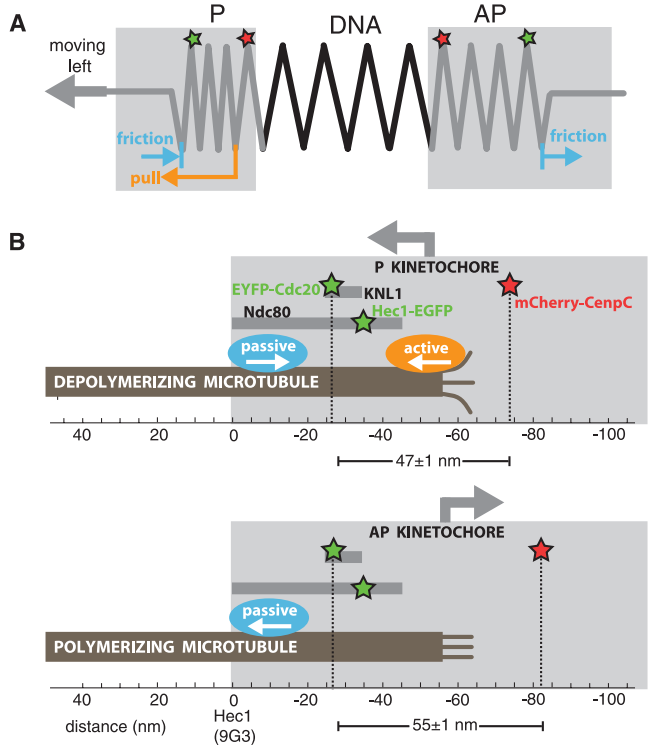

Fig. 4. Mechanical model for kinetochore compliance. (**A**) Kinetochores and inter-kinetochore chromatin viewed as three springs in series, with probes indicated by stars. P kinetochores are compressed, on average, relative to AP kinetochores. We interpret this as indicating that an active force-generating interface that is only engaged in P kinetochores (orange) lies inward of the mean positions of Cdc20 and Hec1(C), whereas a passive frictional interface that is engaged in all kinetochores (blue) lies outward of these markers. (**B**) Preliminary structural interpretation, with inter-probe distances indicated for CenpC(N)–Cdc20 (mean ± SEM). The active and passive interfaces could differ because they comprise different molecules or because force generation is restricted to the end of the microtubule, whereas friction occurs all along the embedded lattice.

References and Notes

1. S. Santaguida, A. Musacchio, *EMBO J.* **28**, 2511 (2009).
2. I. M. Cheeseman, A. Desai, *Nat. Rev. Mol. Cell Biol.* **9**, 33 (2008).
3. A. P. Joglekar, K. Bloom, E. D. Salmon, *Curr. Biol.* **19**, 694 (2009).
4. S. A. Ribeiro *et al.*, *Proc. Natl. Acad. Sci. U.S.A.* **107**, 10484 (2010).
5. R. B. Schittenhelm *et al.*, *Chromosoma* **116**, 385 (2007).
6. X. Wan *et al.*, *Cell* **137**, 672 (2009).
7. T. J. Maresca, E. D. Salmon, *J. Cell Biol.* **184**, 373 (2009).
8. K. S. Uchida *et al.*, *J. Cell Biol.* **184**, 383 (2009).
9. Z. Venkei *et al.*, *Open Biol.* **2**, 110032 (2012).
10. A. P. Joglekar, K. S. Bloom, E. D. Salmon, *Curr. Opin. Cell Biol.* **22**, 57 (2010).
11. E. L. Grishchuk, M. I. Molodtsov, F. I. Ataullakhanov, J. R. McIntosh, *Nature* **438**, 384 (2005).
12. D. E. Koshland, T. J. Mitchison, M. W. Kirschner, *Nature* **331**, 499 (1988).
13. R. B. Nicklas, *J. Cell Biol.* **97**, 542 (1983).
14. A. Khodjakov, C. L. Rieder, *J. Cell Biol.* **135**, 315 (1996).
15. P. Maddox, A. Straight, P. Coughlin, T. J. Mitchison, E. D. Salmon, *J. Cell Biol.* **162**, 377 (2003).
16. T. Hori *et al.*, *Cell* **135**, 1039 (2008).
17. Materials and methods are available as supplementary materials on *Science* Online.
18. R. V. Skibbens, V. P. Skeen, E. D. Salmon, *J. Cell Biol.* **122**, 859 (1993).
19. B. Akiyoshi *et al.*, *Nature* **468**, 576 (2010).

20. S. Dumont, T. J. Mitchison, *Curr. Biol.* **19**, 1086 (2009).
21. L. S. Churchman, Z. Okten, R. S. Rock, J. F. Dawson, J. A. Spudich, *Proc. Natl. Acad. Sci. U.S.A.* **102**, 1419 (2005).
22. B. J. Howell *et al.*, *Curr. Biol.* **14**, 953 (2004).
23. J. S. Tirnauer, J. C. Canman, E. D. Salmon, T. J. Mitchison, *Mol. Biol. Cell* **13**, 4308 (2002).
24. R. V. Skibbens, C. L. Rieder, E. D. Salmon, *J. Cell Sci.* **108**, 2537 (1995).
25. K. Oegema, A. Desai, S. Rybina, M. Kirkham, A. A. Hyman, *J. Cell Biol.* **153**, 1209 (2001).
26. J. R. J. LaFountain Jr., C. S. Cohan, A. J. Siegel, D. J. LaFountain, *Mol. Biol. Cell* **15**, 5724 (2004).

Acknowledgments: We thank J. Shah for the stable Ptk2 EYFP-Cdc20 line, C. Carroll and A. Straight for the mCherry-CenpC construct, J. DeLuca for Hec1 constructs, X. Wan for sharing SpeckleTracker, and M. Kirschner for equipment loan. We thank I. Cheeseman, P. Choi, S. Churchman, J. DeLuca, M. Ginzberg, Q. Justman, J. Shah, X. Wan, and J. Waters (HMS Nikon Imaging Center) for discussions. S.D. was supported by the Charles A. King Trust, Bank of America and by NIH K99GM094335; E.D.S. was supported by NIH R37GM024364; and T.J.M. was supported by NIH R01GM039565. Data are presented in the supplementary materials.

Supplementary Materials
www.sciencemag.org/cgi/content/full/science.1221886/DC1
Materials and Methods
Supplementary Text
Figs. S1 to S4
Tables S1 to S7
References (*27*–*76*)
Movies S1 and S2

13 March 2012; accepted 14 May 2012
Published online 21 June 2012;
10.1126/science.1221886

Regional Astrocyte Allocation Regulates CNS Synaptogenesis and Repair

Hui-Hsin Tsai,[1,2,5] Huiliang Li,[6*] Luis C. Fuentealba,[4,5*] Anna V. Molofsky,[1,3,5*] Raquel Taveira-Marques,[6*] Helin Zhuang,[6] April Tenney,[1,2] Alice T. Murnen,[1,2,5] Stephen P. J. Fancy,[1,2,5] Florian Merkle,[4†] Nicoletta Kessaris,[6] Arturo Alvarez-Buylla,[4,5‡] William D. Richardson,[6‡] David H. Rowitch[1,2,4,5‡]

Astrocytes, the most abundant cell population in the central nervous system (CNS), are essential for normal neurological function. We show that astrocytes are allocated to spatial domains in mouse spinal cord and brain in accordance with their embryonic sites of origin in the ventricular zone. These domains remain stable throughout life without evidence of secondary tangential migration, even after acute CNS injury. Domain-specific depletion of astrocytes in ventral spinal cord resulted in abnormal motor neuron synaptogenesis, which was not rescued by immigration of astrocytes from adjoining regions. Our findings demonstrate that region-restricted astrocyte allocation is a general CNS phenomenon and reveal intrinsic limitations of the astroglial response to injury.

Astrocytes serve roles essential for normal neurological function such as regulation of synapse formation, maintenance of the blood-brain barrier (BBB), and neuronal homeostasis (*1*, *2*). Although astroglia are regionally heterogeneous in terms of gene expression and their electrical and functional properties (*3*–*5*), astrocyte diversification and migration remain poorly understood. Two generally recognized types of astrocytes are fibrous astrocytes (FAs) of white matter that express glial fibrillary acidic protein (GFAP), and protoplasmic astrocytes (PAs) of gray matter that normally express little or no GFAP. *Aldh1L1-GFP* and AldoC are more recently described markers of both PAs

[1]Howard Hughes Medical Institute, University of California San Francisco, San Francisco, CA 94143, USA. [2]Department of Pediatrics, University of California San Francisco, San Francisco, CA 94143, USA. [3]Department of Psychiatry/Langley-Porter Institute, University of California San Francisco, San Francisco, CA 94143, USA. [4]Department of Neurosurgery, University of California San Francisco, San Francisco, CA 94143, USA. [5]Eli and Edythe Broad Center of Regeneration Medicine and Stem Cell Research, University of California San Francisco, San Francisco, CA 94143, USA. [6]Wolfson Institute for Biomedical Research and Research Department of Cell and Developmental Biology, University College London, London WC1E 6BT, UK.

*These authors contributed equally to this work.
†Present address: Departments of Stem Cell and Regenerative Biology and Molecular and Cellular Biology, Harvard University, Cambridge, MA 02138, USA.
‡To whom correspondence should be addressed. E-mail: rowitchd@peds.ucsf.edu (D.H.R.); abuylla@stemcell.ucsf.edu (A.A.-B.); w.richardson@ucl.ac.uk (W.D.R.)

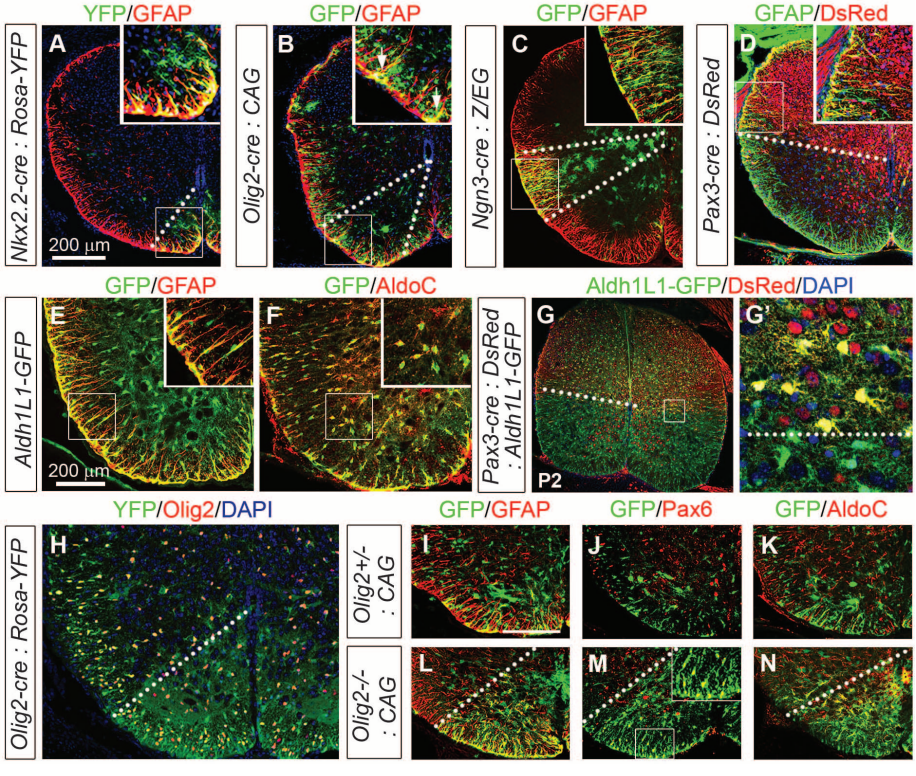

Fig. 1. Segmental distribution of fibrous and protoplasmic astrocytes in spinal cord. (**A**) *Nkx2.2-creERT2* (tamoxifen induction E10.5 to E12.5):*Rosa26-YFP* fate map shows YFP$^+$, GFAP$^+$ cells at the ventral midline at P0. YFP, yellow fluorescent protein. (**B**) In P2 *Olig2-tva-cre:CAG-GFP* mice, astrocytes remain in register with pMN, whereas Olig2$^+$ OPs distribute widely. (**C**) *Ngn3-cre:Z/EG* P1 cord shows intermediate wedge of astrocytes. (**D**, **G**, **G′**) At P2, FAs and PAs in *Pax3-cre* animals remain dorsally restricted. DAPI, 4′,6-diamidino-2-phenylindole. (**E** and **F**) *Aldh1L1-GFP* coexpression with GFAP$^+$ (FAs) and AldoC$^+$ (FAs and PAs) cells. (**H** to **N**) Astrocytes from *Olig2cre/+* spinal cord have a restricted ventral distribution. In *Olig2cre/cre* nulls, we observe significantly (*P < 0.0001) increased p2-type (GFAP$^+$, Pax6$^+$, AldoC$^+$) astrocytes (fig. S1I), which fail to migrate from the ventral domain. Scale bars, 200 μm.

and FAs (*6*, *7*). Embryonic astrocytes derive from radial glia (*8*–*10*) and several lines of evidence indicate that glial subtype specification in the ventral spinal cord is determined according to a segmental template (*11*). For example, basic helix-loop-helix (bHLH) proteins Olig2 and SCL regulate oligodendrocyte versus astrocyte precursor cell fate in the pMN and p2 neuroepithelial progenitor domains, respectively (*12*), and homeodomain proteins Nkx6.1 and Pax6 regulate the region-specific molecular phenotype of FAs in the ventral spinal cord (*13*).

How do astrocytes disseminate from their sites of origin in the ventricular zone (VZ)? Two distinct modes of astrocyte migration have been reported. Retroviral fate mapping of neonatal SVZ progenitors (*14*) and transplantation of glial precursors (*15*) suggest that astrocytes can migrate long distances and in multiple directions, implying that astrocytes derived from radial glia (or other precursors) in different VZ domains might intermix (fig. S1A). Consistent with this model, some PAs have been proposed to derive from migratory NG2 cells (*16*). In contrast, astrocytes might distribute stringently into "segmental" territories correlating with their domains of origin in the patterned VZ (*8*–*10*), without secondary tangential migration. Although little is known about regulation of astrocyte progenitor migration during development, Stat3 signaling and *Cdc42* have been shown to function in reactive astrocyte invasion of lesions after injury (*17*, *18*).

Establishing how astrocytes are allocated to different territories is key to understanding how they might develop to support regionally diversified neurons. We first investigated this in vivo by conditional reporter fate mapping of radial glia and their progeny in distinct dorsal-ventral (DV) spinal cord domains (fig. S1B and table S2). Labeling for the reporter protein together with markers of neurons (NeuN), oligodendrocytes (Olig2), or fibrous astrocytes (GFAP) allowed us to compare production of these cell types across domains (table S1, Fig. 1, and fig. S1) (*19*).

We found that FAs from the p3 progenitor domain (defined by *Nkx2.2-creERT2)* invariably remained close to the ventral midline (Fig. 1A). The pMN domain (*Olig2-tva-cre*) generated mainly oligodendrocyte precursor cells (OPs), which migrated extensively (Fig. 1, B and H), and some FAs [4% of all GFP$^+$ cells in spinal cord at postnatal day 7 (P7)] (fig. S1D and table S1) (*20*), which settled in ventral white matter (Fig. 1B). For intermediate and dorsal domains, we used cre driven by *Ngn3*, *Dbx1*, *Msx3*, *Math1*, or *Pax3* regulatory sequences (Fig. 1, C and D; table S1; and fig. S1, E to H). These data indicate that all spinal cord GFAP$^+$ FAs distribute radially, in register with the DV position of their neuroepithelial precursors.

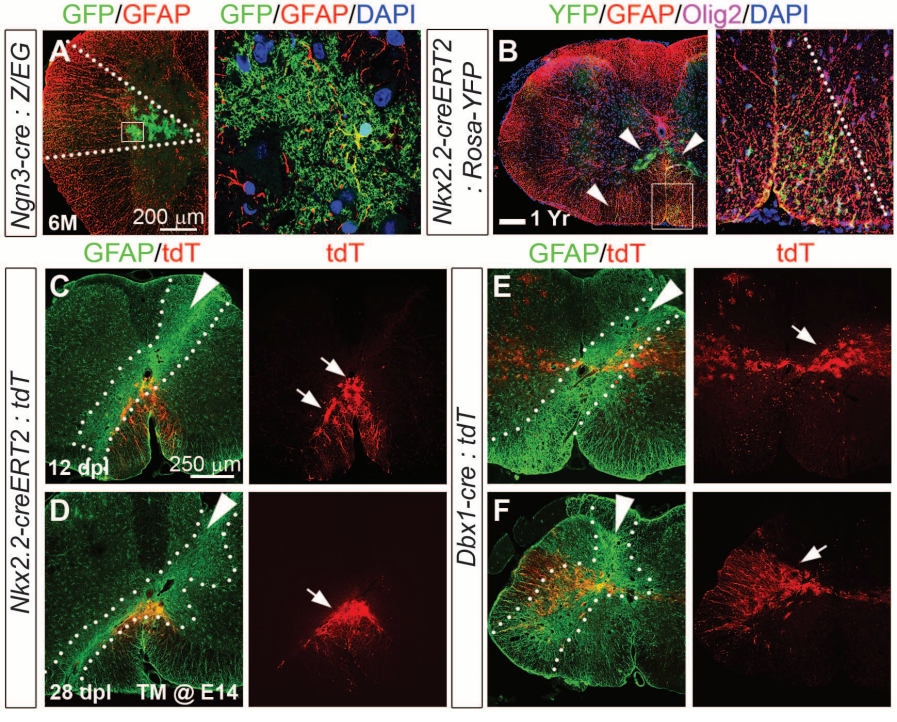

Fig. 2. Absence of tangential astrocyte migration in adult spinal cord even after injury. (**A**) Bushy GFP$^+$ PAs in *Ngn3-cre:Z/EG* cord persisted after 6 months of age. (**B**) Astrocytes in *Nkx2.2-creERT2* (induced E10 to E11)*:Rosa26-YFP* cords remain ventrally restricted at 1 year. (**C** to **F**) Post-stab gliosis does not recruit astrocytes from adjacent domains. Fate-mapped astrocytes (arrows) in *Rosa26-tdTomato* on the *Nkx2.2-creERT2* [induced E14 (C and D)] or *Dbx1-cre* (E and F) background remain confined to ventral or intermediate cord, respectively, 12 and 28 days postlesion (dpl). Intense GFAP staining indicates lesion site (dashed lines, white arrowheads indicate needle trajectory).

PAs and FAs are morphologically and functionally distinct (*21*, *22*). We used *Aldh1L1-GFP* astrocyte-specific reporter mice (*7*) and antibodies recognizing AldoC (*6*), which mark both PAs and FAs but few, if any, neurons or Olig2$^+$ cells (Fig. 1, E and F; figs. S2E and S3, A and B; and movie S1). Fate mapping of *BLBP-cre* expressing precursors (fig. S3, C and D) demonstrated that PA and FA are generated from radial glia and/or their progeny. PAs and FAs originating from the same precursor domain came to rest within overlapping territories. For example, combining *Pax3-cre* with the *Aldh1L1-GFP* reporter confirmed that all *Pax3*-derived PAs and FAs remained confined to dorsal spinal cord (Fig. 1G). Despite reports that FAs and PAs develop via distinct pathways (*16*, *23*, *24*), we did not observe any domain dedicated to either FAs or PAs.

We next attempted to disrupt the radial distribution of astrocytes. First, because embryonic pMN-derived OPs disperse in all directions (Fig. 1I) (*25*), we tested whether this domain might similarly promote tangential astrocyte migration. In *Olig2*-null embryos, the pMN domain is transformed into a p2-like domain that generates astrocytes instead of OPs (*26*). In the embryonic day 18 (E18) *Olig2-cre*-null spinal cord, we found increased numbers of "p2-type" astrocytes (fig. S1I) but, nonetheless, these remained spatially constrained within the ventral cord (Fig. 1, I to N). Although all domains examined produced astrocytes, they showed different potential for the generation of astrocytes versus oligodendrocytes (fig. S1J), most dramatically illustrated by *Olig2*-null animals. Time-lapse imaging of spinal cord slice cultures revealed exclusively radial movement of *Aldh1L1-GFP* cells (fig. S3, E and F), even after a heterotopic transfer of green fluorescent protein (GFP)–labeled VZ progenitors into unlabeled slices (fig. S3, G to K). Together, these data reveal a strictly segmental investment of the developing spinal cord by astrocytes (fig. S1A).

Might astrocytes undergo secondary tangential migration at later stages or during adulthood? *Ngn3* transcripts are transiently expressed in intermediate neural tube from E12.5 to E14.5 (fig. S2, A to D). As shown (Fig. 2A and fig. S2, E and F), intermediate-domain PAs derived from embryonic *Ngn3-cre*–labeled radial glia persisted up to 6 months without attrition or migration. We induced *Nkx2.2-creERT2:Rosa26-YFP* mice with tamoxifen (E10 to E12, after generation of p3-derived neurons) and visualized the labeled astrocytes 1 year later (Fig. 2B). Even at this advanced age, FAs and PAs were confined in a tight ventromedial distribution. These findings show that the long-term distribution of astrocytes in the adult spinal cord is determined during embryogenesis by their site of origin in the VZ (fig. S2G).

We attempted to disrupt the normal "segmental" pattern of astrocytes by acute injury-induced gliosis in adult *Rosa26-tdTomato* conditional reporters crossed into *Nkx2.2-creERT2* (induced at E14) or *Dbx1-cre* backgrounds. However, no ventrally derived astrocytes migrated into a dorsal

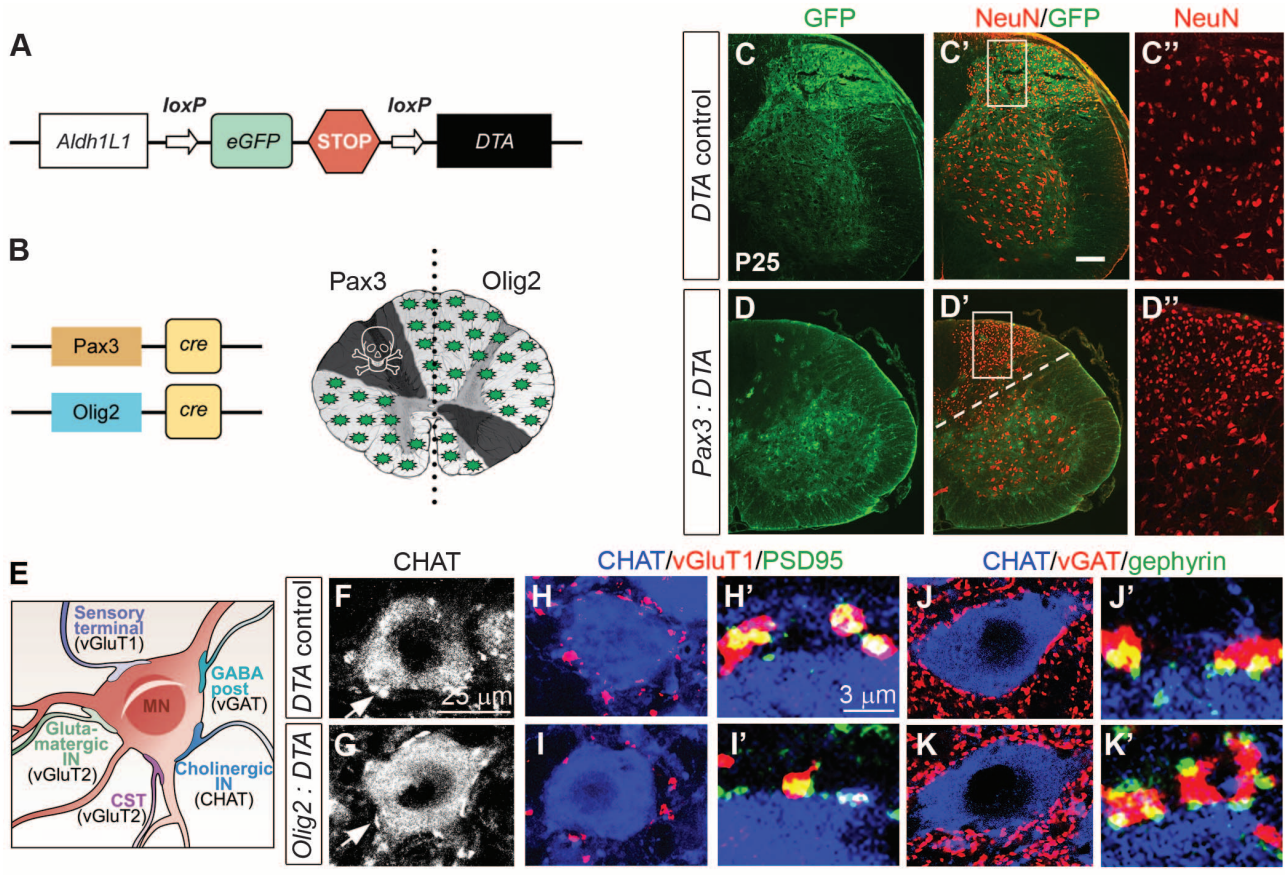

Fig. 3. Regional astrocyte depletion results in neuronal abnormalities. (**A**) Cartoon of *Aldh1L1-DTA* transgene; cre excises eGFP-Stop cassette allowing DTA transcription. (**B**) Regions targeted by *Pax3-cre* or *Olig2-cre*. (**C** and **D**) *Pax3-cre:Aldh1L1-DTA* mice show absence of GFP, neuropil, and congested appearance of NeuN (red) neurons in dorsal cord. (**E**) Cartoon of MN soma and synapse subtypes. CST, corticospinal tract. (**F** and **G**) We observed no differences in the number of cholinergic CHAT or vGlut2 (fig. S5) synapses. (**H** and **I**) Numbers of excitatory vGluT1-PSD95 synapses were significantly decreased, whereas (**J** and **K**) inhibitory vGAT-gephyrin synapses were significantly increased in bigenic animals compared with controls. For quantification, see fig. S5.

stab wound after 12 or 28 days, despite the lesion tract passing very close to the labeled astrocytes (Fig. 2, C to F).

A possible explanation for the lack of mobility was that all astrocyte niches were fully occupied, preventing immigration from other domains. Previously, we achieved selective elimination of OPs using *Diphtheria toxin A* (*DTA*) under *Sox10* transcriptional control (*27*). We generated an analogous *Aldh1L1*-based system in which the nonrecombined transgene expresses *eGFP*, whereas cre exposure deletes *eGFP* and promotes *DTA* expression (Fig. 3A). Intercrosses with *Pax3-cre* mice resulted in perinatal lethality (10% survivors observed versus 25% expected). The dorsal spinal cord (corresponding to the *Pax3* domain) of P25 animals showed atrophy, reduction in the total number of *Aldh1L1*-expressing cells, loss of neuropil, and congested neurons (Fig. 3, C and D, and fig. S4A). We did not observe increased inflammation, gliosis, or BBB permeability in these mice (fig. S4, A and C), suggesting that remaining astrocytes were sufficient for structural maintenance. Although ventral astrocytes might have invaded to rescue the dorsal cord, this possibility was ruled out because they would have continued to express GFP. The mild phenotype of *Pax3-cre:Aldh1L1-DTA* animals suggested astrocyte depletion rather than ablation. We quantified astrocyte depletion by crossing *Aldh1L1-DTA* with *BLBP-cre*, active in radial glia. Double-transgenics died at birth, but at E17.5 we observed 43% excision of transgene GFP and a 28% reduction in AldoC$^+$ astrocytes (fig. S4B). It is possible that some astrocytes survived because they are resistant to attenuated *DTA* (*27*); alternatively, expression of our transgene might be variegated.

We tested whether astrocyte depletion could be used to assess local neuronal support functions using *Olig2-cre:Aldh1L1-DTA* mice, which were suitable because motor neurons (MNs, derived from pMN) are invested with several synaptic terminal types (Fig. 3E). Although we found a ~30% depletion of AldoC$^+$ astrocytes in the ventral horns at P28 (fig. S4C), the number and size of MNs were unaffected (fig. S5, A and B). We counted choline acetyltransferase (CHAT)$^+$ synaptic relays over the entire surface of MN soma but found no significant differences between *DTA* and control mice (fig. S5C). Similarly, we found no change in the number of vGluT2-PSD95$^+$ (postsynaptic density 95) excitatory presynaptic inputs (fig. S5F). In contrast, there was a significant ($P = 0.006$) decrease in vGluT1-PSD95$^+$ excitatory inputs from proprioceptive axons and a significant increase ($P = 0.004$) in vGAT-gephyrin$^+$ inhibitory inputs in *DTA* mice (Fig. 3, H to K, and fig. S5, D and E). Thus, pMN-derived astrocytes are required for genesis and/or maintenance of certain types of synapses on MNs, and this function cannot be rescued by astrocytes from adjacent domains.

Is localized investment of astrocytes a general phenomenon throughout the CNS? We analyzed intercrosses of *Emx1-cre*, *Dbx1-cre*, or *Nkx2.1-cre* drivers, which label dorsal, intermediate, and ventral forebrain precursor cells, respectively, with a conditional *Rosa-tdTomato* reporter line or *Aldh1L1-GFP*. Forebrain astrocytes all demonstrated DV restriction associated with their domains of origin without detectable secondary migration (Fig. 4, A to N, and fig. S7A), even after injury (fig. S6). We observed many GFP$^+$ cortical interneurons in *Nkx2.1-cre:Rosa-tdTomato* mice that migrate from the medial ganglionic eminence during development (Fig. 4, K to N). In sharp contrast, astrocytes derived from *Nkx2.1-cre* territory remained ventral (Fig. 4, J, L, and N).

Our transgenic cre-loxP approach labeled broad progenitor domains. For higher resolution,

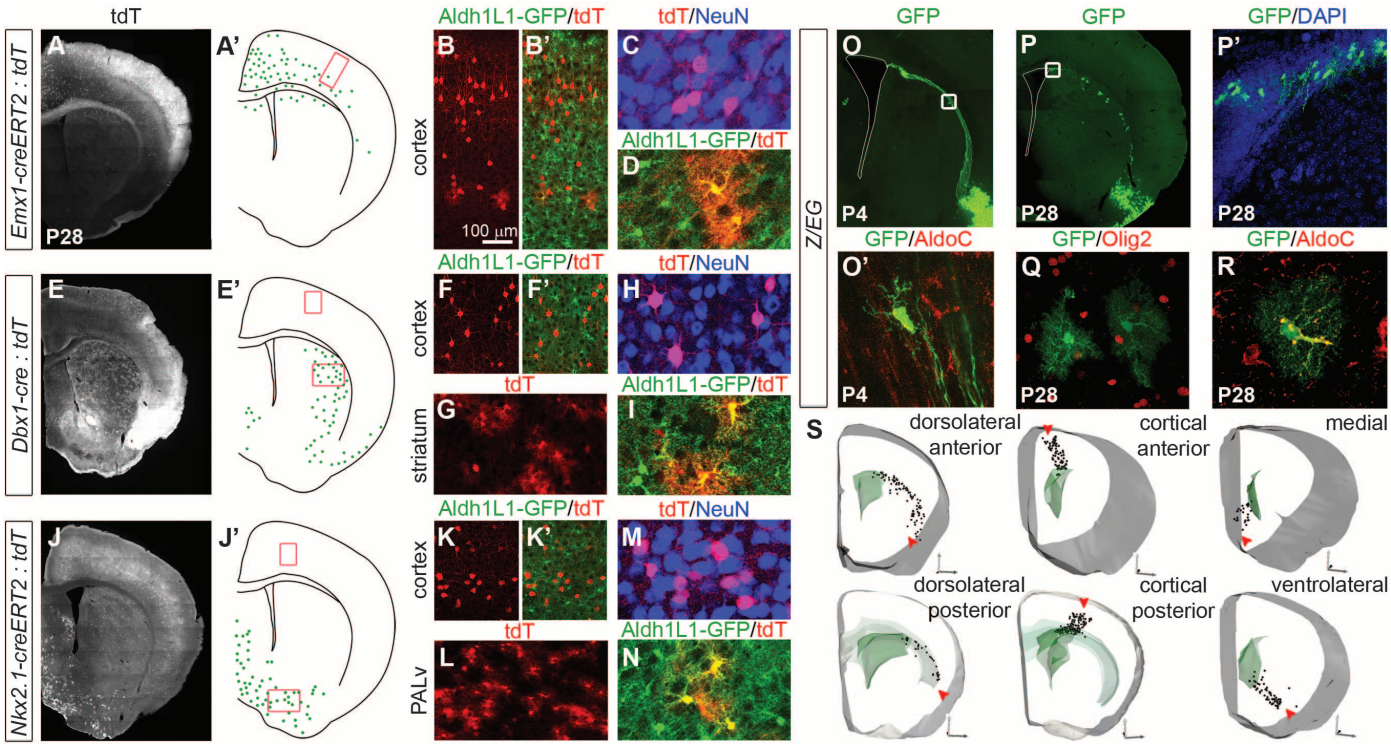

Fig. 4. Region-restricted astrocyte investment from forebrain radial glia. (**A** to **D**) *Emx1-creERT2* (induced E17):*Rosa26-tdTomato* labeled cells; note (**A'**) distribution of astrocytes (green) confined to cortical plate and corpus callosum. Red box indicates region of cortex analyzed in (B) to (D). (**E** to **I**) Distribution of *Dbx1-cre* astrocytes in striatum. Red boxes indicate regions of cortex and striatum analyzed in (F) to (I). (**J** to **N**) Distribution of *Nkx2.1-creERT2* (induced E17) astrocytes in ventromedial forebrain. Red box in cortex indicates fate-mapped interneurons. (**O** to **S**) Distribution of astrocytes after radial glial Ad-cre infection of P1 *Z/EG* reporter mice in the forebrain regions indicated analyzed at P4 or P28. Astrocytes were recognized by morphology and AldoC immunolabeling. We injected dorsal (n = 20), ventral (n = 21), medial (n = 19), and cortical (n = 17) brain regions (red arrows). No tangential astrocyte migration was observed. PALv, ventral pallidum.

we targeted foci of radial glia by adenovirus-cre infection of the cortical surface of P1 *Z/EG* reporter mice (*28*), and analyzed the forebrains by GFP immunolabeling at P4 and P28 (Fig. 4, O to S, and fig. S7B). At P4, GFP^+, $AldoC^+$ immature astrocytes were found in close association with infected radial glial fibers (Fig. 4O). At P28, we observed restricted labeling of ependymal and astrocyte-like cells in the VZ and sub-VZ along with a trail of astrocytes distributed along the former trajectory of the radial glial processes (Fig. 4, P to R). This experiment was performed repeatedly (n = 77) to label DV and rostral-caudal regions comprehensively. Three-dimensional reconstructions of findings are summarized in Fig. 4S and movies S2 to S5. In every case, we found that the distribution of labeled astrocytes corresponded closely to the trajectories of the processes of their radial glial ancestors, in keeping with other findings in cortex (*29*).

Although certain astrocyte functions might be common throughout the CNS (e.g., formation of the BBB), other functions subserve the local neuronal circuitry and might be domain-specific. In this study we tested (i) whether astrocytes generated in different domains become intermixed or remain spatially segregated, (ii) whether neurons are functionally dependent on astrocytes that are generated from the same progenitor domains, and (iii) whether such domain-specific roles can be rescued by astrocytes from adjacent regions. Our data indicate that astrocytes migrate from the VZ in a strictly radial fashion, reminiscent of the columnar distribution of cortical projection neurons (*30*), forming well-defined, stable spatial domains throughout the CNS. We found no evidence for secondary tangential migration of FAs or PAs during development, adulthood, or after injury. Although some astrocytes may be derived from the division of local nonradial glial precursors (*31*), our study shows that they do not disperse tangentially. The restricted distribution of forebrain astrocytes after neonatal adenovirus infection results in exquisite maps that reflect the original trajectory of their radial glial precursors. It follows that astrocytes might serve as a scaffold and retain spatially encoded information established during neural tube patterning—e.g., for purposes of axon guidance.

Astrocytes in various spatial domains might become specialized for interactions with their own particular neuronal neighbors as result of common patterning mechanisms. We selectively removed a fraction of pMN-derived astrocytes by targeted expression of DTA and found that numbers of certain synapses on MNs were altered. Our findings show that astrocytes from neighboring progenitor domains were unable to invade and rescue the depleted area, indicating essential region-specific neuron-astrocyte interactions. The transgenic tools we have developed allow for genetic manipulation of specific astrocyte subgroups, e.g., to mis-specify their positional fate while leaving early VZ patterning and neuronal subtype specification intact. Our findings demonstrate that region-restricted astrocyte allocation is a general CNS phenomenon and reveal intrinsic limitations of the astroglial response to injury. They further suggest that astrocytes might act as stable repositories of spatial information necessary for development and local regulation of brain function.

References and Notes

1. H. Kettenmann, B. R. Ransom, *Neuroglia* (Oxford Univ. Press, Oxford, 2005).
2. D. D. Wang, A. Bordey, *Prog. Neurobiol.* **86**, 342 (2008).
3. J. P. Doyle *et al.*, *Cell* **135**, 749 (2008).
4. V. Houades, A. Koulakoff, P. Ezan, I. Seif, C. Giaume, *J. Neurosci.* **28**, 5207 (2008).
5. A. Nimmerjahn, E. A. Mukamel, M. J. Schnitzer, *Neuron* **62**, 400 (2009).
6. R. M. Bachoo *et al.*, *Proc. Natl. Acad. Sci. U.S.A.* **101**, 8384 (2004).
7. J. D. Cahoy *et al.*, *J. Neurosci.* **28**, 264 (2008).
8. S. C. Noctor, V. Martínez-Cerdeño, L. Ivic, A. R. Kriegstein, *Nat. Neurosci.* **7**, 136 (2004).
9. D. E. Schmechel, P. Rakic, *Anat. Embryol. (Berl.)* **156**, 115 (1979).

10. T. Voigt, *J. Comp. Neurol.* **289**, 74 (1989).
11. D. H. Rowitch, *Nat. Rev. Neurosci.* **5**, 409 (2004).
12. Y. Muroyama, Y. Fujiwara, S. H. Orkin, D. H. Rowitch, *Nature* **438**, 360 (2005).
13. C. Hochstim, B. Deneen, A. Lukaszewicz, Q. Zhou, D. J. Anderson, *Cell* **133**, 510 (2008).
14. S. W. Levison, J. E. Goldman, *Neuron* **10**, 201 (1993).
15. M. S. Windrem *et al.*, *Cell Stem Cell* **2**, 553 (2008).
16. X. Zhu, R. A. Hill, A. Nishiyama, *Neuron Glia Biol.* **4**, 19 (2008).
17. S. Okada *et al.*, *Nat. Med.* **12**, 829 (2006).
18. S. Robel, S. Bardehle, A. Lepier, C. Brakebusch, M. Götz, *J. Neurosci.* **31**, 12471 (2011).
19. Materials and methods are available as supplementary materials on *Science* Online.
20. N. Masahira *et al.*, *Dev. Biol.* **293**, 358 (2006).
21. C. Shannon, M. Salter, R. Fern, *J. Anat.* **210**, 684 (2007).
22. N. A. Oberheim *et al.*, *J. Neurosci.* **29**, 3276 (2009).
23. J. Cai *et al.*, *Development* **134**, 1887 (2007).
24. M. S. Rao, M. Noble, M. Mayer-Pröschel, *Proc. Natl. Acad. Sci. U.S.A.* **95**, 3996 (1998).
25. H. H. Tsai, W. B. Macklin, R. H. Miller, *J. Neurosci.* **26**, 1913 (2006).
26. Q. Zhou, D. J. Anderson, *Cell* **109**, 61 (2002).
27. N. Kessaris *et al.*, *Nat. Neurosci.* **9**, 173 (2006).
28. F. T. Merkle, Z. Mirzadeh, A. Alvarez-Buylla, *Science* **317**, 381 (2007).
29. S. Magavi, D. Friedmann, G. Banks, A. Stolfi, C. Lois, *J. Neurosci.* **32**, 4762 (2012).
30. P. Rakic, *Science* **241**, 170 (1988).
31. W. P. Ge, A. Miyawaki, F. H. Gage, Y. N. Jan, L. Y. Jan, *Nature* **484**, 376 (2012).

Acknowledgments: We thank M. Wong, S. Kaing, U. Dennehy, M. Grist, and S. Chang for technical help and E. Huillard, V. Heine, and C. Stiles for helpful comments. We thank A. Leiter (University of Massachusetts, Worcester) for *Ngn3-cre* mice. L.C.F. is a Howard Hughes Medical Institute (HHMI) Fellow of the Helen Hay Whitney Foundation. R.T.-M. was funded by the Portuguese Fundação para a Ciência e a Tecnologia. This work was supported by grants from the NIH, UK Medical Research Council, Wellcome Trust, and European Research Council. A.A.-B. holds the Heather and Melanie Muss Chair of Neurological Surgery. D.H.R. is a HHMI Investigator.

Supplementary Materials

www.sciencemag.org/cgi/content/full/science.1222381/DC1
Materials and Methods
Figs. S1 to S7
Tables S1 and S2
References (*32*–*43*)
Movies S1 to S5

26 March 2012; accepted 6 June 2012
Published online 28 June 2012;
10.1126/science.1222381

High-Resolution Protein Structure Determination by Serial Femtosecond Crystallography

Sébastien Boutet,[1]* Lukas Lomb,[2,3] Garth J. Williams,[1] Thomas R. M. Barends,[2,3] Andrew Aquila,[4] R. Bruce Doak,[5] Uwe Weierstall,[5] Daniel P. DePonte,[4] Jan Steinbrener,[2,3] Robert L. Shoeman,[2,3] Marc Messerschmidt,[1] Anton Barty,[4] Thomas A. White,[4] Stephan Kassemeyer,[2,3] Richard A. Kirian,[5] M. Marvin Seibert,[1] Paul A. Montanez,[1] Chris Kenney,[6] Ryan Herbst,[6] Philip Hart,[6] Jack Pines,[6] Gunther Haller,[6] Sol M. Gruner,[7,8] Hugh T. Philipp,[7] Mark W. Tate,[7] Marianne Hromalik,[9] Lucas J. Koerner,[10] Niels van Bakel,[11] John Morse,[12] Wilfred Ghonsalves,[1] David Arnlund,[13] Michael J. Bogan,[14] Carl Caleman,[4] Raimund Fromme,[15] Christina Y. Hampton,[14] Mark S. Hunter,[15] Linda C. Johansson,[13] Gergely Katona,[13] Christopher Kupitz,[15] Mengning Liang,[4] Andrew V. Martin,[4] Karol Nass,[16] Lars Redecke,[17,18] Francesco Stellato,[4] Nicusor Timneanu,[19] Dingjie Wang,[5] Nadia A. Zatsepin,[5] Donald Schafer,[1] James Defever,[1] Richard Neutze,[13] Petra Fromme,[15] John C. H. Spence,[5] Henry N. Chapman,[4,16] Ilme Schlichting[2,3]

Structure determination of proteins and other macromolecules has historically required the growth of high-quality crystals sufficiently large to diffract x-rays efficiently while withstanding radiation damage. We applied serial femtosecond crystallography (SFX) using an x-ray free-electron laser (XFEL) to obtain high-resolution structural information from microcrystals (less than 1 micrometer by 1 micrometer by 3 micrometers) of the well-characterized model protein lysozyme. The agreement with synchrotron data demonstrates the immediate relevance of SFX for analyzing the structure of the large group of difficult-to-crystallize molecules.

Elucidating macromolecular structures by x-ray crystallography is an important step in the quest to understand the chemical mechanisms underlying biological function. Although facilitated greatly by synchrotron x-ray sources, the method is limited by crystal quality and radiation damage (*1*). Crystal size and radiation damage are inherently linked, because reducing radiation damage requires lowering the incident fluence. This in turn calls for large crystals that yield sufficient diffraction intensities while reducing the dose to individual molecules in the crystal. Unfortunately, growing well-ordered large crystals can be difficult in many cases, particularly for large macromolecular assemblies and membrane proteins. In contrast, micrometer-sized crystals are frequently observed. Although diffraction data of small crystals can be collected by using microfocus synchrotron beamlines, this remains a challenging approach because of the rapid damage suffered by these small crystals (*1*).

Serial femtosecond crystallography (SFX) using x-ray free-electron laser (XFEL) radiation is an emerging method for three-dimensional (3D) structure determination using crystals ranging from a few micrometers to a few hundred nanometers in size and potentially even smaller. This method relies on x-ray pulses that are sufficiently intense to produce high-quality diffraction while of short enough duration to terminate before the onset of substantial radiation damage (*2*–*4*). X-ray pulses of only 70-fs duration terminate before any chemical damage processes have time to occur, leaving primarily ionization and x-ray–induced thermal motion as the main sources of radiation damage (*2*–*4*). SFX therefore promises to break the correlation between sample size, damage, and resolution in structural biology. In SFX, a liquid microjet is used to introduce fully hydrated, randomly oriented crystals into the single-pulse XFEL beam (*5*–*8*), as illustrated in Fig.1. A recent low-resolution proof-of-principle demonstration of SFX performed at the Linac Coherent Light Source (LCLS) (*9*) using crystals of photosystem I ranging in size from 200 nm to 2 μm produced interpretable electron density maps (*6*). Other demonstration experiments using crystals grown in vivo (*7*), as well as in the lipidic sponge phase for membrane proteins (*8*), were recently published. However, in all these cases, the x-ray energy of 1.8 keV (6.9 Å) limited the resolution of the collected data to about 8 Å. Data collection to a resolution better than 2 Å became possible with the recent commis-

[1]Linac Coherent Light Source (LCLS), SLAC National Accelerator Laboratory, 2575 Sand Hill Road, Menlo Park, CA 94025, USA. [2]Max-Planck-Institut für Medizinische Forschung, Jahnstrasse 29, 69120 Heidelberg, Germany. [3]Max Planck Advanced Study Group, Center for Free-Electron Laser Science, Notkestrasse 85, 22607 Hamburg, Germany. [4]Center for Free-Electron Laser Science, Deutsches Elektronen-Synchrotron (DESY), Notkestrasse 85, 22607 Hamburg, Germany. [5]Department of Physics, Arizona State University, Tempe, AZ 85287, USA. [6]Particle Physics and Astrophysics, SLAC National Accelerator Laboratory, 2575 Sand Hill Road, Menlo Park, CA 94025, USA. [7]Department of Physics, Laboratory of Atomic and Solid State Physics, Cornell University, Ithaca, NY 14853, USA. [8]Wilson Laboratory, Cornell High Energy Synchrotron Source (CHESS), Cornell University, Ithaca, NY 14853, USA. [9]Electrical and Computer Engineering, State University of New York (SUNY) Oswego, Oswego, NY 13126, USA. [10]The Johns Hopkins University Applied Physics Laboratory, 11100 Johns Hopkins Road, Laurel, MD 20723, USA. [11]Nikhef, National Institute for Subatomic Physics, Science Park 105, 1098 XG Amsterdam, Netherlands. [12]European Synchrotron Radiation Facility, 38043 Grenoble Cedex, France. [13]Department of Chemistry and Molecular Biology, University of Gothenburg, SE-405 30 Gothenburg, Sweden. [14]PULSE Institute, SLAC National Accelerator Laboratory, 2575 Sand Hill Road, Menlo Park, CA 94025, USA. [15]Department of Chemistry and Biochemistry, Arizona State University, Tempe, AZ 85287–1604, USA. [16]University of Hamburg, Luruper Chaussee 149, 22761 Hamburg, Germany. [17]Joint Laboratory for Structural Biology of Infection and Inflammation, Institute of Biochemistry and Molecular Biology, University of Hamburg, and Institute of Biochemistry, University of Lübeck, at DESY, Hamburg, Germany. [18]German Centre for Infection Research, University of Lübeck, 23538 Lübeck, Germany. [19]Laboratory of Molecular Biophysics, Department of Cell and Molecular Biology, Uppsala University, Husargatan 3 (Box 596), SE-751 24 Uppsala, Sweden.

*To whom correspondence should be addressed. E-mail: sboutet@slac.stanford.edu

sioning of the LCLS Coherent X-ray Imaging (CXI) instrument (*10*). The CXI instrument provides hard x-ray pulses suitable for high-resolution crystallography and is equipped with Cornell-SLAC Pixel Array Detectors (CSPADs), consisting of 64 tiles of 192 pixels by 185 pixels each, arranged as shown in Fig. 1 and figs. S1 and S2. The CSPAD supports the 120-Hz readout rate required to measure each x-ray pulse from LCLS (*11*, *12*).

Here, we describe SFX experiments performed at CXI analyzing the structure of hen egg-white lysozyme (HEWL) as a model system by using microcrystals of about 1 μm by 1 μm by 3 μm (*4*, *11*). HEWL is an extremely well-characterized protein that crystallizes easily. It was the first enzyme to have its structure determined by x-ray diffraction (*13*) and has since been thoroughly characterized to very high resolution (*14*). Lysozyme has served as a model system for many investigations, including radiation damage studies. This makes it an ideal system for the development of the SFX technique. Microcrystals of HEWL in random orientation were exposed to single 9.4-keV (1.32 Å) x-ray pulses of 5- or 40-fs duration focused to 10 μm^2 at the interaction point (Fig. 1). The average 40-fs pulse energy at the sample was 600 μJ per pulse, corresponding to an average dose of 33 MGy deposited in each crystal. This dose level represents the classical limit for damage using cryogenically cooled crystals (*15*). The average 5-fs pulse energy was 53 μJ. The SFX-derived data were compared to low-dose data sets collected at room temperature by using similarly prepared larger crystals (*11*). This benchmarks the technique with a well-characterized model system.

We collected about 1.5 million individual "snapshot" diffraction patterns for 40-fs duration pulses at the LCLS repetition rate of 120 Hz using the CSPAD. About 4.5% of the patterns were classified as crystal hits, 18.4% of which were indexed and integrated with the CrystFEL software (*14*) showing excellent statistics to 1.9 Å resolution (Table 1 and table S1). In addition, 2 million diffraction patterns were collected by using x-ray pulses of 5-fs duration, with a 2.0% hit rate and a 26.3% indexing rate, yielding 10,575 indexed patterns. The structure, partially shown in Fig. 2A, was determined by molecular replacement [using Protein Data Bank (PDB) entry 1VDS] and using the 40-fs SFX data. No significant differences were observed in an F_{obs}(40 fs) – F_{obs} (synchrotron) difference electron density map (Fig. 2B). The electron density map shows features that were not part of the model (different conformations of amino acids and water molecules) and shows no

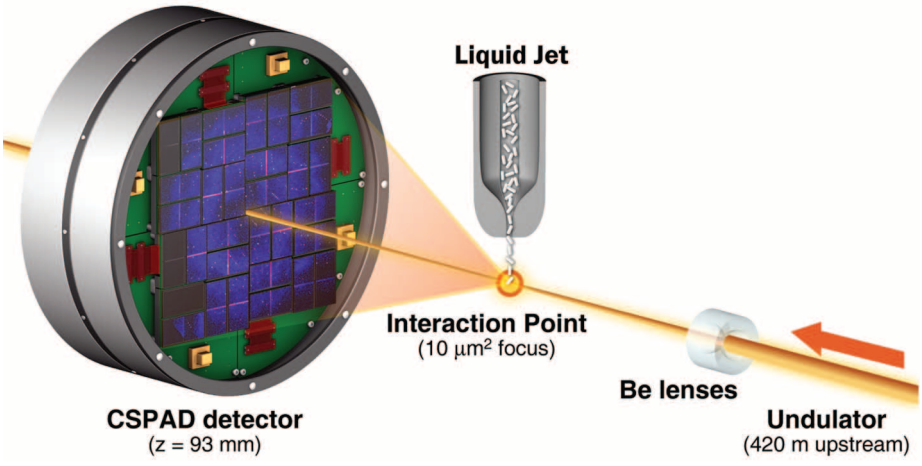

Fig. 1. Experimental geometry for SFX at the CXI instrument. Single-pulse diffraction patterns from single crystals flowing in a liquid jet are recorded on a CSPAD at the 120-Hz repetition rate of LCLS. Each pulse was focused at the interaction point by using 9.4-keV x-rays. The sample-to-detector distance (*z*) was 93 mm.

Table 1. SFX and synchrotron data and refinement statistics. Highest resolution shells are 2.0 to 1.9 Å. R_{split} is as defined in (*16*): $R_{split} = \left(\frac{1}{\sqrt{2}}\right)\cdot\frac{\sum_{hkl}|I^{even}_{hkl} - I^{odd}_{hkl}|}{\frac{1}{2}\sum_{hkl}|I^{even}_{hkl} + I^{odd}_{hkl}|}$. SLS room temperature (RT) data 3 statistics are from XDS (*20*). B factors were calculated with TRUNCATE (*21*). *R* and rmsd values were calculated with PHENIX (*22*). n.a., not applicable. The diffraction patterns have been deposited with the Coherent X-ray Imaging Data Bank, cxidb.org (accession code ID-17).

Parameter	40-fs pulses	5-fs pulses	SLS RT data 3
Wavelength	1.32 Å	1.32 Å	0.9997 Å
X-ray focus (μm^2)	~10	~10	~100 × 100
Pulse energy/fluence at sample	600 μJ/4 × 10^{11} photons per pulse	53 μJ/3.5 ×10^{10} photons per pulse	n.a./2.5 × 10^{10} photons/s
Dose (MGy)	33.0 per crystal	2.9 per crystal	0.024 total
Dose rate (Gy/s)	8.3 × 10^{20}	5.8 × 10^{20}	9.6 × 10^{2}
Space group	$P4_32_12$	$P4_32_12$	$P4_32_12$
Unit cell length (Å), α = β = γ = 90°	*a* = *b* =79, *c* = 38	*a* = *b* = 79, *c* = 38	*a* = *b* = 79.2, *c* = 38.1
Oscillation range/exposure time	Still exp./40 fs*	Still exp./5 fs*	1.0°/0.25 s
No. collected diffraction images	1,471,615	1,997,712	100
No. of hits/indexed images	66,442/12,247	40,115/10,575	n.a./100
Number of reflections	n.a.	n.a.	70,960
Number of unique reflections	9921	9743	9297
Resolution limits (Å)	35.3–1.9	35.3–1.9	35.4–1.9
Completeness	98.3% (96.6%)	98.2% (91.2%)	92.6% (95.1%)
$I/\sigma(I)$	7.4 (2.8)	7.3 (3.1)	18.24 (5.3)
R_{split}	0.158	0.159	n.a.
R_{merge}	n.a.	n.a.	0.075 (0.332)
Wilson B factor	28.3 $Å^2$	28.5 $Å^2$	19.4 $Å^2$
R-factor/*R*-free	0.196/0.229	0.189/0.227	0.166/0.200
Rmsd bonds, Rmsd angles	0.006 Å, 1.00°	0.006 Å, 1.03°	0.007 Å, 1.05°
PDB code	4ET8	4ET9	4ETC

*Electron bunch length

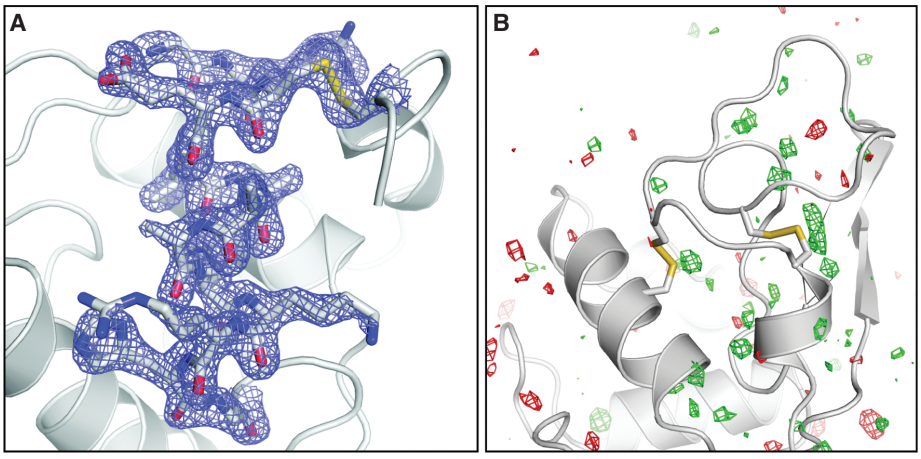

Fig. 2. (**A**) Final, refined $2mF_{obs} - DF_{calc}$ (1.5σ) electron density map (*17*) of lysozyme at 1.9 Å resolution calculated from 40-fs pulse data. (**B**) F_{obs}(40 fs) − F_{obs} (synchrotron) difference Fourier map, contoured at +3 σ (green) and −3 σ (red). No interpretable features are apparent. The synchrotron data set was collected with a radiation dose of 24 kGy.

discernible signs of radiation damage. Also, when the data were phased with molecular replacement by using the turkey lysozyme structure as a search model (PDB code 1LJN), the differences between the two proteins were immediately obvious from the maps (fig. S3).

Even though the underlying radiation damage processes differ because of the different time scales of the experiments using an XFEL and a synchrotron or rotating anode (femtoseconds versus seconds or hours), no features related to radiation damage are observed in difference maps calculated between the SFX and the low-dose synchrotron data (Fig. 2B). In addition to local structural changes, metrics like I/I_0 [the ratio of measured intensities (I) to the ideal calculated intensities (I_0)] and the Wilson B factor are most often used to characterize global radiation damage in protein crystallography (*17*). I/I_0 is not applicable to the SFX data. However, the Wilson B factors of both SFX data sets show values typical for room-temperature data sets and do not differ significantly from those obtained from synchrotron and rotating anode data sets collected with different doses, using similarly grown larger crystals kept at room temperature and fully immersed in solution (*11*) (Table 1 and table S1). The R factors calculated between all collected data sets do not show a dose-dependent increase (fig. S4). However, higher R factors are observed for the SFX data, indicating a systematic difference. This is not caused by nonconvergence of the Monte Carlo integration, because scaling the 40- and 5-fs data together does not affect the scaling behavior. Besides non-isomorphism or radiation damage, possible explanations for this difference could include suboptimal treatment of weak reflections, the difficulties associated with processing still diffraction images, and other SFX-specific steps in the method. SFX is an emerging technique, and data processing algorithms, detectors, and data collection methods are under continuous development.

A simple consideration shows the attainable velocities of atoms in the sample depend on the deposited x-ray energy versus the inertia of those atoms: $\langle v \rangle = \sqrt{3k_B T/m}$, where m is the mass of a carbon atom, for example, T is temperature, and k_B is Boltzmann's constant. For an impulse absorption of energy at the doses of our LCLS measurements, we predict average velocities less than 10 Å/ps, which gives negligible displacement during the FEL pulses. On the time scale of femtoseconds, radiation damage is primarily caused by impulsive rearrangement of atoms and electron density rather than the relatively slow processes of chemical bond breaking typical in conventional crystallography using much longer exposures at much lower dose rates (the dose rate in this experiment was about 0.75 MGy per femtosecond).

Neither the SFX electron density maps nor the Wilson B factors suggest obvious signs of significant radiation damage. Very short pulses (5-fs electron bunch) are not expected to produce observable damage, according to simulations (*3*). Furthermore, it has been reported that the actual x-ray pulses are shorter than the electron bunches for XFELs, making the pulse duration possibly shorter than the relevant Auger decays (*18*). The agreement between the SFX results using 40-fs pulses and 5-fs pulses suggests similar damage characteristics for the two pulse durations on the basis of the available data. Our results demonstrate that under the exposure conditions used, SFX yields high-quality data suitable for structural determination. SFX reduces the requirements on crystal size and therefore the method is of immediate relevance for the large group of difficult-to-crystallize molecules, establishing SFX as a very valuable high-resolution complement to existing macromolecular crystallography techniques.

References and Notes

1. J. M. Holton, K. A. Frankel, *Acta Crystallogr.* **D66**, 393 (2010).
2. R. Neutze, R. Wouts, D. van der Spoel, E. Weckert, J. Hajdu, *Nature* **406**, 752 (2000).
3. A. Barty *et al.*, *Nat. Photonics* **6**, 35 (2011).
4. L. Lomb *et al.*, *Phys. Rev. B* **84**, 214111 (2011).
5. D. P. DePonte *et al.*, *J. Phys. D* **41**, 195505 (2008).
6. H. N. Chapman *et al.*, *Nature* **470**, 73 (2011).
7. R. Koopmann *et al.*, *Nat. Methods* **9**, 259 (2012).
8. L. C. Johansson *et al.*, *Nat. Methods* **9**, 263 (2012).
9. P. Emma *et al.*, *Nat. Photonics* **4**, 641 (2010).
10. S. Boutet, G. J. Williams, *New J. Phys.* **12**, 035024 (2010).
11. Materials and methods are available as supplementary materials on *Science* Online.
12. H. T. Philipp, M. Hromalik, M. Tate, L. Koerner, S. M. Gruner, *Nucl Instrum. Methods A* **649**, 67 (2011).
13. C. C. F. Blake *et al.*, *Nature* **206**, 757 (1965).
14. J. Wang, M. Dauter, R. Alkire, A. Joachimiak, Z. Dauter, *Acta Crystallogr.* **D63**, 1254 (2007).
15. R. L. Owen, E. Rudiño-Piñera, E. F. Garman, *Proc. Natl. Acad. Sci. U.S.A.* **103**, 4912 (2006).
16. T. A. White *et al.*, *J. Appl. Cryst.* **45**, 335 (2012).
17. R. J. Southworth-Davies, M. A. Medina, I. Carmichael, E. F. Garman, *Structure* **15**, 1531 (2007).
18. L. Young *et al.*, *Nature* **466**, 56 (2010).
19. R. J. Read, *Acta Crystallogr.* **A42**, 140 (1986).
20. W. Kabsch, *J. Appl. Cryst.* **26**, 795 (1993).
21. A. J. McCoy, R. W. Grosse-Kunstleve, L. C. Storoni, R. J. Read, *Acta Crystallogr.* **D61**, 458 (2005).
22. P. D. Adams *et al.*, *Acta Crystallogr.* **D66**, 213 (2010).

Acknowledgments: Portions of this research were carried out at the LCLS, a National User Facility operated by Stanford University on behalf of the U.S. Department of Energy (DOE), Office of Basic Energy Sciences (OBES) and at the Swiss Light Source, beamline X10SA, Paul Scherrer Institute, Villigen, Switzerland. The CXI instrument was funded by the LCLS Ultrafast Science Instruments (LUSI) project funded by DOE, OBES. We acknowledge support from the Max Planck Society, the Hamburg Ministry of Science and Research, and the Joachim Herz Stiftung, as part of the Hamburg Initiative for Excellence in Research (LEXI); the Hamburg School for Structure and Dynamics in Infection; the U.S. NSF (awards 0417142 and MCB-1021557); the NIH (award 1R01GM095583); the German Federal Ministry for Education and Research (grants 01KX0806 and 01KX0807); the Deutsche Forschungsgemeinschaft Cluster of Excellence EXC 306; AMOS program within the Chemical Sciences, Geosciences, and Biosciences Division of the OBES, Office of Science, U.S. DOE; the Swedish Research Council; the Swedish Foundation for International Cooperation in Research and Higher Education. We thank A. Meinhart and E. Hofmann for collecting the synchrotron data set, M. Gebhart for help preparing the crystals, and M. Hayes and the technical staff of SLAC and the LCLS for their great support in carrying out these experiments. Special thanks to G. M. Stewart, T. Anderson, and SLAC Infomedia for generating Fig. 1. The structure factors and coordinates have been deposited with the Protein Data Bank (accession codes 4ET8, 4ET9, 4ETA, 4ETB, 4ETC, 4ETD, and 4ETE). The diffraction patterns have been deposited with the Coherent X-ray Imaging Data Bank cxidb.org (accession code ID-17). The Arizona Board of Regents, acting for and on behalf of Arizona State University and in conjunction with R.B.D., U.W., D.P.D., and J.C.H.S., has filed U.S. and international patent applications on the nozzle technology applied herein.

Supplementary Materials

www.sciencemag.org/cgi/content/full/science.1217737/DC1
Materials and Methods
Figs. S1 to S7
Table S1
References (*23*–*26*)

12 December 2011; accepted 21 May 2012
Published online 31 May 2012;
10.1126/science.1217737

New Products: DNA/RNA Analysis

RNA QUANTITATION

The One-Step RT-ddPCR kit for probes provides researchers with the ability to measure target RNA molecules with precision and sensitivity for applications such as gene expression analysis, miRNA analysis, and viral load quantitation. The One-Step RT-ddPCR kit creates a new paradigm for the precise quantitation of RNA by combining reverse transcription with Droplet Digital PCR (ddPCR). Researchers can use the One-Step RT-ddPCR Kit for probes with Bio-Rad's QX100 Droplet Digital PCR system to determine small differences in copy number of target RNA that they were previously unable to measure using real-time polymerase chain reaction (qPCR). In combination with the QX100 ddPCR system, the One-Step RT-ddPCR Kit for probes allows scientists to enrich for rare target RNA sequences, detect small differences in gene expression levels, and determine copies of an RNA molecule without a standard curve.

Bio-Rad

For info: 800-424-6723 | www.bio-rad.com

CHROMATIN IMMUNOPRECIPITATION KIT

The Magna ChIP HT96 kit is designed for high throughput chromatin immunoprecipitation (ChIP). Using the kit, ChIP can be performed on up to 96 samples in a single experiment using as few as 10,000 cells per well. The optimized protocol uses a single, proprietary buffer for sonication, immunoprecipitation, and washing, which yields excellent sensitivity and lower backgrounds than conventional ChIP methods. The Magna ChIP HT96 protocol has been designed and optimized for efficient immunoprecipitation and recovery of DNA. Consequently, in many cases, a separate DNA purification step is not required for downstream analysis. The Magna ChIP HT96 kits utilize a magnetic protein A/G bead blend that provides multiple advantages over single-bead approaches. In contrast to kits with either protein A or protein G, the Magna ChIP A/G beads allow affinity capture of a broader range of antibody isotypes.

EMD Millipore

For info: 800-645-5476 | www.millipore.com/epigenetics

NUCLEIC ACID STAIN

The LabSafe Nucleic Acid Stain is a new and safe nucleic acid stain for the visualization of double-stranded DNA, single-stranded DNA, and RNA in agarose gels. The dyes are developed to replace toxic ethidium bromide (a potent mutagen), commonly used in gel electrophoresis for visualization of nucleic acids in agarose gels. LabSafe Nucleic Acid Stain is noncarcinogenic by the Ames test. The results are negative in both the mouse marrow chromophilous erythrocyte micronucleus and mouse primary spermatocyte chromosomal aberration tests. LabSafe Nucleic Acid Stain emits green fluorescence when bound to dsDNA and red fluorescence when bound to ssDNA or RNA. It has two excitation wavelength peaks when bound to nucleic acid, at 290 nm and 490 nm.

G-Biosciences

For info: 314-991-6034 | www.gbiosciences.com

WHOLE GENOME AMPLIFICATION KIT

The Ampli1 Whole Genome Amplification Kit has been uniquely designed to optimize whole gene amplification of the DNA from a single cell. This new method combines all the amplification steps into single-tube protocol to avoid template loss. DNA released from the single cell is amplified with a single primer generating a library of highly concentrated DNA fragments which represent the complete genome. The DNA fragments can be employed for further targeted genetic research analysis including sequencing, microsatellite analysis, SNPs detection, or copy number variation analysis. The Ampli1 WGA Kit also supports the DNA amplification of samples containing higher numbers of cells. Although the best results are obtained with DNA from live cells, good results have also been obtained with single fixed or fixed and permeabilized cell samples such as paraformaldehyde fixed or cells stained with fluorophore conjugated antibodies.

Silicon Biosystems

For info: +39-051-4071300 | www.siliconbiosystems.com/ampli.page

MULTIPLEX GENE EXPRESSION ANALYSIS

TRAC (Transcript Analysis with the aid of Affinity Capture) is a new approach for measuring gene expression offering several benefits over real-time polymerase chain reaction (qPCR), including higher sample throughput, increased assay speed, and reduced technical variation. The method can reliably analyze the expression of up to 30 transcripts per sample using 96 well plates and avoids the need for RNA extraction, cDNA conversion, and amplification—making it fast, simple, accurate, and cost-effective. While the technology can be used to measure any known gene sequence, several predesigned detection panels are offered, including the recently updated Human ADME-Tox library. This includes validated probes for members of the Cytochrome P450 family of genes, used to investigate in vitro drug interactions during preclinical studies. TRAC also has a wide range of research and process optimization applications and can be easily set up in a user's laboratory, or utilized via the FAST TRAC outsourced service.

Plexpress

For info: +358-50-313-9427 | www.plexpress.com

Electronically submit your new product description or product literature information! Go to **www.sciencemag.org/products/newproducts.dtl** for more information.

Newly offered instrumentation, apparatus, and laboratory materials of interest to researchers in all disciplines in academic, industrial, and governmental organizations are featured in this space. Emphasis is given to purpose, chief characteristics, and availability of products and materials. Endorsement by *Science* or AAAS of any products or materials mentioned is not implied. Additional information may be obtained from the manufacturer or supplier.

Orbitrap mass spec is better, but it's too expensive. I may have to settle for Q-TOF.

think again.


Exactive Plus LC-MS


Q Exactive LC-MS/MS


LTQ Orbitrap XL Hybrid FTMS


Orbitrap Velos Pro Hybrid MS


Orbitrap Elite Hybrid MS

Thermo Scientific Orbitrap mass spec is better! The amazing resolution, accuracy, speed and precision of Orbitrap™ technology is the best solution for complex sample analysis. The good news is that it's more affordable than ever. The Orbitrap mass spec portfolio provides a range of solutions from routine screening to ultra-high performance research instruments that will help virtually any lab achieve more. In doubt? Check out the line of researchers waiting to use an Orbitrap mass spec. Then see if there's a line to use the other mass spectrometers in your lab.

- learn why Orbitrap is better at thermoscientific.com/thinkagain

Thermo SCIENTIFIC

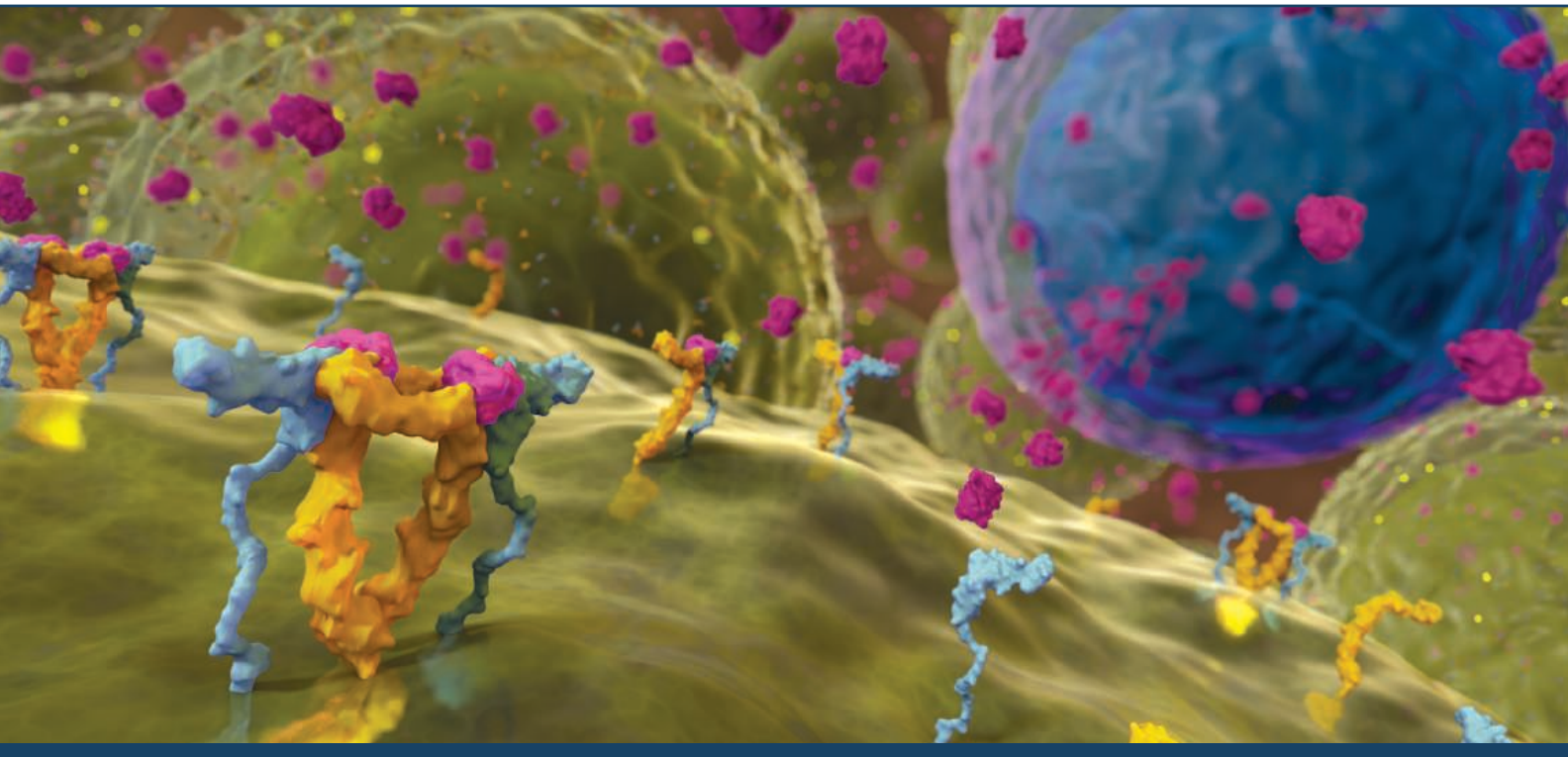

The Highest Quality
Cytokines & Growth Factors
...from Cell Signaling Technology

The world's highest quality antibody provider has now extended its expertise to cytokine production.

- Produced and bioassayed in house with the highest purity and bioactivity.
- Comparison of multiple lots, stringent product specifications, and rigorous quality control ensures maximum lot-to-lot consistency.
- Endotoxin levels are routinely tested and are less than 0.01 ng/µg cytokine.
- Many products are produced in mammalian cells to maximize natural conformation and glycosylation.
- Multi-milligram quantities available.

Human Interleukin-17A (hIL-17A) #8928

Purity

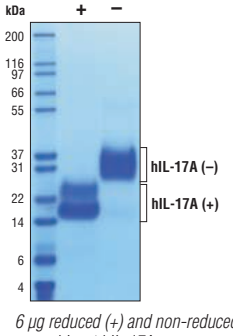

6 µg reduced (+) and non-reduced (-) recombinant hIL-17A.

Bioactivity

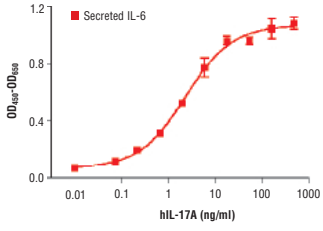

The production of IL-6 by human foreskin fibroblasts cultured with increasing concentrations of hIL-17A for 48 hours was assessed.

Downstream Signaling

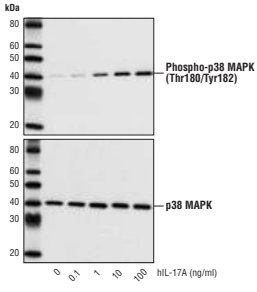

Human foreskin fibroblasts treated with hIL-17A for 15 minutes were examined using phospho- and total p38 MAPK antibodies.

for quality products you can trust...

www.cellsignal.com

Cell Signaling TECHNOLOGY®

Orders (toll-free) 1-877-616-2355 | **Inquiries** info@cellsignal.com | **Environmental Commitment** eco.cellsignal.com

Any sample, any application — no limits

Maximize success with QIAGEN sample technologies

- Innovative, room-temperature sample collection and stabilization
- DNA, RNA, and protein purification from any sample
- Hands-free automated sample preparation
- Reliable genetic, epigenetic, and gene expression analysis from FFPE samples
- Whole genome and transcriptome amplification to overcome sample limitations

Contact QIAGEN today or visit www.qiagen.com/sample-technologies

QIAGEN®

Sample & Assay Technologies

ADNASamplePanf0910511WW

MiSeq. Next-generation sequencing for all you seek.

You want amazing accuracy and performance on your benchtop. Illumina delivers—yet again. The MiSeq Personal Sequencer is the only fully integrated, truly end-to-end benchtop solution around. It's just one more example of why Illumina solutions generate a remarkable 90% of all the world's sequencing data. Discover what's possible.

www.illumina.com/iseek

illumina®

LightCycler®

LightCycler® 480 Real-Time PCR System

Enabling advanced qPCR for the experienced user

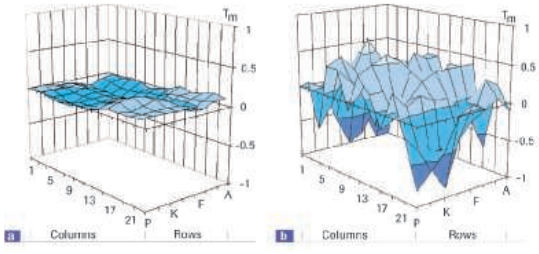

Figure 1: Influence of the Therma-Base layer on temperature homogeneity across a 384-well plate. (a): LightCycler® 480 Real-Time PCR System including Therma-Base; **(b):** 384-well plate on Applied Biosystems 7900HT without Therma-Base.

Data generated at Roche Applied Science.

- **Generate reproducible, reliable data – without ROX dye** (Figure 1)**.**
- **Perform advanced analysis with powerful software.**
- **Easily switch between 96- and 384-well formats – without calibration.**
- **Readily integrate with robotics.**

Visit ***www.lightcycler480.com*** or call **800 262 4911** to learn more.

For life science research only.
Not for use in diagnostic procedures.

Roche Diagnostics Corporation
Roche Applied Science
Indianapolis, Indiana

Roche

44

best practices for overcoming skepticism post-Climategate.

One more data point on why you should spend more time at membercentral.aaas.org. There you can enjoy webinars, videos, blogs, discounts, and downloads geared for people who prefer content based on empirical evidence.

membercentral.aaas.org

AAAS MemberCentral

New Products: DNA/RNA Analysis

RNA QUANTITATION

The One-Step RT-ddPCR kit for probes provides researchers with the ability to measure target RNA molecules with precision and sensitivity for applications such as gene expression analysis, miRNA analysis, and viral load quantitation. The One-Step RT-ddPCR kit creates a new paradigm for the precise quantitation of RNA by combining reverse transcription with Droplet Digital PCR (ddPCR). Researchers can use the One-Step RT-ddPCR Kit for probes with Bio-Rad's QX100 Droplet Digital PCR system to determine small differences in copy number of target RNA that they were previously unable to measure using real-time polymerase chain reaction (qPCR). In combination with the QX100 ddPCR system, the One-Step RT-ddPCR Kit for probes allows scientists to enrich for rare target RNA sequences, detect small differences in gene expression levels, and determine copies of an RNA molecule without a standard curve.

Bio-Rad

For info: 800-424-6723 | www.bio-rad.com

CHROMATIN IMMUNOPRECIPITATION KIT

The Magna ChIP HT96 kit is designed for high throughput chromatin immunoprecipitation (ChIP). Using the kit, ChIP can be performed on up to 96 samples in a single experiment using as few as 10,000 cells per well. The optimized protocol uses a single, proprietary buffer for sonication, immunoprecipitation, and washing, which yields excellent sensitivity and lower backgrounds than conventional ChIP methods. The Magna ChIP HT96 protocol has been designed and optimized for efficient immunoprecipitation and recovery of DNA. Consequently, in many cases, a separate DNA purification step is not required for downstream analysis. The Magna ChIP HT96 kits utilize a magnetic protein A/G bead blend that provides multiple advantages over single-bead approaches. In contrast to kits with either protein A or protein G, the Magna ChIP A/G beads allow affinity capture of a broader range of antibody isotypes.

EMD Millipore

For info: 800-645-5476 | www.millipore.com/epigenetics

NUCLEIC ACID STAIN

The LabSafe Nucleic Acid Stain is a new and safe nucleic acid stain for the visualization of double-stranded DNA, single-stranded DNA, and RNA in agarose gels. The dyes are developed to replace toxic ethidium bromide (a potent mutagen), commonly used in gel electrophoresis for visualization of nucleic acids in agarose gels. LabSafe Nucleic Acid Stain is noncarcinogenic by the Ames test. The results are negative in both the mouse marrow chromophilous erythrocyte micronucleus and mouse primary spermatocyte chromosomal aberration tests. LabSafe Nucleic Acid Stain emits green fluorescence when bound to dsDNA and red fluorescence when bound to ssDNA or RNA. It has two excitation wavelength peaks when bound to nucleic acid, at 290 nm and 490 nm.

G-Biosciences

For info: 314-991-6034 | www.gbiosciences.com

WHOLE GENOME AMPLIFICATION KIT

The Ampli1 Whole Genome Amplification Kit has been uniquely designed to optimize whole gene amplification of the DNA from a single cell. This new method combines all the amplification steps into single-tube protocol to avoid template loss. DNA released from the single cell is amplified with a single primer generating a library of highly concentrated DNA fragments which represent the complete genome. The DNA fragments can be employed for further targeted genetic research analysis including sequencing, microsatellite analysis, SNPs detection, or copy number variation analysis. The Ampli1 WGA Kit also supports the DNA amplification of samples containing higher numbers of cells. Although the best results are obtained with DNA from live cells, good results have also been obtained with single fixed or fixed and permeabilized cell samples such as paraformaldehyde fixed or cells stained with fluorophore conjugated antibodies.

Silicon Biosystems

For info: +39-051-4071300 | www.siliconbiosystems.com/ampli.page

MULTIPLEX GENE EXPRESSION ANALYSIS

TRAC (Transcript Analysis with the aid of Affinity Capture) is a new approach for measuring gene expression offering several benefits over real-time polymerase chain reaction (qPCR), including higher sample throughput, increased assay speed, and reduced technical variation. The method can reliably analyze the expression of up to 30 transcripts per sample using 96 well plates and avoids the need for RNA extraction, cDNA conversion, and amplification—making it fast, simple, accurate, and cost-effective. While the technology can be used to measure any known gene sequence, several predesigned detection panels are offered, including the recently updated Human ADME-Tox library. This includes validated probes for members of the Cytochrome P450 family of genes, used to investigate in vitro drug interactions during preclinical studies. TRAC also has a wide range of research and process optimization applications and can be easily set up in a user's laboratory, or utilized via the FAST TRAC outsourced service.

Plexpress

For info: +358-50-313-9427 | www.plexpress.com

Electronically submit your new product description or product literature information! Go to **www.sciencemag.org/products/newproducts.dtl** for more information.

Newly offered instrumentation, apparatus, and laboratory materials of interest to researchers in all disciplines in academic, industrial, and governmental organizations are featured in this space. Emphasis is given to purpose, chief characteristics, and availability of products and materials. Endorsement by *Science* or AAAS of any products or materials mentioned is not implied. Additional information may be obtained from the manufacturer or supplier.

LOCATION: Jackson Park Health Club
ARTICLE: *An Electronic Second Skin*
DATE: Sep 21, 7:43am

LOCATION: University Faculty Lounge
ARTICLE: *The Visual Impact of Gossip*
DATE: Sep 21, 4:22pm

LOCATION: Gyro King
ARTICLE: *Cavemen Craved Carbs, Too*
DATE: Sep 21, 1:13pm

LOCATION: Hemlock Bar
ARTICLE: *Quantum Simulation of Frustrated Classical Magnetism in Triangular Optical Lattices*
DATE: Sep 21, 9:21pm

LOCATION: Bed
ARTICLE: *Consciousness: What, How and Why*
DATE: Sep 21, 10:56pm

A new way to look at science

The new *Science* Reader app for iPad® from AAAS puts *Science* in your hands, wherever you go. Read abstracts, career advice, and highlights from our newest journals, *Science Signaling* and *Science Translational Medicine*. Plus, AAAS members can access full text articles from *Science*. Visit iTunes App Store℠ or content.aaas.org/ipad for details.

Available on the App Store

Science
AAAS

Problem? Solved.

By phone, online, or on-site, we're here to quickly solve your challenges, no matter how great. Get award-winning support for every issue, every time.

- Expert application scientists ready to answer your specific questions
- Field support in more than 60 countries
- Comprehensive website with easy access to manuals, protocols & technical documents

Let us help at **lifetechnologies.com/support**

life technologies™

Invitrogen™ Applied Biosystems® Gibco® Molecular Probes® Novex® TaqMan® Ambion® Ion Torrent™

ETH

Eidgenössische Technische Hochschule Zürich
Swiss Federal Institute of Technology Zurich

Assistant Professor (Tenure Track) of Computer-Aided Chemistry

The Laboratory of Physical Chemistry of the Department of Chemistry and Applied Biosciences at ETH Zurich (www.chab.ethz.ch) invites applications for the above-mentioned position.

Research should preferably aim at modeling the behavior of (bio)chemical systems at the atomic, molecular, and supramolecular level on a physico-chemical basis. Strong methodological, algorithmic, and computational activities, including practical applications, are desirable. Collaboration with experimental groups at ETH as well as teaching (in German or English) in all areas of physical and computer-aided chemistry is encouraged.

This assistant professorship has been established to promote the careers of younger scientists. The initial appointment is for four years with the possibility of renewal for an additional two-year period and promotion to a permanent position.

Your application should include your curriculum vitae, a list of publications and a statement of future teaching and research activities. The letter of application should be addressed **to the President of ETH Zurich, Prof. Dr. Ralph Eichler. The closing date for applications is 30 September 2012.** ETH Zurich is an equal opportunity and affirmative action employer. In order to increase the number of women in leading academic positions, we specifically encourage women to apply. ETH Zurich is further responsive to the needs of dual career couples and qualifies as a family friendly employer. **Please apply online at www.facultyaffairs.ethz.ch.**

Fellowships

The Radcliffe Institute for Advanced Study at Harvard University annually awards academic-year fellowships that enable scientists and mathematicians to pursue innovative research while participating in the Institute's diverse scholarly community.

While at Radcliffe, these fellows are able to work in Harvard and Boston-area labs and with faculty and other fellows to explore new avenues in their research.

Scientists in any field who have a doctorate in the area of the proposed project (by December 2011) and at least one published article or monograph are eligible to apply for a Radcliffe Institute fellowship. The stipend amount of $70,000 is meant to complement sabbatical leave salaries of faculty members. Residence in the Boston area is required, as is participation in the Institute community.

Applications for 2013–2014 are due by November 1, 2012.

For more information, please visit **www.radcliffe.harvard.edu.**

RADCLIFFE INSTITUTE FOR ADVANCED STUDY HARVARD UNIVERSITY

Neuroethics Program

Georgia State University

Georgia State University is creating a new interdisciplinary Neuroethics Program, a cooperative venture of the **Neuroscience Institute**, the **Department of Psychology**, the **Department of Philosophy**, and the **College of Law**. The Neuroethics Program will include three new open-rank tenured/tenure-track hires, nine PhD fellowships, and new PhD Concentrations in Neuroethics. It will be a part of a thriving interdisciplinary community, including the resources of the **Center for Advanced Brain Imaging**, the **Brains & Behavior Program**, the **Language Research Center**, and the **Blumenfeld Center for Ethics**.

Candidates should have expertise in one or more of the following areas: (1) cognitive or affective neuroscience, specializing in moral cognition, emotion, or behavior; (2) ethical and/or legal theory as applied to neuroscience; (3) philosophy of neuroscience, cognitive science, moral psychology. Candidates must have a record of successful research and PhD or JD at time of application. Anticipated start date is Fall 2013. Applicants apply online at **https://academicjobsonline.org/ajo/jobs/1576**, where they will find more information. Questions to chair of the search committee, Eddy Nahmias, **enahmias@gsu.edu**. In addition to these positions, the 2CI program is supporting hires in neuroimaging; primate social cognition, evolution, and behavior; and neurogenomics. For more information, see **http://www.gsu.edu/secondcentury/**. Review of applications will begin on **October 15, 2012** and continue until the three positions are filled.

Georgia State University is an AA/EEO Employer and encourages applications from women and minority candidates.

Diversity: Promoting New Perspectives

In the United States, women are nearly half the general workforce and are overtaking men in earning Bachelor's degrees. In science, technology, engineering, and math—the STEM fields—more women and minorities are earning Ph.D.s than ever. At the same time, business and university leaders are seeking to increase personnel diversity because heterogeneity in gender, sexual orientation, socioeconomic background, and race/ethnicity are known to promote innovation. A variety of initiatives and programs are connecting the supply of scientists and engineers with the demand for a more diverse workforce. **By Chris Tachibana**

"People who face discrimination from a young age often have extraordinary resilience and problem-solving and coping skills—that's the other side of stigma."
—Shane Snowden

Workplace diversity in the United States is increasing, thanks to legislation beginning with the 1964 Civil Rights Act, the women's and gay rights movements, and immigration. An analysis of the federal STEM workforce showed that in 2009, employment of women was 27 percent compared to 21 percent in 2000. Overall employment of minorities in 2009 was 22 percent (ranging from 9 percent Asians to 1 percent American Indians). However, the overwhelming majority of scientists and engineers in senior executive positions were white men (scim.ag/MbO0ay). The same disparity in leadership is seen in academia. Only 3 to 15 percent of full professors were women in a 2005 survey of U.S. science and engineering departments (scim.ag/LJHvpx). The problem is not lack of candidates: the number of Americans receiving STEM Ph.D.s is growing, largely driven by women and minorities (scim.ag/LN4gfO).

WHY DIVERSITY MATTERS

But why is underrepresentation of women, minorities, and other groups important? Can diversity in color, gender, sexual orientation, and disability status really affect the workplace? Yes, say years of business school studies on performance, productivity, and profitability.

"Companies are investing large amounts of money in programs to increase diversity, especially in upper management—not to be altruistic but because it is more financially successful. They actually tell you that in leadership programs," says **Sandra Schmid.** In addition to a biochemistry Ph.D., Schmid, a professor at the University of Texas Southwestern Medical Center, has a Master's degree in executive leadership. Diverse teams bring multiple perspectives to problem solving, she says, and make strategic decisions that more fully reflect client demographics. The benefits of a diverse personnel are so clear that corporations actively compete to connect to professional organizations for underrepresented groups. **Emily Ceisel** is a diversity and inclusion specialist at the global biotechnology company Life Technologies, which has corporate partnerships with the Society of Women Engineers, the National Society of Black Engineers, and the Society of Hispanic Professional Engineers, among others. She says, "Companies know that in a competitive global market their workforce has to be representative of that market."

Diversity literally pays off, according to Sociology Professor **Cedric Herring,** University of Illinois at Chicago. His 2009 analysis of more than 1,000 general U.S. workplaces showed that personnel diversity correlates positively with sales, number of customers, and profits relative to competitors (scim.ag/N0HAKD). Critics say teams with varied cultures and backgrounds have poorer communication, greater conflict, and less integration than homogenous groups, and possibly lower performance if quotas force companies to hire unqualified workers. However, a hypothesis that melds these pro and con lists says that greater conflict means less groupthink and this is precisely why diverse teams are more innovative. **Jonah Lehrer,** writing about creativity, notes that a wide social network and interdepartmental conversations at work lead to novel exchanges that can spark innovation. Being forced out of a routine makes people more creative and open to new ideas (scim.ag/JBVVMj).

A truly diverse workforce also includes the perspectives and advantages of the LGBT (lesbian, gay, bisexual, transgender) community, says **Shane Snowdon,** founding director of the University of California San Francisco (UCSF) Center for LGBT Health & Equity. "People who face discrimination from a young age often have extraordinary resilience and problem-solving and coping skills—that's the other side of stigma," she says. LGBT professionals are strongly motivated and a lifetime of awareness about others' perceptions and prejudices makes LGBT leaders highly sensitive to team dynamics. Snowdon says that business leaders are realizing this, but surprisingly, life continued>

UPCOMING FEATURES

Annual Postdoc Survey—August 24

Faculty: Balancing Academia and Entrepreneurship—Sept. 14

Top Employers Survey—September 21 (online); October 19 (print)

CREDIT: (FROM TOP) PHOTO: ELIOT KHUNER; © ISTOCKPHOTO.COM/EYETOEYEPIX

Diversity

science researchers can be more conservative. They might say it's because they're focused solely on their research, says Snowdon, "But it's not as if science is divorced from the rest of life. Consider how your employees are being held back if they can't be themselves at work."

HOW WE GET THERE

Achieving workplace diversity requires full organizational commitment. **Debra Leonard** is chief diversity officer at Weill Cornell Medical School, where she also holds academic and clinical positions. Her mandate comes from powerful sources: the Liaison Committee on Medical Education requires student and faculty diversity for program accreditation and the National Institutes of Health have diversity requirements for funding. With this kind of backing, a diversity council or officer can get search committees to consider a wider range of job candidates, beyond those recommended by like-minded colleagues from similar backgrounds. "Otherwise, we tend to recruit people who look like us," says Leonard. "It's not conscious and it's rare that people are just plain bigoted. It's just the way we do things." But Leonard's job of recruiting and retaining members of underrepresented groups is not easy. The competition for qualified women and minority candidates is fierce. The problem, she says, is gaps in the pipeline: "Medical schools have outreach programs for high school students and undergraduates, but don't follow through to the residency and faculty level. The network doesn't have enough women and minorities."

"More than 200 Leadership Alliance students have earned Ph.D.s and are now mentoring the next generation. The country has an urgent need for well-trained employees in the STEM fields."
—Medeva Ghee

This is where mentoring programs can help. They can support students, junior employees, and new faculty by connecting them with veterans who can advocate for them and show them the ropes. Developing a diverse network of role models in academia and the public and private sectors is the goal of the Leadership Alliance, a national consortium of 32 research institutions, teaching colleges, and universities. Through a summer internship program and symposium, students are offered research opportunities and guidance as they consider career options, apply to graduate school, and enter the workforce. Executive Director **Medeva Ghee** explains that the primary focus of the programs is mentoring underrepresented groups but Leadership Alliance supports people from a range of backgrounds in a variety of fields. "We identify students who need the experiences we offer," she says. More than 200 Leadership Alliance students have earned Ph.D.s and are now mentoring the next generation. The country has an urgent need for well-trained employees in the STEM fields, says Ghee. "Leadership Alliance meets the societal need by mentoring and producing scholars and researchers poised to contribute to a competitive 21st century workforce."

STEM-based companies have the same goal: an educated, motivated, diverse workforce. Bayer USA Foundation, the Bayer Corporation's philanthropic arm, promotes science literacy and education through its Making Science Make Sense program. For 16 years, this has included an annual Facts of Science Education survey of teachers, students, CEOs, and others. The most recent surveys have been about diversity. Based on the findings that increasing STEM diversity is a current priority at U.S. colleges and universities, the foundation hosted an April 2012 STEM diversity and higher education forum. **Rebecca Lucore,** the foundation's executive director says, "Bayer and other companies invest a lot in K–12 STEM education programs, but if we put children on track to go to college in STEM only to be discouraged when they get there, it's not a good return on our investment." The critical factors, said forum participants, are setting an expectation of success, encouraging students, and providing them with resources that build their interest and confidence. "The consensus was that traditional weeding-out classes are not good for retaining STEM students," says Lucore. She says that industries must play their part by letting students know about opportunities in STEM-based careers, and being partners in mentoring programs and internships that connect students to real-world scientists. Lucore says an additional challenge raised at the forum was how to encourage people with disabilities to pursue STEM careers.

Mentoring students with disabilities who are majoring in STEM fields is the goal of Entry Point!, a summer internship program from the American Association for the Advancement of Science. This year, Merck & Co. selected five Entry Point! students for their Future Talent internship program. **Stephanie Pallante,** global university recruiting leader at Merck, says that internship opportunities are in research, manufacturing, and beginning this year, in global services, which includes information technology. Pallante says the Merck managers who work with the interns say they rarely need special accommodations and any adjustments are outweighed by the benefits of having eager, talented students who are "really at the top of their game." Scientists who work with the interns say that they are a breath of fresh air and bring a university perspective to the Merck knowledge base. In turn, the students get a meaningful experience, says Pallante. "They're not just an extra set of hands working on a project that we make up for them. They work alongside our scientists and production managers on something that is critical for our business."

LGBT scientists also need role models and mentors, says UCSF's Snowdon. A 2009 survey found that most LGBT employees are not out at work about their sexual orientation or gender identity (scim.ag/KMVlt5). Companies and academic institutions can create a better work environment by offering partner benefits, and by using inclusive language in everyday announcements and conversations. To LGBT scientists, Snowdon's message is to think about how the world is changing because of LGBT people taking the risk of coming out. "The transformation of society we're seeing in LGBT issues didn't arise from marches or court decisions or large organizations," she says, "but one person at a time coming out to other people. Take a chance and come out. It's inspiring for junior employees, and other people will see that someone they worked with for many years is still the same person after they've come out."

Business school studies show that a work culture continued>

CREDIT: HANK RANDALL

Diversity

that embraces diversity with a goal of learning and integration is more effective at reaping the benefits of multiculturalism than one that tries to be "colorblind." Valuing diversity is the philosophy at Life Technologies, says Diversity and Inclusion Leader **Ronita Griffin.** The company doesn't stop at recruiting a varied workforce, but engages employees as diversity champions who act as mentors internally and as company ambassadors externally, at community diversity events. Life Technologies also trains its workforce in inclusion, which Griffin describes as "activating, respecting, leveraging, and enabling differences—learning how to recognize and take advantage of the rich diversity in our workforce." Although workplace diversity training can be met with resistance, it can be engaging if it is practical, and answers questions that people feel uncomfortable asking. LGBT diversity training sessions can be intriguing, says Snowdon. "People welcome the opportunity to get their questions answered about populations they don't know much about, like transgender people. Even employees who dread mandatory training often tell me they'll go home and talk about LGBT issues—it's 'news they can use'."

"The bottom line is that we have to go beyond just celebrating diversity. We have to include people on an equitable basis."
—Cedric Herring

Featured Participants

Bayer USA Foundation
www.bayerus.com

Leadership Alliance
www.theleadershipalliance.org

Life Technologies
www.lifetechnologies.com

Merck & Co.
www.merck.com

University of California San Francisco Center for LGBT Health & Equity
lgbt.ucsf.edu

University of Illinois at Chicago
www.uic.edu

University of Texas Southwestern Medical School
www.utsouthwestern.edu

Weill Cornell Medical School
www.med.cornell.edu

Additional Resources

Association of Women in Science
www.awis.org

EntryPoint! Program
www.entrypoint.org

McNair Scholars
mcnairscholars.com

National Organization of Gay and Lesbian Scientists and Technical Professionals
www.noglstp.net

National Society of Black Engineers
www.nsbe.org

Out in Science, Technology, Engineering, and Mathematics
www.ostem.org

Society of Hispanic Professional Engineers
www.shpe.org

Society of Women Engineers
www.swe.org

OVERHAULING THE SYSTEM

The pool of diverse, talented STEM-educated workers is increasing, but will not automatically flow into the workplace without institutional changes that require careful planning and flexibility. Debra Leonard says current career expectations in medical schools are "not realistic and not healthy. They are based on an old system when women took care of home responsibilities so men could work long hours. Today, we need to consider family care, for example offering childcare for travel to meetings, which are so important for professional development." In a step in this direction, American Society for Cell Biology members can apply for childcare grants to attend the organization's annual meeting, which offers advisory sessions on dual-career issues and other contemporary professional challenges. The National Science Foundation recently announced flexible funding policies to allow for time spent on family care.

Sandra Schmid calls for similar changes in academia. With two grown children and a husband, William Balch who is also a molecular biology professor, Schmid walks the walk of a modern scientist. She says the academic tenure system is an outdated, inflexible, "one size fits all" path that no longer serves science. Expecting to hit certain milestones at precise times is too limiting to accommodate a diverse scientific workforce. In the general U.S. population, more than 70 percent of mothers with children work, and science is no exception. People do their most exciting work at different times in their career, says Schmid, and should be evaluated for their overall potential, not just what they have done recently.

This is supported by results from a 2010 study of life science faculty at 50 universities (scim.ag/LZIIvW). Junior women faculty worked fewer hours per week than junior-level men, mainly in the research arena; the women's teaching, administration, clinical, and professional activities were similar to men. However, women who were full professors worked more hours a week than men at the same level, especially in internal administration and external professional activities. This pattern probably reflects the greater family responsibilities of junior-level women, and the higher demand for senior-level women as institutions seek to demonstrate their diversity. This is why Schmid's advice to scientists and administrators is, "Take the long view. Priorities are different at different stages of life, and demands and responses will change over time. Try to balance them over a career."

In an upcoming book, *Critical Diversity: The New Case for Inclusion and Equal Opportunity*, Herring, with co-author Loren Henderson, is expanding his work on the benefits of corporate diversity to address LGBT, education, class, and wealth issues. "The bottom line," says Herring, "is that we have to go beyond just celebrating diversity. We have to include people on an equitable basis." Achieving this will take fundamental institutional changes, he says. "When you have groups of people who are systematically underrepresented, you have to change things to make sure they are systematically included."

Chris Tachibana is a science writer based in Seattle, USA, and Copenhagen, Denmark

DOI: 10.1126/science.opms.r1200120

CREDIT: PHOTO COURTESY OF CEDRIC HERRING

Immuno-Oncology at the EMD Serono Research Institute:

A Unique Center of Excellence for Cancer Immunotherapy

The new state-of-the-art EMD Serono Research Institute in Billerica, MA, equips scientists with cutting-edge technology, an environment that fosters collaboration locally and globally, and a culture centered on innovation. The primary mission of the Immuno-Oncology team is to create an interdisciplinary environment, which allows critical scientific questions in cancer immunology to be addressed, and paves the way for the development of new immunotherapeutic modalities aimed at treating cancer patients.

Postdoctoral Research Fellowship Immuno-Oncology

Billerica, MA Ref: 1201568

The postdoctoral program at the EMD Serono Research Institute provides a venue for researchers and clinicians to have regular, meaningful interaction with a global network of internationally recognized experts. In this highly competitive and unique program, young scientists develop and hone their talents through training exercises, by providing forums for the exchange of scientific ideas, and through funding early efforts in translational cancer immunology.

This is an unrivaled opportunity to be at the forefront of the field of Immuno-Oncology, working with some of the world's most well-known scientists. Research will be focused on studying mechanisms which lead to immunosuppression in the tumor environment, and tumor inflammation.

Qualifications Include: completed doctoral training in a relevant discipline, preferably immunology; strong background in immunology or cancer immunology is required. Understanding of cancer biology is a strong plus; productive track record and lead-author publications in peer-reviewed journals are required, as is a strong desire to contribute creatively to the field of tumor immunology; and must be able to conduct research independently, while effectively collaborating with others in a team.

EMD Serono Inc. is dedicated to its purpose of advancing scientific and medical knowledge. Tapping into the creativity of the best scientific minds is key to the company's innovation strategy. EMD Serono Research Institute's highly Marketing-specialized team of researchers is continuously exploring novel concepts with the passion of developing potential new treatments for patients.

To learn more and apply, please visit:
www.emdserono.com/careers

EMD Serono, Inc. is an Equal Opportunity/Affirmative Action Employer

LIVING SCIENCE – TRANSFORMING LIVES

EMD Serono

EMD™

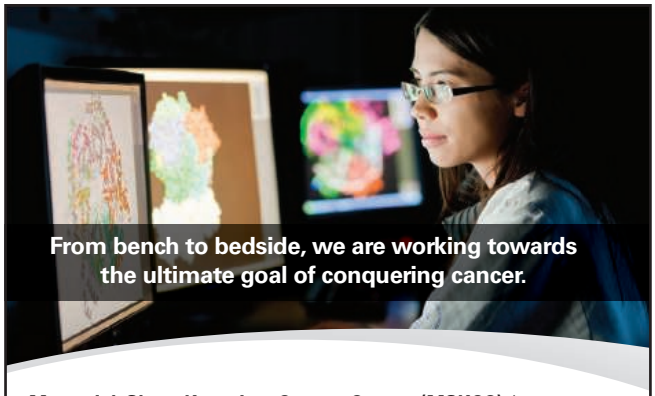

Memorial Sloan-Kettering Cancer Center (MSKCC) is one of the world's premier cancer centers, committed to exceptional patient care, leading-edge research, and superb educational programs. The blending of research with patient care is at the heart of everything we do. At the **Sloan-Kettering Institute (SKI)**, state-of-the-art scientific research flourishes side-by-side with clinical investigation and treatment at **Memorial Hospital**, the nation's oldest cancer hospital. We are also one of 41 National Cancer Institute-designated Comprehensive Cancer Centers, affirming our leadership in research, patient care, and education.

In our nearly 150 investigator-led laboratories, our investigators, 500 postdoctoral researchers and over 250 graduate students are conducting innovative, cutting-edge research to advance understanding in the biomedical sciences to improve the detection, diagnosis and treatment of cancer. Our research programs are broad and encompass: cancer biology and genetics, human oncology and pathogenesis, genomic integrity, regulation of cell behavior, developmental and stem cell biology, computational biology, immunology/immunotherapy/translation, inflammation and microbial biology, neuroscience, structural biology, chemical biology and drug discovery. Our investigators also pursue translational research that bridges discoveries made in the laboratory and those made in the clinical setting; study factors that affect cancer incidence; and conduct mathematical and computational research directed at analyzing and interpreting biomedical data.

We believe the close collaboration between our physicians and scientists is one of our unique strengths, enabling us to provide patients with the best care available today as we work to discover more effective strategies to prevent, control, and ultimately cure cancer in the future. To learn more about how your knowledge, skills and expertise can best be utilized in the pursuit of innovative research — whether your background lies in the basic studies of cells' inner workings or late-stage clinical trials of new drugs — or anything in between — connect with us today.

TO APPLY

Tenure-track faculty positions:
http://facultysearch.ski.edu

Postdoc positions:
www.mskcc.org/research/postdoctoral-research/how-apply

Research Staff positions:
www.mskcc.org/jobs

MEMORIAL SLOAN-KETTERING CANCER CENTER · ESTABLISHED 1884 ·

Memorial Sloan-Kettering Cancer Center

The Best Cancer Care. Anywhere.

www.mskcc.org/jobs

MSKCC is an equal opportunity and affirmative action employer committed to diversity and inclusion in all aspects of recruiting and employment. All qualified individuals are encouraged to apply.

UNIVERSITY of MARYLAND
SCHOOL OF MEDICINE

PULMONARY AND CRITICAL CARE MEDICINE FACULTY POSITION

Asthma Research – The Pulmonary and Critical Care Medicine Division at the University of Maryland School of Medicine seeks a Physician Scientist at the Associate or Full Professor level to join the University of Maryland Asthma Research Program. Applicants must be BC in pulmonary and critical care medicine and have ongoing NIH-sponsored basic or translational research programs focused on asthma. Please reference position **#03-309-692** when applying.

All interested candidates should submit cover letter, CV and a brief statement summarizing clinical and research interests to **Jeffrey D. Hasday, MD, Division Head, University of Maryland Pulmonary and Critical Care Medicine Division, c/o Robyn Crandell (rcrandel@medicine.umaryland.edu), Academic Programs Office, 22 S. Greene Street, N3E10, Baltimore, MD, 21201-1192**.

Candidates can learn more about the division from our website **www.umm.edu/pulmonary/index.html**.

The University of Maryland, Baltimore encourages women and minorities to apply and is an AA/EEO/ADA Employer.

PEKING UNIVERSITY 1898

Deanship at Peking University School of Life Sciences

Peking University (PKU) is recruiting a dean for the School of Life Sciences. PKU is a leading university in China and intends to strengthen and expand life sciences. The dean is expected to be an internationally recognized scientist with enthusiasm to advance education and research in the life sciences at PKU. The dean will play a major role with full support from the university and the Life Sciences Committee, the Peking-Tsinghua Center for Life Sciences, and the Protein Research Platform. Interdisciplinary interaction is a major strength at PKU, with faculty members carrying out life sciences research in the Schools of Chemistry, Medicine, Physics, Information Sciences, Psychology, Mathematics, Engineering, as well as the Biodynamic Optical Imaging Center, Synthetic and Functional Biomolecules Center, the Center for Quantitative Biology and the Institute of Molecular Medicine. The dean will lead the School of Life Sciences in a new phase of growth.

Please send a full CV, names of references and a vision statement on leading the school to the following address (Email preferred) before **August 20, 2012**.

Mr. Jie CHEN
Rm 1118, Red Building No. 1
Peking Univeristy
Beijing 100871
P. R. China

Tel: +86-10-62753563
Fax: +86-10-62766260

E-mail: zzbgbs@pku.edu.cn

Search Committee of Peking University
July 2, 2012

DIVERSITY

Assistant/Associate/ Full Professor

Stony Brook University's Department of Biomedical Engineering is inviting applications for an Assistant, Associate or Full Professor tenure-track faculty position in any BME area. Candidates must have a PhD in BME or related field. A minimum of two years of postdoctoral experience is preferred. Outstanding candidates wishing to be considered at the Associate or Full Professor level must have active, funded research programs in their area of expertise. Candidates are expected to develop and maintain competitive extramurally funded interdisciplinary research programs and to excel in teaching at both graduate and undergraduate levels. Applications should be received by August 15, 2012, but the position will remain open until filled. Possible start date: January 2013.

Qualified individuals should submit their full CV, statement of research and teaching interests, and contact information of three references to: Stefan Judex, PhD, Biomedical Engineering, Bioengineering Building, Rm 213, Stony Brook University, Stony Brook, NY 11794-5281

Stony Brook University

Stony Brook University/SUNY is an equal opportunity, affirmative action employer.

PROFESSOR/ASSOCIATE PROFESSOR

HARVARD SCHOOL OF DENTAL MEDICINE

Harvard School of Dental Medicine is recruiting a full time Investigator at the level of Professor or Associate Professor in the Department of Oral Medicine, Infection and Immunity (Chair: Dr. Roland Baron) or Department of Developmental Biology (Chair: Dr. Vicki Rosen).

The Professor/Associate Professor will have laboratory/office space in the Research and Education Building in the Longwood Medical Area adjacent to Harvard Medical School and Harvard School of Public Health. The successful candidate will complement and strengthen current basic and translational research in skeletal and vascular biology, genetics and pathology.

The successful candidate must have an outstanding record of innovative, internationally recognized and well-funded programs in basic science or translational research in extracellular matrix biology or in areas of skeletal development and disease mechanisms. Significant experience in teaching medical/dental and/or graduate students and training of postdoctoral fellows is also required. Administrative experience with initiating/overseeing/evaluating research programs at the level of laboratory/division/or department is highly desirable.

Interested candidates may submit their curriculum vitae to:

Bjorn R. Olsen, MD, PhD
Dean for Research
Harvard School of Dental Medicine
188 Longwood Avenue
Boston, MA 02115
Email: bjorn_olsen@hms.harvard.edu

Harvard Medical School/Harvard School of Dental Medicine are equal opportunity/affirmative action employers. Minorities and women are strongly encouraged to apply.

HARVARD SCHOOL OF DENTAL MEDICINE

University of Minnesota
Medical School

Tenure – Track Faculty Positions

The Department of Integrative Biology and Physiology at the University of Minnesota Medical School seeks outstanding faculty candidates in integrative systems biology, including areas of focus in the cardiovascular system, muscle, metabolism, obesity, diabetes and stress open to all ranks (Assistant, Associate, Full Professor). Substantial resources including new state-of-the-art research building are committed to this effort: **http://www.ahc.umn.edu/research/bdd/**.

Successful candidates will have an innovative research program that embraces biological complexity from molecular building blocks to the living organism. Applicants must have a strong record of research accomplishments, as documented by publications in leading peer-reviewed journals. A commitment to excellence in teaching is essential. Minimum requirements are a PhD, MD or MD/PhD with two or more years postdoctoral training. Additional information about the department: http://physiology.med.umn.edu/. Information on the vibrant Twin Cities community and Minnesota's acclaimed high quality of life: http://www1.umn.edu/wishyouwerehere/. Applicants please apply on-line **http://employment.umn.edu**; **requisition number #179062**; submit cover letter, curriculum vitae, statement of research interests and reference letters to this web address.

The University of Minnesota is an Equal Opportunity Educator and Employer.

MEETINGS

POSITIONS OPEN

POSTDOCTORAL SCHOLARS PROGRAM
Arizona State University Bisgrove

Arizona State University Graduate College is now accepting applications for the Bisgrove Postdoctoral Scholars Program. The award (sponsored by Science Foundation Arizona) is designed to attract the nation's best early career scientists and engineers who exhibit the potential for outstanding competence and creativity in their research areas, strong communication skills, a passion for communicating the importance of their research to society, and a keen interest in educational science outreach to the community. *Individuals eligible to apply are U.S. citizens or permanent residents of the U.S.* Applicants should demonstrate research training and potential to transform ideas into value for society and the interest to work at the convergence of several disciplines. For application and submission procedures, go to **website: http://graduate.asu.edu/bisgrove.**

ASSISTANT PROFESSOR of Terrestrial Paleoecology & Plant Ecology
University of Maine

The School of Biology & Ecology and the Climate Change Institute at the University of Maine (UMaine) seek a **TERRESTRIAL PALYNOLOGIST** with a strong background in plant ecology.

Responsibilities: Develop an internationally recognized research program addressing fundamental questions of response in terrestrial plant ecosystems to past and present climate change. We are especially interested in applicants with interdisciplinary interests and skills that will result in an integrative and collaborative approach to complex problems in basic and applied biology. The individual's research interests should complement the substantial interdisciplinary and international program in the Climate Change Institute (**website: http://climatechange.umaine.edu**) and the School of Biology and Ecology (**website: http://biology.umaine.edu**). The successful applicant will have a joint appointment in the two units, with position responsibilities distributed as 50% research and 50% teaching. Teaching responsibilities include two advanced undergraduate/graduate courses (one in terrestrial plant ecology, and the other in paleoecology) offered in alternating years, an undergraduate course in some aspect of plant biology, and a graduate seminar course. The faculty member is also expected to participate in undergraduate advising and graduate student training, and to have an active and successful extramurally supported research program. The University of Maine offers a variety of interdisciplinary collaborative opportunities for faculty and students as well as access to a diverse range of field sites and modern research facilities and instrumentation.

Qualifications: A Ph.D. is required by date of hire in a relevant area of biological or environmental sciences, with a background in terrestrial plant ecology. In addition, a documented ability to conduct high-quality scientific research, as evidenced by publications in peer-reviewed journals, is essential. Other measures of potential for success such as postdoctoral experience, prior success in obtaining funding, student teaching, mentoring, and interdisciplinary collaboration are desirable.

To apply, submit curriculum vitae, statements of teaching and research interests, unofficial copies of transcripts, and three letters of recommendation in PDF form to **e-mail: sbe@umit.maine.edu** or in hard copy to: **Chair, Terrestrial Paleoecology Search Committee, School of Biology & Ecology, 5751 Murray Hall, University of Maine, Orono, ME, 04469**. Review of applications will begin August 27, 2012 and will continue until the position is filled. Incomplete applications cannot be considered. *Appropriate background checks will be required.*

On January 1, 2011, UMaine became a tobacco-free campus. Information regarding UMaine's tobacco-free policy is online at **website: http://umaine.edu/tobaccofree/.**

The University of Maine is an Equal Employment Opportunity/Affirmative Action Employer.

POSITIONS OPEN

SENIOR RESEARCH POSITIONS
Molecular Biology & Biotechnology
Weill Cornell Medical College

Positions available for development of innovative therapeutic and diagnostic approaches. Applicant should have a Ph.D. with at least three years of postdoctoral training preferably in infectious disease or cancer research, with expertise in molecular biology, genomics, bioinformatics, liquid-handling robotics, and/or automation in protein, DNA, and PCR technology. Excellent communication skills and ability to co-write grant applications is required. Competitive salary commensurate with experience. Send curriculum vitae and names of three references to: **Professor Francis Barany, Department of Microbiology, Box 62, Weill Cornell Medical College, 1300 York Ave, New York, NY 10065. Fax: 212-746-7983. E-mail: barany@med.cornell.edu** *Equal Opportunity Employer.*

DUKE UNIVERSITY FACULTY POSITION

The Department of Dermatology at Duke University Medical Center is seeking outstanding applicants for a research faculty position at the **ASSISTANT, ASSOCIATE,** or **FULL PROFESSOR** level. Applicants should have an M.D., Ph.D., or M.D.-Ph.D. degree. Although applicants with expertise in epigenetics/genomics research are preferred, we are looking for applicants with creativity and demonstrated research excellence in any area of skin research including skin cancer, immunology, and cell biology. A competitive startup package, as well as opportunities for joint appointment in a basic science department, will be available for this position.

Interested candidates should send a copy of his/her curriculum vitae, a statement of research goals, and contact information for three references to:

Russell P. Hall III, M.D.
J. Lamar Callaway Professor and Chair
Department of Dermatology
Duke University School of Medicine
Box 3135
Durham, NC 27710
Telephone: 919-684-3110; fax: 919-684-3002

Applications will be accepted via **e-mail: virginia.king-barker@duke.edu.**

Duke is committed to achieving excellence through diversity. Duke University is an Equal Opportunity/Affirmative Action Employer.